An optical particle counter for the regular application onboard a passenger aircraft: instrument modification, characterization and results from the first year of operation

Von der Fakultät für Physik und Geowissenschaften

der Universität Leipzig

genehmigte

DISSERTATION

zur Erlangung des akademischen Grades

Doctorum rerum naturalium

(Dr. rer. nat.)

vorgelegt

von Diplom-Meteorologe Andreas Weigelt

geboren am 10. Juli 1982 in Zittau

Gutachter: Prof. Dr. Alfred Wiedensohler

Dr. Carl A.M. Brenninkmeijer

Tag der Verleihung: 22. Juni 2015

Referat:

Um die Rolle von Aerosolpartikeln beim Strahlungsantrieb und der heterogenen chemischen Prozessen in der oberen Troposphäre und untersten Stratosphäre (OT/US) verstehen zu können, ist es unabdingbar die Partikelgrößenverteilung zu kennen. Messungen der Partikelgrößenverteilung in dieser Region sind allerdings aufwendig. Der Einsatz von Forschungsflugzeugen ist teuer und deshalb zeitlich und räumlich nur begrenzt. Satellitenmessungen bieten zwar eine gute zeitliche und räumliche (horizontal) Abdeckung, aber nur eine begrenzte vertikale Auflösung. Weiterhin können bisherige Satellitenmessungen die Partikelgrößenverteilung nicht auflösen. Im Rahmen dieser Arbeit wurde deshalb ein optischer Partikelzähler (OPC) Messeinschub für den Einsatz an Bord eines Langstrecken-Passagierflugzeugs aufgebaut (CARIBIC Projekt, www.caribic-atmospheric.com). Mit diesem Messeinschub kann regelmäßig und kosteneffizient die Partikelgrößenverteilung des Akkumulationsmodes in der OT/US gemessen werden. Im April 2010 wurde der neue OPC Einschub erstmals an Bord des Lufthansa Airbus A340-600 (D-AIHE) installiert um die Vulkanasche der Eyjafjallajökull Eruption (April bis Mai 2010) zu messen. Seit Juni 2010 misst der OPC Einschub auf durchschnittlich vier Interkontinentalflügen pro Monat die Partikelgrößenverteilung der OT/US im Größenbereich zwischen 125 und 1300 nm Partikeldurchmesser. Während des Fluges speichert die Datenerfassung alle Rohsignale ab und ermöglicht dadurch eine nutzerspezifische Datenauswertung nach dem Flug (z. B. Anzahl der Größenkanäle oder Zeitauflösung). Im Rahmen dieser Arbeit wurden die Daten mit 32 Größenkanälen und 300 Sekunden analysiert.

Da fluggetragene Messungen immer sehr aufwendig sind, beanspruchte die Entwicklung des OPC Einschubs und des Analysealgorithmus, sowie die Charakterisierung und Zertifizierung mehr als zwei Drittel der Gesamtarbeitszeit dieser Arbeit. Daher ist die Analyse der Messdaten auf das erste Jahr der regulären Messungen bis Mai 2011 beschränkt. Dennoch ist dieser Datensatz geeignet um die wissenschaftliche Relevanz dieser Messungen zu demonstrieren. Um die OPC-Daten zu validieren, wurde ein Vergleich mit bisherigen OPC Messungen von Bord Forschungsflugzeugen durchgeführt. Die Analyse der Vulkanascheflüge im April und Mai 2010 zeigte in der Abluftfahne stark erhöhte Partikelmassekonzentrationen, welche in einigen Vergleichsregionen sehr gut mit der Vorhersage eines Disperionsmodells übereinstimmten. Eine weitere Fallstudie zeigt das Auftreten einer überraschend großen (1000 km) und hoch konzentrierten Abluftfahne über Ostasien nahe Osaka (Japan). In der Abluftfahne wurde die im Analysezeitraum höchste mit dem CARIBIC OPC gemessene

---

Partikelanzahl- und Massenkonzentration beobachtet (ausgenommen Vulkanascheflüge). Eine detaillierte Analyse der parallel gemessenen Spurengase, sowie meteorologischer Daten und LIDAR Profile zeigte, dass die beobachtete Abluftfahne eine Mischung aus Biomasseverbrennungs- und Industrieabgasen aus Ost-China war. Eine dritte Fallstudie stellt einen ersten Versuch einer Massenschließung/Validierung zwischen der aus den CARIBIC OPC-Daten abgeleiteten Partikelmasse und der Partikelmasse aus CARIBIC Impaktorproben dar. Erste statistische Analysen zur vertikalen, meridionalen und saisonalen Variabilität der Partikelgrößenverteilung im Akkumulationsmode und daraus abgeleiteten Parametern zeigen einen vertikal ansteigenden Gradienten für die Partikelanzahl- und Massenkonzentration. Generell war in der US der mittleren Breiten die Konzentration von Akkumulationsmode Partikeln im Mittel um 120% höher als in der OT der mittleren Breiten. Weiterhin wurde in der US der mittleren Breiten eine jahreszeitliche Schwankung gefunden. Im Frühling war die mit dem OPC gemessene Partikelkonzentrationen im Mittel um 120% höher als im Herbst. Diese Befunde lassen sich mit der atmosphärischen Dynamik in der Stratosphäre (Brewer-Dobson Zirkulation) und in der Tropopausenregion (Stratosphäre-Troposphäre-Austauschprozesse) erklären. Eine gefundene negative Korrelation von gasförmigen Quecksilber mit der stratosphärischen Partikeloberflächenkonzentration ($R^2=0.97$) ist ein starker Indikator dafür, dass in der US Aerosolpartikel eine Senke für gasförmiges Quecksilber darstellen. Zum Abschluss unterstreichen zwei Vergleiche der OPC-Daten mit Satellitenmessungen und Ergebnissen eines globalen Aerosolmodels das Potential und den Nutzen der CARIBIC OPC Daten als in-situ gemessenen Referenzdatensatz.

Bibliographic Description:

Weigelt, Andreas

<u>An optical particle counter for the regular application onboard a passenger aircraft: instrument modification, characterization and results from the first year of operation</u>

University of Leipzig, Dissertation

204 pp.[*], 236 Ref.[†], 58 Fig., 7 Tab.

Abstract:

To understand the contribution of aerosol particles to radiative forcing and heterogeneous chemical processes in the upper troposphere and lowermost stratosphere (UT/LMS), the knowledge of the particle size distribution is mandatory. Unfortunately, measurements in the UT/LMS are costly. Research aircrafts are expensive and thus their application is limited in time and space. Satellite remote sensing measurements provide a good temporal and spatial (horizontal) coverage, but only a limited vertical resolution and currently cannot resolve the particle size distribution. Therefore, within this thesis an optical particle counter (OPC) unit was modified for the application onboard a passenger long-haul aircraft within the CARIBIC project (www.caribic-atmospheric.com). The CARIBIC OPC unit provides regular and cost-efficient particle size distribution measurements of accumulation mode particles in the UT/LMS. In April 2010, the new OPC unit was installed for the first time onboard the Lufthansa Airbus A340-600 (D-AIHE) for the measurement of the volcanic ash cloud from the Eyjafjallajökull eruption (April to May 2010). Since June 2010 the OPC unit measures on usually four intercontinental flights per month the UT/LMS particle size distribution in the particle size range 125 to 1300 nm particle diameter. As the data acquisition stores the scattering raw signal and all housekeeping data as well, during the post flight data analysis the temporal- and size channel resolution can be flexible set. Within this work the data were analyzed with 32 size channels and 300 seconds.

As aircraft-borne measurements are always time-consuming, the development of the OPC unit and the analysis routine, as well as its characterization and certification took more than two thirds of the total working time of this thesis. Therefore, the analysis of the data is limited to the first year of regular measurements until May 2011. Nevertheless, this dataset is sufficient to demonstrate the scientific relevance of these measurements. To validate the OPC data, a comparison to particle size distributions measured from board research aircraft was carried out. The analysis of the volcanic ash flights in April and May 2010 showed strongly enhanced particle mass concentrations inside the plumes and agreed in some regions very well to the particle mass concentration predicted by a dispersion model. A further case study shows the occurrence of a surprising large (1000 km) and high concentrated pollution plume over eastern Asia close to Osaka (Japan). Inside the plume the highest particle number- and mass concentrations measured with the OPC unit in the analysis period were observed (except volcanic ash flights). A detailed analysis of the in parallel measured trace gasses as well as meteorological- and LIDAR data showed, the observed plume originate from biomass burning

---

[*] 204 pp. (number of pages)
[†] 236 Ref. (number of references)

and industrial emissions in eastern China. A third case study gives a first attempt of a mass closure/validation between the particle masses derived by the CARIBIC OPC unit and the CARIBIC impactor particle samples. First statistical analyses to the vertical, meridional, and seasonal variation of the accumulation mode particle size distribution and therefrom derived parameter indicate a stratospheric vertical increasing gradient for the particle number- and mass concentration. In general in the mid-latitude LMS the concentration of accumulation mode particles was found to be on average 120% higher than in the mid-latitude UT. The mid-latitude LMS particle size distribution shows a seasonal variation with on average 120% higher concentrations during spring compared to fall. This results can be explained with general dynamics in the stratosphere (Brewer-Dobson Circulation) and in the tropopause region (stratosphere-troposphere-exchange, STE). An anti-correlation of gaseous mercury to the stratospheric particle surface area concentration ($R^2=0.97$) indicates that most likely stratospheric aerosol particles do act as a sink for gaseous mercury. Finally, two comparisons of the OPC data to data from satellite remote sensing and a global aerosol model underline the OPC potential and the benefits of creating an in situ measured reference dataset.

Contents

List of Figures

Figure	Caption	Page

Figure	Caption	Page
5.10	Transmission efficiency of the CARIBIC aerosol inlet (a) and transport efficiency through the CARIBIC sampling line to the OPC unit with respect to sedimentation (b), diffusion (c), and inertial deposition (d). The red arrow indicates the size range, covered by the OPC unit.	67
5.11	Total sampling efficiency of the CARIBIC aerosol inlet and the sampling lines to the OPC unit. Calculations were performed for $p = 260$ hPa, $p = 490$ hPa, $\rho = 1.1$ g/cm^3, and $\rho = 1.8$ g/cm^3. The grey area represents the range between the minimum and the maximum curves out of these four curves. The red curve indicates the mean sampling efficiency.	68
5.12	Width of the signal distribution for different size calibration points. The size of the latex and the ammonium sulfate particles was related to refractive index of mid-latitude UT aerosol particles ($m_{c,total}(\lambda) = 1.48\text{-}0.0143\cdot i$ ($\lambda = 830$ nm)) using a Mie scattering program.	69
5.13	Positive ($unc\_d_p^+$) and negative ($unc\_d_p^-$) absolute uncertainty of the particle size as a function of the particle size (UTA calibration).	71
5.14	Ratio of the MTA and LSA counting efficiency calibration to the UTA counting efficiency calibration. The data points were calculated for the particle size of each size channel, used regularly for data analysis. Particle sizes were transferred from latex and ammonium sulfate calibration using a Mie scattering program.	74
6.1	CARIBIC flights with OPC data between April 2010 and May 2011. All together data from 39 flights were obtained. The dashed lines mark the borders of the analyzed climatologically regions, namely the tropics and subtropics (-35°N to 35°N), as well as the northern hemispheric mid-latitudes (north of 40°N).	80

Figure	**Caption**	**Page**

Figure	Caption	Page
6.15	Overview of the CARIBIC measurements during the plume event on flight LH299 and LH300 from Frankfurt to Osaka/Japan and back. Figure by courtesy of T. Schuck, MPI-Chemistry, Mainz, Germany.	100
6.16	MODIS fire counts from June 20 to 24, 2010 in eastern Asia (red dots). The aircraft flight tracks for flight LH299 and LH300 from Frankfurt to Osaka and back are indicated as solid blue lines. Backward trajectories are indicated as dashed lines in magenta (plume) and olive (background). The position of the trajectories 24 and 48 hours back in time are illustrated as violet and light blue stars, respectively.	101
6.17	CALIPSO space LIDAR CALIOP level 1 data analysis product (http://www-calipso.larc.nasa.gov/products/ last access 20.07.2014) for June 22, 2010. Between 18:20:43 and 18:34:12 UTC the satellite passed east China from north-east to south-west (a; magenta marked track). The "532 nm Total Attenuated Backscatter" signal (b) indicates different vertical layers along the flight track. The "Vertical Feature Mask" analysis product (c) further provides an aerosol- cloud differentiation (explanation of colors given below the time line).	102
6.18	Overview plots for CARIBIC flight LH312 from Osaka to Frankfurt on September 24, 2010. The sampling times of the six particle samples (100 min each) are marked as red line and numbered from one to six.	104
6.19	Ratio of the particle mass concentrations from the OPC analysis to the impactor masses along flight LH312 from Osaka to Frankfurt on September 24, 2010. The impactor sample particle mass concentration was derived by summing up the individual masses of all analyzed elemental materials from the PIXE and PESA analysis.	105

List of Tables

List of Abbreviations

Acronym	Explanation
3d	**3 d**imensional
AS	**A**mmonium **S**ulfate
BM	OPC **B**egin **M**asure mode
BPS	**B**asic **P**ower **S**upply
CALIPSO	**C**loud-**A**erosol **L**idar and **I**nfrared **P**athfinder **S**atellite **O**bservations
CALIOP	**C**loud-**A**erosol **LI**dar with **O**rthogonal **P**olarization
CARIBIC	**C**ivil **A**ircraft for the **R**egular **I**nvestigation of the atmosphere **B**ased on an **I**nstrumented **C**ontainer
CAT-6	twisted pair cable
CCN	**C**loud **C**ondensation **N**uclei
CF	**C**ompact **F**lash card
CFD	**C**omputational **F**luent **D**ynamics
Ch-1	OPC **C**hannel **1**
Ch-2	OPC **C**hannel **2**
Ch-3	OPC **C**hannel **3**
CNRS	**C**entre **N**ational de la **R**echerche **S**cientifique (National Center for Scientific Research), Paris/France
CONTRAIL	**C**omprehensive **O**bservation **N**etwork for **TR**ace gases by **AIr**L**iner**
CPC	**C**ondensation **P**article **C**ounter
CWC	**C**loud **W**ater **C**ontent

Acronym	Explanation
DLR	**D**eutsches Zentrum für **L**uft und **R**aumfahrt, Oberpfaffenhofen/Germany
DMA	**D**ifferential **M**obility **A**nalyzer
DMT	**D**roplet **M**easurement **T**echnologies
DOAS	**D**ifferential **O**ptical **A**bsorption **S**pectrometer
EASA	**E**uropean **A**viation **S**afety **A**gency
EC	**E**lemental **C**arbon
ECMWF	**E**uropean **C**entre for **M**edium-range **W**eather **F**orecasts
EMC	**E**lectro**M**gnetic **C**ompatibly
EMI	**E**lectro**M**agnetic **I**nterference
ERBS	**E**arth **R**adiation **B**udget **S**atellite
EURAD	**EUR**opean **Ai**r pollution **D**ispersion model
FLEXPART	**FLEX**ible **PART**icle dispersion model
GASP	**G**lobal **A**tmospheric **S**ampling **P**rogram
GC-MS	**G**as **C**hromatography – **M**ass **S**pectrometry
GEM	**G**aseous **E**lemental **M**ercury
GLOMAP	**GLO**bal **M**odel of **A**erosol **P**rocesses
GOM	**G**aseous **O**xidized **M**ercury
GOME-2	**G**lobal **O**zone **M**onitoring **E**xperiment–**2**
HZG	**H**elmholtz **Z**entrum **G**eesthacht, Geestacht/Germany
IAGOS	**I**n-service **A**ircraft for a **G**lobal **O**bserving **S**ystem
IfT/TROPOS	Leibniz **I**nstitut **f**ür **T**roposphärenforschung, Leipzig/Germany
IIN	**I**on **I**nduced **N**ucleation
IMK	Institut für **M**eteorologie und **K**limatologie
IN	OPC **IN**itialization mode
INDOEX	**IND**ian **O**cean **E**xperiment
IPCC	**I**ntergovernmental **P**anel on **C**limate **C**hange
ITCZ	**I**nter**T**ropical **C**onvergence **Z**one

Acronym	Explanation
JAL	**J**apan Air**L**ines
KIT	**K**arlsruhe **I**nstitut für **T**echnologie, Karlsruhe/Germany
KNMI	**K**oninklijk **N**ederlands **M**eteorologisch **I**nstituut (Royal Netherland Meteorological Institute), De Bilt/Netherlands
KS-93	OPC model from the Japanese company RION CO., LTD.
LIDAR	**LI**ght **D**etection **A**nd **R**anging
LMS	**L**ower**M**ost **S**tratosphere
LS	**L**ower **S**tratosphere
LSA	mid-latitude **L**owermost **S**tratospheric **A**erosol
MFC	**M**ass **F**low **C**ontroller
MODIS	**MOD**erate-resolution **I**maging **S**pectroradiometer
MOZAIC	**M**easurement of **OZ**one and water vapor by **A**irbus **I**n-servi**C**e aircraft
MPI-C	**M**ax-**P**lank **I**nstitute for **C**hemistry
MS	OPC **M**ea**S**ure mode
MT	**M**iddle **T**roposphere
MTA	tropical **M**id-**T**ropospheric **A**erosol
MUT	tropical and subtropical **M**id- and **U**pper **T**roposphere
NASA	**N**ational **A**eronautics and **S**pace Administration
NDIR	**N**on-**D**ispersive **I**nfra**R**ed absorption
NMHC	**N**on-**M**ethane **H**ydro**C**arbons
NOXAR	measurements of **N**itrogen **OX**ides and ozone along **A**ir **R**outes
OC	**O**rganic **C**arbon
OPC	**O**ptical **P**article **C**ounter
PESA	**P**article **E**lastic **S**cattering **A**nalyses
PID	**P**roportional-**I**ntegral-**D**erivative controller algorithm
PIXE	**P**article-**I**nduced **X**-ray **E**mission
PTR-MS	**P**roton **T**ransfer **R**eaction **M**ass **S**pectrometer

Acronym	Explanation
PV	**P**otential **V**orticity
PVU	**P**otential **V**orticity **U**nit (1 PVU = 10^{-6} m$^2 \cdot$ K $\cdot$ kg$^{-1} \cdot$ s^{-1})
SA	**S**ulfuric **A**cid (H_2SO_4), 75% solution with water
SAGE II	**S**tratospheric **A**erosol and **G**as **E**xperiment
SB	OPC **S**tand**B**y mode
SILAM	**S**ystem for **I**ntegrated mode**L**ling of **A**tmospheric co**M**position
SMB	**S**ub-**M**iniature-**B** output connector
SPARC	**S**tratosphere-troposphere **P**rocesses **A**nd their **R**ole in **C**limate
ST	command "**ST**atus" of master computer
STE	**S**tratosphere-**T**roposphere air **E**xchange
STP	**S**tandard **T**emperature and **P**ressure conditions (T = 273.15 K; p = 1013.25 hPa)
TGM	**T**otal **G**aseous **M**ercury
TOMCAT	**T**oulouse **O**ff-line **M**odel of **C**hemistry **A**nd **T**ransport
TP	**T**ropo**P**ause
TRAJKS	KNMI trajectory server
TROZ	**TR**opospheric **OZ**one campaign
TRU	**T**ransformer **R**ectifier **U**nit
TTL	**T**ropical **T**ropopause **L**ayer
UB	**U**niversity of **B**ern, Bern/Switzerland
UEA	**U**niversity of **E**ast **A**nglia, Norwich/England
UH	**U**niversity of **H**eidelberg, Heidelberg/Germany
UHSAS	**U**ltra **H**igh **S**ensitive **A**erosol **S**pectrometer
UK	**U**nited **K**ingdom
UKCA	**U**nited **K**ingdom **C**hemistry and **A**erosol climate model
UL	**U**niversity of **L**und, Lund/Sweden
UNEP	**U**nited **N**ations **E**nvironment **P**rogram
US	**U**pper **S**tratosphere
USB	**U**niversal **S**erial **B**us
UT	**U**pper **T**roposphere
UTA	mid-latitude **U**pper **T**ropospheric **A**erosol
UV	**U**ltra**V**iolet

Acronym	Explanation
VAAC	**V**olcanic **A**sh **A**dvisory **C**entre
VAF	**V**olcanic **A**sh **F**lights
VDC	**D**irect-**C**urrent **V**oltage
VEI	**V**olcanic **E**ruption **I**ndices
WMO	**W**orld **M**eteorological **O**rganization

List of Symbols

Latin letters

Symbol	Unit	Explanation
A_0	[A_0, STP]	Measured parameter at standard conditions
A_1	[1]	Approximation parameter
A_2	[1]	Maximum asymptotic counting efficiency
A_a	[A_a]	Measured parameter at ambient conditions
C_a	[m²]	Absorption effective cross section
C_c	[1]	Cunningham slip correction factor
C_e	[m²]	Extinction effective cross section
C_s	[m²]	Scattering effective cross section
$C(d_{p,1})$	[1/cm^3]	Measured particle concentration at the associated size channel where the erroneous counts are located on average
$C(d_{p,2})$	[1/cm^3]	Measured concentration at a certain size channel
$C_{callib}(d_{p,2})$	[1]	Integral number of all "correct" counts for a certain size channel ($d_{p,2}$)
$C\_error_{callib}(d_{p,2})$	[1]	Integral number of all erroneous counts for a certain size channel ($d_{p,2}$)

Symbol	Unit	Explanation
c	[m/s]	Velocity of light in vacuum ($c = 2.9979 \cdot 10^8$ m/s)
D_p	[m²/s]	Diffusion coefficient of a aerosol particle
d_p	[nm]	Particle diameter
$\left[d_{p,i} \right]$	[1/cm³]	Measured particle concentration at a certain size channel with $d_{p,i}$
$d_{p,i}(LSA)$	[nm]	Calculated particle diameter for the same OPC signal intensity as for $d_{p,i}(UTA)$, but with the LSA calibration
$d_{p,i}(MTA)$	[nm]	Calculated particle diameter for the same OPC signal intensity as for $d_{p,i}(UTA)$, but with the MTA calibration
$d_{p,i}(UTA)$	[nm]	Mean particle diameter of a certain size channel (i) using the UTA calibration
$d_{p,i,error}$	[nm]	Diameter of size channel at which erroneous pulses are counted
$d_{p,i,\text{true}}$	[nm]	Mean particle diameter causing erroneous counts
d_{tb}	[m]	Inner diameter of tubing
$d_{p,dry}$	[nm]	Particles dry diameter
$d_{p,\text{wet}}$	[nm]	Particles wet diameter
$E(\lambda)$	[J]	Energy of a single photon
$Error(d_{p,2})$	[1]	Relative fraction of erroneous counts, caused by a certain size channel ($d_{p,2}$)
$Error\_fraction(d_{p,1})$	[1]	Relative fraction of potential erroneous counts in a certain size channel ($d_{p,1}$)
e	[C]	Elementary charge ($e = 1.6022 \cdot 10^{-19}$ C)

Symbol	Unit	Explanation
G	[m²]	Ratio of the individual effective cross section to the particle geometric cross section
g	[m/s²]	Acceleration of gravity (g = 9.81 m/s²)
h	[J·s]	Planck constant ($h = 6.626 \cdot 10^{-34}\,\text{J}\cdot\text{s}$)
I_i	[J/(m² · s)]	Energy flux density of the incident radiation
k_b	[J/K]	Bolzmann constant ($k_b = 1.38 \cdot 10^{-23}$ J/K)
l_{DMA}	[m]	Length of DMA electrode
l_{tb}	[m]	Length of tubing
$\left[m_i \right]$	[µg/m³]	Particle mass concentration of a certain size channel (i)
$m(\lambda)$	[1]	Complex refractive index
$m_{c,i}(\lambda)$	[1]	Complex refractive index of a certain compound i
$m_{c,total}(\lambda)$	[1]	Complex refractive index of the internally mixed aerosol particles
N_4	[1/cm³]	Particle number concentration of aerosol particles with a diameter larger than 4 nm
$N_{4\text{-}12}$	[1/cm³]	Particle number concentration of aerosol particles with a diameter between 4 and 12 nm
N_{12}	[1/cm³]	Particle number concentration of aerosol particles with a diameter larger than 12 nm

Symbol	Unit	Explanation
N_{18}	[1/cm^3]	Particle number concentration of aerosol particles with a diameter larger than 18 nm
N_i	[1]	Number of counts in a certain size channel
N_{CPC}	[1/cm^3]	Particle number concentration measured with the CPC
$N_{CPC,s}$	[1/cm^3]	Total number of singly charged particles the CPC counted
$N_{multiple}$	[1]	Number of all multiple charged particles
N_{OPC}	[1/cm^3]	Particle number concentration measured with the OPC
$N_{OPC,s}$	[1/cm^3]	Total number of singly charged particles the OPC counted
n	[1]	Refractive index real part
n'	[1]	Refractive index imaginary part
n_e	[1]	Number of charges of a aerosol particle
n_{OPC}	[1]	Number of size channels in the OPC particle size distribution

Symbol	Unit	Explanation
$P(\theta)$	[1/sr]	Scattering phase function
p	[hPa]	Gas pressure
p_0	[hPa]	Standard condition pressure (p_0 = 1013.25 hPa)
p_a	[hPa]	Ambient gas pressure

Symbol	Unit	Explanation
Q_a	[1]	Absorption efficiency
Q_e	[1]	Extinction efficiency
Q_s	[1]	Scattering efficiency
$Q_{DMA,ma}$	[m³/s]	Quasi monodisperse aerosol volume flow at DMA exit
$Q_{DMA,pa}$	[m³/s]	Polydisperse aerosol volume flow at DMA entrance
$Q_{DMA,s}$	[m³/s]	DMA sheath air volume flow

Symbol	Unit	Explanation
RF	[m²/particle]	OPC theoretical response function
$r_{DMA,1}$	[m]	Radius of inner DMA electrode
$r_{DMA,2}$	[m]	Radius of outer DMA electrode
r_{eff}	[μm]	Effective particle radius
r_p	[μm]	Particle radius
$rel\_unc_{\varepsilon,i}^{+}$	[1]	Positive relative uncertainty when using UTA
$rel\_unc_{\varepsilon,i}^{+}$	[1]	Positive relative uncertainty when using UTA counting efficiency curve for all aerosol types
$rel\_unc_{\varepsilon,i}^{-}$	[1]	Negative relative uncertainty when using UTA counting efficiency curve for all aerosol types
rel_unc_{MFC}	[1]	Relative uncertainty of the MFCs
rel_unc_{p}	[1]	Relative uncertainty of p-sensor
$rel\_unc_{T,1}$	[%]	Relative uncertainty of T-sensor 1
$rel\_unc_{T,2}$	[%]	Relative uncertainty of T-sensor 2
rH	[%]	Relative humidity
rs_i	[V]	Response signal for a certain size channel (i)
S	[μm²]	Particle surface
Stk	[1]	Stokes number
$s_1(\theta)$	[1]	Mie scattering amplitude function perpendicular to the plane of scattering
$s_2(\theta)$	[1]	Mie scattering amplitude function parallel to the plane of scattering
$[s_i]$	[μm²/cm³]	Particle surface area concentration of a certain size channel (i)
T	[K]	Temperature
T_0	[K]	Standard condition temperature (T_0 = 273.15 K)
T_a	[K]	Ambient gas temperature

Symbol	Unit	Explanation
U_{DMA}	[V]	Voltage at DMA electrodes
$unc\_d_{p,i}^{\pm}$	[nm]	Overall absolute uncertainty concerning the particle size
$unc_{c,i}^{\pm}$	[1/cm^3]	Overall absolute uncertainty of a certain size channel (i) concerning particle number concentration
$unc_{c,int}^{\pm}$	[1/cm^3]	Overall absolute uncertainty of the integral particle number concentration
$(unc_{s,i}^{\pm})$	[μm²/cm^3]	Overall absolute uncertainty of a certain size channel (i) concerning particle surface area concentration
$unc_{s,int}^{\pm}$	[μm^2/cm^3]	Overall absolute uncertainty of the integral particle surface area concentration
$unc_{m,i}^{\pm}$	[μg/m^3]	Overall absolute uncertainty of a certain size channel (i) concerning particle mass concentration
$unc_{m,int}^{\pm}$	[μg/m^3]	Overall absolute uncertainty of the integral particle mass concentration
$unc_{gauss,i}$	[nm]	Absolute uncertainty of the size calibration for each size channel
$unc_{refr,i}^{+}$	[nm]	Positive absolute uncertainty concerning the used refractive index for each size channel
$unc_{refr,i}^{-}$	[nm]	Negative absolute uncertainty concerning the used refractive index for each size channel
$(unc_{erroneous}(d_{p,i,error}))$	[1/cm³]	Absolute uncertainty of a certain particle size channel
unc_{MFC}	[l/min]	Absolute uncertainty of the MFC
unc_{MFC_sample}	[l/min]	Absolute uncertainty of the MFC, controlling the sample air flow
unc_{MFC_sheath}	[l/min]	Absolute uncertainty of the MFC, controlling the sheath air flow
unc_{sample}	[l/min]	Absolute uncertainty of sample air
unc_{ρ}	[μg/nm^3]	Absolute uncertainty of particle density

Symbol	Unit	Explanation
V	[μm³]	Particle volume
v_{gas}	[m/s]	Flow velocity of fluid inside tubing
$v_{p,sed}$	[m/s]	Settling speed of a particle in a fluid
W_a	[J/s]	Energy flux of absorption
W_e	[J/s]	Energy flux of extinction
W_i	[J/s]	Incident energy flux (total energy flux)
W_s	[J/s]	Energy flux of scattering
$W_s(\theta,\psi)$	[J/(s · sr)]	Energy flux of scattering to a certain solid angle
x	[1]	Dimensionless size parameter (ratio of particle circumference to wavelength)
Z_{DMA}	[m²/(V · s)]	Electrical mobility of an DMA
Z_p	[(C · s)/kg]	Electrical mobility of an aerosol particle

Greek letters

Symbol	Unit	Explanation
$\alpha_{tb,b}$	[rad]	Bend angle of tubing
$\alpha_{tb,t}$	[rad]	Tilt angle of tubing referring to the horizontal direction
$\gamma(\theta)$	[1/(m · sr)]	Azimuthal symmetric volume scattering function
$\gamma(\theta,\psi)$	[1/(m · sr)]	Not azimuthal symmetric volume scattering function

Symbol	Unit	Explanation
$\delta_{error}(d_{p,i})$	[1]	Size dependent fraction of additional small erroneous particle counts
$\delta_{error}(d_{p,i})$	[1]	Size dependent fraction of additional small erroneous particle counts
$\varepsilon(d_p)$	[1]	Counting efficiency
$\varepsilon(d_{p,UTA}(rs_i))$	[1]	Counting efficiency for a particle diameter, calculated from a certain response signal (rs_i) using the UTA calibration curve
$\varepsilon(d_{p,LSA}(rs_i))$	[1]	Counting efficiency for a particle diameter, calculated from the same response signal (rs_i) as for $d_{p,UTA}(rs_i)$, but using the LSA calibration curve
$\varepsilon(d_{p,MTA}(rs_i))$	[1]	Counting efficiency for a particle diameter, calculated from the same response signal (rs_i) as for $d_{p,UTA}(rs_i)$, but using the MTA calibration curve
ε_{dif}	[1]	Transport efficiency with respect to diffusion losses
ε_i	[1]	Counting efficiency for a certain size channel
ε_{imp}	[1]	Transport efficiency with respect to impaction losses
ε_{inlet}	[1]	Transmission efficiency of the CARIBIC aerosol inlet
ε_{sampl}	[1]	Total sampling efficiency of the CARIBIC aerosol inlet system (aerosol inlet + sampling line)
ε_{sed}	[1]	Transport efficiency with respect to sedimentation due to the gravitational force
η	[kg/(m·s)]	Dynamic viscosity

Symbol	Unit	Explanation
Θ	[K]	Potential temperature
θ	[rad]	Plane angle of scattering
θ_{min}	[rad]	Minimum plane angle of scattering
θ_{max}	[rad]	Maximum plane angle of scattering
κ_1	[1]	Dimensionless parameter for calculation of transport efficiency with respect to sedimentation losses
κ_2	[1]	Dimensionless parameter for calculation of transport efficiency with respect to diffusion losses
λ	[nm]	Wavelength
π	[1]	Ratio of a circle's circumference to its diameter ($\pi = 3.14159$)
ρ_p	[kg/m^3]	Density of particle material
ρ_{UTA}	[µg/nm^3]	Particle density of UTA
σ_s	[1/m]	Volume scattering coefficient
τ_p	[s]	Atmospheric lifetime of aerosol particles
τ_{ns}	[s]	Characteristic aerosol particle wet removal time
υ	[1/s]	Frequency of the incident radiation

Symbol	Unit	Explanation
Φ_{tb}	$[m^3/s^1]$	Volume flow of fluid inside tubing
ϕ_{MFC_sample}	$[l/min]$	Gas volume flow at the MFC, controlling the sample air flow
ϕ_{MFC_sheath}	$[l/min]$	Gas volume flow at the MFC, controlling the sheath air flow
ϕ_{sample}	$[l/min]$	sample air flow
φ	$[°N]$	Latitude
ψ	$[rad]$	Azimuthal angle of scattering
Ω	$[sr]$	Solid angle of scattering

Other symbols

Symbol	Unit	Explanation
$\partial T / \partial z$	$[K/m]$	Vertical temperature gradient

Chemicals

Name	Formula
Acetone	C_3H_6O
Americium 241	Am^{241}
Ammonia	NH_3
Ammonium sulfate	$(NH_4)_2SO_4$
Benzene	C_6H_6
Beryllium isotopes	$^{7/10}Be$
Bromine	Br

Name	Formula
Calcium	Ca
Carbon dioxide	CO_2
Carbone monoxide	CO
Carbonyl sulfide (commonly written as COS)	OCS
Dimethyl sulfide (DMS)	$(CH_3)_2S$
Hydroxyl radical	OH
Iron	Fe
Mercury	Hg
Methanol	CH_3OH
Methyl chloride	CH_3Cl
Nitrogen	N_2
Nitrogen oxides	NO_y
Oxygen	O_2
Ozone	O_3
Silicon	Si
Sulfur dioxide	SO_2
Sulfur hexafluoride	SF_6
Sulfuric acid	H_2SO_4
Titanium	Ti
Water (vapor)	H_2O

1 Introduction

Atmospheric aerosol particles are of great importance for quantifying changes in the Earth´s radiation budget and the associated anthropogenic climate change [Intergovernmental Panel on Climate Change, IPCC 2013, p.604-605, p. 614-624]. First, solar radiation is scattered and absorbed by aerosol particles (direct radiative forcing). Whereas backscattering into the outer space causes cooling, the absorption causes warming of the atmosphere. Scattering and absorption are strongly influenced by particle properties, i.e. chemical and physical composition, size, and shape (cf. Sec. 4.1). In the net balance, the cooling effect of atmospheric aerosol particles dominates the warming effect. The overall direct radiative forcing due to anthropogenically emitted aerosol particles is quantified to be -0.77 to +0.23 W/m² (mean: -0.27 W/m²) [IPCC 2013, p. 14]. Particles in the size range 100 nm < d_p < 1000 nm in diameter (accumulation mode particles) have the largest scattering efficiency and the longest atmospheric life time [Seinfeld and Pandis 1998 p. 1132-1133, Winkler et al., 2000, p. 31]. Thus measurements of accumulation mode particles are of particular interest.

Secondly, the influence of aerosol particles on cloud properties affects the Earth´s radiation budget, too (indirect effect, [Seinfeld and Pandis, 1998, p.1170-1180, IPCC, 2013, p. 576-578]). An increased number of cloud condensation nuclei (CCN) results in an increased number of cloud droplets. The available cloud water is thus distributed to more condensation nuclei and hence the cloud droplets are smaller. Higher concentrations of small cloud droplets reflect more light than mass equivalent lower concentrations of large cloud droplets (Twomey effect [Twomey, 1977]). This phenomenon is called the first indirect radiative forcing [Hobbs, 1993, p. 33-52; Brenguier et al., 2000]. Moreover, smaller cloud droplets lead to a longer cloud life time and less precipitation. This phenomenon is called the second indirect radiative forcing [Albrecht, 1989]. Again, the accumulation mode particles (and slightly smaller particles with diameters larger than about 70 nm) represent the majority of CCN and are hence important. In the recent IPCC report (2013), the radiative forcing caused by the above mentioned indirect aerosol effects is summarized to be -1.33 to -0,06 (mean -0.55) W/m² [IPCC 2013, p. 14]. The overall contribution of aerosol particles to

the global radiative forcing (direct and indirect effects together) is calculated to be -1.9 to -0.1 (mean -0.9) W/m² [IPCC, 2013, p.13].

The uncertainty of the aerosol particle's influence (-1.9 to -0.1 W/m²) still belongs to the largest uncertainties of the total anthropogenic radiative forcing (+1.1 to +3.3 W/m²) [IPCC, 2013, p. 13-14, 661]. Besides the complexity of the roles of aerosol, a basic reason for the still large uncertainty is the lack of regular aerosol measurements, in particular in regions that are hard to access (e.g. tropics and polar regions). The upper troposphere (UT) and lower stratosphere (LS) also is poorly undersampled. The UT/LS radiative forcing is highly sensitive to changes in atmospheric composition [Riese et al., 2012]. Submicrometer aerosol particles in the UT/LS influence the Earth`s radiation budget not only directly [Lacis et al., 1992] and indirectly [Lohmann and Feichter, 2005], but also by changing trace gas concentrations through heterogeneous chemical processes [Hanson et al., 1994]. Existing in situ measured UT/LS aerosol datasets are mostly based on short measurement campaigns (cf. Tab. 6.1). The deployment of research aircraft on a regular basis over large regions is laborious, time-consuming and therefore prohibitively expensive. Consequently, regular in situ measurements in the UT/LS did not exist in the past. Data from satellite remote sensing provide a good temporal and spatial (horizontal) coverage. However, active and passive remote sensing methods offer together mostly limited vertical resolution and cannot resolve the particle size distribution.

Since 1997, the CARIBIC project (Civil Aircraft for the Regular Investigation of the atmosphere Based on an Instrument Container, www.caribic-atmospheric.com, last access: 30.08.2014) offers the possibility to conduct regular (once per month) and cost-efficient (a factor of more than ten lower costs compared to research aircraft flight hours) measurement flights in the upper troposphere and lowermost stratosphere (UT/LMS). The CARIBIC aircraft, since 2005 a Lufthansa Airbus A340-600, that carries the scientific equipment flies mostly in the altitude rage of the mid-latitude tropopause (9-12 km). Thereby CARIBIC creates a unique dataset for the better understanding of the atmospheric composition and the tropospheric- stratospheric air mass exchange.

The objective of the work presented here was the modification and subsequent deployment of a commercial optical particle counter (OPC) onboard the CARIBIC aircraft. To this purpose, the OPC was securely mounted into a 19" rack unit and a new gas flow system, a data acquisition, a unit control, as well as a data analysis routine were developed. The whole unit was comprehensively tested and characterized in laboratory. At the end the new OPC unit was successfully certified for installation into the CARIBIC aircraft. In future the data of this new instrument onboard the CARIBIC aircraft will significantly contribute to the following scientific questions:

1) **What is the average UT/LMS particle size distribution in different climatic regions?**
   ➔ Previous in situ measurements are based only on individual research aircraft flights commonly on short campaigns with limited spatial coverage and a focus on special (local) conditions. With the OPC onboard the CARIBIC aircraft, regular long-term measurements of the UT/LMS particle size

distribution with a nearly global coverage (cf. Fig. 3.1) becomes possible for the first time. This dataset can be used to determine the average particle size distribution in different climatic regions, which can be used in climate models to reduce the uncertainty of the aerosol particle influence on the radiative forcing.

2) Is there a trend in the UT/LMS particle size distribution?

➔ Several recent publications have indicated that there is a trend in the stratospheric aerosol and how important that trend is [Solomon et al., 2011]. For the UT/LMS there was until the time of submitting this thesis too little information available to make a statement about a trend. As however CARIBIC is projected to continue its regular flights on different intercontinental routes, statistically valid seasonality and long-term trend analyses may be derived in the future.

3) What are the source and sink processes for accumulation mode particles in the UT/LMS and how effective are they?

➔ In addition to the particle size distribution, the CARIBIC system measures other aerosol parameters and a large number of trace gases (Tab. 3.1), which allows the identification of air mass origins, as well as of plumes from natural or anthropogenic sources. Combining the short-term (plume) measurements with the long-term background air measurements, the relative contribution of plumes to the background concentration can be estimated.

4) How does the air mass exchange between UT and LS influence the particle size distribution in the tropopause region?

➔ Stratospheric aerosols have a much longer atmospheric life time compared to UT aerosols and therefore the concentration of accumulation mode particles often is higher in the LS [Hofmann 1990, Minikin et al., 2003; Young et al., 2007]. By studying the relation of aerosol particle concentration to specific trace gases, the influence of the exchange processes can be understood.

5) How does the particle surface area concentration influence the concentration of trace gases?

➔ One major sink for "sticky" trace gases in the UT/LMS region is the condensation onto preexisting aerosol or ice particles. In the analyzed region the total particle surface area concentration is dominated by accumulation mode particles (cf. Fig. 2.3). Correlating the OPC derived particle surface area concentration with concentrations of trace gases could thus indicate sink (and source) processes.

6) How well do remote sensing measurements and global models represent the UT/LMS aerosol?

➔ Aerosol parameters and properties derived from remote sensing methods (e.g. surface LIDAR[1] and satellite based LIDAR and passive measurements) or from modelling need to be validated by in situ measurements. The growing CARIBIC dataset will provide a keystone dataset for the particle size distribution in the UT/LMS.

The development of the OPC unit and the analysis routine, as well as its characterization and certification took more than two thirds of the total effort of the work for this thesis. Therefore, the analysis of the measurement data is limited to only the first year of routine operation which is ample to demonstrate the contribution of the OPC data to the scientific questions raised above. The subsequent Ch. 2 briefly describes the structure of the Earth´s atmosphere, focusing on the UT/LMS and the aerosol dynamics in this region. The CARIBIC project with the aircraft, the gas- and aerosol inlet system, and the measurement container is introduced in Ch. 3. In the beginning of Ch. 4 a short overview of the scattering and absorption of light by aerosol particles is given and the modifications of the OPC for installation onboard the aircraft are described. The characterization of the modified OPC, the calibration for particle size and number concentration, as well as an estimate of measurement uncertainty is given in Ch. 5. Chapter 6 presents the results of the first year of measurements until May 2011. In this chapter the regular data analysis is presented, the measured particle size distributions are compared to previous measurements, and three case study analyses are made (volcanic ash measurements, the observation of a strong pollution plume, and a first attempt of a mass closure study). Furthermore, Ch. 6 introduces first statistical analyses to the vertical, meridional, and seasonal variation of the particle size distribution and the anti-correlation of gaseous mercury to the stratospheric particle surface area concentration. To demonstrate the OPC potential and the benefits, the OPC dataset is compared to data from satellite remote sensing and model data. Chapter 7 summarizes this work and gives conclusions and outlook.

---

[1] Light detection and ranging

2 The upper troposphere and lowermost stratosphere

The present work describes the development and characterization as well as the first year of operation of an OPC onboard a civil long-haul aircraft. This OPC measures the aerosol particle size distribution along intercontinental flight tracks. The aircraft cruise altitude is between 8 and 12 km, thus repeatedly crossing the tropopause from the UT into the LMS and back. Section 2.1 shortly describes the vertical structure of the Earth´s atmosphere. The air mass exchange between the troposphere and the stratosphere is briefly discussed in Sec. 2.2. Finally, the aerosol particles in the UT/LMS are described in Sec. 2.3.

2.1 The vertical structure of the Earth´s atmosphere

According to the US standard atmosphere defined in 1976, the Earth´s atmosphere is composed of four main layers and crossover areas in between (Fig. 2.1). The lowermost layer is the troposphere, extending from the earth surface to about 8 km at the poles and up to 18 km in the tropics [Seinfeld and Pandis, 1998 p. 8]. The troposphere is characterized by a negative vertical temperature gradient of about -0.0065 K/m and therefore by rapid vertical mixing. All weather related processes take place inside this layer. The tropopause with temperatures around -56°C (US standard atmosphere)[2] separates the troposphere from the stratosphere. In the stratosphere high O_3 concentration effectively absorb short wavelength radiation, leading to warming. From the tropopause up to about 20 km no vertical temperature gradient is apparent (isotherm, US standard atmosphere). There above the temperature increases up to the stratopause, which is the upper border of the stratosphere at 45 to 55 km. Due to this warming, the stratosphere is stable stratified and vertical mixing within this layer is slow. Above the

---

[2] The 1976 defined US standard atmosphere gives a tropopause temperature of -56°C in the altitude range 11 to 20 km. At the poles the tropopause temperature is about -50°C and at the equator about -80°C.
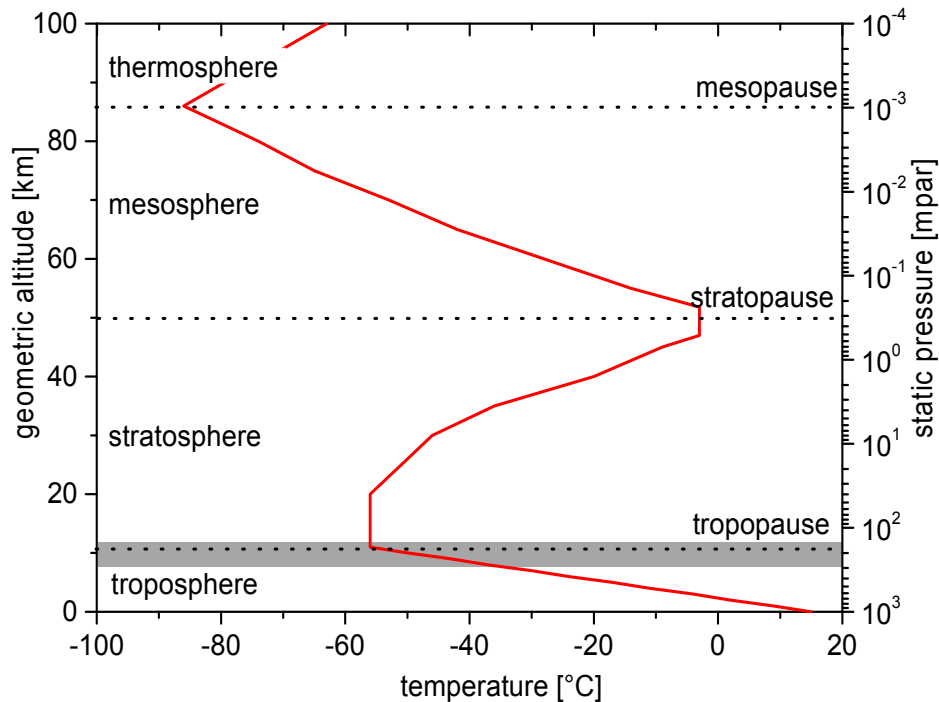
Figure 2.1: Vertical temperature profile of the US-standard atmosphere (1976), taken from Seinfeld and Pandis [1998] p. 7, 1293. The gray area indicates usual CARIBIC cruise altitude (8-12 km).

stratopause the mesosphere extend up to an altitude of 80 to 90 km. Within the mesosphere the temperature again decreases to about -85 °C (187 K) leading to a fast vertical mixing. The mesopause separates the mesosphere from the thermosphere. In the thermosphere N_2 and O_2 effectively absorb short wavelength radiation and the temperature increases with increasing altitude, like in the stratosphere. Above 500 km altitude the exosphere represent the transition from the earth atmosphere into the outer space (not shown in Fig. 2.1).

2.2   Stratosphere-troposphere air exchange

This work focuses on aerosol measurements in the UT and LMS. This region is important because strong concentration gradients of various species exist across the tropopause (TP). Inside the well mixed troposphere, measurements can be strongly influenced by different weather phenomena (e.g. thunderstorm systems or large scale circulation cells). On the contrary, in the stratosphere vertical air motion is inhibited by the stratification due to the temperature inversion. The TP separates these two entirely different layers, acting as a barrier for air exchange [James and Legras, 2009]. Nevertheless, large scale dynamic processes (e.g. circulation cells) and small scale synoptic phenomena (e.g. deep convection) can induce stratosphere-troposphere air exchange (STE). Figure 2.2 displays the main dynamic processes of STE [after Holton et al., 1995, SPARC report N°4, 2006[3], and Spackman et al., 2007]. The stratosphere

---

[3] Stratospheric processes and their role in climate (SPARC): "Assessment of Stratospheric Aerosol Properties (ASAP)", Thomason and Peter (editor), 2006

can be divided into the lower stratosphere (LS) and the upper stratosphere (US). The boundary between the LS and the US is defined by potential temperature isentropes (Θ) that do not intersect with the TP at any latitude [Gettelman et al., 2011]. This means that except the Brewer-Dobson circulation which will be described later no air exchange takes place between the UT and the US. Therefore, in the literature the US is often called "stratospheric overworld". Holton et al. [1995] gives the $\Theta \sim 380\,K$ isentrope as the boundary between LS and US. Outside the tropics the lower part of the LS is called the lowermost stratosphere (LMS) and is confined by the $\Theta = 380\,K$ isentrope at the top and the extratropical TP at the base [Spackman et al., 2007]. Inside the tropics the TP is embedded in the tropical tropopause layer (TTL). As the upper part of the TTL belongs to the LS, Gettelman et al., [2011] defines the boundary between LS and the stratospheric overworld to be located at isentropic surfaces of $\Theta \sim 400$ to $440\,K$. The TTL encapsulates the transition between localized deep convection in the UT and large scale diabatic ascent in the LS and US (Fig. 2.2 path 1 and 3) [Holton et al., 1995, Spackman et al., 2007]. The tropical large scale diabatic ascent into the tropical US is part of the Brewer-Dobson circulation, which is a global-scale overturning mass circulation [Dobson et al., 1946, Brewer, 1949]. In the US the air is transported poleward (path 4), which is caused mainly by the dissipation of planetary Rossby waves, propagating from the troposphere into the stratosphere [Gettelman et al 2011 and references therein]. Large scale subsidence processes towards the pole (path 5) mix the transported tropical tropospheric air from the US into the LS. The traveling time of air parcels from the TTL to the polar LS along this path is estimated to be on the order of five years [Spackman et al., 2007 and references therein]. Consequently, the extratropical US is influenced mainly by tropical, but not by extratropical tropospheric air [Hoor et al., 2005]. On the contrary, extratropical LS air can be influenced by fresh air from the tropical LS (path 6), the tropical UT (path 7), and the extratropical troposphere (path 8, 9). The poleward transport of tropical LS air consists of three stepwise transport processes: (6a) quasi-horizontal isentropic transport between the upper TTL and the mid-latitudes, (6b) diabatic descent into the LMS between the subtropical jet (purple circle) and the polar jet (purple solid and dashed line), and (6c) quasi-horizontal isentropic mixing in the upper part of the LMS $(350\,K < \Theta < 380\,K)$ [Spackman et al., 2007]. With about one year, the traveling time along path (6) is estimated to be much faster than the path along the Brewer-Dobson circulation. The temperature gradient between the mid-latitudes and the pole induce the westerly polar jet in the lower part of the US and the LS [Schoeberl et al., 1992], representing the edge of the polar vortex and acting as barrier for quasi-horizontal isentropic mixing [Spackman et al., 2007]. In the LMS this barrier erodes and horizontal mixing along the isentropes (path 6c, 7, 8) becomes possible. The subtropical jet separates the isentropic mixing between the lower TTL and LMS (above $\Theta = 350\,K$, path 7) from the isentropic mixing between the extratropical UT and the LMS (below $\Theta = 350\,K$, path 8).
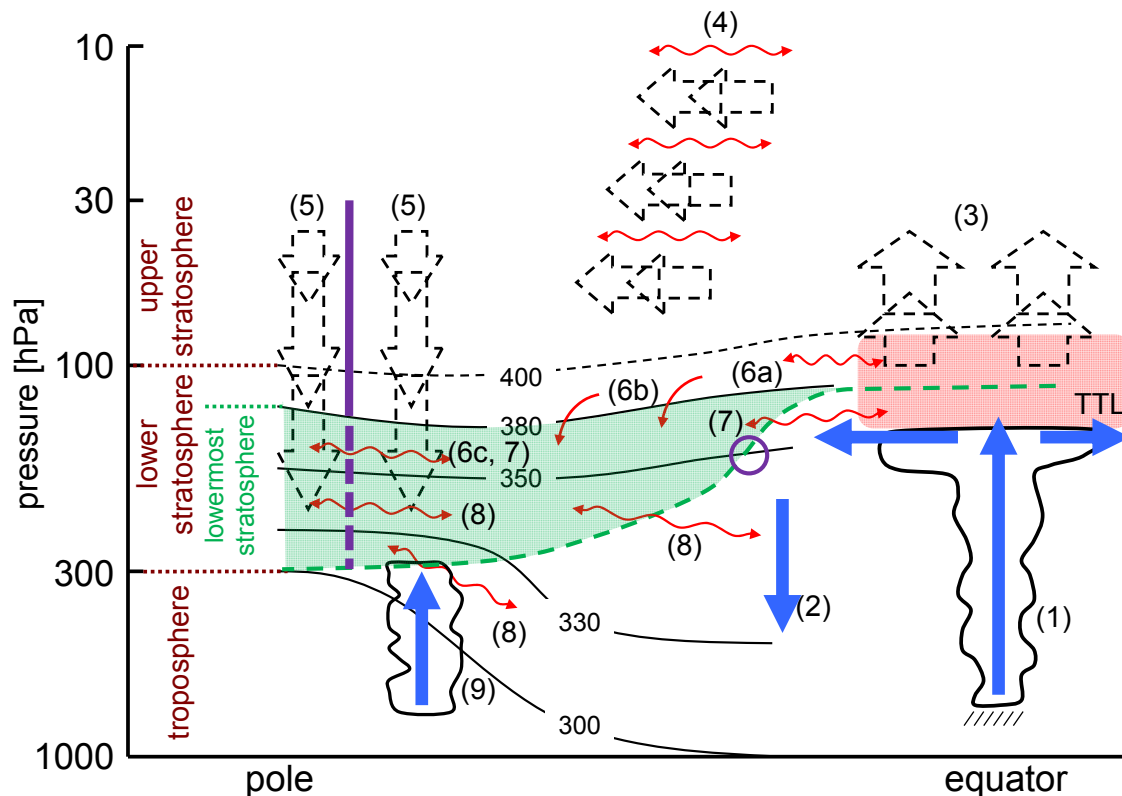
Figure 2.2: Stratospheric - tropospheric air exchange through the tropopause (green dashed line) [after Holton et al., 1995, the SPARC report N°4, 2006, and Spackman et al., 2007]. Areas with the same potential temperature Θ are indicated as solid black line (isentrope). The Θ = 400 K isentrope (dashed) indicate the border between lower stratosphere (LS) and upper stratosphere (US). The lowermost stratosphere (LMS) is embedded in the extratropical lower stratosphere (green area), like the tropical tropopause layer (TTL, red area) in the tropics. The polar jet marks the edge of the polar vortex and is indicated as vertical purple solid and dashed line. The purple circle indicates the location of the subtropical jet. The transport processes are: (1) tropical deep convective transport; (2) subtropical downwelling air motion (Headley circulation); (3) large-scale diabatic ascent (Brewer-Dopson circulation); (4) poleward transport (caused by dissipation of planetary Rossby waves); (5) large-scale subsidence; (6a) quasi-horizontal isentropic transport between upper TTL and mid-latitude LS; (6b) diabatic descent into the LMS; (6c) quasi-horizontal isentropic mixing; (7) isentropic mixing between lower TTL and LMS; (8) isentropic transport between extratropical UT and LMS (cyclones, tropopause folds); (9) convective upwelling transport.

In extratropical regions adiabatic processes dominate STE [Chen, 1995; Hintsa et al., 1998; Tuck et al., 2003; Jing et al., 2004, 2005]. The air is transported along isentropic areas below Θ = 350 K (path 8). Outside the tropics the transport of tropospheric air through the TP into the LMS is often caused by tropopause folds [Zahn et al., 2000; Sprenger et al., 2003; Olsen et al., 2004]. Seldom[4] diabatic transport processes through the TP into the LMS (convective vertical transport) were observed (path 9) [Fischer et al., 2003; Fromm and Servranckx, 2003; Dessler and Sherwood, 2004; Hegglin et al., 2004; Jost et al., 2004; Fromm et al., 2005 Hanisco et al., 2007]. However, tropopause folds can also cause downward mixing of LS air into the UT [Zahn et al., 2000; Seo and Bowman, 2001; Kim et al., 2002]. This downwelling air motion (dry airstream) was

---

[4] mainly during summer

found to be most effective in a cyclone above the North Atlantic Ocean [Morgenstern and Carver, 2001; Stohl, 2001; Cooper et al., 2002a; Sprenger and Wernli, 2003].

Please note, extratropical STE along isentropic areas only takes place between the UT and the LMS. Isentropic transport from the UT into the US is not possible [Holton et al., 1995]. At tropical latitudes, only diabatic processes like deep convection and large scale ascent can transport tropospheric air into the stratosphere [Hintsa et al., 1998; Dessler, 2002; Gettelman et al., 2002]. Tropical downwelling air motion from the stratosphere into the troposphere is linked with fast advection or with downwelling air motion inside tropical cyclones [Williams et al., 2002]. However, inside the tropics downwelling STE takes place much less frequently than upwelling transport. Furthermore, STE might be influenced dynamically by atmospheric gravity waves [Seo and Bowman, 2001; Wang, 2003], or by synoptic processes such as the Indian Monsoon [Chen, 1995; Fujiwara and Takahashi, 2001; Zachariasse et al., 2001; Seo and Bowman, 2002; Gettelman et al., 2004] or El Nino [Zeng and Pyle, 2005]. The overall STE shows a seasonality with maximum net exchange during late spring/early summer and minimum exchange during fall/winter [Appenzeller et al., 1996; Gettelman and Sobel, 2000; Seo and Bowman, 2002]. The upwelling air motion from the troposphere into the stratosphere in both hemispheres is most effective in late summer, fall, and early winter and smallest in late winter, spring, and early summer [Seo and Bowman, 2001; Škerlak et al., 2014]. On the contrary the downwelling STE is maximum in winter and spring and minimum in summer and fall [Seo and Bowman, 2001; Jordan et al., 2003; Škerlak et al., 2014]. Jing et al. [2005] showed the STE seasonality is reflected by the ozone (O_3) concentration, showing a UT maximum in spring time and a minimum in the LS.

There are several definitions of the TP [Pan et al., 2004]. The World Meteorological Organization (WMO) defines the thermal TP (thermal definition) by a local minimum in the vertical temperature profile. Following this definition, the thermal TP is located at the lowest altitude at which the vertical temperature gradient $\left(\partial T / \partial z \right)$ decreases below 2 K/km for at least 2 km in altitude. The thermal definition of the TP works best in tropical regions, where it is located at the $\Theta = 380\,\mathrm{K}$ potential temperature isentrope (cf. Fig. 2.2). Outside the tropics the location of the TP can be described better by using the vertical gradient of the potential vorticity (PV) [Holton et al., 1995]. Following this dynamical definition[5], the extratropical TP is located at an isentrope PV area of 1.6 PVU < PV < 3.5 PVU [WMO 1986, p. 152; Hoerling et al., 1991].

Considering the existing gradients over the TP of specific trace gases, the TP can be defined chemically, too [Zahn and Brenninkmeijer, 2003]. Stratospheric air can be identified by increased[6] O_3 concentrations [Esler et al., 2001; Gettelman et al., 2004; Jing et al., 2005]. Moreover the beryllium isotope ^7Be [Dibb et al., 2000, 2003], as well as the isotopic ratio $^{10}Be/^7Be$ [Jordan et al., 2003] indicate stratospheric air. The most common tracer for tropospheric air is carbon monoxide (CO) [Fischer et al., 2000;

---

[5] The potential vorticity quantifies the shear of a fluid. It is proportional to the dot product of the absolute vorticity (rotation of the wind vector) and the gradient of the potential temperature. The unit of the PV is Potential Vorticity Unit (PVU) with 1 PVU = $10^{-6}\,\mathrm{m^2 \cdot K \cdot kg^{-1} \cdot s^{-1}}$

[6] Zahn and Brenninkmeijer, 2003 showed, the TP Ozone mixing ratios vary seasonal between about 65 ppb in October/November and about 130 ppb in April/May.

Williams et al., 2002a; McCaffery et al., 2004; Hoor et al., 2005] and the content of water vapor [Esler et al., 2001; Gettelman et al., 2004]. However, acetone (C_3H_6O), methanol (CH_3OH), benzene (C_6H_6) [Fischer et al., 2003], as well as some halogen compounds [Mullendore et al., 2005] are further tracers for tropospheric air. Performing highly resolved in situ trace gas measurements, the chemical definition of the TP allows a clear identification of tropospheric and stratospheric air masses. Within CARIBIC, CO and O_3 was measured with a temporal resolution of 1 s (Tab. 3.1 in Cap. 3). However, as these measurements failed during some measurement flights, within this work the above described dynamical definition of the TP is used to separate tropospheric and stratospheric measurements.

2.3 Aerosol particles in the upper troposphere and lower stratosphere

The atmospheric particle size distribution can be mostly described using four logarithmic normal distributions, the aerosol modes [Jaenicke, 1993, p. 2-3; Winkler, 2000, p. 2]. The "nucleation mode" represents the smallest particles with a particle diameter (d_p) of about 1 nm < d_p < 15 nm. Particles with a diameter of 15 nm < d_p < 100 nm belong to the "Aitken mode". The "accumulation mode" describes particles with a size of 100 nm < d_p < 1000 nm. Particles larger than 1000 nm in diameter are classified as "coarse mode". Figure 2.3 shows a mean particle size distribution in the free troposphere, measured during the INDian Ocean Experiment (INDOEX) in February and March 1999 over the Indian Ocean in 8 to 12.5 km altitude [de Reus et al., 2001]. The uppermost graph shows the particle number size distribution, plotted as dN/dlog(d_p), i.e. the measured particle number concentration at a certain particle diameter is normalized by the decade logarithm of the measurement instrument size channel width. Using logarithmic x- and y-Axis, the four aerosol modes can be clearly identified (indicated as red dashed lines).

Below the dN/dlog(d_p) plot in Fig. 2.3 the same data were plotted, but with a linear y-scale and without the size channel width normalization. Integrating this curve over all size channels would give the total particle number concentration. It is obvious that the total particle number concentration is dominated by the number of nucleation- and Aitken mode particles. The particle surface size distribution and the particle volume size distribution can be derived from the particle number size distribution (lower two graphs in Fig. 2.3). Therefore for each size channel the particle concentration was multiplied with the surface[7] ($S = \pi \cdot d_p^2$) or the volume[7] ($V = \frac{1}{6}\pi \cdot d_p^3$) of a single particle. Please note that the particle surface- and volume size distribution are both plotted on a linear y-scale and without the size channel width normalization. As for the particle number concentration, the integration over the whole size range provides the total particle surface concentration and the particle volume concentration, respectively. Opposite to the particle number size distribution, the particle surface size distribution is

---

[7] assumption of spherical particles
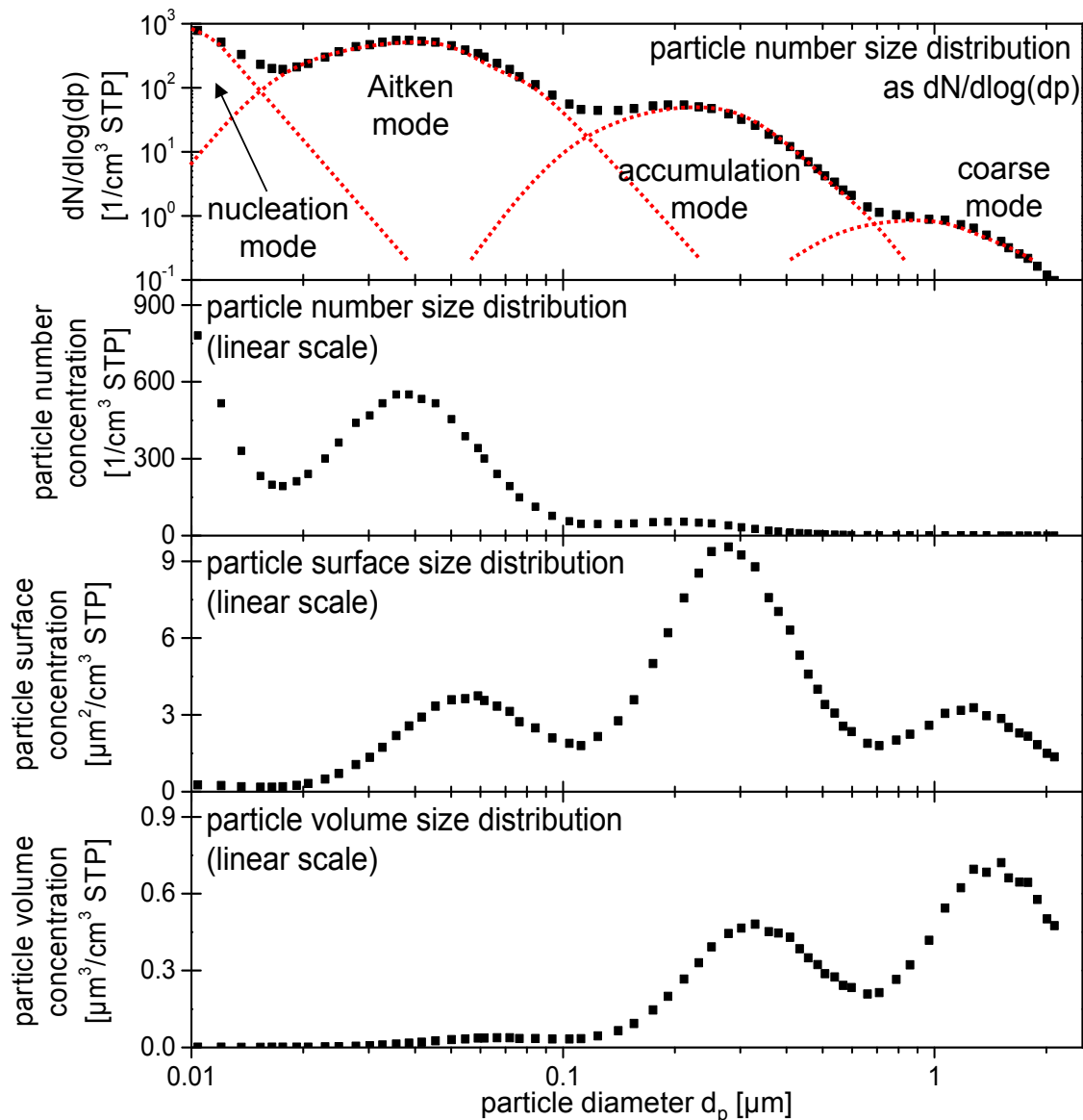
Figure 2.3: Typical free tropospheric particle size distribution, observed during the Indian Ocean Experiment (INDOEX) in February and March 1999 in 8 to 12.5 km altitude [de Reus et al., 2001]. The uppermost graph indicates the measured particle number size distribution, plotted as dN/dlog(d_p). The four aerosol modes are indicated as red dashed curves. The lower three graphs shows the same data, but as particle number size distribution (N(d_p)), particle surface size distribution (S(d_p)), and particle volume size distribution (V(d_p)) on a linear y-scale.

dominated by the accumulation mode. The particle volume size distribution, which can be transformed to a particle mass size distribution by multiplying with a certain (size dependent) particle density (not shown), is dominated by the coarse mode. This shift of the dominating aerosol mode is caused by the dependency from the square (surface) and cube (volume) of the particle diameter. It is assumed that in the mid-latitude UT/LMS particle volume size distribution the accumulation mode is dominating, because of the low appearance of sources for primary (coarse mode) particles (described below).

Aircraft emissions are the only source of directly emitted particles (primary particles) in the UT/LS. They are furthermore the only anthropogenic source in that region [Paladino et al., 2000; Jacobson et al., 2011; Presto et al., 2011]. Most of the present particles and particle precursor gases originate from the Earth´s surface or the

outer space. Typical natural sources for UT primary aerosol particles are volcanic eruptions [e.g. Martinsson et al., 2009; Schumann et al., 2011; Rauthe-Schöch et al. 2012 and references therein], biomass burning [e.g. Fromm et al., 2000; Mühle et al., 2002; Li et al., 2003], as well as mineral dust plumes [e.g. Ansmann et al., 2011]. Primary natural aerosol particles inside the LS are volcanic ash [e.g. Baumann et al 2003b] and meteoritic material [Murphy et al 1998, Klekociuk et al., 2005]. Furthermore at the Earth´s surface anthropogenically emitted primary particles (e.g. industrial emissions) can be transported into the UT/LS region. The main tropospheric vertical transport processes are described later in this section.

Within the UT/LS region aerosol particles are also formed from the gas phase (secondary particles) by gas to particle conversion. The most common inorganic precursor gases are sulfur dioxide (SO_2), dimethyl sulfide (DMS, $(CH_3)_2S$), and carbonyl sulfide (OCS, commonly written COS) which are oxidized to SO_2 [Thornton et al., 1997; Wilson et al., 2008]. Especially in regions with dense vegetation, organic precursor gasses (mainly alkenes, alkynes, and aldehydes) are present [Solomons, 1996; Mäkelä et al., 1997; O'Dowd et al., 2002]. During the vertical transport from the boundary layer to the free and upper troposphere SO_2 is oxidized to sulfuric acid[8] (H_2SO_4) [Laaksonen et al., 2000; Nothold et al., 2005] and the organic compounds frequently to organic acids [Kavouras et al., 1998], respectively. The oxidation products condense onto already existing particles (heterogeneous nucleation), or nucleate together with water vapor to new particles (homogeneous nucleation) [Laaksonen et al., 2000]. It is assumed that the binary homogeneous nucleation of H_2SO_4 and water vapor is the most common nucleation process inside the UT/LS region [Brock et al., 1995; Laaksonen et al., 2000; Clarke and Kapustin et al., 2002; SPARC report N°4, 2006, p16]. Ternary homogeneous nucleation of sulfuric acid, water, and ammonia (NH_3) [e.g. Korhonen et al., 1999; Kulmala et al., 2000; Lee et al., 2004] is unlikely in the UT/LS because of the low amount of ammonia. Another mechanism, ion induced nucleation (IIN) [Yu and Turco, 1997; Eichkorn et al., 2002; Laakso et al., 2002; Lee et al., 2003; Haverkamp et al., 2004; Lovejoy et al., 2004; Kanawade and Tripathi, 2006] is favored in the UT/LS as the cosmic radiation there is strong enough to produce abundant ions [Lee et al., 2003; Kanawade and Tripathi, 2006]. Nevertheless, for model applications it was shown by English et al. [2011] that for the UT/LS the knowledge of the exact nucleation mechanism is not needed, to reproduce Aitken mode (or larger) particle number concentrations correctly. Hence, binary homogeneous nucleation of sulfuric acid and water works well in modelling UT/LS particle nucleation.

Increased concentrations of freshly formed particles (nucleation mode particles) were often observed in air masses which were influenced by (deep convective) clouds and mid-latitude thunderstorms in the recent past [de Reus et al., 2001; Clement et al., 2002; Twohy et al., 2002; Lee et al., 2004; Kulmala et al., 2004, 2006; Kojima et al., 2004; Kanawade and Tripathi, 2006; Weigelt et al., 2009]. It is assumed that nucleation takes place mainly in the cloud outflow region. The temperature there is low, relative humidity is high, actinic fluxes are high, the pre-existing particle surface area is low,

---

[8] With OH the SO_2 is oxidized to $HOSO_2$, which reacts with O_2 to SO_3 and HO_2. Together with H_2O the SO_3 forms H_2SO_4.

and oxidized precursor gases may be available. All these conditions favour particle formation [Clarke and Kapustin, 2002; Williams et al., 2002b; Kulmala, 2003; Kulmala et al., 2004, 2006]. However, nucleation can be also caused by mixing of two air masses having different temperature and humidity [Nilsson and Kulmala, 1998]. This behaviour was observed also at the TP [de Reus et al., 1998; Zahn et al., 2000; Khosrawi and Konopka, 2003]. Furthermore, mixing caused by atmospheric waves can cause nucleation [Bigg, 1997; Nilsson et al., 2000].

The two most important vertical transport mechanisms for the UT are conveyor belts and convective clouds. Conveyor belts are present at mid-latitude cyclones. The air motion in a cyclone can be separated to four different airstreams [Cooper et al., 2002a, b]. The "cold conveyor belt" is the cold upwelling air mass in front of the warm front, reaching altitudes of about 500 hPa (about 5.5 km). In front of the cold front, warm air can ascent from the Earth´s surface to about 300 hPa (about 9 km) near the tropopause ("warm conveyor belt"). The "dry air stream" behind the cold front is a downwelling air motion from the upper troposphere to the middle and lower troposphere. Moreover, behind the cold front the "post-cold-front" airstream is present. This thermodynamic stable airstream initiate no vertical air motion.

Inside convective clouds a very fast vertical air motion can occur (up to 15 m/s), especially within the tropics [Dye et al., 2000]. Thus primary aerosol particles and precursor gasses can be lifted rapidly from the boundary layer to the UT or even through the TP (Sec. 2.2). During the transport inside the cloud most accumulation- and coarse mode particles are activated to cloud droplets and are mostly removed by precipitation [Seinfeld and Pandis 1998, p. 99]. Consequently, vertical transport inside clouds is most relevant for Aitken mode particles [Ekman et al., 2006]. If the cloud droplets do not precipitate, evaporation of smaller cloud droplets might lead to additional (residual) particles in the cloud outflow region. Model calculations, which were compared to in situ measurements, indicate that the vertical transport inside convective clouds can increase the particle number and mass concentration by a factor of 2-3 and 3-4, respectively [Yin et al., 2005; Cui and Carslaw, 2006]

The main source for stratospheric aerosol particles in periods of volcanic quiescent is the transport of particles [Brock et al., 1995] or particle precursor gases, mostly COS, [Brühl et al., 2012] via the TTL into the stratosphere (Sec. 2.2). Inside the stratosphere the particles mainly serve as condensation nuclei for the precursor gases oxidation product sulfuric acid. Therefore, an increased particle mass concentration, the Junge layer is present at altitudes of 15 km to 25 km [Junge et al., 1961]. Inside the stratosphere the nucleation of new particles is in general rare compared to the UT, because of the smaller amounts of sulfuric acid and water vapor [Brock et al., 1995].

Volcanic eruptions with volcanic eruption indices (VEIs) of 5 or more can strongly increase the amount of atmospheric sulfur compounds in the stratosphere [McCormick et al., 1995]. The increased concentration of stratospheric sulfuric acid increases the probability for new particle formation inside the stratosphere [Hamill et al., 1997]. Furthermore, stratospheric nucleation might be caused by temperature fluctuations due to atmospheric gravity waves [Meilinger et al., 1995; Tsias et al., 1997; Bacmeister et al., 1999; Carslaw et al., 1999].

Major sinks for UT/LS particles are sedimentation (dry deposition) and wet deposition [Wilson et al., 2008]. Dry deposition means that the particles sink slowly and deposit on the Earth's surface without the aid of precipitation. Conversely, wet deposition encompasses all aqueous processes by which particles are washed out (e.g. by rain, snow, or fog) [Seinfeld and Pandis, 1998 p. 50]. The depletion of stratospheric particles takes place mainly by STE processes (cf. Sec. 2.2), i.e. by transport of stratospheric particles into the troposphere.

Coagulation is the most important transformation process for freshly formed particles (nucleation mode) in nucleation bursts (high number concentrations). Two (or more) small particles coagulate and form a new, larger particle [Pandis et al., 1995; Seinfeld and Pandis, 1998, p. 656-680]. Particle growth by condensation of gaseous compounds onto the particle surface is also important [Seinfeld and Pandis, 1998 p.649-655]. Accumulation mode particles (especially hygroscopic particles) can be activated to cloud droplets [Seinfeld and Pandis, 1998, p. 99-100]. Moreover, atmospheric particle transformations are caused by evaporation and by chemical reactions [Pandis et al., 1995].

The atmospheric lifetime of aerosol particles τ_p mainly depends on the efficiency of deposition and of the transformation inside clouds [Jaenicke et al., 1998, p. 22]. Because those processes strongly depend on the particle size, τ_p can be described as a function of the particle diameter. For wet deposition, τ_p can be described with an empirical formula from Jaenicke et al., [1998], p. 23:

$$\frac{1}{\tau_p} = \frac{1}{1.28 \cdot 10^8} \cdot \left(\frac{r_p}{0.3}\right)^2 + \frac{1}{1.28 \cdot 10^8} \cdot \left(\frac{r_p}{0.3}\right)^{-2} + \frac{1}{\tau_{ns}} \qquad (2.1)$$

r_p particle radius [μm]

τ_{ns} characteristic wet removal time [s]

Applying Eq. 2.1, a characteristical particle residence time for boundary layer aerosol ($\tau_{ns} = 8$ d), mid-tropospheric aerosol ($\tau_{ns} = 21$ d), and upper tropospheric aerosol ($\tau_{ns} = 200$ d) was calculated [Mészáros et al., 1991; Baltensberger and Nyeki, 1998, p. 299-300; Jaenicke, 1998, p. 23]. The resulting size dependent data are shown in Fig. 2.4. Within all three altitude ranges nucleation mode and large coarse mode particles show the shortest atmospheric lifetime of only few minutes to one day. The lifetime of nucleation and Aitken mode particles is mainly controlled by coagulation processes[9]. On the contrary, the lifetime of large coarse mode particles is limited mainly by dry deposition [Mészáros et al., 1991, p. 74; Jaenicke, 1998, p.23; Winkler, 2000, p. 31].

---

[9] When two or more nucleation- or Aitken mode particles collide and form a larger new particle, this is a sink process for small particles and a source process for larger particles. Therefore, coagulation is a sink for nucleation or Aitken mode particles and at the same time a source for Aitken or accumulation mode particles. However, the total particle mass within a certain volume is not influenced by coagulation, only the particle number.
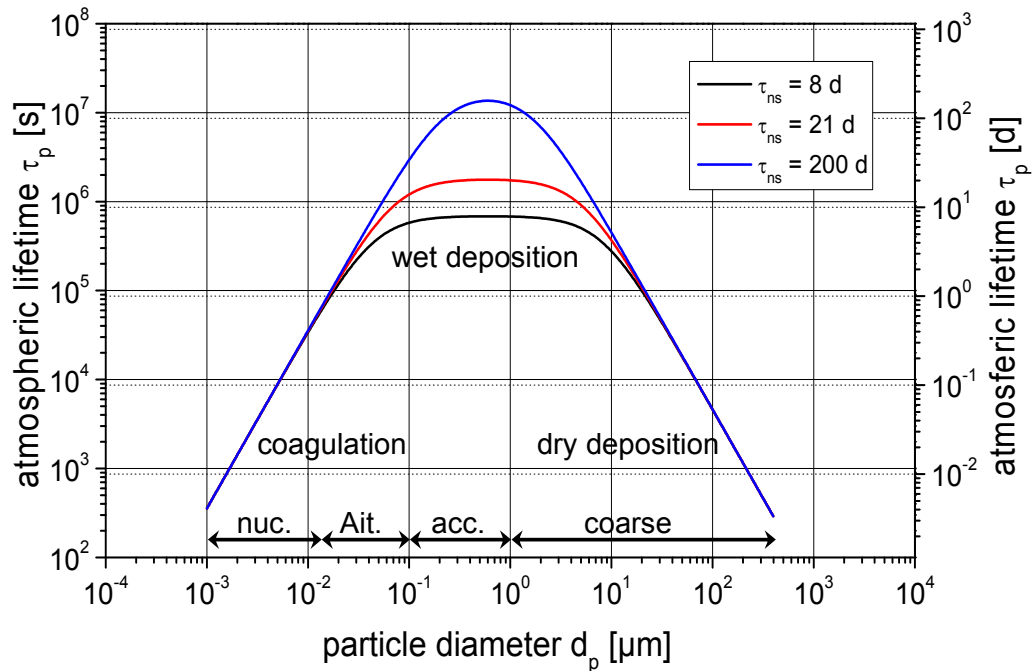
Figure 2.4: Calculation of the size dependent atmospheric lifetime of aerosol particles inside the boundary layer (τ_{ns}= 8 d), the free troposphere (τ_{ns}= 21 d), and the upper troposphere (τ_{ns}= 200 d) [after Mészáros et al., 1991; Baltensberger and Nyeki, 1998, p. 299-300; Jaenicke, 1998, p.23]. The data were obtained, using Eq. 2.1.

Coagulation and dry deposition are less important for accumulation mode particles [Winkler et al., 2000, p. 31]. Therefore, these particles have the longest atmospheric lifetime. Wet deposition is the most effective sink for this particle mode. As wet deposition decreases with increasing altitude, accumulation mode particles inside the upper troposphere have a much longer lifetime (up to half a year) than in the boundary layer (up to 8 days) (cf. Fig. 2.4). Due to the dry conditions, inside the stratosphere particle lifetimes are even longer.

The pressure and temperature normalized[10] vertical profile of the total particle number concentration quite often follows a 'c-shape', with high concentrations (up to several 1000 1/cm³ STP) in the boundary layer, a local minimum in the middle troposphere (several 100 1/cm³ STP) and high concentrations in the UT (again up to several 1000 1/cm³ STP) [Brock et al., 1995; de Reus et al., 2001; Schröder et al., 2002; Singh et al., 2002; Krejci et al., 2003; Spracklen et al., 2005a; Heintzenberg et al., 2011]. Above the tropopause, the total particle concentration again decreases with increasing altitude [Deshler et al., 2003; Heintzenberg et al., 2011]. However, as already discussed for Fig. 2.3, the total particle number concentration is dominated by the nucleation and the Aitken mode. The number of accumulation mode particles (the focus of this work) inside the UT is much lower with concentrations of about 100 1/cm³ (STP) or even lower [de Reus et al., 2001; Krejci et al., 2003]. However, due to e.g. advection or cloud scavenging the concentration can vary very strongly. Inside the stratosphere the accumulation mode concentration is more constant and often higher than in the UT [Hofmann 1990, Deshler et al., 2003; Minikin et al., 2003; Young et al., 2007].

---

[10] To compare the particle concentrations of different measurement altitudes, the measurements have to be related to standard conditions (STP: p=1013.25 hPa, T=273.15 K).

3   The CARIBIC project

Within the CARIBIC project (www.caribic-atmospheric.com; last access: 29.03.2014) the developed OPC is regularly (usually once per month) flown onboard a passenger long-haul aircraft. CARIBIC is the acronym for Civil Aircraft for the Regular Investigation of the Atmosphere Based on an Instrument Container. Section 3.1 explains the Idea and the history of CARIBIC and related projects. The CARIBIC aircraft and the necessary gas and aerosol inlet system are described in Sec. 3.2, whereas the instrumentation in the measurement container is described in Sec. 3.3.

3.1   Idea and history of the CARIBIC project

The principal idea behind the CARIBIC project is the need for regular in situ measurements of trace gas and aerosol parameters in the UT and LMS. However, using research aircraft for regular investigation of the atmosphere over a period of several years, covering a nearly global scale would be unaffordable. By using a long-haul commercial aircraft as measurement platform, costs can be reduced and a nearly global coverage becomes possible.

The idea of using a commercial aircraft for atmospheric measurements of trace gases or aerosol particles exists already since the 1960s. From 1962 to 1968 Bischof used DC-8 aircraft of the Swedish Air Force for atmospheric carbon dioxide (CO_2) measurements (Bischof, 1970; Bolin and Bischof, 1970). In the 1970s commercial aircraft were used as measurement platform in the Tropospheric Ozone campaign (TROZ; [Fabian and Pruchniewicz, 1977]) and the Global Atmospheric Sampling Program (GASP, [Perkins and Papathakos, 1978]). Within the TROZ campaign ozone (O_3) measurements were carried out on four flights above Europe and Africa. Because the aircraft had no gas inlet system, the instruments got the measurement air via the air conditioning of the cabin. In contrast, during the GASP campaign starting in 1975, four Boeing 747 were equipped with two air inlet systems to obtain high quality measurements of O_3, carbon monoxide (CO), water vapor (H_2O), and different nitrogen oxides (NO_y). Within GASP for the first time the aerosol particle number concentration

and the particle size distribution was measured onboard a commercial aircraft [Detwiler, et al., 2000. Unfortunately the inlet systems of GASP were not optimized for aerosol particles and hence the data bear very large uncertainties. Until CARIBIC was established in 1997, no further aerosol measurements were carried out onboard a passenger aircraft.

In the 1990s, besides CARIBIC also the MOZAIC (Measurement of Ozone and Water Vapor by Airbus in-service Aircraft), the CONTRAIL (Comprehensive Observation Network for Trace gases by Airliner), and the NOXAR (Measurements of Nitrogen Oxides and ozone along Air Routes) projects used passenger aircraft. During NOXAR within one year more than 500 measurement flights onboard a Boeing 747 were carried out in different regions of the globe, measuring NO and NO_2 [Dias-Lalcaca et al., 1998; Brunner, et al., 2001]. The ongoing Japanese CONTRAIL project, which is in the literature also named JAL project (Japan Airlines) started in 1993 with flask samples over the western Pacific between Japan and Australia onboard a Boeing 747. The flask samples are analyzed for CO_2 and other trace gases [Matsueda and Inoue, 1996]. In 2005 the program was expanded to cover additional regions from Japan to Europe, Asia, Hawaii, and North America, using five JAL aircraft (Boeing 747 and 777) [Machida et al., 2008]. Since 1994 MOZAIC used five Airbus A340 from different airlines to measure O_3, H_2O, CO, and NO_y in the upper troposphere [Marenco et al., 1998]. Like MOZAIC and CONTRAIL, the CARIBIC measurements were developed to operate for many years with a nearly global coverage. The different approach used in CARIBIC compared to MOZAIC and CONTRAIL, allows to measure as many atmospheric trace species as possible, including aerosol parameters (cf. Sec. 3.3), however with lower frequency compared to the other two projects.
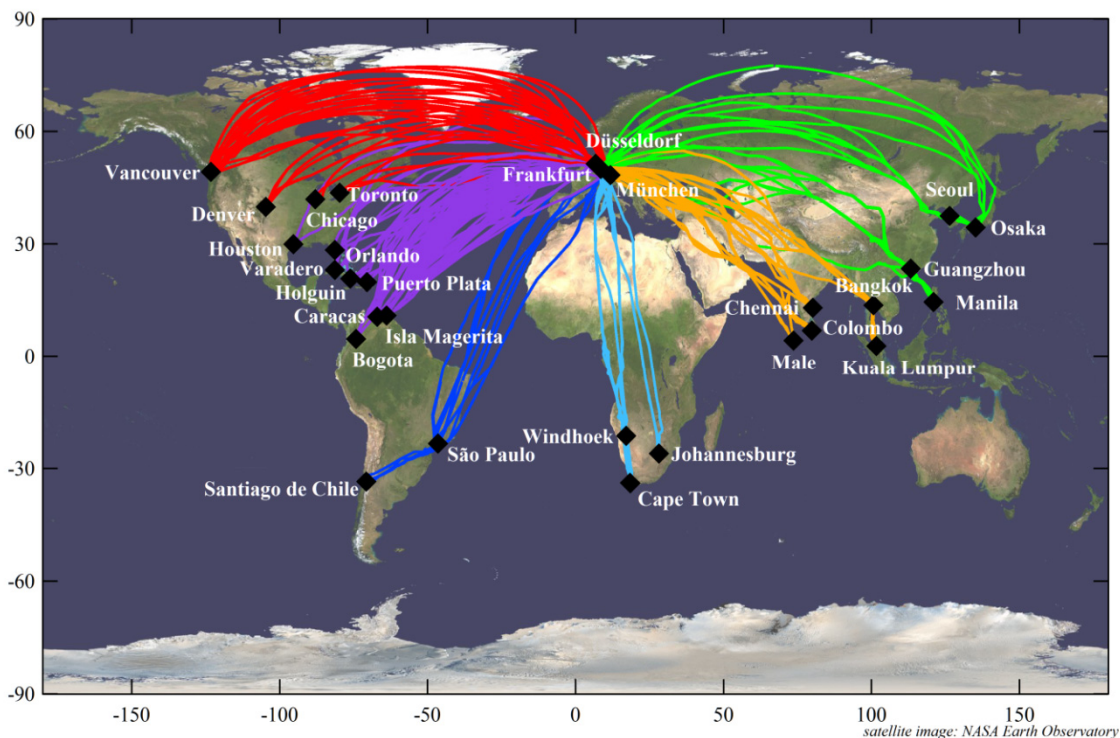
Figure 3.1: CARIBIC flight tracks between June 1997 and December 2013. The colors indicate the different flight routes to North America (red), Central America (purple), South America (blue), South Africa (turquoise), Southern Asia (orange), and Eastern Asia (green).

The CARIBIC project can be divided into two phases. The first phase (CARIBIC-1) started in 1993 with the Max-Plank Institute for Chemistry (MPI-C) in Mainz, the Institute for Meteorology and Climatology (IMK) at the Karlsruhe Institute of Technology (KIT), the Leibniz Institute for Tropospheric Research in Leipzig, and LTU International Airways. After the development of the concept, the inlet system, and the measurement container with the modified instruments, the first measurement flight took place in June 1997. Until 2002 a Boeing 767-300ER was used as measurement platform [Brenninkmeijer, et al., 1999]. Unfortunately, LTU sold the modified CARIBIC aircraft in summer 2002 and hence it was not longer available for measurements. However, because of the great success of CARIBIC, the project was continued with a new carrier. In CARIBIC-2, an Airbus A340-600 from the German Lufthansa AG is used since December 2004 with a newly developed measurement container, as well as a new inlet system [Brenninkmeijer, et al., 2007] (Sec. 3.2 and 3.3). Since June 1997 until December 2013 441 measurement flights were carried out on six intercontinental flight directions (cf. Fig. 3.1). In 2013 CARIBIC was integrated in the In-service Aircraft for a Global Observing System (IAGOS, www.iagos.org; last access: 29.03.2014) European Research Infrastructure. In that way the now IAGOS-CARIBIC system will be a platform for routinely monitoring of trace gas and aerosol parameters in the UT/LMS for the coming years. From October 2009 until April 2010 several new instruments were implemented or old instruments were replaced in the container, to improve the scientific impact of CARIBIC (Sec. 3.3). The OPC, the subject of this work, was one of the replacement instruments and is described in detail in Chapter 4 and 5.

3.2   CARIBIC aircraft and inlet system

Since December 2004, the Airbus A340-600 "Leverkusen", D-AIHE, from the German Lufthansa AG serves as measurement platform for CARIBIC (Fig. 3.2a). This long-haul aircraft with a maximum travel distance of 14,200 km has a capacity for up to 380 passengers. The cruising speed is about 250 m/s (about 900 km/h) at an altitude of around 12.5 km.

To conduct successful measurement flights, the interests of the scientists and of the airline have to be balanced. On the one hand scientists want to have regular measurements on different flight routes to cover a large measurement area and to get good seasonal statistics. On the other hand the interest of the airline is to minimize the influence of the measurements on the regular flight plan and the routine operation of the aircraft because of the costs. Only one aircraft was modified for CARIBIC with a permanently mounted air inlet system and can thus be used for measurements. One reason for choosing the A340-600 was the fact that Lufthansa ordered 24 aircraft of this type. Because of this large number of aircraft, for Lufthansa it is much easier to employ the "Leverkusen" on the flight route, the scientists ask for.

Figure 3.2: The CARIBIC aircraft with the gas and aerosol inlet. Figure (a) shows the aircraft, the Airbus A340-600 "Leverkusen" (D-AIHE) from the German Lufthansa AG. The arrow marks the position of the inlet, and the red box the position of the measurement container inside the forward cargo bay. Figure (b) shows the permanently mounted inlet, which is located about 23 m behind the nose of the aircraft.

Because of safety regulations, it is not allowed to be in the cargo bay of the aircraft during a measurement flight. Consequently the measurement container with all scientific- and service instruments has to run automatically. For the container operation on board, several modifications at the aircraft were required. Most important were the structural changes to the hull because of the mounting of the inlet (Fig. 3.2 (b)). To avoid unloading of the container at the destination airport, it is located at the last position of the forward cargo bay just above the leading edge of the belly fairing. Due to mechanical reasons it was not possible to mount the inlet at the belly fairing directly below the container but about 2 m in front of the container and about 23 m behind the nose of the aircraft. Sampling air tubing and cables are installed between the inlet and the container in the fuselage. To mount and remove the measurement container as fast as possible, a container connector interface with quick connectors for all necessary sampling air tubing as well as power and communication cables was installed in the floor of the cargo bay below the position of the container. To switch the container on and off and to indicate overheating and smoke in the container, a control panel was installed in the cockpit. These modifications at the aircraft were finally realized in November 2004, after two years of planning.

The CARIBIC inlet system consists of the inlet, mounted at the aircraft fuselage, and the sampling lines inside the aircraft. The inlet has a pylon with three separate inlet tubes, one for water vapor, one for aerosol particles and one for trace gas measurements (cf. Fig. 3.3). To avoid influences of the aircraft on the sampled air, the pylon has a length of 35 cm. With that length, the three inlet tubes are outside of the boundary layer of the aircraft, which is assumed to be 24 cm at the position of the inlet, according to information given by the aircraft manufacturer. During flight, all three inlet tubes are heated to avoid icing. The pylon also carries a video camera, observing the vicinity of the aircraft in flight direction, thus enabling the detection of "events" during day time
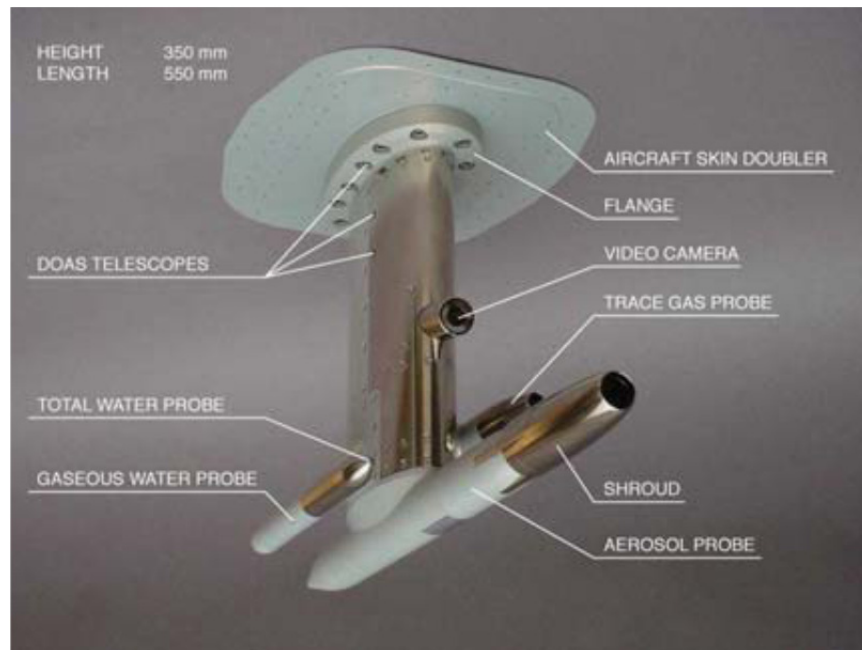
Figure 3.3: CARIBIC inlet with all components. The picture was taken from Breninkmeijer et al., [2007].

flights (e.g. passing a deep convective cloud). Moreover, three telescopes of a Differential Optical Absorption Spectrometer (DOAS) are integrated into the pylon. The sampling lines for the inlet tubes and the power cables for the heaters complement the inlet system. The OPC is connected to the aerosol inlet. Therefore in the following only this inlet is described in more detail. More information to the trace gas and the water inlets is given in Brenninkmeijer et al., [2007].

To align the airflow with the axis of the aerosol tube and thus to minimize particle losses, a specially designed shroud is mounted upstream the aerosol inlet tube. As the velocity of the measurement air outside the aircraft is much higher than inside the sampling lines to the aerosol instruments (about 250 m/s vs. 6-7 m/s), the air has to be slowed down after entering the aerosol inlet tube. This is realized with a conical diffuser. The air velocity is slowed down due to the expanding cross section of the tube in the diffuser and the law of mass conservation. The slowing of the air flow increases the pressure and temperature of the sample air ("ram heating"). The large temperature increase (from about -60°C ambient to about +30°C inside the instruments) dries the aerosol particles and they shrink [Hermann et al., 2001]. Hence, all CARIBIC aerosol measurements are referring to dried aerosol particles. From the aerosol inlet tube, the air is pulled directly to the measurement instruments inside the container via a about 4 m long 3/8' stainless steel tube. Particle losses, caused by the inlet and the sampling lines have to be taken into account for the data analysis.

3.3   CARIBIC container and aerosol instrumentation

Because of the aircraft changeover from a Boeing 767-300ER to an Airbus A340-600, a new measurement container had to be designed. The new CARIBIC container has a total weight of 1.5 tons and is 1.6 x 3.1 x 1.5 meter in size ($h \times w \times d$). All together 23 measurement instruments in 17 housings, as well as 9 service instruments are installed in 8 racks (Fig. 3.4). The container and its instrumentation are described in detail in Brenninkmeijer et al. [2007]. Therefore, below only the aerosol instruments are described.

The aerosol instrumentation consists of the new OPC, which is detailed described in chapter 4 and 5, three Condensation Particle Counters (CPCs) and an impactor sampler, collecting aerosol particles onto impactor foils for a post-flight analysis. These instruments are installed in units called "Aerosol 1" and "Aerosol 2". The CPCs measure the integral particle number concentration in a size range between the lower threshold diameter of the CPC and about 3 μm. The lower cut off diameter of the CPCs was set to about 4 nm (N_4), about 12 nm (N_{12}), and about 18 nm (N_{18}), respectively, by adjusting the temperature difference inside the CPCs [Hermann and Wiedensohler, 2001]. By subtracting N_{12} from N_4 the concentration of nucleation mode particles (e.g. 4 nm $\leq d_p \leq$ 12 nm, N_{4-12}) can be calculated. As in the UT the Aitken mode number concentration mostly dominates strongly over the accumulation mode number concentration (e.g., Clarke and Kapustin, 2002; Heintzenberg et al., 2002), N_{12} can be considered as the number concentration of Aitken mode particles only. All three CPCs have a temporal resolution of 2 seconds. The impactor system in the Aerosol 2 unit consists of 16 separate impactor foils. During one flight sequence 14 probes are taken
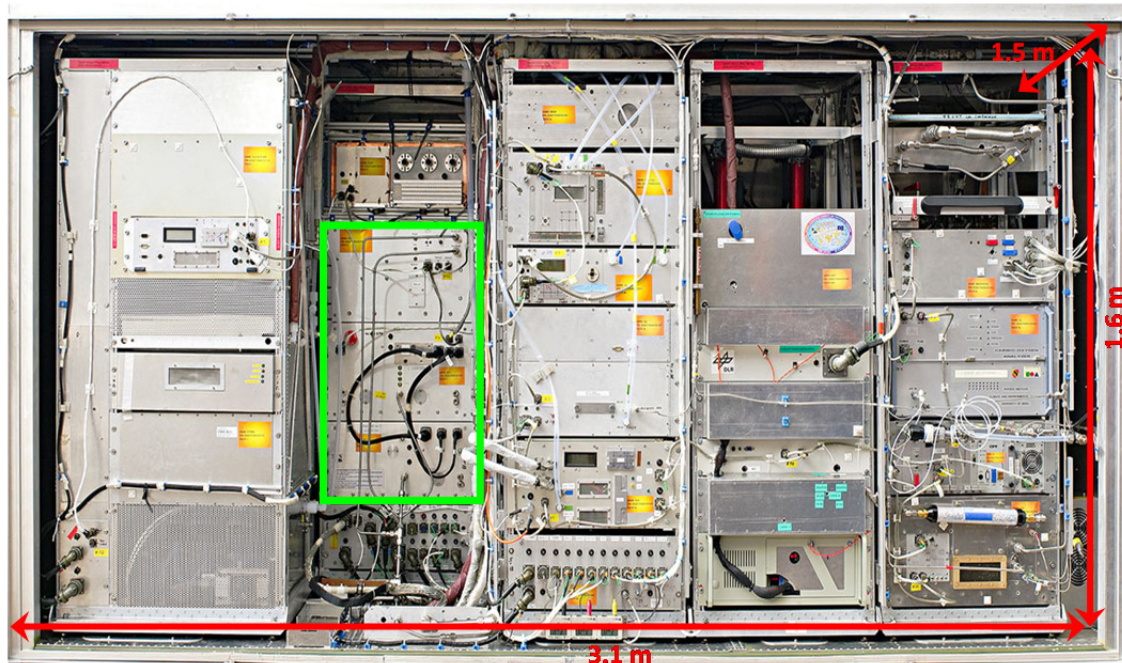
Figure 3.4: Front view of the CARIBIC container. The section with aerosol instruments is marked with a green frame. They consist of the new OPC (uppermost instrument), two condensation particle counters (CPCs) in the "Aerosol 1" unit (instrument in the middle), as well as one CPC and an impactor sampler in the "Aerosol 2" unit (lowest instrument).

sequently with 100 min time resolution, while the other two probes are each taken during two whole flights. The impactor system collects particles between 0.08 and 2.0 μm. The samples are analyzed in laboratory at the University of Lund (Sweden) using the Particle-Induced X-ray Emission (PIXE) [Papaspiropoulos et al., 1999] and Particle Elastic Scattering Analyses (PESA) [Nguyen and Martinsson, 2007; Nguyen et al., 2008] methods. The PESA method can determine the masses of hydrogen, carbon, nitrogen, and oxygen whereas the PIXE method is used for heavier elements, like sulfur, chlorine, calcium, titanium, vanadium, chromium, manganese, iron, and nickel. The sum of the elemental masses yields the total particle mass concentration (impactor mass) with an overall uncertainty of only 10% [Breninkmeijer et al., 2007].

As the CARIBIC system is a fully automated system a central computer, the "master", controls all functions of the container. Via an Ethernet network the master is connected with the computers of all measurement instruments, the "slaves". Using a specific communication protocol, the status of the slave instruments is precisely controlled. This measure is necessary because of safety and power management reasons. The measurement status of the whole container is pressure controlled, i.e. below the pressure altitude 700 hPa (about 3 km) during start and 850 hPa (about 1.5 km) during landing, respectively, the instruments are not allowed to consume power.

Another aerosol related unit in the container is the pump unit (two Vacuubrand MD4-C diaphragm pumps), providing the vacuum necessary for Aerosol 1 and 2, the OPC, and the CO instrument. Electrical power for all instruments is provided by the Basic Power Supply (BPS) and the Transformer Rectifier Unit (TRU). The BPS transforms the 115 V 400 Hz AC voltage from the aircraft into 24 V DC. The TRU transforms the aircraft voltage into 28 V DC. As the aircraft needs much electrical power during the take off, only the BPS is on at that time. The TRU power supply is switched on by the master when reaching the pressure altitude 700 hPa. Instruments with high power consumption (e.g. using large pumps) get their power from the TRU, whereas instruments, needing a longer warm up time and having less power consumption, are powered from the BPS. Because the OPC unit has a power consumption of only about 150 W, it is connected to the BPS, like the master, and Aerosol 1 and 2.

For data interpretation, flight parameters such as time, 3 dimensional (3d) location, temperature, pressure, wind speed and direction, as well as cruising speed of the aircraft are needed. These data are provided to the CARIBIC master computer by one of the aircraft´s ARINC bus systems. Using this data connection, all relevant flight parameters are stored. If required for instrument control, the master can forward the 3d aircraft location in nearly real-time to slave instruments.

With the newly developed measurement container, in 2004, an OPC was already added to the CARIBIC system [Reichelt, 2007]. Unfortunately this OPC worked unreliable. Hence in winter 2010 the OPC was replaced by the new instrument, which is the subject of this work. Also in winter 2010 some other trace gas instruments were exchanged and some new instruments were added to the container. A summary of all newly installed instruments as well as the already existing measurement instruments is given in Tab 3.1. Because of the substantial changes, the container needed a new

EASA[11] flight certification, which was given in April 2010. Shortly afterwards the first measurement flight with the new equipment was carried out on April, 20th 2010.

Table 3.1: Summary of all parameter, measured with the CARIBIC container. The aerosol instruments are indicated in grey, the trace gas instruments in blue and other instruments in green. The institute acronym are: CNRS: Centre National de la Recherche Scientifique (National Center for Scientific Research), Paris/France; DLR: Deutsches Zentum für Luft und Raumfahrt, Oberpfaffenhofen/Germany; HZG: Helmholtz Zentrum Geesthacht, Geestacht/Germany; IfT/TROPOS: Leibniz Institute for Tropospheric Research, Leipzig/Germany; KIT: Karlsruher Institute for Technology, Karlsruhe/Germany; MPI-C: Max Plank Institute for Chemistry, Mainz/Germany; UB: University of Bern, Bern/Switzerland; UEA: University of East Anglia, Norwich/England; UH: University of Heidelberg, Heidelberg/Germany; UL: University of Lund, Lund/Sweden

parameter	method	in-situ or laboratory	institute
integral particle number concentration for three different size ranges	Condensation Particle Counter (CPC) with different lower cut off diameter: $d_p > 4$ nm; $d_p > 12$ nm; $d_p > 18$ nm	in-situ	IfT/ TROPOS
particle size distribution	Optical Particle Counter (OPC)	in-situ	IfT/ TROPOS
particle elemental composition	impactor collection; Particle Induced X-Ray Emission (PIXE) and Particle Elastic Scattering Analysis (PESA)	laboratory analysis	UL
O_3 fast/precise	chemiluminescence on an organic dye (fast) UV absorption (precise)	in-situ	KIT
CO	VUV fluorescence	in-situ	MPI-C
H_2O total/gaseous	laser photo acoustic and dew point mirror	in-situ	KIT
NO/NO_2 (day/night) NO_y	chemiluminescence with O_3 chemiluminescence after conversion to NO	in-situ	DLR
Hg	enrichment and atomic fluorescence	in-situ	HZG
CO_2	Non-Dispersive InfraRed Absorption (NDIR)	in-situ	CNRS MPI-C
O_2 (precise)	Electrochemical cells with ultimate temperature and pressure stabilization	in-situ	UB

---

[11] European Aviation Safety Agency (EASA)

Table 3.1: (continued)

parameter	method	in-situ or laboratory	institute
C_3H_6O, C_2H_3N, CH_4O, C_2H_4O, and other Volatile Organic Compounds (VOC)	Proton Transfer Reaction Mass Spectrometer (PTR-MS)	in-situ	KIT
H_2O Isotopes	laser absorption spectroscopy	in-situ	KIT
CH_4	absorption spectroscopy	in-situ	KIT
SO_2, BrO, HCHO, OCIO, O_4	3 x Differential Optical Absorption Spectroscopy (DOAS)	remote sensing	UH
Volatile organic Compounds (VOC)	whole air sampler with 88 stainless steel flasks analysis by Gas Chromatography – Mass Spectrometry (GC-MS)	laboratory analysis	MPI-C
Greenhouse Gases (GHG), Non Methane Hydrocarbons (NMHC)	whole air sampler with 14 glass flasks (air sampler – 1), analysis by GC and GC-MS	laboratory analysis	MPI-C UEA
Chlorofluorocarbons (CFC), Halocarbons (N_2O, SF_6)	whole air sampler with 14 glass flasks (air sampler – 2), analysis by GC and GC-MS	laboratory analysis	MPI-C UEA
Clouds	video camera	remote sensing	MPI-C

To interpret the measured data, additional large scale meteorological information is needed. Therefore the Royal Netherlands Meteorological Institute (Koninklijk Nederlands Meteorologisch Instituut; KNMI) calculates for every measurement flight along the flight track important parameters like potential vorticity, equivalent potential temperature, specific humidity, cloud cover, cloud water content, and wind vector (http://www.knmi.nl/samenw/campaign_support/CARIBIC/index.html; last access: 29.03.2014). These calculations are based on ECMWF data. Using the TRAJKS trajectory model [Scheele et al., 1996], KNMI also calculates five day backward-, as well as two day forward trajectories every three minutes along the flight track of the aircraft.

4 CARIBIC OPC

Operation of standard laboratory equipment onboard aircraft requires several modifications to comply with safety requirements, operation conditions, and handling. For example, only incombustible materials are allowed in the aircraft and the emission of electromagnetic radiation must be minimized and meet stringent specifications. For the latter, the instrument has to pass an Electro Magnetic Compatibly (EMC) test. All components inside the instrument have to be securely fixed to withstand vibrations and shocks during the flight, take-off, and landing. Because persons are not allowed in the cargo compartment during flight, the control and the data acquisition of the instrument has to be automated, controlled by the CARIBIC container master computer.

OPCs use scattered light signals to derive information on particle size. Therefore the theory of light scattering by particles is briefly summarized in Sec. 4.1. Section 4.2 describes the core features of the original laboratory OPC. The 19" rack unit housing the OPC is described in Sec. 4.3. The data acquisition, the communication with the master, and the control system is described in section 4.4. In the following the term "OPC unit" is used for the whole CARIBIC OPC instrument, including the optical part, the data acquisition, all electronics, the gas flow components, and the housing. The original instrument, the RION OPC type "KS-93", from which only the flow system, the electronics and the optics is used, is called "OPC" or "KS-93".

4.1   Scattering and absorption of light by aerosol particles

The movement of electromagnetic waves inside a medium is influenced by inhomogeneities inside the medium, which is described in in detail by van de Hulst [1981, p 114 – 130] and Bohren and Huffman [1983, p 82 – 129]. If an electromagnetic wave strikes an inhomogeneity, an oscillation is initialized in this scattering medium. Due to the oscillation the scattering medium reemits electromagnetic waves, the scattered radiation. A part of the incident energy is transferred to other energy forms (e.g. thermal energy). The energy transformation is described by the absorption. In general the scattering and absorption of a certain inhomogeneity is a function of the

wavelength (λ) of the incident radiation and of the size, shape, and chemical composition of the inhomogeneity. Within this work the medium is the measurement air passing the optics of an OPC. The electromagnetic wave is the laser beam of the OPC, and the inhomogeneity is a single aerosol particle. For particles with $d_p \ll \lambda$ ($d_p < 0.2 \cdot \lambda$), the scattering behavior can be described with the Rayleigh scattering [van de Hulst, 1981 p. 85-102; Bohren and Huffman, 1983, p. 132-134; Seinfeld and Pandis, 1998, p.1120-1122]. The classical (geometrical) optics provides a good approach for the solution of the scattering problem for particles with $d_p \gg \lambda$ ($d_p > 2...10 \cdot \lambda$). In the size range $d_p \approx \lambda$ neither the Rayleigh, nor the geometrical scattering describes adequately the scattering behavior. The exact solution of the Maxwell equations for the scattering of an electromagnetic wave at a homogeneous spherical medium was developed by Gustav Mie and Ludvig Lorenz in the Lorenz-Mie (or only Mie) theory [Mie, 1908]. The Mie theory is valid for all size ranges, but is restricted to the elastic scattering. The wavelength of incident and scattered radiation are equal. Furthermore the scattering has to be incoherent. This means that the particles have to be statistically distributed in a homogeneous medium to prevent phase correlations. The distance between two neighboring particles has to be large enough to avoid particle interaction by their own electromagnetic fields[12]. As the OPC, this work is focusing on, do measure in the size range $d_p \approx \lambda$ (cf. Ch. 5) and the Mie theory provides an exact solution for the scattering problem, the Rayleigh and the geometrical scattering are not described further.

The complex refractive index $m(\lambda)$ describes the dependency of the scattering of radiation on the chemical composition of the scattering object [van de Hulst, 1981, p. 67].

$$m(\lambda) = n - i \cdot n' \qquad\qquad (4.1)$$

n refractive index real part [1]
n' refractive index imaginary part [1]
λ wavelength of the incident radiation [m]

While the refractive index real part describes the scattering, the imaginary part describes the absorption. The sum of both effects is called extinction and gives the total degradation of an electromagnetic wave during a scattering process. The individual effective cross sections C_x give the ratio of how much of the incident energy per time and area unit becomes transformed by extinction, absorption, and scattering within the same time unit [van de Hulst, 1981, p. 13, Bohren and Huffman, 1983, p. 71].

$$C_e = \frac{W_e}{I_i}, \quad C_a = \frac{W_a}{I_i}, \quad C_s = \frac{W_s}{I_i} \qquad\qquad (4.2)$$

---

[12] Only if the distance is large enough, the incident electromagnetic field is large compared to the electromagnetic field caused by particle interaction.

$$C_e = C_a + C_s \tag{4.3}$$

C_e extinction effective cross section [m²]

C_a absorption effective cross section [m²]

C_s scattering effective cross section [m²]

I_i energy flux density of the incident radiation [J/(m² · s)]

W_e energy flux of extinction [J/s]

W_a energy flux of absorption [J/s]

W_s energy flux of scattering [J/s]
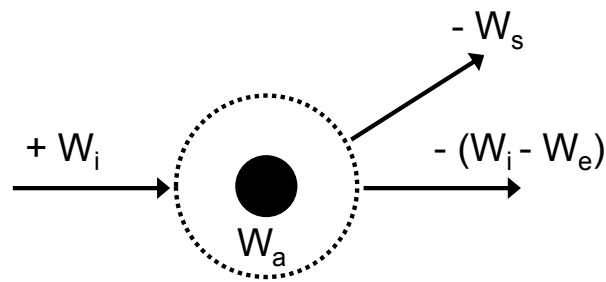
Figure 4.1: Energy flux through a sphere around a scattering aerosol particle [after Bohren and Huffman, 1983, p. 70].

The relation of the energy flux through a sphere around a scattering aerosol particle (Fig. 4.1) is given to be [Bohren and Huffman, 1983, p. 70]:

$$W_a = W_i - W_s - (W_i - W_e) = W_e - W_s \tag{4.4}$$

W_a energy flux of absorption [J/s]

W_e energy flux of extinction [J/s]

W_i incident energy flux (total energy flux) [J/s]

W_s energy flux of scattering [J/s]

The ratio of the individual effective cross section to the particle geometric cross section (G) are the efficiency factors Q_x, for extinction (Q_e), absorption (Q_a), and scattering (Q_s) [van de Hulst, 1981, p. 14].

$$Q_e = \frac{C_e}{G}, \quad Q_a = \frac{C_a}{G}, \quad Q_s = \frac{C_s}{G} \tag{4.5}$$

$$G = \pi \cdot \frac{d_p^2}{4} \tag{4.6}$$

C_e	extinction effective cross section [m²]
C_a	absorption effective cross section [m²]
C_s	scattering effective cross section [m²]
d_p	particle diameter [m]

The energy of a single photon $E(\lambda)$ of the incident radiation can be calculated by:

$$E(\lambda) = h \cdot \upsilon = \frac{h \cdot c}{\lambda} \tag{4.7}$$

h	Planck constant [$h = 6.626 \cdot 10^{-34} \, \text{J} \cdot \text{s}$]
υ	frequency of the incident radiation [1/s]
c	velocity of light in vacuum [$c = 2.9979 \cdot 10^8 \, \text{m/s}$]
λ	wavelength of the incident radiation [m]

Consequently the extinction, absorption, and scattering efficiency are a function of the particle size and the wavelength.

The dimensionless size parameter x is the ratio of the particle circumference to the wavelength [van de Hulst, 1981, p. 123, Bohren and Huffman, 1983, p. 100].

$$x = \frac{\pi \cdot d_p}{\lambda} \tag{4.8}$$

| d_p | particle diameter [m] |
| λ | wavelength of the incident radiation [m] |

The extinction efficiency (Q_e) describes the efficiency of interaction between the incident radiation and the scattering particle. For $Q_e = 1$ only the particle geometric cross section influences the scattering event. For aerosol particles the extinction efficiency can reach values smaller and larger 1 [Bohren and Huffman, 1983, Fig. 4.6]. As the size parameter x increases ($\lambda \ll d_p$), Q_e approach a limiting value of 2, which is twice as large as that predicted by the geometrical optic [Bohren and Huffman, 1983, p. 107].

$$\lim_{x \to \infty} Q_e(x, m) = 2 \tag{4.9}$$

| x | size parameter [1] |
| m | complex refractive index [1] |

This phenomenon is called extinction paradox. It implies that the incident wave is influenced beyond the physical boundaries of the particle. The edge of the particle

deflects rays in its neighborhood (ray bending). From the viewpoint of geometrical optics these rays would have passed the particle unimpeded [Seinfeld and Pandis, 1998, p. 1123]. For particles with $d_p \ll \lambda$, the behavior of the extinction efficiency follows the Rayleigh scattering, which is not described further.

The spatial distribution of the scattering light intensity at single particles or a particle fraction can be described with the volume scattering function $\gamma(\theta,\psi)$ [1/(m·sr)], [after Agrawal, 2005 and Slade and Boss, 2006].

$$\gamma(\theta,\psi) = \frac{1}{I_i} \cdot \frac{\mathrm{d}^2 W_s(\theta,\psi)}{\mathrm{d}\Omega \mathrm{d}V} \tag{4.10}$$

I_i	energy flux density of the incident radiation [J/(m^2·s)]
V	volume of scattering medium [m³]
$W_s(\theta,\psi)$	energy flux of scattering to a certain solid angle [J/(s·sr)]
Ω	solid angle of scattering [sr]
θ	plane angle of scattering [rad]
ψ	azimuthal angle of scattering [rad]

For a fraction of random orientated particles, as well as for single spherical particles the spatial distribution of the scattering light intensity behaves azimuthally symmetric. Hence, for this special case the volume scattering function only depends on the plane angle of scattering and $\gamma(\theta,\psi) = \gamma(\theta)$ [Horvarth, 1998, p. 557]. The scattering phase function $P(\theta)$ [1/sr] describes the angle dependence of the scattering light intensity [Agrawal, 2005]:

$$P(\theta) = \frac{\gamma(\theta)}{\sigma_s} \tag{4.11}$$

$\gamma(\theta)$	azimuthal symmetric volume scattering function [1/(m·sr)]
σ_s	volume scattering coefficient [1/m]
θ	plane angle of scattering [rad]

Within Eq. 4.11 the volume scattering coefficient σ_s can be calculated for spherical particles [Horvarth, 1998, p. 557; Slade and Boss, 2006]:

$$\sigma_s = \int_{4\cdot\pi} \gamma(\theta,\psi)\mathrm{d}\Omega = 2\cdot\pi\cdot\int_0^\pi \gamma(\theta)\cdot\sin(\theta)\mathrm{d}\theta \tag{4.12}$$

$$\mathrm{d}\Omega = \sin(\theta)\mathrm{d}\theta\mathrm{d}\psi$$

$\gamma(\theta)$ azimuthal symmetric volume scattering function [1/(m · sr)]

$\gamma(\theta,\psi)$ not azimuthal symmetric volume scattering function [1/(m · sr)]

Ω solid angle of scattering [sr]
θ plane angle of scattering [rad]
ψ azimuthal angle of scattering [rad]

As described above, the intensity of the light scattered by a single aerosol particle depends on the particle size, the particle composition (complex refractive index), the wavelength of the incident radiation, and the angular range of the OPC detection optics. Knowing all parameters, the Mie scattering amplitude functions $(S_1(\theta),$ $S_2(\theta))$[13] can be calculated [van de Hulst, 1981 p. 35, 124-126]. Combining these amplitude functions and integrating over the plane angle of scattering, the OPC theoretical response function (RF) [m²/particle] is obtained. In general the theoretical RF of an optical instrument describes the intensity of the scattered light for a specific particle type and size. Most OPCs work with a monochromatic laser. Therefore, integration over a certain wavelength range is not necessary. The amplitudes of the scattering light have to be integrated only along the angular range of the OPC detection optics. Consequently, for spherical particles the OPC theoretical *RF* can be written as [after Pinnick and Auvermann, 1979]:

$$RF = \frac{\lambda^2}{4 \cdot \pi} \cdot \int_{\theta_{min}}^{\theta_{max}} \left[\left|s_1(\theta)\right|^2 + \left|s_2(\theta)\right|^2 \right] \cdot \sin(\theta) d\theta \qquad (4.13)$$

$s_1(\theta)$ Mie scattering amplitude function perpendicular to the plane of

scattering [1]

$s_2(\theta)$ Mie scattering amplitude function parallel to the plane of

scattering [1]

θ plane angle of scattering [rad]
θ_{min} minimum plane angle of scattering [rad]
θ_{max} maximum plane angle of scattering [rad]
λ wavelength of the incident radiation [m]

---

[13] The amplitude functions of the scattering light are only valid for spherical particles. Therefore S_1 and S_2 are only functions of the plane angle of scattering.
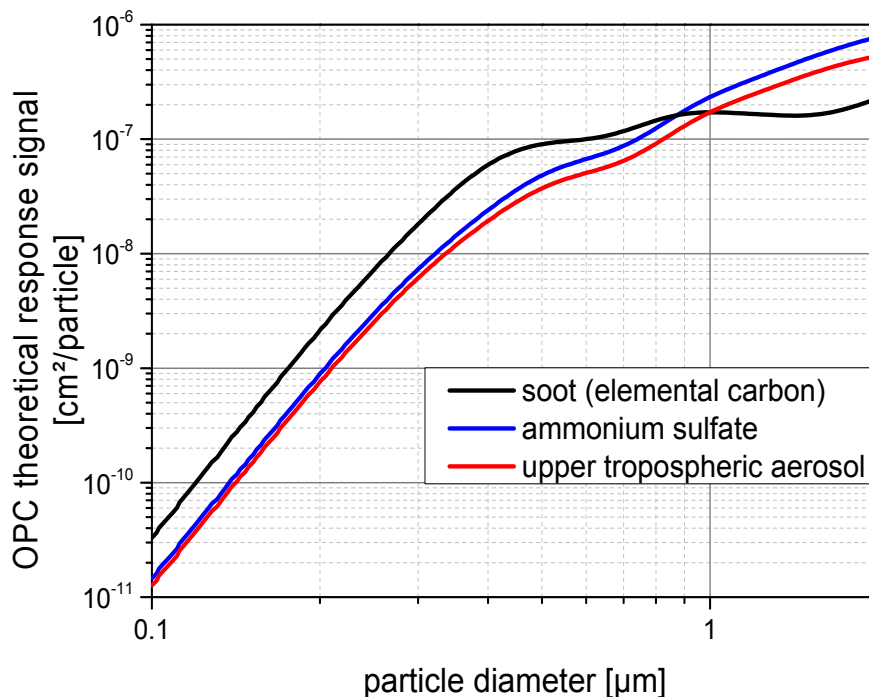
Figure 4.2: Theoretical response function RF for the CARIBIC OPC in the particle size range 0.1 μm < d_p < 2 μm. The RF was calculated with a Mie scattering program written by Thomas Müller (TROPOS). The used complex refractive indices at λ = 830 nm are 1.85-0.71·i (soot; Tab 5.2) 1.52-1.41 ·10^{-7}·i (ammonium sulfate; Tab. 5.2), and 1.48-0.0143·i (mid-latitude upper tropospheric aerosol; Tab. 5.3).

The OPC modified within this work detects the 90° side-way scattering. The exact plane angles of scattering are known, but for proprietary reasons not allowed to be publish. Using a Mie scattering program written by Thomas Müller (TROPOS), the OPC theoretical RF was calculated for different aerosol materials. Figure 4.2 compares the theoretical response signal for pure soot (elemental carbon), pure ammonium sulfate (AS), and an internally mixed aerosol composition, representing mid-latitude upper tropospheric aerosol (UTA; 44% AS, 44% SA[14], 10% organics, 2% soot; cf. Tab 5.3).

From Fig. 4.2 it is obvious that AS and the mid-latitude UTA composition behave similar with only a small offset for particles smaller than approx. 0.4 μm. This offset is caused by the slightly different refractive index real part (1.52 for AS and 1.48 for mid-latitude UTA). Consequently, for the mid-latitude UTA the OPC response signal will be somewhat weaker than for pure AS particles. With increasing particle size (relative to the wavelength) the particle absorption becomes more important. Above 0.4 μm the AS curve lies more clearly above the mid-latitude UTA. This increase is caused as AS has a smaller refractive index imaginary part ($1.41·10^{-7}$) and therefore less absorption than the mid-latitude UTA ($1.43·10^{-2}$). Both curves indicate a dip in the range 0.6 μm < d_p < 0.9 μm. This dip is located in the particle diameter size range around the laser wavelength ($λ ≈ d_p$).

The OPC RF for pure soot particles behaves differently. For particles d_p < 0.5μm the RF shape is comparable to that of AS and mid-latitude UTA, but with a significant offset. The offset is caused by the much higher refractive index real part (1.85). For

---

[14] Sulfuric acid (H$_2$SO$_4$), 75% solution with water (SA)

particles larger than 0.5 µm the RF slope differ from those of AS and mid-latitude UTA. This is caused by the much higher refractive index imaginary part (0.71). Soot absorbs the incident radiation much more efficient than AS and mid-latitude UTA and the OPC response signal is attenuated.

4.2   Original instrument: OPC KS-93 (RION)

To ensure stable and high-quality measurements, the small, light, and very robust KS-93 OPC from RION CO., LTD. (www.rion.co.jp/english/; last access: 20.07.2014) was chosen as basis instrument for the new CARIBIC OPC unit (cf. Fig. 4.3). This OPC has a size of 135 x 280 x 150 mm ($h \times w \times d$) and a total weight of only 6.5 kg. As light source a 200 mW laser diode with a wavelength of $\lambda = 830$ nm is used. With this infra red laser and the given optics, the measurable particle size range of the KS-93 is specified to 0.1 to 2 µm for polystyrene latex particles with a refractive index of $m = 1.6 - 0.0 \cdot i$ [RION, 2008]. Own calibrations showed that the limits for size resolved measurements are at about 0.125 and 1 µm (Sec. 5.2). Larger particles are counted by the KS-93, but as the signal is in saturation, no size information can be derived and these particles are attributed to the highest channel. The original RION data acquisition provides a particle size distribution in only five channels and has a maximum counting efficiency of 50 %, which is caused by the optics of the KS-93. With a modified gas flow inside the KS-93 (Sec. 4.3.3) and the new data acquisition (Sec. 4.4), the CARIBIC OPC unit has a maximum counting efficiency of about 90 % and the size resolution can be variably set during the post-flight data analysis. The great advantage of this OPC in contrast to most of the other OPCs measuring down to 100 nm, is the independence of the scattering signal on the working pressure. The

Figure 4.3: Optical Particle Counter KS-93 (RION) with power supply KZ-50 (from www.rion.co.jp/english/; last access: 20.07.2014).

KS-93 uses a robust synthetic quartz optical cell where the measurement air passes the laser beam outside the laser cavity. Due to this set-up the operation pressure can vary from 0 to 5000 hPa. Intracavity OPCs, where the measurement air flows directly through the cavity of the laser beam and cause a stronger signal of the scatted light, can detect particles with a diameter of 100 nm or smaller. However, because of the measurement technique these OPCs are highly pressure depended and therefore less suited for airborne measurements.

As described in Sec. 4.4, a new data acquisition was developed to improve the size resolution of the measured particle size distribution. Therefore RION added three Sub-Miniature-B (SMB) output connectors at the rear side of the KS-93. These connectors provide directly the amplified scattering signals of the detected particles. Because the KS-93 has three different amplifiers, three SMB connectors are used, one for each amplifier stage. Each of the amplified signals yields an output signal in the range of 0 V to 10 V. For comparison and data evaluation the signals of the second and third amplifier are amplified by a factor of 30 and 125, respectively.

4.3   OPC unit

4.3.1   General unit set-up

To operate the OPC unit fully automated, a gas flow system, a data acquisition system, and new electronic components were added to the original RION OPC (Fig. 4.4). From the KS-93 only the housing, the optics with the internal flow system, and the detection electronics for the scattered light are still used. All components are mounted on a 20 mm thick aluminum alloy ground plate (alloy code EN AW-7175) inside a 19''
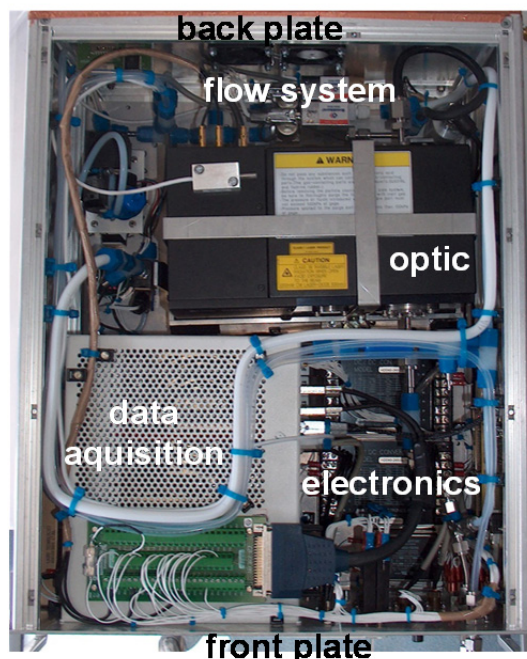
Figure 4.4: CARIBIC OPC unit top view with all components. The "optic" is the original KS-93 displayed in Fig. 4.3.
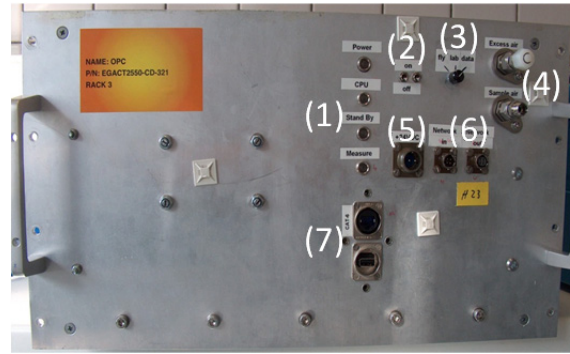
Figure 4.5: CARIBIC OPC unit front plate. Highlighted components are the four status LEDs (1), the main switches/fuses (2), the unit operation mode switch (3), the air inlet tubing (4), the 24 VDC in power connector (5), the Ethernet network in and out connectors (6), and the CAT6 network- and USB connectors (7).

EMC rack unit housing (CS2007, Knürr). Using a honeycomb structure the weight of the plate is reduced by ~17.4 kg to 2.6 kg. For the same reason the steel sheet cover plates are replaced by 4 mm thick aluminum coated honeycomb sandwich panels (Euro Composites), thus saving another 2 kg. The front plate (Fig. 4.5) is a 3 mm aluminum alloy plate (2024 clad T351), which is much stronger than normal aluminum, but has nearly the same weight.

When the OPC unit is mounted in the CARIBIC container, only the front- and the rear plate are accessible. Therefore all air tubing and cable connectors are placed at the front plate (Fig. 4.5). Beside the 24 VDC power in (5) and the Ethernet network in and out (6) (needed for communication with the master computer during measurement flights), also a CAT-6 network and a USB (7) connector for communication with the unit in the laboratory are mounted at the front plate. To switch the unit between aircraft and laboratory mode, a rotary switch (3, Grayhill, 56SD36-01-2-AJN) is installed beside the air inlet tubing (4). Four LEDs (1, Marl) indicate the actual measurement status of the OPC unit (cf. Sec. 4.4). Two thermal fuses (ETA, 41020-G111-K1M1-A1S0ZN-7.5A) at the front plate (2) are used also as main switch for the OPC unit. To protect all electronic compounds from excess voltage, voltage fluctuations, and electromagnetic influences, an excess voltage diode, two DC/DC converters (Chinfa, HDD60-24S24T and HDD60-24S12T), and an Electro Magnetic Interference (EMI) filter (Schaffner, FN 660-16/06) are installed, respectively.

The original KS-93 is sensitive to shocks and vibration, which is a severe problem for operation onboard aircraft. Therefore the OPC is mounted on a purpose-made aluminum alloy frame, which is shown in Fig. 4.6. With three wire rope isolators (ENDINE, WR3-800) the frame is fixed on the ground plate. The isolators are symmetrically arranged around the centroid of KS-93. In that way the remaining maximum shock on the OPC was calculated by ENDINE to be 4 g (20 milliseconds) for the landing of the aircraft. All other shocks (e.g. caused by air turbulence) were considered to be weaker than the shocks during landing. Because of the free swinging construction, all air tubing to the OPC (TSI, electroconductive Silicone tubing with 4.83 mm inner diameter, 3001788), as well as the power and signal cables are flexibly connected. Padded backsquares prevents the OPC from larger displacements, which might lead to damaging of the OPC or the components in its vicinity. To decouple the
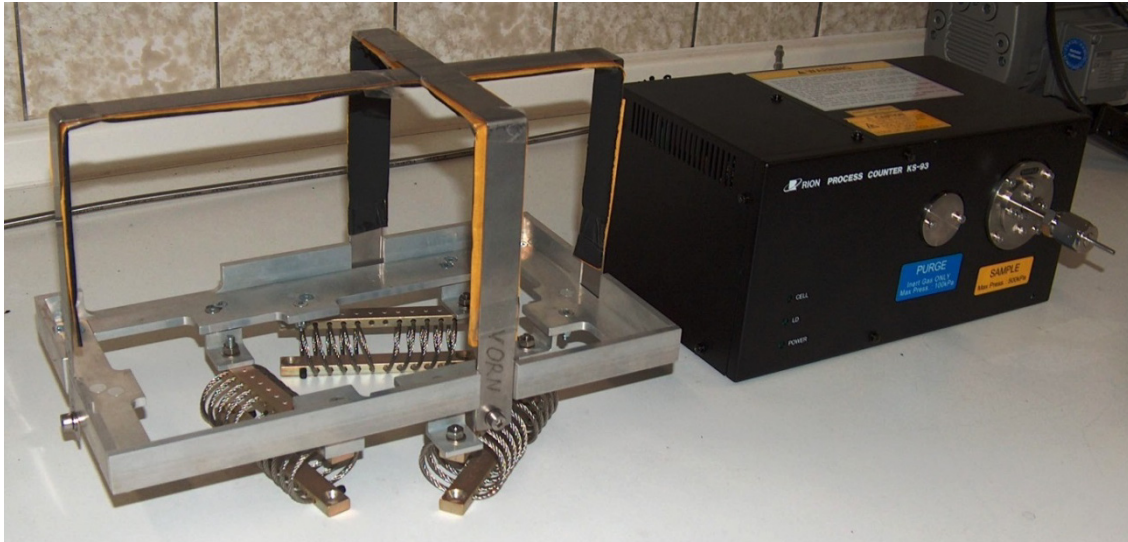
Figure 4.6: Purpose-made aluminum alloy frame with wire rope isolators (left) to decouple the KS-93 (right) from vibrations and shocks during the measurement flight.

OPC from vibrations, caused by the external vacuum pump or the engines of the aircraft, the whole rack with the OPC unit is mounted on shock mounts (MEGI, 786214_60). The small compressor inside the OPC unit is also mounted on four compact wire rope isolators (ENIDINE, CR1-300) to prevent vibration transmission to the frame.

Most of the 150 W power consumption of the OPC unit is transformed into heat. Therefore, five fans are used to generate a flow of fresh cool air through the OPC unit. At the side panels, near the front plate, the fresh air is pulled into the unit (three fans, Orion, OD6010-12HB) and at the back plate the heated air is blown out (two fans, ebm-papst, 624HH). In that way about 2 m^3/min are pulled through the OPC unit. During the first year of operation in the CARIBIC aircraft, the observed air temperature inside the OPC unit varied between 27°C and 45°C, depending on the cooling of the aircraft cargo bay.

To get the aeronautic certification for implementation in the aircraft, the CARIBIC container had to pass an EMC test (RTCA DO-160E). For every system mode of the OPC unit, the energy of the emitted electromagnetic radiation has to be below a well-defined threshold in the frequency spectrum between 150 kHz and 6 GHz. This is particular important near the communication frequencies of the aircraft around 100 MHz. Consequently, all ventilation openings of the OPC unit are covered with EMC screens. A preliminary EMC test was carried out in November 2009 at the GKSS (Gesellschaft für Kernenergieverwertung in Schiffbau und Schiffahrt mbH, since 2011 Helmholtz-Zentrum Geesthacht, HZG) in Geesthacht/Germany to ensure that the emitted radiation of the OPC unit is continuously below the given threshold values. Figure 4.7 shows the intensity of the emitted radiation from the OPC unit. The level H threshold is the most limiting threshold given in the EMC norm DO-160E [RTCA/DO-160E 2004] and is in the minimum peaks 10 dBμV/m lower than the threshold for the certificated EMC test for the whole container (not shown in Fig. 4.7). For no frequency
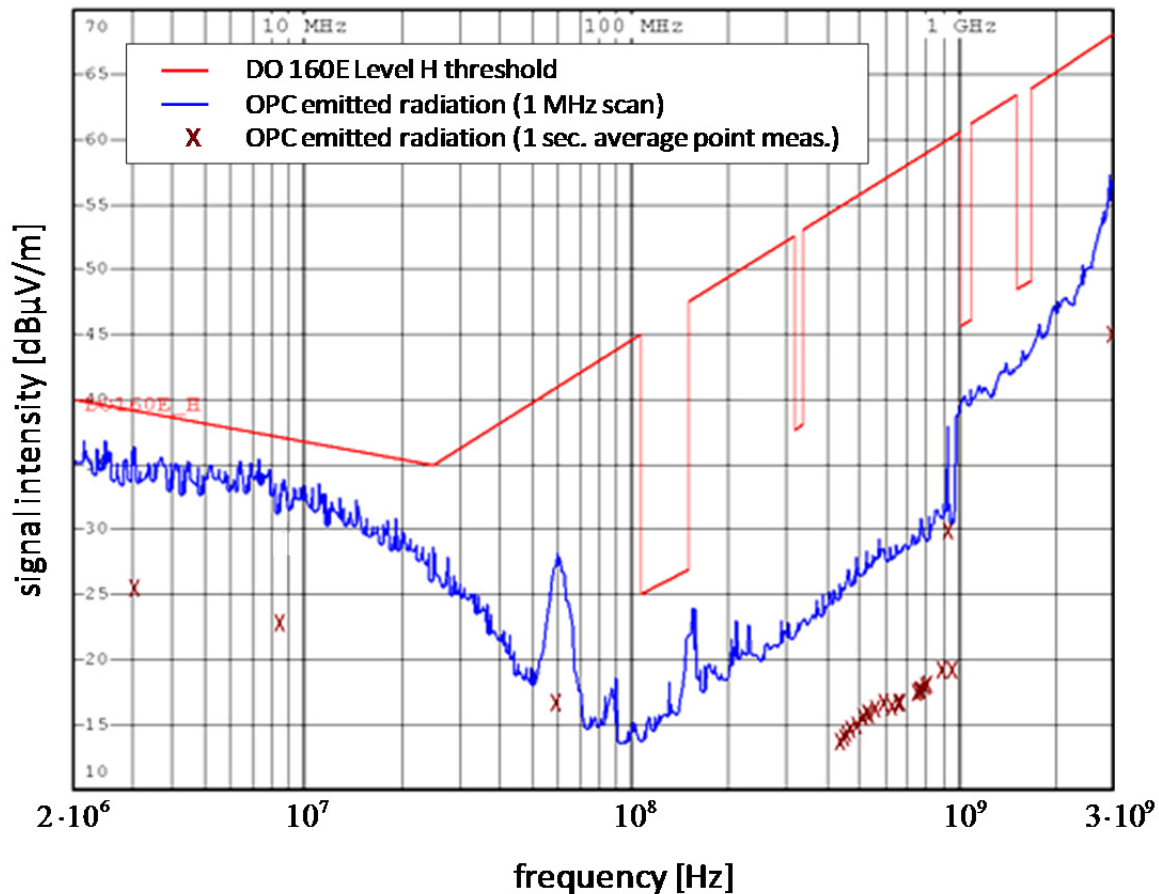
Figure 4.7: Intensity of the electromagnetic radiation emitted by the CARIBIC OPC unit when measuring. The red line gives the DO 160E Level H threshold for comparison.

the energy of the radiation emitted by the OPC unit is above the level H threshold: neither for the rapid scan (blue), nor for the more accurate 1 second average point measurements (crosses).

4.3.2 Gas flow system

The original KS-93 has no internal gas flow control system. Therefore a gas flow system was developed for the CARIBIC OPC unit, providing the optic with a well-defined air sample volume flow.

First calibration measurements with the KS-93 showed the occurrence of artificial noise particle signals in the size spectrum. Figure 4.8a shows the distribution of the output signal for a measurement of 350 nm polystyrene latex particles. The experimental set-up (cf. Sec. 5.2) provides a very narrow monomodal aerosol particle distribution. The monomodal structure of generated particle distribution was verified by a second OPC[15], operated in parallel. However, besides the main peak, the signal spectrum of the KS-93 contained also many counts which had a lower signal intensity, suggesting the existence of smaller particles. Compared to the integral number of counts

---

[15] Ultra-High Sensitivity Aerosol Spectrometer, Droplet Measurement Technologies, 0.06 µm < d_p < 1 µm
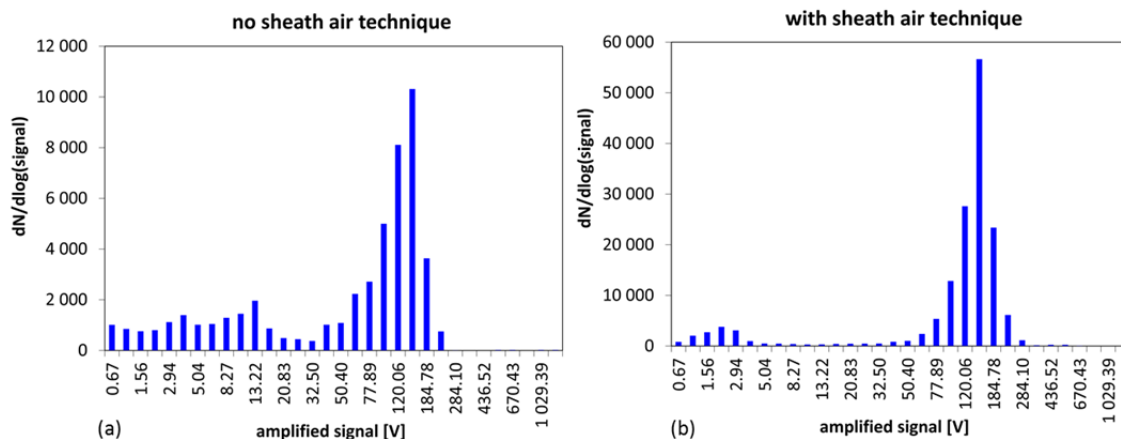
Figure 4.8: Signal intensity distribution of KS-93 for 350 nm polystyrene latex particles, (a) for the original KS-93 gas flow set-up, (b) with the sheath air technique inside the CARIBIC OPC unit.

within the main peak (96.7 V < signal < 436.5 V), the integral number of all counts lower than the main peak (signal < 96.7 V) was about 57% of the main peak. The additional small signals were observed only when measuring particle loaded air. For filtered air measurements no signals were observed. Hence the additional small signals were not caused by background noise. The reason for this signal intensity spread likely is the set-up of the optics inside the KS-93. The intensity of the laser light from the edge to the center of the beam follows a Gaussian curve with the maximum in the center. When a latex particle passes the laser not in the center of the beam, but in the edge region, the intensity of the scattered light and therefore the output signal is lower than the signal for the same particle passing in the center. Moreover, in the original set-up the laser beam illuminated only half of the air sample, which led to a limited counting efficiency of the original KS-93 of maximum 50%.

To focus the aerosol particles to the center of the laser beam, the measurement air is surrounded by particle free sheath air in the new flow system of the KS-93. Unfortunately, the gas inlet of the KS-93 is a 1/4'' tubing with a so called "VCR" connection. This VCR connection may cause turbulence downstream which in turn would ruin the focusing of the measurement air to the center of the optics. Consequently, the laminar embedding of the measurement air into the center of the sheath air takes place 30 mm behind the VCR connection. Different combinations of Swagelok fittings, as well as 1/4'' and 1/16'' tubing were tested and the one finally used is shown in Fig 4.9. The measurement air flows through the 1/16'' tubing (inner diameter 0.5 mm). The particle free sheath air flows through a Swagelok tee union with the 1/16" tubing at the unions center line. To hold the 1/16'' tubing in the center of the surrounding 1/4'' tubing, the original gasket of the VCR connection was replaced by a blind gasket in which seven holes were drilled. The hole in the center holds and aligns the 1/16'' tubing. The other six holes are arranged symmetrically around the center, supplying the sheath air. Around 30 mm behind the gasket the flow of the sheath air is assumed to be laminar. Using this sheath air technique with a flow rate ratio of 1:9 (sample to sheath air; cf. Sec. 5.1), the distribution of the signal intensity for 350 nm polystyrene latex particles is much less noisy compared to the one without sheath air (Fig. 4.8b). Nearly all counts are in the main peak of the distribution, i.e., only a few particles cause too small signals. The treatment of the remaining signals lower than the
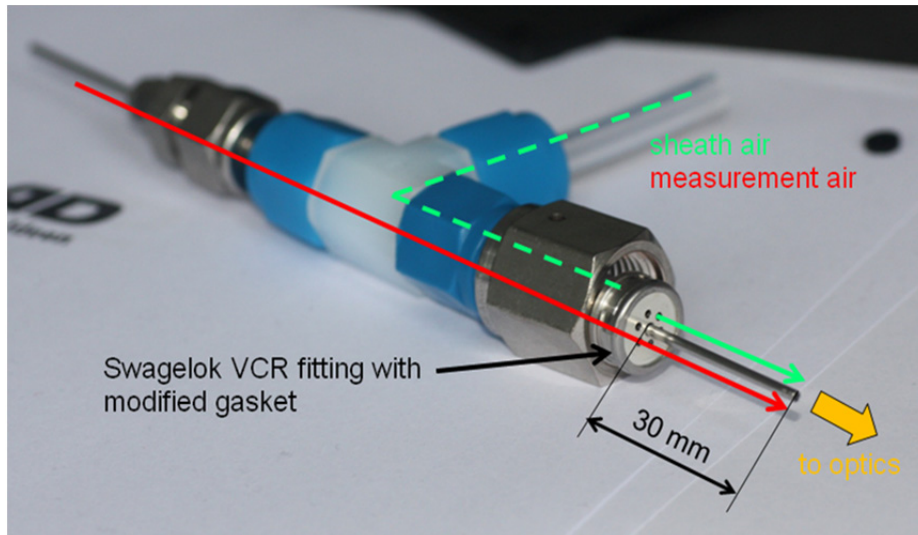
Figure 4.9: Sheath air implementation upstream the KS-93 optics. The construct is a combination of different Swagelok fittings, 1/4'', and 1/16'' tubings, as well as a modified VCR blind gasket to center the 1/16'' aerosol sampling air tube.

main peak will be discussed in Sec. 5.1. Additionally, the sample air focusing improves the maximum counting efficiency of the OPC unit to 89%. The reason why the counting efficiency did not reach 100 % unfortunately could not be clarified up to now. Sensitivity studies indicated that the remaining small signals with the new sheath air technique (Fig. 4.8b) are not caused by particles, passing the laser beam in the edge region (cf. Sec. 5.1, 5.2.4). However, as this new counting efficiency proofed to be very stable with time, the measured particle number concentrations can be corrected for.

During flight, the OPC unit can be set to three different operation modes (cf. Sec. 4.4), namely Initialization (IN), Stand By (SB), and Measure (MS). This measure is required by the CARIBIC system operation concept. For each of these modes the gas flow inside the OPC unit is different. A gas flow system schematic is displayed in Fig. 4.10. IN is the initial operation mode of the unit after getting power and system boot-up. In this mode only the computer has power, but no other component. This mode is used during aircraft take-off and landing to save power for the aircraft systems. As the external pump has no power either, there is no gas flow inside the OPC unit.

When the OPC unit is in SB mode, it is provided with the external vacuum. The three-way valve (Bürkert, 6012 NC) is switched in direction 1-3 and the internal membrane pump (KNF, NMP850KNDC B) blows ~ 3 l/min of filtered air into the tubing system. About 1 l/min is pulled through the critical orifice to the vacuum exit at the rear plate (OPC excess air). The vacuum is monitored by another aerosol rack unit and is always below 35% of the operation pressure at the OPC unit inlet, thus ensuring proper critical orifice operation. Because both Mass Flow Controllers (MFCs, Bronkhorst, F-201D-ABD-00-V) are closed, the remaining 2 l/min are blown through the flow splitter and the sample air inlet out of the unit toward the aerosol inlet. This purging mechanism prevents contamination of all aerosol instruments by polluted air in the vicinity of airports.

In MS mode the valve is switched in direction 1-2, MFC 1 is set to 0.150 l/min, and MFC 2 to 0.135 l/min. Using the pressure and the temperature data from the sensors in the gas flow, the MFCs are adjusted to a constant volume flow through the optics by
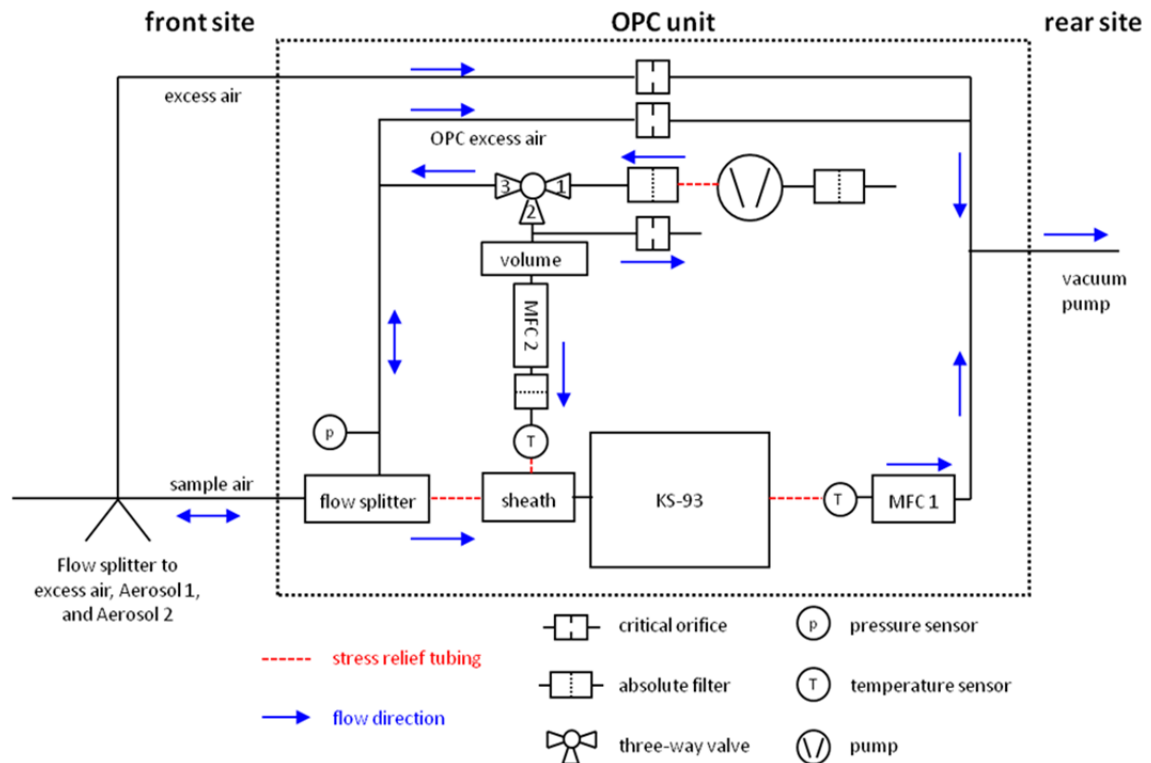
Figure 4.10: Gas flow diagram of the CARIBIC OPC unit. When measuring (MS), the three-way valve is switched in direction 1-2, the pump is working, MFC 1 is set to 0.150 l/min, and MFC 2 is set to 0.135 ml/min. In stand by (SB) mode, the valve is switched to 1-3, the pump is working, but both MFCs are closed. For the init (IN) mode, also the pump is switched off and no external vacuum is available (external pump is off).

a 1 Hz LabVIEW proportional-integral-derivative (PID) controller algorithm. This measure guarantees for each MFC a constant air volume flow with 1% accuracy despite pressure changes during the flight. MFC 2 provides only 90% of the air (filtered sheath air) pulled through the optics and MFC 1 to the vacuum exit of the OPC unit. The residual sample air flow of 0.015 l/min is taken from the CARIBIC inlet, via flow splitters and the sheath air device upstream the KS-93 optics. To reduce the residence time of the sample air in the tubing between the inlet and the aerosol instruments (Aerosol 1 and 2, OPC) and to minimize wall effects (e.g., particle losses), only the core flow is use by the three units at the first flow splitter (Fig. 4.10 outside the OPC unit). The depleted air near the tubing wall (~4.2 l/min, excess air) is pulled through the OPC unit to the vacuum exit. The excess air flow is controlled by a critical orifice. From the first flow splitter ~1 l/min of measurement air is pulled through a 1/4'' tubing to the second flow splitter inside the OPC unit. At the second flow splitter, which is located about 10 cm in front of the sheath air implementation, again only the less influenced core flow is taken for the measurement. The surrounding excess air is transported through the critical orifice to the vacuum exit of the unit. Due to the increased volume flow between the aerosol inlet and the second flow splitter, the total residence time of the measurement air in the sampling line is minimized and is less than 1 s.

The membrane pump inside the OPC unit (providing the sheath air) causes small pressure fluctuations which disturb the flow control of MFC 2. Consequently, an additional buffer volume upstream the pump was installed which reduces these

fluctuations. Unfortunately, the chosen three-way valve cannot be switched from direction 1-2 to direction 1-3 (from mode MS to SB) when the pressure between pump and MFC 2 is higher than 2000 hPa. Therefore, a pressure compensation tube open to the ambient is mounted between the valve and the volume. To ensure high enough pressure for running MFC 2 (about two times the pressure downstream the MFC), a critical orifice is inserted in the pressure compensation tube.

4.4   Unit control and data acquisition

To control the OPC unit a Real-Time Embedded Controller (NI PXI-8106 RT) mounted into a 4-Slot DC-powered PXI chassis from National Instruments is used (www.ni.com; last access: 20.07.2014). For system control and recording the data from the sensors and the KS-93, a relay card (NI PXI-6521), an M series multifunction data acquisition card (NI PXI-6220M), and a high speed R series data acquisition card (NI PXI-7851R) are mounted in the chassis, too. The above PXI components together are called "PXI system". The software controlling the OPC unit and recording the data was designed by the author of this thesis and was mainly written by Thomas Conrath (TROPOS) in LabVIEW. The unit control works as follows.

During flight all measurement instruments in the CARIBIC container are controlled by the master computer, by providing the instruments with the measurement status of the container every 20 s. Generally, the master can send one of the following commands to the measurement instruments via an Ethernet network: ST (status), IN (initialize), SB (stand by), or MS (measure). When a slave instrument (in the following the OPC unit) receives a command from the master, it has to acknowledge its receipt, sends its current status to the master, and executes the command of the master. If the OPC unit receives no command from the master for three minutes, for safety reasons the OPC unit sets itself to IN mode. The IN mode is the basis mode of all measurement instruments, where only the computer has power to communicate with the master and all other power is shut off.

About 40 seconds after the OPC unit gets power the boot-up is finished and it is set to the IN mode. This status is send to the master, as response to the ST request the master sends directly after booting to all slaves. When the master receives the status of the OPC unit correctly, SB is send to the OPC unit thereafter. As described in Sec. 4.3.2, in SB mode the OPC unit is purged with filtered air to prevent contamination of the optics. Because the laser diode of KS-93 needs up to 10 minutes to stabilize, the KS-93 has already power in SB mode. When the CARIBIC aircraft reach a pressure level allowing to start the measurements[16], the master sends the MS command. The OPC unit responds by switching the three-way valve to position 1-2 and enabling the flow control. Because both MFCs need about 40 seconds to adjust the volume flow to the set values (0.150 l/min for MFC 1 and 0.135 l/min for MFC 2, respectively), the OPC unit changes from SB first in the intermediate mode "begin measure" (BM). After 45 seconds the gas flow is stable and the unit mode changes to MS. When the pressure

---

[16] currently 700 hPa, measured with a pressure sensor inside the master unit

increases above 850 hPa during landing the measurement status of the container changes to SB again. When the OPC unit receives the SB command from the master, the measurement is stopped and the unit is purged with filtered air, again.

The actual measurement mode of the OPC unit is indicated by four LEDs at the unit front plate as requested by the CARIBIC container concept. To track the communication between master and OPC unit, it is stored in a log file. Moreover internal error messages are logged in the same file to find possible reasons for errors in the OPC unit due to instrument malfunctioning. When the OPC unit is operated in the laboratory (e.g. for calibration measurements) the unit operation mode switch (Fig. 4.5, (3)) is switched from "aircraft" to "laboratory". In the laboratory mode no master computer is needed to operate the unit.

In all modes (IN, SB, BM, MS) the data acquisition records the signals of the pressure and temperature sensors with 10 Hz resolution. In BM and MS mode additionally the current volume flow at the two MFCs are recorded with the same resolution. The amplified signal of the scattered light at the three SMB connectors of KS-93 (Sec. 4.2) can be recorded with a temporal resolution of up to 750 kHz for each channel. As the signal pulses have an average duration of ~ 60 µs (Sec. 5.1) the time resolution was set to 333 kHz to save disc space and computational power. With this resolution each signal pulse (roughly Gaussian shape) can be clearly resolved with 20 data points on average. When the signal intensity at the most sensitive channel 1 (Ch-1) increases above 0.35 V (trigger level), the signal intensity of all three channels are recorded until the voltage at Ch-1 decreases below the trigger level. The recording of the pulse form enables the post flight data analysis (Sec. 5.3.1) with the determination of the pulse maxima for each detected particle, the respective signal intensity and the exact detection time. Using these single particle data, the temporal, as well as the size channel resolution of the particle size distribution can be flexible set during later analysis.

After a sequence of usually four measurement flights the CARIBIC container is removed from the cargo bay of the aircraft and the raw data of all instruments are uploaded on a data server at the MPI-C in Mainz for post-flight analysis. To aid the transfer of the data from the OPC unit to the server, all data are stored on a Compact Flash (CF) card, which can be easily removed from the backside of the OPC unit without the need to boot the PXI system.

5 Characterization and calibration of the new CARIBIC OPC unit

While the theory of light scattering by particles as well as the OPC unit general setup and the data acquisition/unit control software is described in Ch. 4, this chapter deals with the signal characterization and the calibration. The signal behavior of the modified OPC is described in Sec. 5.1. Thereafter the laboratory calibration setup (Sec. 5.2.1) and the particle size calibration is described (Sec. 5.2.2). The atmospheric aerosol particle composition differs strongly for different atmospheric regions (cf. references in Sec. 5.2.3). A sensitivity study was carried out to analyze the influence of the chemical composition on the refractive index and the particle density and thus on the OPC-measured particle size distributions and derived particle mass concentrations. The results of this sensitivity study are discussed in Sec. 5.2.3. While the counting efficiency calibration is explained in Sec. 5.2.4, coincidence measurement results are discussed in Sec. 5.2.5. The calibration of the temperature and pressure sensors, as well as the two MFCs is summarized in Sec. 5.2.6. Finally, the data analysis procedure, including the calculations for particle losses in the inlet system and an uncertainty estimate is given in Sec. 5.3.

5.1 Characterization of the modified KS-93 with the new data acquisition

To cover a large particle size range with high resolution, the KS-93 scattered light signal is amplified by three different linear amplifiers. These amplifiers are connected to the newly installed three SMB connectors (Sec. 4.2). The amplified signals have a roughly Gaussian shape and an intensity of 0 to 10 VDC, depending on the measured particle size. The signal of SMB connector 1 (Channel 1; Ch-1) is amplified most strongly to resolve the signals of particles smaller than about 227 nm in diameter (with respect to UT aerosol; cf. Sec. 5.2). Particles, larger than about 227 nm and smaller than
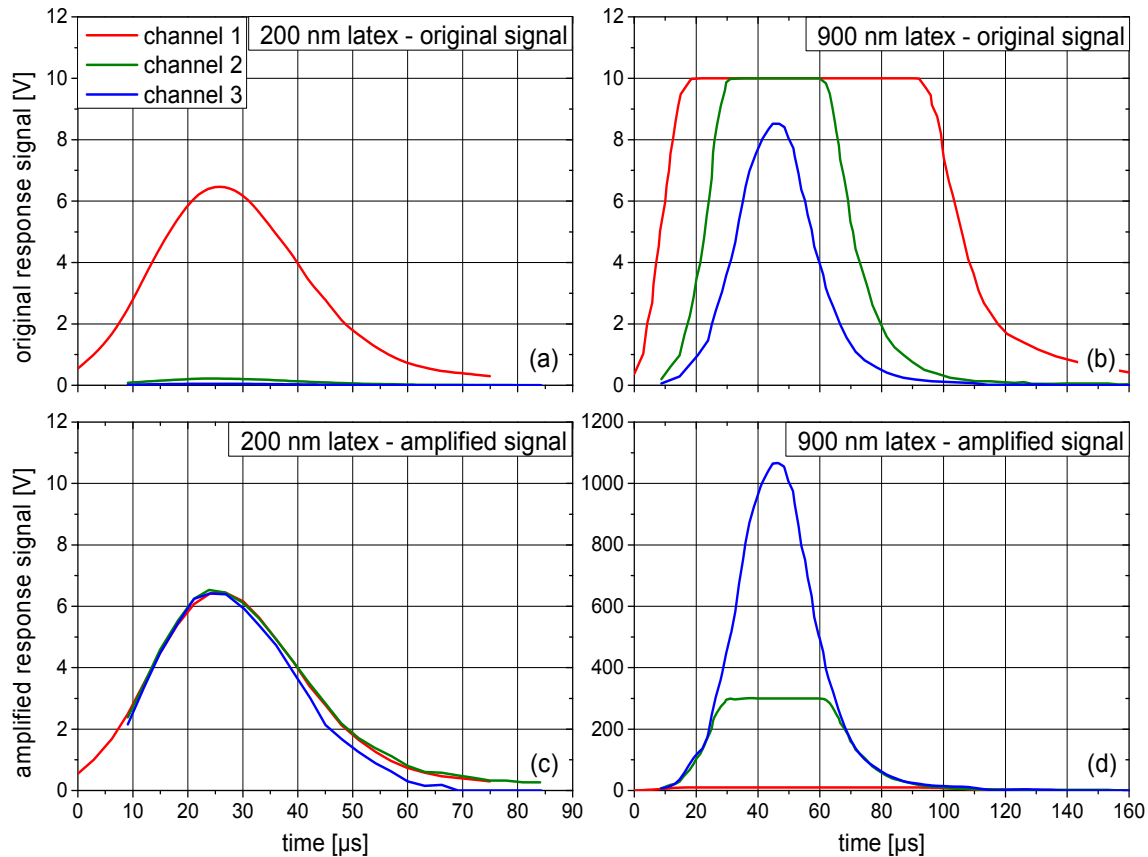
Figure 5.1: Typical signal pulses for all three channels for 200 nm and 900 nm diameter polystyrene latex particles. Figure (a) and (b) show the original signals at the SMB connectors of the KS-93 OPC. The amplified response signals (factor of 30 for channel 2 and 125 for channel 3), used for data analysis, are shown in (c) and (d), respectively.

about 598 nm (UT aerosol) are resolved best with the second amplifier and the respective signal is available at SMB 2 output (Channel 2; Ch-2). All particles larger than about 598 nm are resolved by the third amplifier, SMB output 3 (Channel 3; Ch-3). The upper limit of Ch-3 and therefore the upper limit for size resolved measurements of the OPC is given by the saturation of the third amplifier and was analyzed to be at about 1312 nm (10 VDC signal) for UT aerosol particles. The OPC counts also particles larger than about 1312 nm (likely to the upper diameter limit determined by the inlet system), but all these particles cause a 10 V signal and are thus attributed to the last diameter size bin. Figure 5.1 shows two examples for a typical signal of a 200 nm and a 900 nm diameter polystyrene latex particle with a complex refractive index of $m = 1.59 - 0.0 \cdot i$. The small 200 nm particles cause on average signal pulses with a duration of about 60 µs and a maximum pulse height of 6.6 VDC in Ch-1 (Fig. 5.1a). The maximum of Ch-2 and Ch-3 is on average 0.22 VDC and 0.05 VDC, respectively. For large particles with 900 nm diameter, the amplifiers of Ch-1 and Ch-2 are saturated and therefore the signal is truncated at 10 V (Fig. 5.1b). This particle size is resolved in Ch-3 with a pulse width of about 90 µs and a maximum value of 8.65 VDC on average. Because Ch-1 is most sensitive, the signal increase first and decrease last.

For later analysis, the three channels are combined to one quantitative signal for each particle (combined signal). If Ch-1 is not saturated (pulse maximum < 10 VDC), its signal is taken as the combined signal. In case Ch-1 is saturated but not Ch-2, the

signal of Ch-2 multiplied with 30 is used. If only Ch-3 resolves the particle pulse, this signal multiplied with 125 is used. Consequently, the combined signal ranges between 0 and 1250, covering all three channels. The combination of the three channels using the described amplification is shown in Fig. 5.1c and 5.1d for the 200 nm and 900 nm diameter latex particles. The comparison of the three amplified signals shows that they agree well and thus the amplification factors of Ch-2 and Ch-3 are correct.

To resolve the particle pulse form, the temporal resolution of the data acquisition was set to 3 µs. As the signal of one particle has duration of about 60 to 90 µs on average, the pulse is resolved with 20 to 30 data points. When analyzing the pulse form and properties, a delay of 9 µs was found for Ch-1 compared to Ch-2 and Ch-3. For Fig. 5.1 this time shift was corrected by shifting Ch-2 and Ch-3 three data points to the right. Because Ch-1 is the most sensitive, the signal recording of all three channels is triggered by the intensity of Ch-1. The trigger level was set to 0.35 VDC as for particle free air measurements with a trigger level of 0.30 VDC small signals were recorded. The trigger level determines the lower detection limit of the OPC unit, which is calculated to be 117 nm (UT aerosol; Sec. 5.2).

Onboard the aircraft the OPC unit has to measure at variable operating pressure between 950 hPa during takeoff and landing and ~ 250 hPa at cruising altitude (both ram pressures). Hence, the scattered light signal was analyzed as a function of pressure. The signal for 350 nm diameter latex particles increases by less than 4% in peak maximum when decreasing the pressure in the optical cell from 1000 to 200 hPa. Hence, pressure changes do not influence the measurements strongly.

To determine the optimum ratio of measurement to sheath air (Sec. 4.3.2), two criteria had to be considered. On the one hand the sampled air has to be focused in the center of the air flow to prevent particles from passing the laser beam at the less illuminated edge regions. This can be reached by a small sample air tubing (inner tubing in Fig. 4.9). Moreover, to avoid turbulence, the Reynolds number has to be in the laminar flow regime and the flow speed of the sample and sheath air has to be approximately equal. On the other hand, as much sample air as possible should pass the optics in order to get good statistics, which allows to increase the OPC time resolution and the number of size channels. Therefore, several test measurements with 1/8'' and 1/16'' measurement air tubes with different inner diameter and different flow ratios were carried out. Using an acuminated 1/16'' tubing with an inner diameter of 0.5 mm, an acceptable signal to noise behavior was found for a flow ratio of 1:9 (sample air : sheath air, cf. Fig. 5.2a to 5.2c). A further increase of the flow ratio in favor of the sheath air does not significantly decrease the fraction of additional small counts (Fig. 5.2c vs. 5.2d). As this increase would worsen the OPC counting statistics and by this the resolution of the size distribution, a ratio of 1:9 was taken and the sample and sheath air flows were set to 150 cm^3/min and 135 cm^3/min, respectively (cf. Fig. 4.10). The remaining 15 cm^3/min of sample air are sucked through the center of the optics.
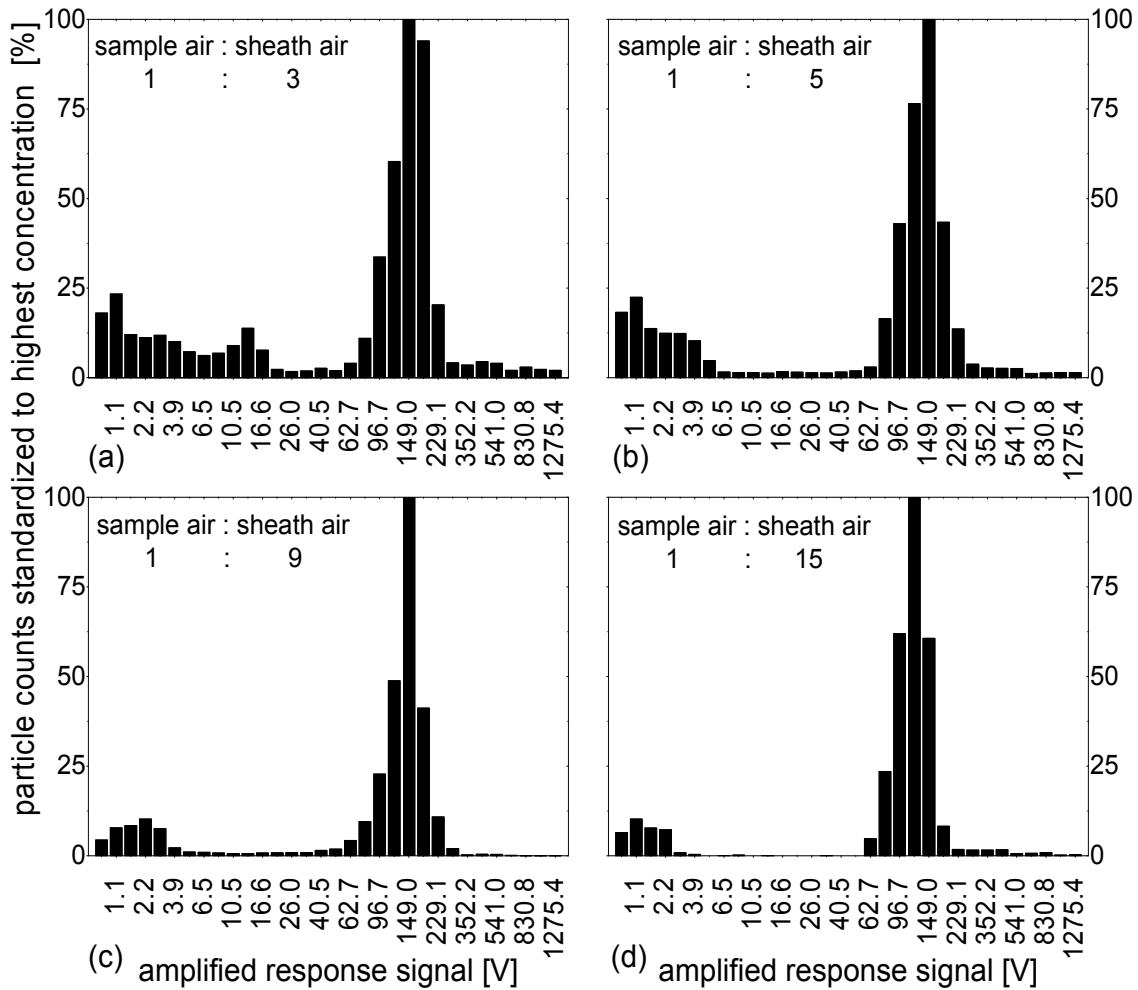
Figure 5.2: Signal intensity distribution of KS-93 for 350 nm polystyrene latex particle measurement with implemented sheath air technique. The measurement air to sheath air ratio was 1:3 (a), 1:5 (b), 1:9 (c), and 1:15 (d). Within each graph the bin values are normalized to the highest bin.

A small amount of small, artificial signals still remains (Fig. 5.2c) when the flow ratio is set to 1:9. The reason for these additional signals occurring only for particle measurements larger than ~250 nm is unclear. They are connected to signals from real particles, because they were not observed when measuring filtered particle free air. One possible explanation would be recirculation inside the optics due to small turbulence at the lens. In this case, some particles would be counted twice, likely as smaller ones because of passing the laser beam in the edge region. However, according to the optics geometry and the flow Reynolds number, the flow should be laminar. Another explanation could be small reflections of the scattered light at the walls of the optical cell. Nevertheless, the following sensitivity study shows that the influence of erroneous particle counts on the particle concentration within a size bin of the size distribution usually measured in the UT/LMS region is less than 1.5%. Figure 5.3a displays the integral fraction of erroneous counts with respect to the integral number of "correct" counts for different particle diameter. For instance, measuring particles with a diameter of 259 nm (250 nm ammonium sulfate particle transferred to UT aerosol; cf. Sec. 5.2.2), the fraction of additional small scale counts is about 10% compared to the real particle number (main peak within the size distribution, not shown). These additional counts are located in a size range between 117 nm and 182 nm (error bar in Fig. 5.3b). The average
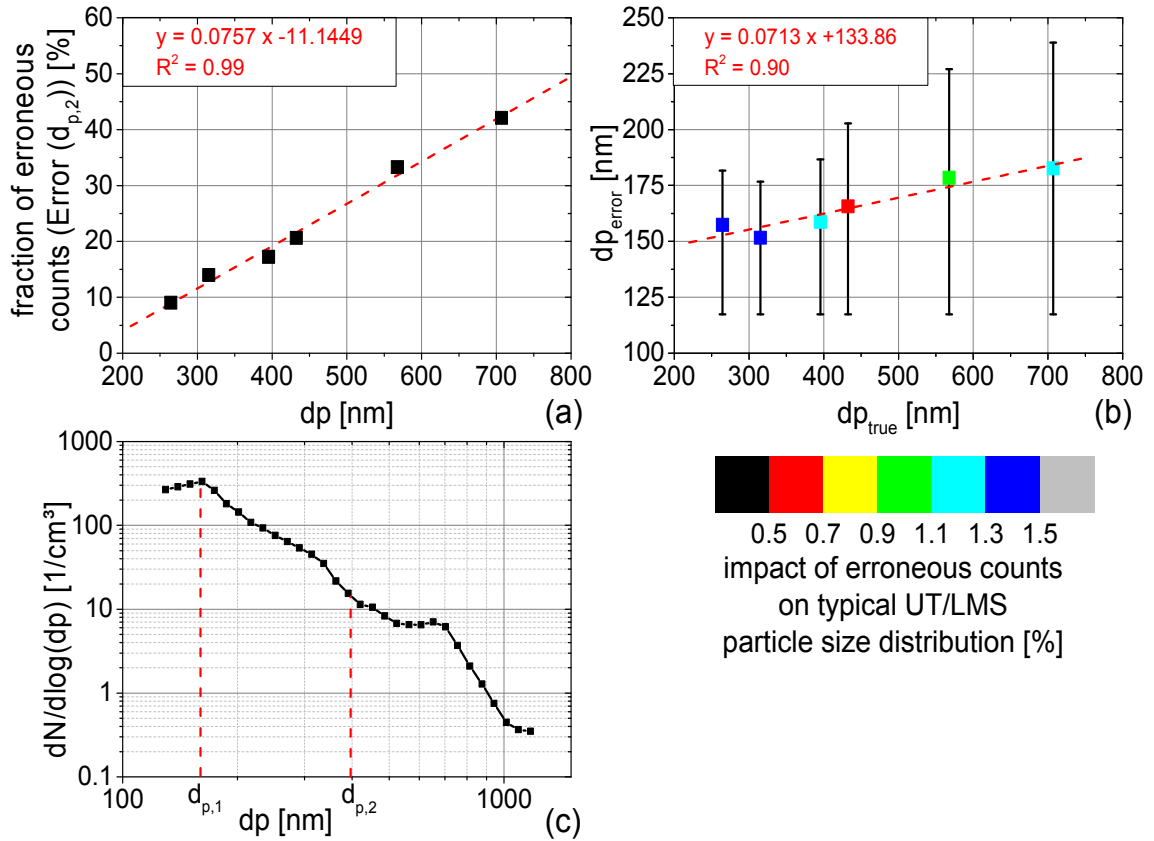
Figure 5.3: Estimation of the influence of erroneous counts on the measured particle size distribution in the UT/LMS region. The fraction of error counts, obtained additionally to the "correct" counts at a certain particle size (x-axis) is shown in (a). Figure (b) indicates the distribution (error bars) and averaged size (squares) of erroneous counts, caused by real particle counts of a certain size (x-axis). The color of the squares indicates the impact of the erroneous counts onto the real particle size distribution. The calculation of the impact is based on an averaged particle size distribution, measured with the OPC unit on 37 intercontinental CARIBIC flights between Germany, Canada, Venezuela, South Africa, and Japan (c).

size of all erroneous counts caused by the 259 nm measurement is 157 nm (square in Fig. 5.3b). For 702 nm particles (500 nm latex particles transferred to UT aerosol) the fraction of false pulses is about 42% (Fig. 5.3a) and the averaged diameter of all false pulses is 183 nm (Fig. 5.3b). To analyze the impact of this error on a typical particle size distribution of the UT/LMS region, the fraction of potential erroneous counts $Error\_fraction(a)$ in a certain size channel of the particle size distribution is calculated with Eqs. 5.1 and 5.2.

$$Error(d_{p,2}) = \frac{C\_error_{callib}(d_{p,2})}{C_{callib}(d_{p,2})} \tag{5.1}$$

$$Error\_fraction(d_{p,1}) = \frac{C(d_{p,2}) \cdot Error(d_{p,2})}{C(d_{p,1})} \tag{5.2}$$

$Error(d_{p,2})$ relative fraction of erroneous counts, caused by a certain

size channel ($d_{p,2}$) (Fig. 5.3a) [1]

$C\_error_{callib}(d_{p,2})$ integral number of all erroneous counts for a certain size channel ($d_{p,2}$) (obtained during calibration measurements) [1]

$C_{callib}(d_{p,2})$ integral number of all "correct" counts for a certain size channel ($d_{p,2}$) (obtained during calibration measurements) [1]

$Error\_fraction(d_{p,1})$ relative fraction of potential erroneous counts in a certain size channel ($d_{p,1}$) (Fig. 5.3b color code) [1]

$C(d_{p,2})$ measured concentration at a certain size channel (e.g. at $d_{p,2}$ in Fig. 5.3c) [1/cm^3]

$C(d_{p,1})$ measured particle concentration at the associated size channel where the erroneous counts are located on average ($d_{p,1}$ in Fig. 5.3c) [1/cm^3]

For this calculation the data of 37 intercontinental measurement flights between Frankfurt, Vancouver, Bogota, Caracas, Cape Town, Johannesburg, and Osaka were averaged to obtain a representative particle size distribution (Fig. 5.3c). As shown in Fig. 5.3a and 5.3c, with increasing particle size $Error(d_{p,2})$ increases, $C(d_{p,2})$ decreases, and $C(d_{p,1})$ is about a factor of 20 to 40 larger than $C(d_{p,2})$. Consequently for all size channels the resulting $Error\_fraction(d_{p,1})$ is smaller than 1.5% (color code in Fig. 5.3b). Unfortunately this analysis was only possible for particles smaller than 702 nm (500 nm latex particles transferred to UT aerosol). The limitation is caused by the used calibration setup (Sec. 5.2.1) with no pure latex particles larger than 500 nm. However, due to the rapid decrease of the UT/LMS particle number concentration with increasing particle size, the influence of erroneous counts can be neglected compared to the true concentration[17]. As the uncertainties due to the calibration, the used refractive index, and the used sample air volume are estimated to be much larger (cf. Sec. 5.3.3) than the overall influence of erroneous counts on the true particle size distribution, this effect can be neglected in the CARIBIC OPC data analysis. In the calculation of the uncertainty, however, this error is included (Sec. 5.3.3). For applications, where the particle size distribution shows not the steep decrease as it is seen in the UT/LMS (e.g. measurements in the boundary layer) the effect of the erroneous particle counts cannot be neglected.

---

[17] Using the equations obtained from the linear fits in Fig. 5.3a,b, for 1000 nm particles (dp$_2$) the fraction of erroneous counts is 65% and the corresponding dp$_1$ is 205 nm. With the averaged UT/LMS particle number size distribution (Fig 5.3c) the resulting $Error\_fraction(d_{p,1})$ is only 0.2%.

5.2   Calibration of the OPC unit

5.2.1   Calibration setup

To calibrate the CARIBIC OPC unit with respect to particle size and counting efficiency, several measurements at different particle sizes were carried out. The calibration setup is shown in Fig. 5.4. The particle material (polystyrene latex or ammonium sulfate) was dissolved in deionized water (1). After atomizing this solution in a TSI 3076 particle generator (atomizer) (2), the aerosol flew into a droplet trap (3). While large droplets were removed by impaction, only the small ones followed the air stream into a glass bottle dilution unit (4). In this glass bottle the calibration air was mixed with dry particle free air to reduce the total particle concentration and to dry the droplets, containing the desired particle material. By adjusting the dilution the particle concentration of the measurement air was set between 20 and 1000 1/cm³ using a needle valve. To obtain really dry aerosol particles, the aerosol passed a second drier (5). Inside this 40 cm tall glass tube, the calibration air was dried with water absorbing silica gel.

Because commercial available polystyrene latex calibration standards (Duke Scientific Corporation, Nanosphere Size Standards NIST Traceable Mean Diameter) were used, the resulting particle size distribution after the drier was quasi monodisperse. But some small particles were present due to the remaining impurity of the atomized water (Fig. 5.5a water peaks). For ammonium sulfate (AS; $(NH_4)_2SO_4$) the generated particle size distribution was polydisperse because the evaporated droplets of the atomized salt solution released aerosol particles of various sizes. However, for the size and counting efficiency calibrations, particles of the same size were needed. Therefore, the particles carried by the calibration air were charged inside a bipolar diffusion charger (Am^{241}) (6) and separated using a Differential Mobility Analyzer (DMA, type Vienna medium) (7). Inside the DMA, which is a cylindrical capacitor, particles are
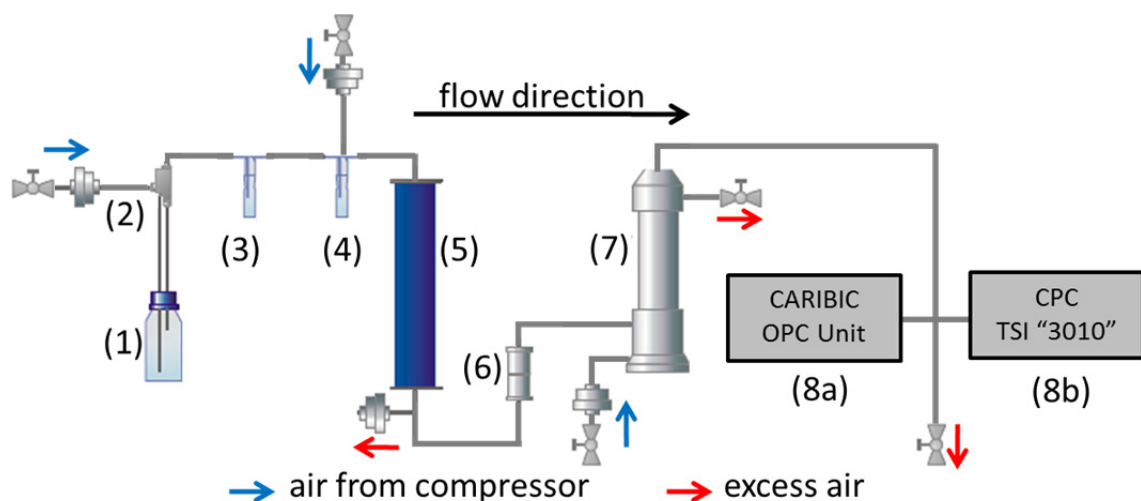
Figure 5.4: Calibration setup for the CARIBIC OPC with the glass bottle containing the particle material in aqueous solution (1), particle generator (atomizer) (2), droplet trap (3), dilution unit (4), drier (5), bipolar diffusion charger (6), and the Differential Mobility Analyzer (DMA) (7). A Condensation Particle Counter (CPC) was operated in parallel to the CARIBIC OPC unit (8a and 8b) as reference for the counting efficiency measurements.

separated by their mobility in an electric field (electrical mobility) [Wiedensohler, 1989; Winklmayr et al., 1991; Birmili et al., 1997, Baron and Willeke, 2001, p. 66, 78; Flagan, 2001, pp. 553-555]. The electrical mobility of a particle (Z_p, Eq. 5.3) mainly depends on the particle size and the number of charges on the particles. Operating the DMA at a constant voltage, only particles having an particle electrical mobility equal to the DMA electrical mobility (Z_{DMA}, Eq. 5.5) are transported to the DMA aerosol exit.

$$Z_p = \frac{n_e \cdot e \cdot C_c}{3 \cdot \pi \cdot \eta \cdot d_p} \tag{5.3}$$

$$C_c = 1 + \frac{1}{p \cdot d_p} \cdot \left(15.60 + 7.00 \cdot e^{-0.059 \cdot p \cdot d_p}\right) \tag{5.4}$$

C_c	Cunningham slip correction factor [1]
n_e	number of charges of a aerosol particle [1]
e	elementary charge [$1.6022 \cdot 10^{-19}$ C]
η	air dynamic viscosity [kg·m^{-1}·s^{-1}]
d_p	particle diameter [m]
p	air pressure [Pa]

$$Z_{DMA} = \frac{Q_s + Q_{pa} - \dfrac{Q_{ma} + Q_{pa}}{2}}{2 \cdot \pi \cdot l_{DMA} \cdot U_{DMA}} \cdot \ln\left(\frac{r_{DMA,2}}{r_{DMA,1}}\right) \tag{5.5}$$

$Q_{DMA,s}$	DMA sheath air volume flow [m³/s]
$Q_{DMA,pa}$	polydisperse aerosol volume flow at the DMA entrance [m³/s]
$Q_{DMA,ma}$	quasi monodisperse aerosol volume flow at the DMA exit [m³/s]
l_{DMA}	length of the DMA electrode [m]
$r_{DMA,1}$	radius of the inner DMA electrode [m]
$r_{DMA,2}$	radius of the outer DMA electrode [m]
U_{DMA}	voltage at the electrodes [V]

From the DMA aerosol exit the calibration air was pulled directly to the OPC unit (8a) and a reference instrument, in this set-up a Condensation Particle Counter (CPC, TSI Model 3010) (8b). The OPC unit and the CPC pulled together about 2 l/min of calibration air whereas the particle generator with the dilution unit provided about 3 to 6 l/min, depending on the dilution. To balance this air flow excess, a pressure compensation was integrated directly downstream the drier. Particle losses due to sedimentation, coagulation, and diffusion were minimized by a vertical arrangement of the calibration setup, avoiding strong bendings, and keeping the tubing as short as
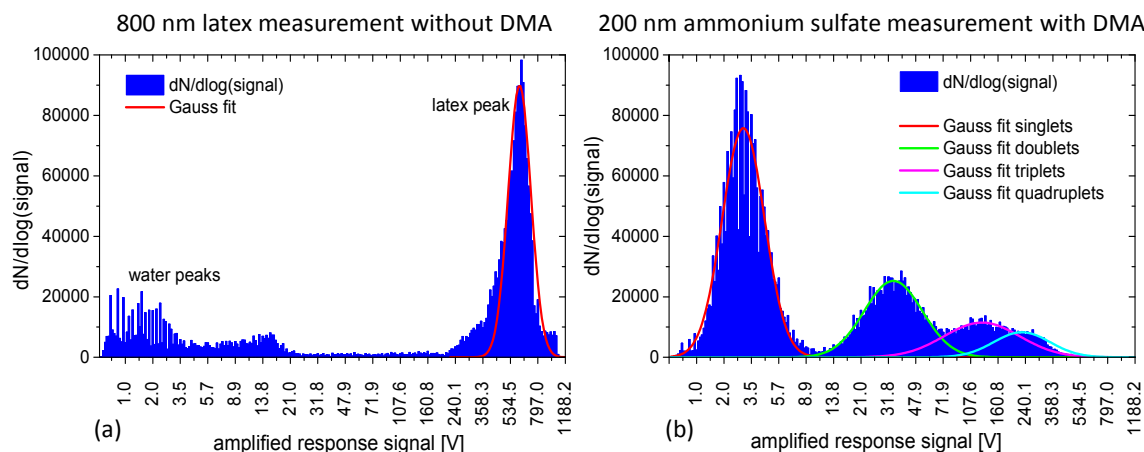
Figure 5.5: Highly resolved signal distribution for 800 nm latex particles (a) and 200 nm ammonium sulfate particles (b). For both measurements the calibration setup of Fig. 5.4 was used, but for the latex measurement without bipolar diffusion charger and DMA.

possible. Furthermore, the two tubes from the crossing to the OPC and the CPC, respectively, had the same length.

When operated with latex calibration standards, the remaining water peaks were removed by the DMA. The resulting monomodal particle size distribution with a known particle diameter was directly used for calibration measurements. As seen in Fig. 5.5b, a polydisperse particle size distribution was provided by the DMA when operated with AS. This distribution is caused by the presence of larger multiple charged particles having the same electrical mobility as the smaller particles having only a single charge (cf. Eq. 5.3). Using a resolution of 256 size channels for data analysis, the single charged (singlets), double charged (doublets), triple charged (triplets), as well as the quadruple charged (quadruplets) particle peaks could be resolved (Fig. 5.5b). The polydisperse size distribution of the AS particles had the great advantage that the particle size could be variable set. When using latex particles, the size calibration was limited to the available standard sizes (125, 200, 350, 500, 800, and 900 nm for this work).

5.2.2 Size calibration

For the particle size calibration, the intensity of the amplified OPC output signal (Ch. 5.1) was averaged over several thousand counting events for each particle diameter. Using the DMA theory [Wiedensohler, 1989, Winklmayr et al., 1991; Birmili et al., 1997, Baron and Willeke, 2001, p. 66, 78; Flagan, 2001, pp. 553-555], the size of multiple charged particles was calculated (Eq. 5.3 and 5.4). Thus the clearly identifiable peaks of multiple charged AS particles could also used for the size calibration. For the example shown in Fig. 5.5b also the doublets (324 nm) and the triplets (439 nm) were used in addition to the singlets (200 nm). However, due to the flow setup of the DMA only particles smaller than 620 nm could be selected for calibration. To extend the size calibration to the upper detection limit of the OPC, latex particles were used. For the latex calibration standards 800 nm and 900 nm, the calibration setup was used without the DMA, which implied the measurement of the additional water peaks (cf. Fig. 5.5

Table 5.1: Particle material, sizes, and charges used for the size calibration of the CARIBIC OPC. All particle diameters were related to a internal mixture of mid-latitude UT aerosol particles (fourth column). The amplified response signal of the KS-93 OPC is given in the last column.

material	particle diameter (nm)	particle charge (e)	calculated new particle diameter (nm) $m_{c,total}(\lambda) = 1.48-0.0143 \cdot i$ $\lambda = 830$ nm	amplified response signal (V)
latex	125	1	133	0.62
latex	200	1	215	6.94
latex	350	1	396	137.0
latex	500	1	702	429.6
latex	800	-	978	609.0
latex	900	-	1141	1092.9
$(NH_4)_2SO_4$	125	1	128	0.69
$(NH_4)_2SO_4$	135	1	138	0.85
$(NH_4)_2SO_4$	150	1	154	1.40
$(NH_4)_2SO_4$	152	2	156	1.35
$(NH_4)_2SO_4$	168	2	173	2.37
$(NH_4)_2SO_4$	175	1	180	3.03
$(NH_4)_2SO_4$	193	2	199	4.84
$(NH_4)_2SO_4$	197	3	203	5.14
$(NH_4)_2SO_4$	200	1	206	6.16
$(NH_4)_2SO_4$	210	2	216	7.60
$(NH_4)_2SO_4$	219	3	226	9.28
$(NH_4)_2SO_4$	236	2	244	15.47
$(NH_4)_2SO_4$	250	1	259	22.53
$(NH_4)_2SO_4$	254	3	263	22.01
$(NH_4)_2SO_4$	279	2	290	36.05
$(NH_4)_2SO_4$	300	1	313	54.77
$(NH_4)_2SO_4$	324	2	339	72.12
$(NH_4)_2SO_4$	400	1	427	164.4
$(NH_4)_2SO_4$	415	2	446	195.6
$(NH_4)_2SO_4$	439	3	479	211.5
$(NH_4)_2SO_4$	500	1	582	286.0
$(NH_4)_2SO_4$	508	2	598	273.2
$(NH_4)_2SO_4$	600	1	713	394.7

and its discussion). As the water peaks are clearly separated from the signal peak of the latex particles, the latex particles peaks could be safely used for the size calibration. The refractive index of polystyrene latex ($m(\lambda) = 1.59 - 0.0 \cdot i$ ($\lambda = 830$ nm); [Hinds, 1999],
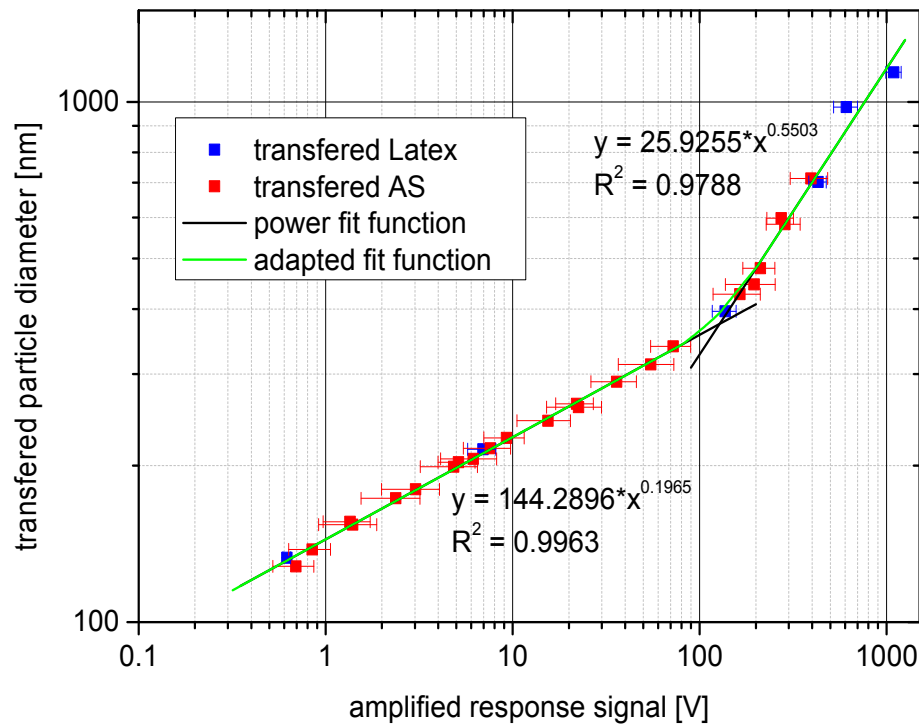
Figure 5.6: CARIBIC OPC size calibration curve for mid-latitude upper troposphere aerosol (UTA) particles ($m_{c,total}(\lambda) = 1.48-0.0143 \cdot i$ ($\lambda = 830$ nm)). All calibration points were converted from latex (blue) and ammonium sulfate (AS, red) to UTA using a Mie scattering program. The adjusted fit function (green) is a combination of the two power functions. At the intersection point (amplified signal 127.98; $d_p = 374.4$ nm) the adapted function is increased by 5%.

p. 351) and therefore the intensity of the scattered light differs from AS ($m(\lambda) = 1.52 - 1.41 \cdot 10^{-7} \cdot i$ ($\lambda = 830$ nm); [Toon et al., 1976]). To take this difference into account, the AS as well as the latex calibration points were related to a uniform complex refractive index ($m(\lambda) = 1.48 - 0.0143 \cdot i$ ($\lambda = 830$ nm)), using a light scattering program written by Thomas Müller (TROPOS) based on Mie theory [van de Hulst, 1981, p. 35, 124-126]. The adapted refractive index was calculated to be characteristic for an internal mixture of mid-latitude upper tropospheric aerosol particles (UTA), which will be discussed in connection with Tab. 5.2, Tab. 5.3, and Fig. 5.7. Using the Mie scattering program and geometry parameters of the KS-93 optics, the theoretical response of the OPC was calculated for different types of aerosol particles (cf. Sec. 4.1). Comparing the response signal for AS and latex to the response signal for UTA, the AS and latex particle sizes could be related to UTA sizes (e.g. a 350 nm latex particle cause the same scattered light intensity as a 396 nm UTA particle). The equivalent particle sizes are listed in Tab. 5.1 together with the corresponding amplified signal intensity of the scattered light. Altogether 29 different particle sizes were used for the size calibration of the OPC.

The particle size calibration curve resulting from the AS and latex calibration is shown in Fig. 5.6. The converted calibration points can be described by two power functions with a discontinuity between them (amplified signal 127.98; $d_p = 374.4$ nm). To create a smooth crossover in the overlap region around the intersection point, the two curves were adjusted by an iterative developed correction function (green curve; Eq. 5-6). At the intersection point, due to the correction function the particle diameter is

larger by 5%, to the left and right this value gets lower. For signals smaller than 80.75 V ($=10^{(\log(127.98)-0.2)}$) and larger than 202.84 V ($=10^{(\log(127.98)+0.2)}$) the correction becomes zero. Between the lowermost and uppermost points and the intersection point the correction functions were calculated using a linear approximation. The maximum overestimation of 5% was chosen as a result of a sensitivity study (not shown here).

$$f(x) = \begin{cases} x < 80.75 & 144.2896 \cdot x^{0.1965} \\ 80.75 \le x < 127.98 & 144.2896 \cdot x^{0.1965} + (0.001059 \cdot x - 0.085486) \cdot 25.9255 \cdot x^{0.5503} \\ 127.98 \le x < 202.84 & 25.9255 \cdot x^{0.5503} + (-0.000668 \cdot x - 0.135486) \cdot 144.2896 \cdot x^{0.1965} \\ 202.84 \le x & 25.9255 \cdot x^{0.5503} \end{cases}$$

$$(5.6)$$

5.2.3 Application to atmospheric aerosol particles

The CARIBIC system probes different atmospheric regions and hence different kinds of aerosols are encountered. At mid-latitudes the aircraft flies quite often in lower stratospheric air [van Velthoven, 2014]. For such air masses the aerosol composition is dominated by sulfuric acid [Murphy et al., 2007; Deshler 2008]. In the mid-latitude UT and tropical middle troposphere (MT) ammonium sulfate, different organics (organic carbon, OC), and soot (elemental carbon, EC) must be considered too [Dibb et al., 1999; Kojima et al.,2004; Schwarz et al., 2006; Lauer and Hendricks, 2006; Froyd et al.,2009; Morgan et al.,2009; Pratt and Prather, 2010; Schwarz et al., 2010]. The different chemical composition and hence the different optical properties of the aerosol particles (Tab. 5.2) influence their detection by the OPC unit.

   Because the CARIBIC system cannot measure the aerosol chemical composition for single particles, an internally mixed aerosol was assumed. This assumption is valid for the UT/LMS as aircraft emissions are the only direct particle source and all other particles were already aged during their transport into the UT/LMS. Therefore the complex refractive index ($m_{c,total}(\lambda)$; Eq. 5.7) of the internally mixed particles was

Table 5.2: Complex refractive index and density of the most important atmospheric aerosol particle materials in the UT/LMS region.

particle material	complex refractive index (λ = 830 nm)	density (g/cm³)	reference
H$_2$SO$_4$ (75% solution with water)	1.4255-1.503E-7i	ρ =1.67	Hummel et al., 1988
organics (OC)	1.4551-0.001i	ρ =1.40	Jaenicke, 1993; Dick et al., 2007
(NH$_4$)$_2$SO$_4$	1.52-1.41E-7i	ρ =1.83	Toon et al., 1976
soot (EC)	1.85-0.71i	ρ =1.80	Bond and Bergstrom, 2006

calculated, using a volume mixing rule [Seinfeld and Pandis, 1998; p. 1134].

$$m_{c,total}(\lambda) = \sum_{i=1}^{n} f_i \cdot m_{c,i}(\lambda) \qquad\qquad (5.7)$$

f_i	volume fraction of compound i [1]
$m_{c,i}(\lambda)$	complex refractive index of compound i [1]
λ	wavelength of the incident radiation [m]

Previous CARIBIC measurements of the aerosol elemental composition (impactor probe samples; cf. Sec. 3.3) showed that sulfur (sulfuric acid or ammonium sulfate) is more abundant than organic carbon at mid-latitudes [Nguyen et al., 2008]. The same author showed, in tropical regions carbonaceous compounds (most likely OC) are as frequent as sulfuric compounds. To analyze the influence of different refractive indices on the derived particle size distribution and total particle volume or mass, a sensitivity study was carried out. Three different calibration curves, representing three different particle compositions, were applied to one dataset, obtained during the CARIBIC flight LH317 on Nov. 15th, 2010 between Frankfurt/Germany and Johannesburg/South Africa. This flight sampled the three major atmospheric regions for CARIBIC measurements: mid-latitude lowermost stratosphere, mid-latitude upper troposphere and tropical middle troposphere. For each of the three calibration curves, the complex refractive index was calculated for a characteristic internal aerosol mixture given in Tab. 5.3. The first mixture is characteristic for aerosol particles in the mid-latitude lowermost stratosphere

Table 5.3: Complex refractive index and density for internally mixed (volume mixing rule) aerosol particles. The given volume fractions are assumed "typical" aerosol compounds for the regions the CARIBIC measurements take place most frequently.

region	composition (volume fraction)		mixed complex refractive index $m(\lambda) = n - n\`\cdot i$ $\lambda = 830$ nm	mixed density (g/cm³)
mid-latitude lowermost stratosphere	H_2SO_4: Organics: $(NH_4)_2SO_4$: Soot:	90% 10% 0% 0%	$m_{c,total}(\lambda) = 1.43 - 0.0001 \cdot i$	$\rho = 1.64$
mid-latitude upper troposphere	H_2SO_4: Organics: $(NH_4)_2SO_4$: Soot:	44% 10% 44% 2%	$m_{c,total}(\lambda) = 1.48 - 0.0143 \cdot i$	$\rho = 1.72$
tropical mid troposphere	H_2SO_4: Organics: $(NH_4)_2SO_4$: Soot:	19% 40% 40% 1%	$m_{c,total}(\lambda) = 1.48 - 0.0075 \cdot i$	$\rho = 1.63$

(LSA), where sulfuric acid is dominant. The second mixture characterizes aerosol from the mid-latitude UT (UTA), where AS is assumed to be as important as sulfuric acid. For this region the soot fraction is assumed to be 2%, because of considerable emissions from aircraft and industry [Lauer and Hendricks 2006, Schwarz et al., 2006; 2010]. The third mixture was chosen to be characteristic for tropical mid-tropospheric aerosol (MTA). As ~ 94% of all CARIBIC measurements are above 8 km altitude, mineral dust and sea salt were assumed to be encountered less frequent in all regions.

Figure 5.7 shows the influence of the different aerosol compositions (refractive indices and density) on the particle size distribution (a) and the derived particle mass (b and c). As this CARIBIC flight LH317 passed all three regions, it is assumed this sensitivity study provide a realistic assessment of the influence of the refractive index. The particle size distribution in Fig. 5.7a is averaged over the whole flight. The refractive index real part of LSA and therefore the intensity of the scattered light of such particles is lower than for UTA and MTA. Using the correct calibration for each type of aerosol compensates the difference in the intensity of the scattering light. Considering a particle with a certain diameter, in case the true real part of this particle is larger than those of the used calibration, the measured scattering light intensity would be stronger and therefore the particle would been seen larger than it is. Consequently, compared to the UTA and MTA calibration, with the LSA calibration the measured particle size distribution is somewhat shifted to larger particle diameters. As the real part for UTA and MTA are equal, the difference in the comparison of those size distributions can be explained by the different imaginary part. Because the UTA particles absorbs more light than MTA particles ($n'_{UTA} > n'_{MTA}$), UTA particles have to be larger than the MTA particles when both OPC signals are equal. While the upper detection limit of the OPC (signal intensity at Ch-3 = 1250 V) is 1351 nm for the LSA calibration, it is 1312 nm for UTA, and 1252 nm for MTA, respectively. The lower detection limit (signal intensity at Ch-1 = 0.35 V) is 121 nm for LSA, 117 nm for UTA, and 117 nm for MTA. For polystyrene latex the lower and upper detection limit is calculated to be 111 nm and 972 nm, respectively.

Comparing the integral particle mass concentration along this flight (Fig. 5.7b and 5.7c; three minutes average values), differences are not only caused by the refractive index but also by the particle density. In case of UTA calibration the total mass is in between the mass concentrations of the LSA and MTA calibration. To visualize the differences more clearly, Fig. 5.7c shows the relative difference of the two aerosol types from the UTA mass. For the whole flight the MTA and LSA masses are on average 10.5% lower and 8.3% higher (medians), respectively, than the UTA mass.

To obtain a uniform data analysis for all flight regions and as the real particle composition is not known, for this study all data were analyzed with respect to the complex refractive index and particle density of the internal mixed UTA. The apparent uncertainty, shown in Fig. 5.7 for the particle size distribution and particle mass concentration, indicate the quantitative uncertainty of the measurements concerning refractive index and particle density. For the presentation of the results, this uncertainty was included in the uncertainty calculation (Sec. 5.3.3). In case the aerosol type is well
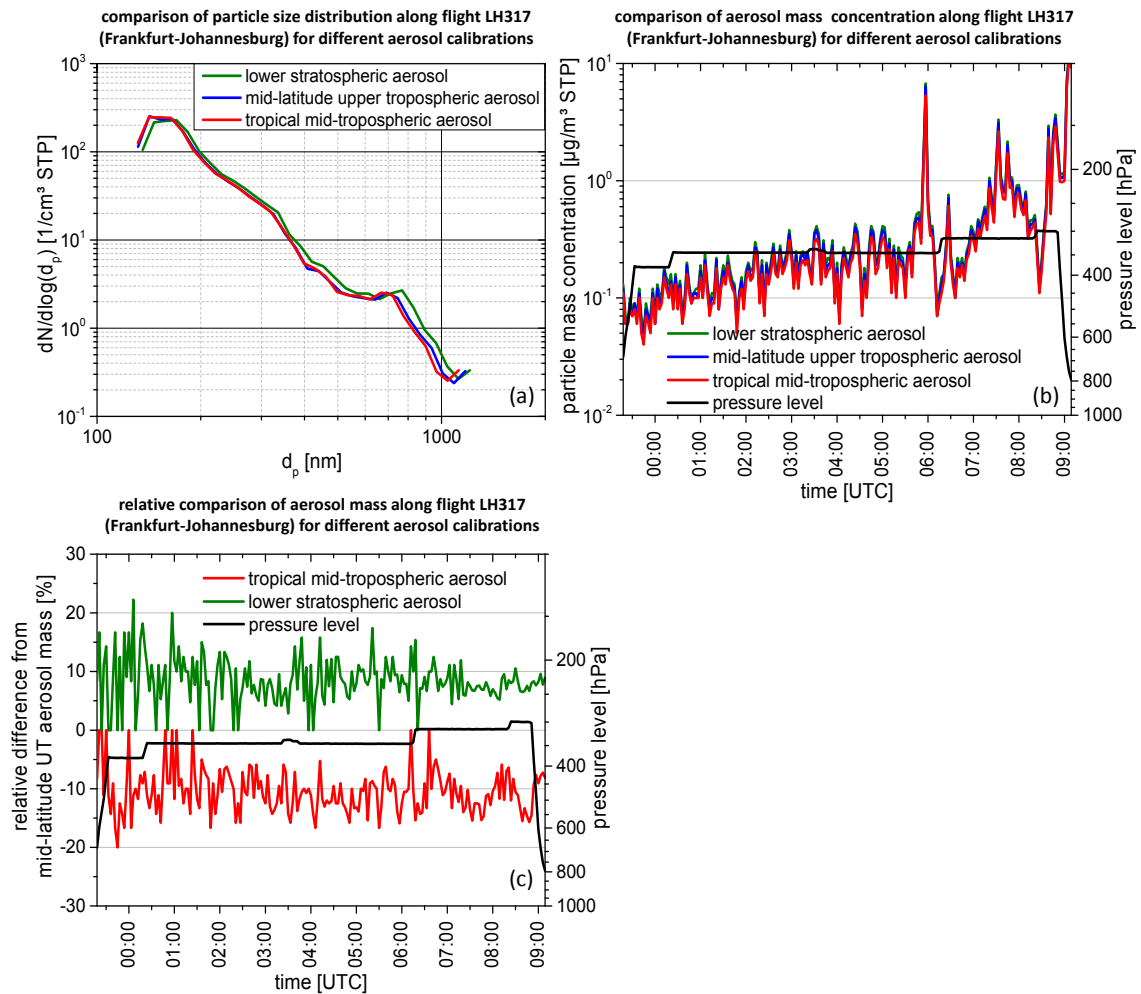
Figure 5.7: Influence of the aerosol composition (complex refractive index, particle density) on the particle size distribution (a) and the particle mass concentration (b), measured with the CARIBIC OPC unit along a measurement flight between Frankfurt/Germany and Johannesburg/South Africa on November 15th, 2010. The analyzed data were related to an internal mixture of mid-latitude lowermost stratospheric aerosol (LSA) (green), mid-latitude upper tropospheric aerosol (UTA) (blue), and tropical mid tropospheric aerosol (MTA) (red), using a Mie scattering program. The relative difference from the UTA mass concentration is displayed in (c).

known, of course the measured values can be related to the exact refractive index and particle density, using the Mie scattering program and the geometry parameters of the KS-93 optics.

5.2.4 OPC counting efficiency

As the intensity of the scattered light decreases with decreasing particle size, not all small particles passing the optics are counted. The counting efficiency $\varepsilon(d_p)$ for a certain particle size d_p is the ratio of the number of particles the OPC unit counts to the number of available particles. The latter one was measured with a reference instrument, in this study a CPC, type "TSI 3010" (Fig. 5.4).

$$\varepsilon(d_p) = \frac{N_{OPC}}{N_{CPC}} \tag{5.8}$$

N_{OPC} particle concentration measured with OPC [1/cm^3]

N_{CPC} particle concentration measured with CPC [1/cm^3]

The measured particle concentrations can be directly compared for each particle size when using the monodisperse latex calibration standard. However, as described in the discussion of Fig. 4.5 and Fig. 5.3, for particles larger than ~250 nm, erroneous counts occur at the small end of the size distribution. Consequently only the counts of the main peak were included in the calculation of the particle concentration.

To obtain more than four measurement points (latex calibration standards 125 nm, 200 nm, 350 nm, and 500 nm), AS was used too. Multiple charged particles were resolved in size and number by setting the OPC size distribution to 256 channels. In this way the counting efficiency of the OPC unit was calculated gradually from large particle sizes to smaller ones. For each singlet maximum diameter the number of all multiple charged particles was summed up ($N_{multiple}$). Thereby the counting efficiency for the doublets, triplets and larger particle sizes was taken into account (Eq. 5.9). The respective counting efficiencies were taken from the previous calibration steps. By subtracting $N_{multiple}$ from the number of particles the CPC counted (N_{CPC}), the total number of singly charged particles was calculated ($N_{CPC,s}$; Eq. 5.10). Dividing the number of singly charged particles the OPC unit counted ($N_{OPC,s}$; Eq. 5.11) by $N_{CPC,s}$, the OPC counting efficiency ($\varepsilon(d_p)$) at the d_p of the singlets was finally determined (Eq. 5.12). The obtained $\varepsilon(d_p)$ was used for the next smaller particle size calibration step. For the first calibration step (largest particles, 500 nm AS, 582 nm UTA), particles larger than the singlet size were not present in the OPC size distribution[18]. The absence of multiple charged particles is reasonable, because the used particle generator did not generate such large particles [TSI, 2008], hence $N_{multiple} = 0$.

$$N_{multiple} = \sum_{i=b+1}^{n_{OPC}} \frac{N_i}{\varepsilon_i} \tag{5.9}$$

$$N_{CPC,s} = N_{CPC} - N_{multiple} \tag{5.10}$$

$$N_{OPC,s} = \sum_{i=a}^{b} N_i \tag{5.11}$$

---

[18] For 500 nm AS singlets the doublets are calculated to be 889 nm and the triplets 1269 nm .
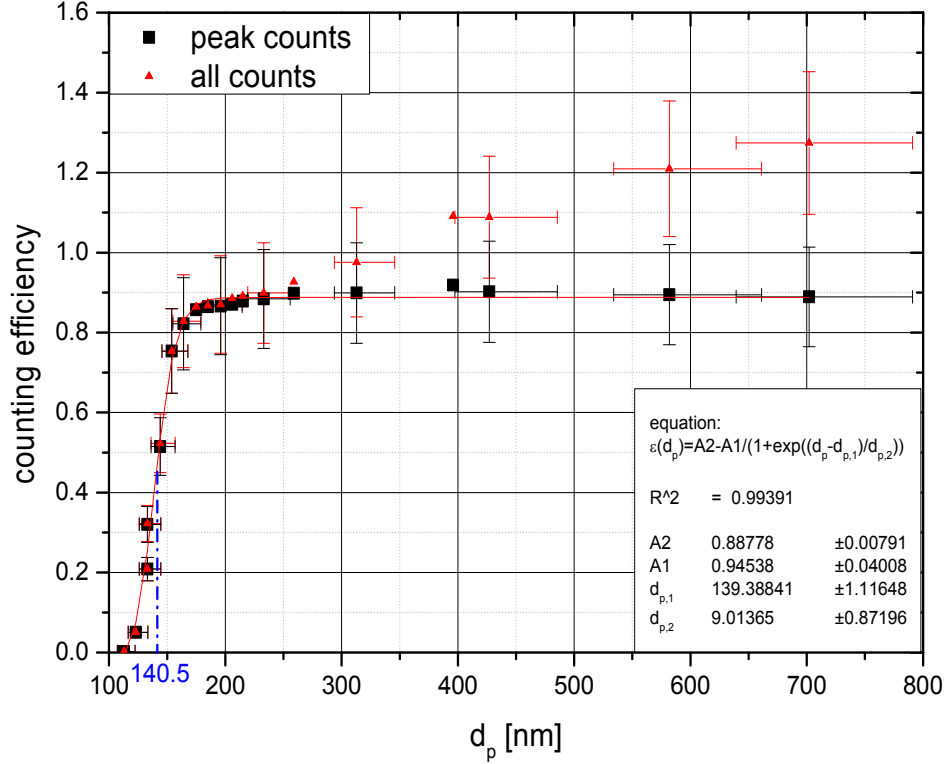
Figure 5.8: OPC unit counting efficiency for mid-latitude UT aerosol particles ($m_{c,total}(\lambda) = 1.48-0.0143\cdot i$ ($\lambda = 830$ nm)). Black squares represent measurement, where only the main peaks of the singlets were taken into account. Red triangles represent calculations where the erroneous counts (cf. Sec. 5.1) were included. The x-axis error bars indicate the maximum uncertainty due to the combination of the different aerosol type calibrations and the Gaussian width of the DMA distribution (Sec. 5.3.3). The y-axis error bars indicate the maximum uncertainty concerning the measurement air volume (Sec. 5.3.3). As the black and the red measurement points were obtained from the same dataset, a potential shift of the true counting efficiency (within the error bars) would be in the same direction for both curves. Hence, the overlap of the positive error bar (peak counts) with the negative error bar (all counts) does not indicate that the counting efficiency might be equal.

$$\varepsilon_i = \varepsilon(d_p) = \frac{N_{OPC,s}}{N_{CPC,s}} \tag{5.12}$$

N_i	number of counts in a certain size channel [1]
ε_i	counting efficiency for a certain size channel [1]
n_{OPC}	number of size channels in the OPC particle size distribution [1]; ($n_{OPC} = 256$ for calibration)
a	first channel, in which the singlets were seen [1]
b	last channel, in which the singlets were seen [1]

The resulting OPC counting efficiency curve is displayed in Fig. 5.8. Like for the size calibration, all particle diameters were related to UTA. Above about 250 nm, the OPC counting efficiency is more or less constant (maximum asymptotic counting efficiency). For smaller particle diameters the counting efficiency decreases. The particle diameter where the counting efficiency is 50% of the maximum asymptotic counting efficiency

($d_{p,50}$), is a characteristic size for the lower detection limit of an optical aerosol counting instrument. Using Eq. 5.13 as fitting function [Wiedensohler et al., 1997], the UTA $d_{p,50}$ was calculated to be 140.5 nm. For the LSA calibration $d_{p,50}$ is 146 nm and 141 nm for the MTA, respectively.

$$\varepsilon(d_p) = A_2 - \frac{A_1}{1 + \exp\left(\dfrac{d_p - d_{p,1}}{d_{p,2}}\right)} \qquad (5.13)$$

d_p	particle diameter [nm]
A_1	approximation parameter [1]
A_2	maximum asymptotic counting efficiency [1]
$d_{p,1}$	approximation parameter [nm]
$d_{p,1}$	approximation parameter [nm]

In addition to the true counting efficiency (black squares), Fig. 5.8 illustrates the effect of considering the erroneous counts too (red triangles). For particle sizes smaller than ~250 nm only few erroneous counts occurred, influencing $\varepsilon(d_p)$ only slightly (cf. also discussion to Fig. 5.3). For particle measurements larger than about 250 nm, $\varepsilon(d_p)$ increased significantly above 100%. Because for all measurements the used particle size was much larger than the CPC $d_{p,50}$ (~10 nm), the CPC was assumed to count 100% [TSI 2002]. Consequently, OPC counting efficiencies much higher than 100% are unrealistic. Hence, the additional small pulses must be erroneous. As the black and the red measurement points were derived from the same dataset, the overlap in the error bars (positive for peak counts vs. negative for all counts) does not indicate that the two counting efficiency curves might be equal. If the true counting efficiency is shifted within the shown error bars, for both curves the shift is in the same direction. The relative large error bars are mainly caused by subtracting the two roughly equal mass flow controller readings in order to derive the sampling volume flow (Sec. 4.3.2 and 5.3.3 Eq. 5.32).

Because the water peak (Fig. 5.5a) would be also counted by the CPC, only DMA selected particles were used for calibrating the OPC counting efficiency. Consequently, the calibration could not be extended to particles larger than 500 nm (latex, 702 nm UTA). However, the OPC unit already reached the maximum counting efficiency of ~ 89% at a particle size of about 250 nm (UTA) and this asymptotic maximum counting efficiency stayed constant with increasing particle diameter. Therefore, the counting efficiency was assumed to be at 89% for particles larger than 702 nm, too.
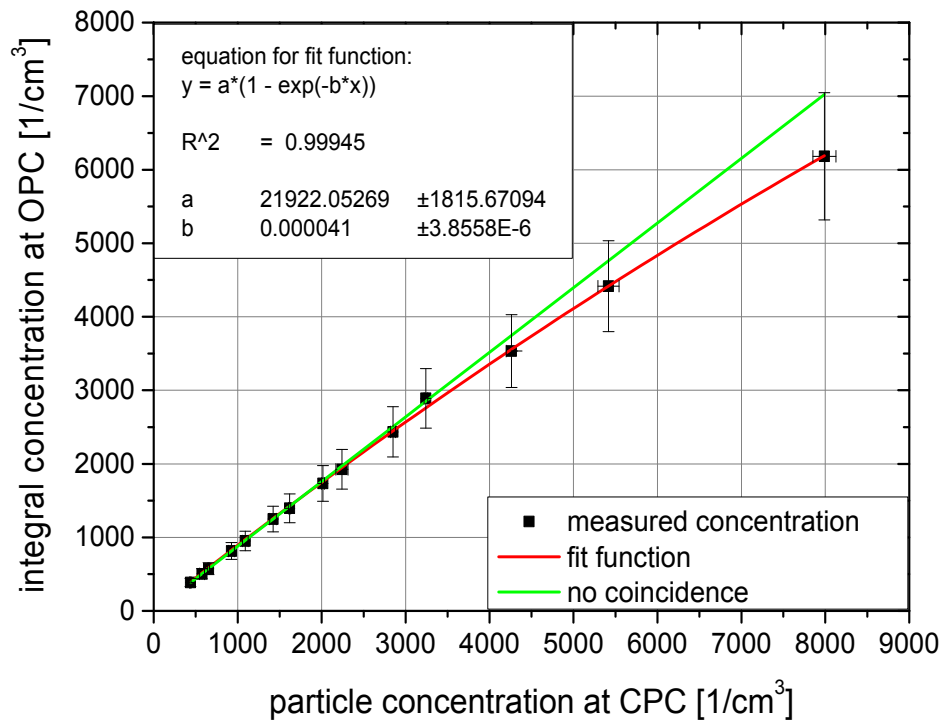
Figure 5.9: Coincidence behavior of the CARIBIC OPC. The integral particle concentration, measured with the OPC is plotted against the particle concentration of a reference instrument (CPC, TSI model 3010). For the used particles (200 nm diameter latex equal to 215 nm diameter mid-latitude UT aerosol), the OPC counting efficiency was determined to be 89%. The green line indicates the integral particle concentration, the OPC would measure in case of no coincidence (not corrected for OPC counting efficiency). While the x-axis error bars indicate the CPC statistical uncertainty (one sigma standard deviation), the y-axis error bars indicate the uncertainty concerning the measurement air volume (Sec. 5.3.3).

5.2.5 Particle coincidence

Due to the aerodynamic focusing inside KS-93, usually aerosol particles pass the optics separately. However, if the particle concentration increases, two or more particles might pass the laser beam at the same time, which is called coincidence. Depending on the intensity of the scattered light, these particles might be seen as one large particle. Because the CARIBIC OPC unit is operated in the less polluted UT/LMS region (compared to for instance the atmospheric boundary layer), coincidence is assumed to be negligible for the later data analysis. However, to complete the OPC unit characterization and to ensure to be below critical concentrations, coincidence measurements were carried out. Therefore again the calibration setup described in Sec. 5.2.1 and 200 nm polystyrene latex particles (215 nm UTA) were used. For this particle size the OPC unit already reached nearly the maximum counting efficiency and uncertainties due to erroneous counts and multiple charged particles were avoided. In Fig. 5.9 the particle concentration measured with the OPC unit is plotted against the particle concentration measured with the CPC. The particle concentration was increased stepwise from 400 to 8000 1/cm³. The CPC coincidence error was given to be 0.02% for a particle concentration of 35 1/cm³ and 6% for 10^4 1/cm³, respectively [TSI 2002]. In Fig. 5.9 the coincidence effect for the OPC is visible for particle concentration above

about 2000 1/cm³ (2.5% coincidence). As the number concentration of accumulation- and coarse mode particles in the UT/LMS region is typically inbetween 1 and 100 1/cm³ STP (cf. references, given in Tab. 6.1 and the overview plots 6.2, 6.9, 6.12, and 6.18), for the CARIBIC OPC size distributions the error by coincidence can be neglected ($< 1\%$).

5.2.6 Other sensors

Besides the OPC counting properties, the mass flow controllers needed for adjusting the gas flow, the temperature and the pressure sensors had also to be calibrated. Three PT-100 temperature sensors were calibrated, using a 0.1K accurate digital thermometer (Greisinger electronic, type 3750) as reference. The pressure sensor was calibrated against a DRUCK (series PDCT 910) pressure sensor with an accuracy of 0.1 mbar. For calibrating the two MFCs, a Dry-Cal DC-2 gas flow sensor (cell MC-1) was used. All sensors follow linear calibration curves with a correlation of 0.99 (not shown).

5.3   Data analysis algorithm, sampling line losses and uncertainty estimation

5.3.1 Regular post-flight data analysis

For the post-flight analysis of the CARIBIC OPC data a program was written in FORTRAN which converts the obtained raw data of the OPC into a particle size distribution and derived parameters (e.g. particle surface, volume, mass, average particle diameter, etc.). The program first converts the amplified raw signal of a particle pulse to a particle size using the size calibration curve (Cap. 5.2.2). The obtained particle sizes are then sorted into a histogram with logarithmically equidistant size bins. The number of channels as well as the analysis period for the histograms can be chosen by the user. For regular analysis, the resolution was set to 180 s with 32 size channels and 30 s with 5 size channels. The 30 s data are mainly used for intercomparison with other highly resolved CARIBIC data and for quick looks. To obtain the particle size distribution, i.e., the number concentration for each size bin (1/cm³), the program calculates the exact volume flow through the KS-93 from the gas temperature (T), pressure (p), and the MFC-derived mass flows. In addition to the particle size distribution, the integral particle number concentration, surface concentration, volume concentration, mass concentration, and the average particle diameter are calculated for later analysis. The particle surface distribution, the particle volume distribution, and the particle mass distribution can also be calculated. All concentration data are converted from ambient conditions (T_a, p_a) to standard conditions $(T_0 = 273.15\ \text{K}$, $p_0 = 1013.25\ \text{hPa})$ according to Eq. 5.14.

$$A_0 = A_a \cdot \frac{T_a}{T_0} \cdot \frac{p_0}{p_a}$$ (5.14)

A_a	measured parameter at ambient conditions [A_a]
A_0	measured parameter at standard conditions [A_0, STP]
T_a	ambient gas temperature (inside OPC) [K]
T_0	standard condition temperature [273.15 K]
p_a	ambient gas pressure (inside OPC) [hPa]
p_0	standard condition pressure [1013.25 hPa]

The program also corrects the data for the counting efficiency of the OPC unit (Sec. 5.2.4) and for particle losses in the inlet and the sampling line between the inlet and the OPC unit (Sec.5.3.2).

5.3.2 Particle losses in the CARIBIC aerosol inlet and the sampling line

The particle size dependent transmission efficiency of the aerosol inlet (ε_{inlet}) was estimated to be equal to the losses in the CARIBIC-1 inlet. For this inlet, particle losses were determined by wind tunnel measurements [Hermann et al., 2001]. The results are displayed in Fig. 5.10a. Particle losses inside the sampling line between the aerosol inlet and the OPC unit (~4 m length) are caused mainly by sedimentation, diffusion, and inertial deposition. As the exact CARIBIC aerosol sampling line geometry is known and empirical equations for the above processes are available, the transport efficiency through the sampling line could be calculated. All equations used for this calculation were taken from Baron and Willeke [2001, p. 67, 74] and Brockmann [2001, p. 145, 172, 174, 179].

The transport efficiency with respect to **sedimentation** due to the gravitational force (ε_{sed}) can be calculated by

$$\varepsilon_{sed} = 1 - \frac{2}{\pi} \cdot \left(2 \cdot \kappa_1 \cdot \sqrt{1 - \kappa_1^{2/3}} - \kappa_1^{1/3} \cdot \sqrt{1 - \kappa_1^{2/3}} + \arcsin\left(\kappa_1^{1/3} \right) \right)$$ (5.15)

The dimensionless parameter κ_1 is calculated by

$$\kappa_1 = \frac{3}{4} \cdot \frac{l_{tb} \cdot v_{p,sed}}{d_{tb} \cdot v_{gas}} \cdot \cos\left(\alpha_{tb,t} \right)$$ (5.16)

l_{tb}	length of tubing [m]
d_{tb}	inner diameter of tubing [m]

v_{gas} flow velocity of fluid inside tubing $[m \cdot s^{-1}]$

$\alpha_{tb,t}$ tilt angle of tubing referring to the horizontal direction
                                       [rad]

The settling speed of a particle in a fluid ($v_{p,sed}$) is given by

$$v_{p,sed} = \frac{g \cdot \rho_p \cdot d_p^2 \cdot C_c}{18 \cdot \eta} \qquad (5.17)$$

g acceleration of gravity $[9.81 m \cdot s^{-2}]$

ρ_p density of particle material $[kg \cdot m^{-3}]$

d_p particle diameter [m]

C_c Cunningham-Slip correction (Eq. 5.4)

η dynamical viscosity of fluid $[kg \cdot m^{-1} \cdot s^{-1}]$

For the CARIBIC sampling line, sedimentation losses become important for particles larger than 3 µm (Fig.5.10b).

In a laminar flow system, where particle transport in turbulence eddies can be neglected, Brownian motion is the responsible force for particle losses by **diffusion**. The sampling line transport efficiency with respect to diffusion losses (ε_{dif}) is a function of the dimensionless parameter κ_2:

$$\kappa_2 = \pi \cdot \frac{D_p \cdot l_{tb}}{\Phi_{tb}} \qquad (5.18)$$

l_{tb} length of tubing [m]

Φ_{tb} volume flow of fluid inside tubing $[m^3 \cdot s^{-1}]$

The diffusion coefficient of a particle (D_p) is calculated by

$$D_p = \frac{k_b \cdot T \cdot C_c}{3 \cdot \pi \cdot \eta \cdot d_p} \qquad (5.19)$$

k_b Bolzmann constant $[1.38 \cdot 10^{-23} J \cdot K^{-1}]$

T temperature [K]

C_c Cunningham-Slip correction (Eq. 5.4) [1]

η dynamical viscosity of fluid $[kg \cdot m^{-1} \cdot s^{-1}]$

d_p particle diameter [m]
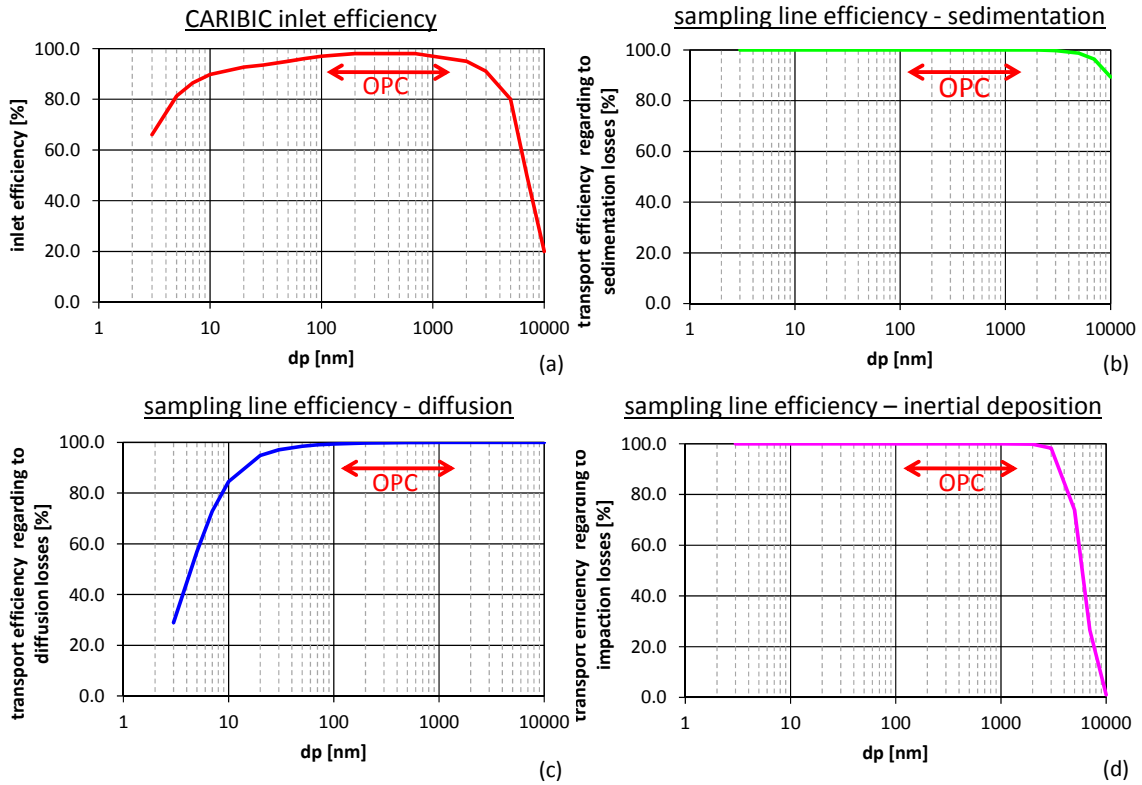
Figure 5.10: Transmission efficiency of the CARIBIC aerosol inlet (a) and transport efficiency through the CARIBIC sampling line to the OPC unit with respect to sedimentation (b), diffusion (c), and inertial deposition (d). The red arrow indicates the size range, covered by the OPC unit.

$$\kappa_2 < 0.02:$$

$$\varepsilon_{dif} = 1 - 2.56 \cdot \kappa_2^{2/3} + 1.2 \cdot \kappa_2 + 0.177 \cdot \kappa_2^{4/3} \tag{5.20}$$

$$\kappa_2 > 0.02:$$

$$\varepsilon_{dif} = 0.819 \cdot 10^{-3.657 \cdot \kappa_2} + 0.097 \cdot 10^{-22.3 \cdot \kappa_2} + 0.032 \cdot 10^{-57 \cdot \kappa_2} \tag{5.21}$$

This loss process increases with decreasing operating pressure and is particular relevant for small particles ($d_p < 30$ nm) inside the sampling line (cf. Fig. 5.10c).

Inertial deposition by impaction on the walls occurs e.g., at tube bends. At strong bending large particles cannot follow the streamlines of the fluid and therefore impact on the tube wall. The transport efficiency with respect to impaction losses (ε_{imp}) can be calculated by:

$$\varepsilon_{imp} = \left(1 + \left(\frac{Stk}{0.171} \right)^{\frac{0.452 \cdot Stk}{0.171} + 2.242} \right)^{\frac{2}{\pi} \cdot \alpha_{tb,b}} \tag{5.22}$$

$\alpha_{tb,b}$ bend angle of tubing [rad]
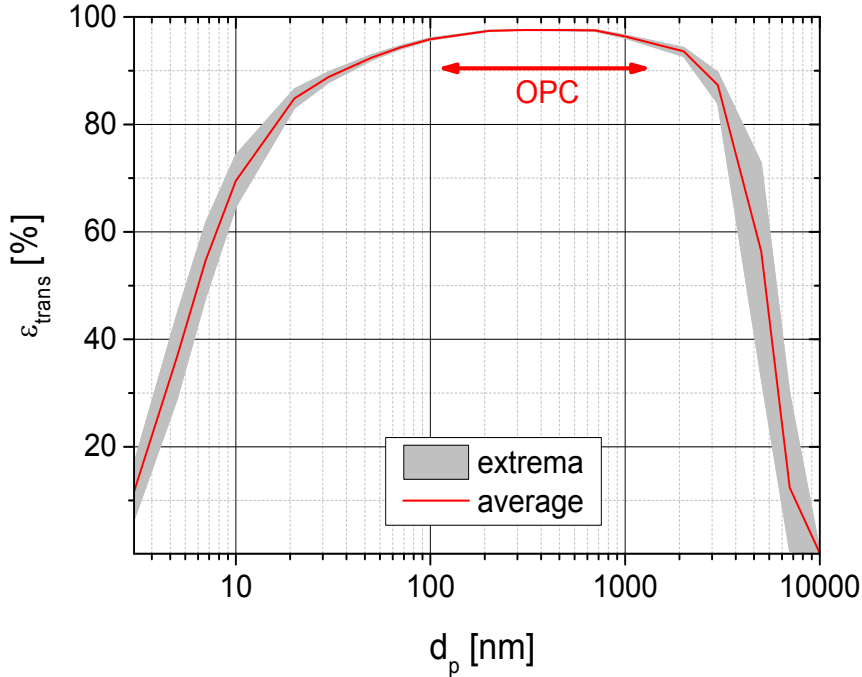
Figure 5.11: Total sampling efficiency of the CARIBIC aerosol inlet and the sampling lines to the OPC unit. Calculations were performed for $p = 260$ hPa, $p = 490$ hPa, $\rho = 1.1$ g/cm^3, and $\rho = 1.8$ g/cm^3. The grey area represents the range between the minimum and the maximum curves out of these four curves. The red curve indicates the mean sampling efficiency.

Thereby the Stokes number (Stk) is given by:

$$Stk = \frac{\rho_p \cdot d_p^2 \cdot v_{gas} \cdot C_c}{18 \cdot \eta \cdot d_{tb}} \tag{5.23}$$

ρ_p	density of particle material [kg$\cdot$ m^{-3}]
d_p	particle diameter [m]
C_c	Cunningham-Slip correction (Eq. 5.4)
η	dynamical viscosity of fluid [kg$\cdot$ m$^{-1}\cdot$ s^{-1}]
d_{tb}	inner diameter of tubing [m]

Figure 5.10d shows for the CARIBIC sampling line significant losses for particles larger than 3 μm.

To calculate the particle losses for each of the described processes, the sampling line between the inlet and the OPC unit was separated into five sections for sedimentation and diffusion losses and 9 sections (bends with different angles) for impaction losses, respectively. The total sampling efficiency of the inlet system (aerosol inlet + sampling line) (ε_{sampl}) was obtained by multiplying all individual efficiencies:

$$\varepsilon_{sampl} = \varepsilon_{inlet} \cdot \varepsilon_{sed} \cdot \varepsilon_{dif} \cdot \varepsilon_{imp} \tag{5.24}$$

To investigate the influence of different flight conditions on the inlet system sampling efficiency, calculations were performed for two typical cruise altitude pressure levels (p_1 = 260 hPa, p_2 = 490 hPa), and two particle density extremes (ρ_1 = 1.1 g/cm^3, ρ_2 = 1.8 g/cm^3). The respective results are displayed in Fig. 5.11. As the four curves are very similar, an average and a minimum and maximum sampling efficiency are indicated. In the size range the OPC unit is measuring, with $97 \pm 1\%$ the sampling efficiency is relative high. This is reasonable, because particle loss processes mainly act in the particle size ranges below or above the accumulation mode size range. Finally, the averaged curve is used to correct all OPC data for particle losses in the inlet system.

5.3.3 Uncertainty estimation

The **uncertainty concerning particle sizing** by the OPC is dominated by two effects: the uncertainty of the size calibration (Sec. 5.2.1) and the use of a constant complex refractive index for the uniform analysis of data obtained in different atmospheric measurement regions (Sec. 5.2.3). The uncertainty of the size calibration can be estimated, using the width of the Gaussian signal distribution when measuring a (quasi) monodisperse aerosol (cf. Fig. 5.5). Figure 5.12 shows the width of the transferred calibration signal plotted against the particle diameter. The width of the signal follows a power function best[19]. Using the fitted function, the absolute uncertainty of the size calibration can be directly calculated for each size channel ($unc_{gauss,i}$, Eq. 5.25).
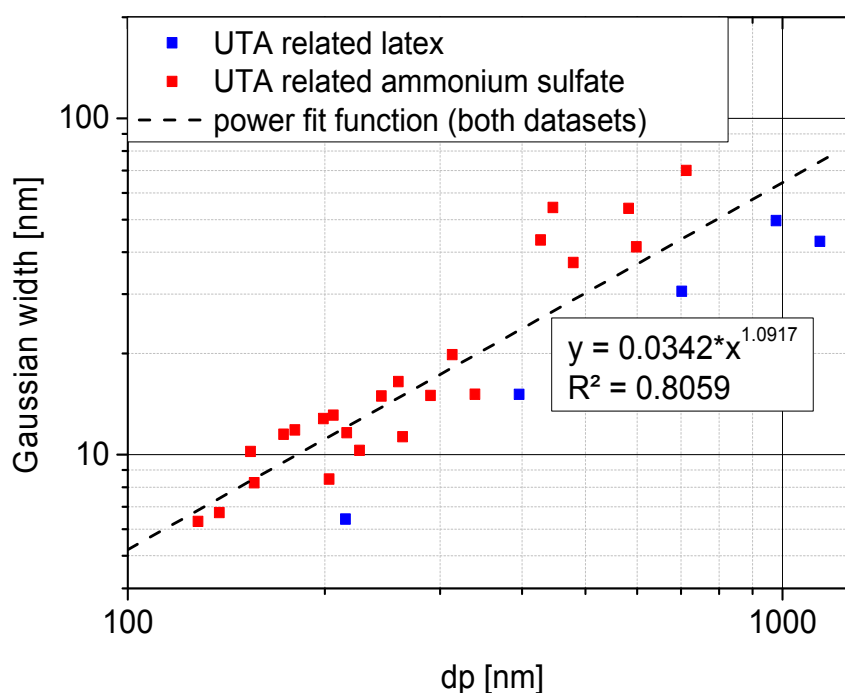
Figure 5.12: Width of the signal distribution for different size calibration points. The size of the latex and the ammonium sulfate particles was related to refractive index of mid-latitude UT aerosol particles ($m_{c,total}(\lambda)$ = 1.48-0.0143·i (λ = 830 nm)) using a Mie scattering program.

---

[19] OriginLab 9.0.0G (2012) Power fit function "Allometric1"

$$unc_{gauss,i} = 0.0342 \cdot d_{p,i}^{1.0917}$$ (5.25)

$d_{p,i}$ mean particle diameter of a certain size channel (i) [nm]

Comparing the particle size distributions in Fig. 5.7a, the uncertainty concerning the use of the UTA refractive index becomes obviously. The MTA would be seen larger, whereas the LSA would be seen smaller. Subtracting the true UTA size from the true LSA size and the true MTA size, for each size channel (i) the positive (+) and the negative (-) OPC unit absolute uncertainty concerning the used refractive index is defined here.

$$unc_{refr,i}^{+} = d_{p,i}(LSA) - d_{p,i}(UTA)$$
$$unc_{refr,i}^{-} = d_{p,i}(MTA) - d_{p,i}(UTA)$$ (5.26)

$d_{p,i}(UTA)$ mean particle diameter of a certain size channel (i) using
                                 the UTA calibration (Fig. 5.6; Eq. 5.6) [nm]
$d_{p,i}(LSA)$ calculated particle diameter for the same OPC signal
                                 intensity as for $d_{p,i}(UTA)$, but with the LSA calibration
                                 (not shown) [nm]
$d_{p,i}(MTA)$ calculated particle diameter for the same OPC signal
                                 intensity as for $d_{p,i}(UTA)$, but with the MTA calibration
                                 (not shown) [nm]

The overall absolute uncertainty concerning the particle size is the root of the sum of the square of the individual uncertainties (Eq. 5.27). Figure 5.13 shows the overall absolute particle size uncertainty for all 32 size channels.

$$unc\_d_{p,i}^{\pm} = \sqrt{\left(unc_{refr,i}^{\pm}\right)^2 + \left(unc_{gauss,i}\right)^2}$$ (5.27)

For calculating the **particles concentration uncertainty**, the erroneous counts (discussion to Fig. 5.3), uncertainty in the gas flow, and counting efficiency uncertainty due to different refractive indices have to be taken into account. To estimate the influence of erroneous counts, a linear function was fitted through the measurement points of Fig. 5.3a. Using this equation, the size dependent fraction of additional small erroneous particle counts ($\delta_{error}(d_{p,i})$) can be calculated from the particle concentration at each size channel (i) (Eq. 5.28). The obtained formula (Fig. 5.3a) has to be divided by 100 to transfer the unit from percentage to fraction.
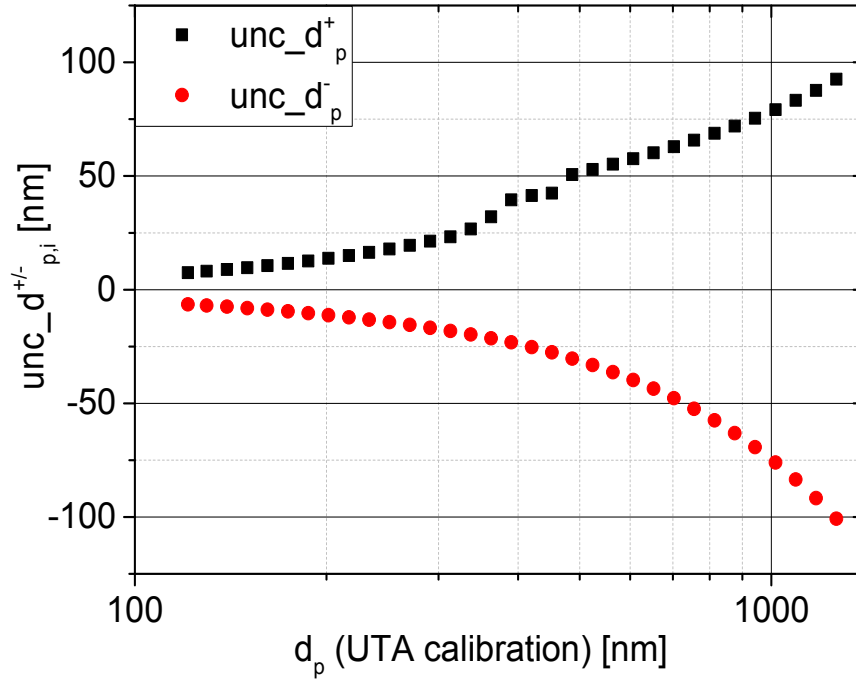
Figure 5.13: Positive ($unc\_d_p^+$) and negative ($unc\_d_p^-$) absolute uncertainty of the particle size as a function of the particle size (UTA calibration).

$$\delta_{error}(d_{p,i}) = \frac{0.0757 \cdot d_{p,i} - 11.1449}{100} \tag{5.28}$$

$d_{p,i}$ mean particle diameter of a certain size channel (i) [nm]

Fitting a linear function through the x-y distributed squares in Fig. 5.3b gave an equation for the diameter ($d_{p,i,error}$) and therefore the size channel (i) at which the erroneous pulses are counted.

$$d_{p,i,error} = 0.0713 \cdot d_{p,i,\text{true}} + 133.86 \tag{5.29}$$

$d_{p,i,\text{true}}$ mean particle diameter causing erroneous counts [nm]

The absolute uncertainty of a certain particle size channel (i) due to erroneous counts ($unc_{erroneous}(d_{p,i,error})$) is calculated by

$$unc_{erroneous}\left(d_{p,i,error}\right) = \delta_{error}\left(d_{p,i}\right) \cdot \left[d_{p,i}\right] \tag{5.30}$$

$\delta_{error}(d_{p,i})$ fraction of additional small erroneous particle counts at a
                                certain size channel with $d_{p,i}$ [1]

$\left[d_{p,i} \right]$ measured particle concentration at a certain size channel

with $d_{p,i}$ [1/cm^3]

The **uncertainty concerning the gas flow** is composed of the uncertainty of the two MFC (1% of reading, Bronkhorst 2009), the pressure sensor (0.2% of reading, SensorTechnics 2008), and the temperature sensors (0.1% linearity uncertainty, LKM electronic 2004). As the measurement air is obtained by the difference between the two MFCs (cf. Ch. 4.3) the relative uncertainty of the MFCs (rel_unc_{MFC}) is calculated to be 14%.

$$unc_{MFC} = \sqrt{\left(\frac{\partial \left(\phi_{MFC\_sample} - \phi_{MFC\_sheath} \right)}{\partial \phi_{MFC\_sample}} \cdot unc_{MFC\_sample} \right)^2 \cdots + \left(\frac{\partial \left(\phi_{MFC\_sample} - \phi_{MFC\_sheath} \right)}{\partial \phi_{MFC\_sheath}} \cdot unc_{MFC\_sheath} \right)^2} \qquad (5.31)$$

$$= \sqrt{\left(unc_{MFC\_sample} \right)^2 + \left(-unc_{MFC\_sheath} \right)^2} = 0.002018 \; {}^{l}\!/\!_{min}$$

$$rel\_unc_{MFC} = \frac{unc_{MFC}}{\phi_{MFC\_sample} - \phi_{MFC\_sheath}}$$

$$\qquad (5.32)$$

$$= \frac{0.002018 \; {}^{l}\!/\!_{min}}{0.015 \; {}^{l}\!/\!_{min}} = 0.1345$$

unc_{MFC}	absolute uncertainty of both MFCs [l/min]
ϕ_{MFC_sample}	gas volume flow at the MFC, controlling the sample air flow [set to 0.150 l/min]
unc_{MFC_sample}	absolute uncertainty of the MFC, controlling the sample air flow at set point 0.150 l/min [0.0015 l/min]
ϕ_{MFC_sheath}	gas volume flow at the MFC, controlling the sheath air flow [set to 0.135 l/min]
unc_{MFC_sheath}	absolute uncertainty of the MFC, controlling the sheath air flow at set point 0.135 l/min [0.00135 l/min]
rel_unc_{MFC}	relative uncertainty of both MFCs [1]

The resulting relative uncertainty of the measurement air flow is

$$\frac{unc_{sample}}{\phi_{sample}} = \sqrt{\left(\frac{unc_{MFC}}{\phi_{sample}}\right)^2 + \left(rel\_unc_p\right)^2 + \left(rel\_unc_{T,1}\right)^2 + \left(rel\_unc_{T,2}\right)^2}$$

(5.33)

$$= \sqrt{0.1345^2 + 0.002^2 + 0.001^2 + 0.001^2} = 0.13452 \approx 0.14$$

unc_{sample}	absolute uncertainty of sample air [l/min]
ϕ_{sample}	sample air flow [0.015l/min]
unc_{MFC}	absolute uncertainty of both MFCs [l/min]
rel_unc_p	relative uncertainty of p-sensor [0.2%]
$rel\_unc_{T,1}$	relative uncertainty of T-sensor 1 [0.1%]
$rel\_unc_{T,2}$	relative uncertainty of T-sensor 2 [0.1%]

For different kinds of aerosol having different refractive indices, the counting efficiency ε of the OPC at a given diameter differs. Measuring LSA, the counting efficiency curve (Fig. 5.8) is shifted somewhat to larger particle size compared to UTA. On the contrary the calibration curve is shifted somewhat to smaller particles when measuring MTA. The counting efficiency curve for UTA is used for all data to have a uniform data analysis for all atmospheric measurement regions. To estimate the resulting positive and negative relative uncertainty ($rel\_unc_{\varepsilon,i}^+$, $rel\_unc_{\varepsilon,i}^-$), for each size channel the relative difference in the counting efficiency was calculated by

$$rel\_unc_{\varepsilon,i}^+ = \frac{\varepsilon\left(d_{p,LSA}\left(rs_i\right)\right) - \varepsilon\left(d_{p,UTA}\left(rs_i\right)\right)}{\varepsilon\left(d_{p,UTA}\left(rs_i\right)\right)}$$

(5.34)

$$rel\_unc_{\varepsilon,i}^- = \frac{\varepsilon\left(d_{p,MTA}\left(rs_i\right)\right) - \varepsilon\left(d_{p,UTA}\left(rs_i\right)\right)}{\varepsilon\left(d_{p,UTA}\left(rs_i\right)\right)}$$

$\varepsilon\left(d_{p,UTA}\left(rs_i\right)\right)$	counting efficiency for a particle diameter, calculated from a certain response signal (rs_i) using the UTA calibration curve (Fig. 5.6; Eq. 5.6); the used response signal is related to a mean particle diameter of a size certain channel (i), using the UTA calibration [1]
$\varepsilon\left(d_{p,LSA}\left(rs_i\right)\right)$	counting efficiency for a particle diameter, calculated from the same response signal (rs_i) as for $d_{p,UTA}\left(rs_i\right)$, but using the LSA calibration curve [1]
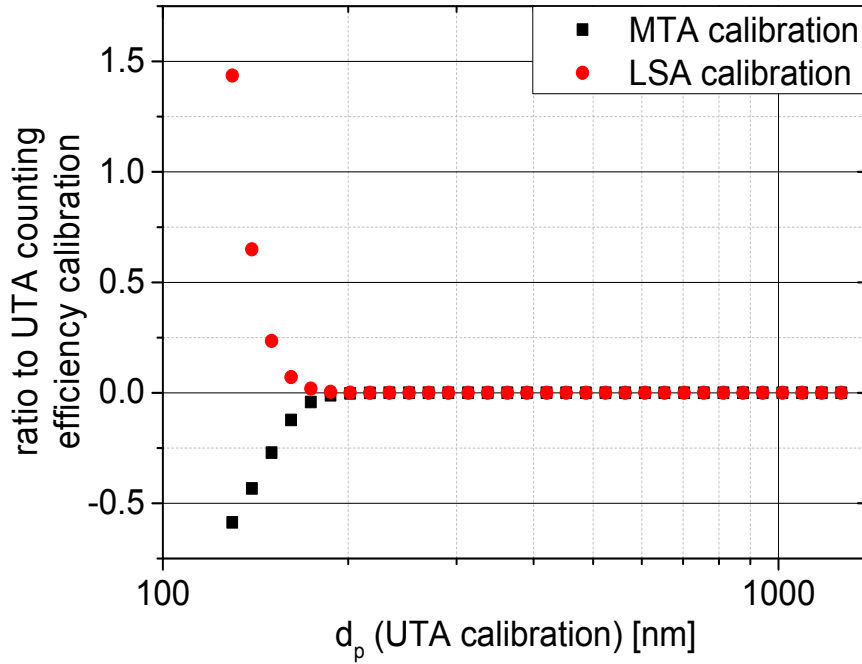
Figure 5.14: Ratio of the MTA and LSA counting efficiency calibration to the UTA counting efficiency calibration. The data points were calculated for the particle size of each size channel, used regularly for data analysis. Particle sizes were transferred from latex and ammonium sulfate calibration using a Mie scattering program.

$\varepsilon\left(d_{p,MTA}\left(rs_i\right)\right)$ counting efficiency for a particle diameter, calculated

from the same response signal (rs_i) as for $d_{p,UTA}\left(rs_i\right)$, but

using the MTA calibration curve [1]

The resulting relative uncertainty ($rel\_unc_{\varepsilon,i}^{\pm}$) is displayed for each size channel in Fig. 5.14. Because the counting efficiency of the OPC increases for all particle compositions with increasing particle diameter to the asymptotic maximum value of ~89% (Ch. 5.2.4), the uncertainty ratios quickly converge to zero.

The overall **absolute particle number concentration** uncertainty for each size channel ($unc_{c,i}^{\pm}$) is the sum of the uncertainty due to erroneous counts plus the root of the sum of the square of the sample air flow uncertainty and the counting efficiency uncertainty multiplied with the measured concentration.

$$unc_{c,i}^{\pm} = unc_{erroneous}\left(d_{p,i,error}\right) + \sqrt{\left(\frac{unc_{sample}}{\phi_{sample}}\right)^2 + \left(rel\_unc_{\varepsilon,i}^{\pm}\right)^2} \cdot \left[d_{p,i}\right] \quad (5.35)$$

$unc_{c,i}^{\pm}$ absolute uncertainty of a certain size channel (i)

concerning particle number concentration [1/cm^3]

$unc_{erroneous}\left(d_{p,i,error}\right)$ absolute uncertainty of a certain particle size channel (i)

with $d_{p,i,error}$ due to erroneous counts [1/cm^3]

$$\frac{unc_{sample}}{\phi_{sample}}$$ relative uncertainty of sample air flow [1]

$rel\_unc_{\varepsilon,i}^{\pm}$ relative uncertainty of a certain size channel (i) due to the use of the UTA calibration for all measurement regions [1]

$\left[d_{p,i}\right]$ measured particle concentration at a certain size channel with $d_{p,i}$ [1/cm^3]

The absolute uncertainty concerning the derived **particle surface area concentration** ($unc_{s,i}^{\pm}$) is composed of the uncertainty concerning particle size and concentration. The particle surface concentration for each size channel (i) is calculated by

$$\left[s_i\right] = \pi \cdot d_{p,i}^2 \cdot \left[d_{p,i}\right] \tag{5.36}$$

$\left[s_i\right]$ particle surface area concentration of a certain size channel (i) [μm^2/cm^3]

$d_{p,i}$ mean particle diameter of a certain size channel (i) [μm]

$\left[d_{p,i}\right]$ measured particle concentration at a certain size channel with $d_{p,i}$ [1/cm^3]

From Eq. 5.36 the absolute uncertainty ($unc_{s,i}^{\pm}$) is calculated by

$$unc_{s,i}^{\pm} = \sqrt{\left(\frac{\partial\left[s_i\right]}{\partial d_{p,i}} \cdot unc\_d_{p,i}^{\pm}\right)^2 + \left(\frac{\partial\left[S_i\right]}{\partial\left[d_{p,i}\right]} \cdot unc_{c,i}^{\pm}\right)^2}$$

$$\tag{5.37}$$

$$= \sqrt{\left(2 \cdot \pi \cdot d_{p,i} \cdot \left[d_{p,i}\right] \cdot unc\_d_{p,i}^{\pm}\right)^2 + \left(\pi \cdot d_{p,i}^2 \cdot unc_{c,i}^{\pm}\right)^2}$$

$unc_{s,i}^{\pm}$ absolute uncertainty of the particle surface concentration of a certain size channel (i) [μm^2/cm^3]

$\left[s_i\right]$ particle surface concentration of a certain size channel (i) [μm^2/cm^3]

$d_{p,i}$ mean particle diameter of a certain size channel (i) [μm]

$unc\_d_{p,i}^{\pm}$ absolute uncertainty concerning particle size [μm]

$\left[d_{p,i}\right]$ measured particle concentration at a certain size channel with $d_{p,i}$ [1/cm^3]

$unc_{c,i}^{\pm}$ absolute uncertainty of a certain size channel (i)

                                       concerning particle number concentration [1/cm^3]

The absolute uncertainty concerning the derived **particle mass concentration** ($unc_{m,i}^{\pm}$) is composed of the uncertainty concerning particle size, density, and concentration. The calculation of the uncertainties for particle size and concentration are described above. The absolute uncertainty of the particle density (unc_{ρ}) is estimated to be 0.09 g/cm^3, which is the difference between LSA and MTA (Tab. 5.3). The density of the used UTA calibration is in between the LSA and MTA density. The particle mass concentration for each size channel (i) is calculated by

$$\left[m_i \right] = \frac{1}{6} \cdot \pi \cdot d_{p,i}^3 \cdot \rho_{UTA} \cdot \left[d_{p,i} \right] \tag{5.38}$$

$\left[m_i \right]$ particle mass concentration of a certain size channel (i)

                                       [μg/m^3]

$d_{p,i}$ mean particle diameter of a certain size channel (i) [nm]

ρ_{UTA} particle density (UTA) [$1.64 \cdot 10^{-15}$ μg/nm^3]

$\left[d_{p,i} \right]$ measured particle concentration at a certain size channel

                                       with $d_{p,i}$ [pt/m^3]

From Eq. 5.38 the absolute uncertainty ($unc_{m,i}^{\pm}$) is calculated by

$$
unc_{m,i}^{\pm} = \sqrt{\left(\frac{\partial [m_i]}{\partial d_{p,i}} \cdot unc\_d_{p,i}^{\pm} \right)^2 + \left(\frac{\partial [m_i]}{\partial \rho_{UTA}} \cdot unc_{\rho} \right)^2 + \left(\frac{\partial [m_i]}{\partial [d_{p,i}]} \cdot unc_{c,i}^{\pm} \right)^2}
$$

$$
= \sqrt{ \begin{array}{l} \left(\frac{1}{2} \cdot \pi \cdot d_{p,i}^2 \cdot \rho_{UTA} \cdot [d_{p,i}] \cdot unc\_d_{p,i}^{\pm} \right)^2 \dots \\[2mm] \dots + \left(\frac{1}{6} \cdot \pi \cdot d_{p,i}^3 \cdot [d_{p,i}] \cdot unc_{\rho} \right)^2 \dots \\[2mm] \dots + \left(\frac{1}{6} \cdot \pi \cdot d_{p,i}^3 \cdot \rho_{UTA} \cdot unc_{c,i}^{\pm} \right)^2 \end{array} } \tag{5.39}
$$

$unc_{m,i}^{\pm}$ absolute uncertainty of the particle mass concentration of a

                                       certain size channel (i) [μg/m^3]

$\left[m_i \right]$ particle mass concentration of a certain size channel (i)

                                       [μg/m^3]

$d_{p,i}$ mean particle diameter of a certain size channel (i) [nm]

$unc\_d^{\pm}_{p,i}$ absolute uncertainty concerning particle size [nm]

ρ_{UTA} particle density (UTA) [$1.64 \cdot 10^{-15}$ µg/nm^3]

unc_{ρ} absolute uncertainty of particle density

                                            [$0.09 \cdot 10^{-15}$ µg/nm^3]

$[d_{p,i}]$ measured particle concentration at a certain size channel

                                            with $d_{p,i}$ [1/m^3]

$unc^{\pm}_{c,i}$ absolute uncertainty of a certain size channel (i)

                                            concerning particle number concentration [1/m^3]

The **integral particle number-, particle surface-, and particle mass concentration** is obtained by summing up the concentration of all OPC size channels. As the individual size channel absolute uncertainties are not independent (e.g. the flow uncertainty points to the same direction for all size channels), a Gaussian summation of the channel individual absolute uncertainties would be wrong. Consequently, the absolute uncertainty of the integral concentrations is the (linear) sum of the channel individual absolute uncertainties (linear uncertainty propagation).

$$unc^{\pm}_{c,int} = \sum_{i=1}^{n} unc^{\pm}_{c,i} \tag{5.40}$$

$$unc^{\pm}_{s,int} = \sum_{i=1}^{n} unc^{\pm}_{s,i} \tag{5.41}$$

$$unc^{\pm}_{m,int} = \sum_{i=1}^{n} unc^{\pm}_{m,i} \tag{5.42}$$

$unc^{\pm}_{c,int}$ absolute uncertainty of the integral particle number

                                            concentration [1/cm^3]

$unc^{\pm}_{c,i}$ absolute uncertainty of a certain size channel (i)

                                            concerning particle number concentration [1/cm^3]

$unc^{\pm}_{s,int}$ absolute uncertainty of the integral particle surface area

                                            concentration [µm^2/cm^3]

$unc^{\pm}_{s,i}$ absolute uncertainty of a certain size channel (i)

                                            concerning particle surface concentration [µm^2/cm^3]

$unc^{\pm}_{m,int}$ absolute uncertainty of the integral particle mass

                                            concentration [µg/m^3]

$unc^{\pm}_{m,i}$ absolute uncertainty of a certain size channel (i)

                                            concerning particle mass concentration [µg/m^3]

Implementing Eq. 5.25 to 5.42 in a FORTRAN algorithm, the uncertainties are individually calculated for all measurements. On average, the relative uncertainty is about 40% for the integral particle number concentration, 31% for the integral particle surface concentration, and 33% for the integral particle mass concentration. The relative uncertainty for the number concentration is largest, because of the large uncertainty of the counting efficiency due to the use of the UTA calibration for all measurement regions ($rel\_unc_{\varepsilon,i}^{\pm}$, Fig. 5.14). At the OPC lower detection limit $rel\_unc_{\varepsilon,i}^{\pm}$ is largest and the particle concentration is highest, resulting in a high absolute uncertainty. While the UT/LMS integral number concentration is dominated by Aitken mode particles, the integral particle surface and mass concentration is dominated by accumulation and coarse mode particles (cf. Sec. 2.3). With increasing particle size the OPC reaches the maximum asymptotic counting efficiency of 89% and $rel\_unc_{\varepsilon,i}^{\pm}$ converge to zero.

6 Results

For this work CARIBIC data obtained between April 2010 and May 2011 were considered. The respective flights include three volcanic ash flights (VAF, April and May 2010, Sec. 6.2.1), as well as 48 intercontinental flights (IF, first year of regular measurements from June 2010 until May 2011). As usual for brand new instruments, also the OPC unit had some teething problems and did not work on one VAF and eight IF. Additionally during two IF the whole CARIBIC container got no power from the aircraft and hence did not measure. Excluding the power failure, the OPC unit availability was 81 % with most failures occurring during the first flights. After improving the data acquisition and unit control software in December 2010, the OPC unit ran much more stable with only two failures during the last 24 flights of the investigated period.

The flight tracks of all CARIBIC flights with successful OPC measurements are shown in Fig. 6.1. All these flights either started or ended in Frankfurt (Germany). The other destination or departure airports were Vancouver (Canada; North American route, 4 flights), Caracas (Venezuela) or Bogota (Columbia) (South American route, 14 flights), Johannesburg or Cape Town (both South Africa; South African route, 9 flights) and Osaka (Japan, Asian route, 10 flights). The two successful VAF above the Baltic Sea and the Norwegian Sea are also shown in Fig. 6.1. Summarizing all flights until May 2011, data from ~381 flight hours (~ 343 000 km or ~ 8 ½ times around the globe) were available for this thesis.

Section 6.1 describes with an example the routine data analysis developed in this work, also identifying potential measurement artifacts when flying through clouds. This section also compares the measured particle size distributions with literature data and discusses the occurrence of an unexpected particle mode. Case study analyses including the VAF, the observation of a strong pollution plume, and a first attempt of a mass closure study along a stratospheric measurement flight are discussed in Sec. 6.2. The vertical profile of the particle size distribution from the UT into the LMS, a comparison of the mid-latitude tropospheric to stratospheric accumulation mode, a stratospheric seasonality analysis, as well as a latitudinal gradient is given in Sec. 6.3. Section 6.4 shows results, which indicate that stratospheric aerosol particles are a sink for gaseous
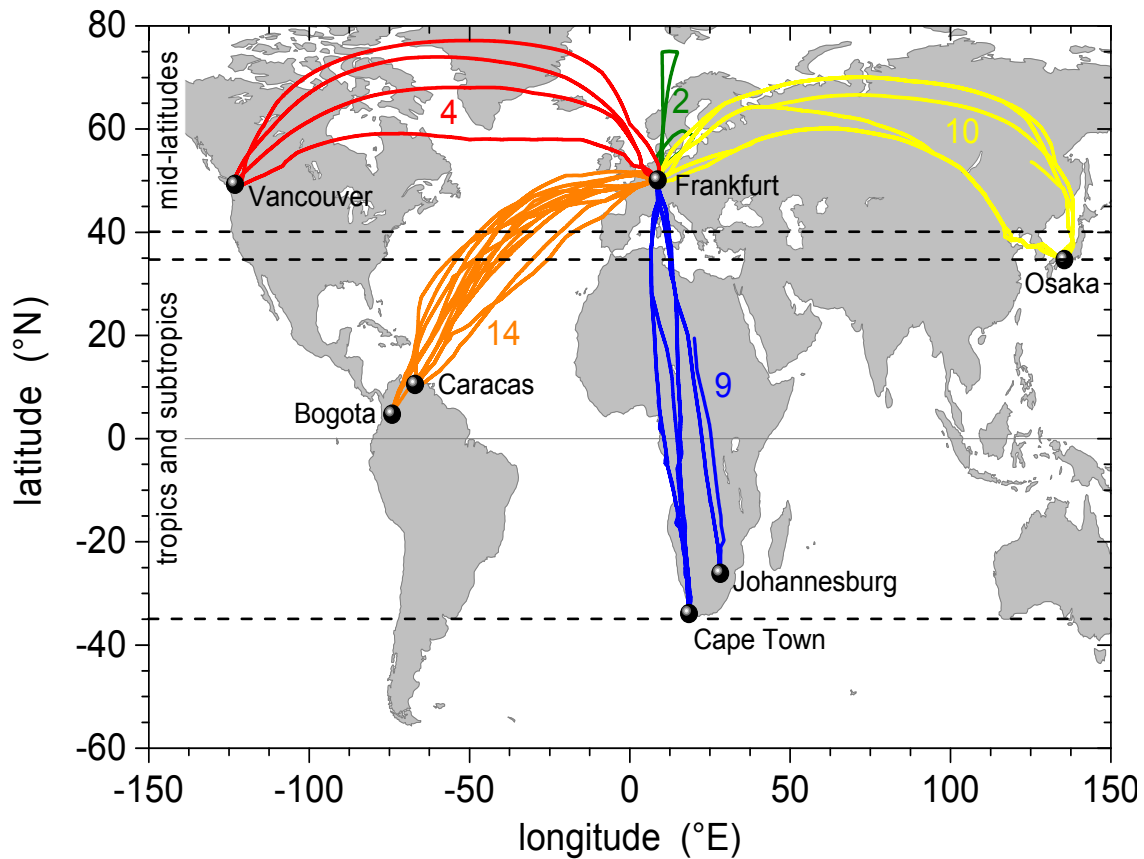
Figure 6.1: CARIBIC flights with OPC data between April 2010 and May 2011. All together data from 39 flights were obtained. The dashed lines mark the borders of the analyzed climatologically regions, namely the tropics and subtropics (-35°N to 35°N), as well as the northern hemispheric mid-latitudes (north of 40°N).

mercury. As an example of model validation application, in Sec. 6.5 the measured CARIBIC particle size distributions are compared to model data from the GLObal Model of Aerosol Processes (GLOMAP). Finally Sec. 6.6 compares OPC derived stratospheric aerosol parameters to climatological data from the Stratospheric Aerosol and Gas Experiment (SAGE II). The analyses in section 6.3 to 6.6 might be statistically not well constrained, because the dataset is limited to only one year. As a much longer dataset is needed for conclusions on higher significance level, however, the presented analyses are intended to exemplify different applications for the growing unique CARIBIC OPC dataset.

6.1   Regular data analysis and evaluation

6.1.1   Flight overview

As a part of the OPC data evaluation routine, the data of each flight are visualized in two overview plots as described below for the flight LH319. This 11 hour long flight was carried out on 16th of November 2010 between Frankfurt and Bogota.
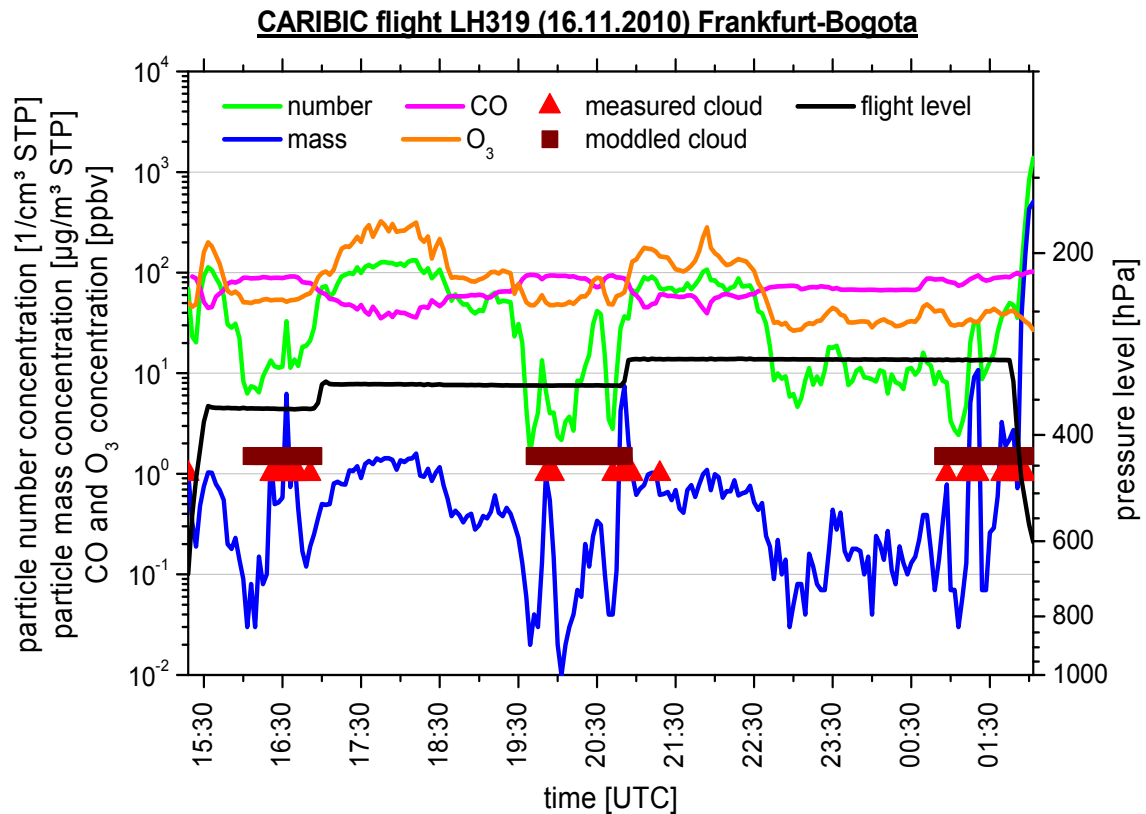
Figure 6.2: OPC data evaluation overview plot for the CARIBIC flight LH319 from Frankfurt (Germany) to Bogota (Columbia). Particle number and mass concentration are normalized to standard conditions (p = 1013.25 hPa, T = 273.15 K). The flight level is given as pressure altitude at the right hand scale.

As described in Sec. 5.3.1, the raw data are processed using a FORTRAN algorithm. The 180 s average values of the integral particle number and mass concentration (125 nm < d_p < 1312 nm) are plotted as time series (Fig. 6.2 green and blue, respectively). The air pressure (black) indicates the flight altitude of the aircraft. Carbon monoxide (CO, magenta) and ozone (O_3, orange) as tracers for boundary layer air and stratospheric air, respectively [Seinfeld and Pandis, 1998, p. 86; Zahn and Brenninkmeijer, 2003], are also shown. As expected, the CO and O_3 concentrations are anti-correlated nearly during the whole flight. To check whether the measurements are influenced by clouds, the in situ measured cloud water content (CWC; Sec. 3.3, Brenninkmeijer et al., 2007) is used to determine inside cloud measurements. If the CWC was at least 20 seconds above 4% of the measured gaseous water content[20], the 180 s OPC measurement was marked to be (partly) obtained inside a cloud (red triangles). As the water instrument did not work on some flights, the modeled cloud data from KNMI (Sec. 3.3) were alternatively used and are shown as brown squares. Fig. 6.2 shows that the modeled and observed clouds mostly coincide. However, because of the coarse resolution of the model input data[21], the modeled clouds have a

---

[20] The numbers were set to account for the CWC uncertainties.

[21] ECMWF data have a temporal resolution of 6h and a spatial resolution of 1° in latitude and longitude (/www.knmi.nl/samenw/campaign_support/CARIBIC/plotexplanation.html; last access 20.07.2014).
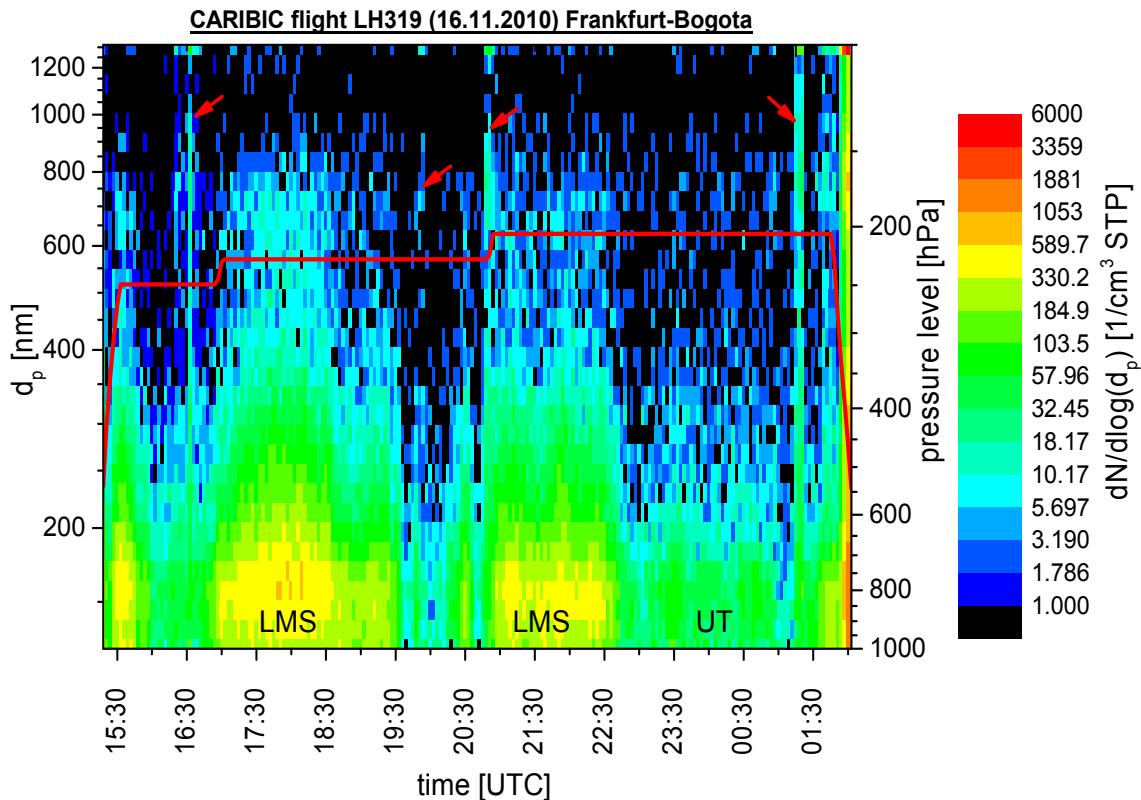
Figure 6.3: Particle size distribution (32 channels) along the CARIBIC flight LH319 from Frankfurt to Bogota. The color code indicates the particle concentration (dN/dlog(d$_p$)) for the particle size, given at the left y-axis. The pressure altitude of the aircraft is indicated as red line. Particle concentrations are normalized to standard conditions (p = 1013.25 hPa, T = 273.15 K).

much larger extent than the observed ones. Nevertheless, the modeled clouds give a good idea, which measurements might be influenced by clouds if the CWC data are not available.

In Fig. 6.2 some short peaks in particle number and mass concentration correlate well with the occurrence of clouds. This finding might be an evidence for artifacts when measuring inside a cloud and will be discussed in section 6.1.2.

In a second OPC data evaluation plot, the particle size distribution is plotted as contour plot for every flight (Fig. 6.3). While the left y-axis scale indicates the particle size, the color gives the particle number concentration for each of the 32 size channels. Please note the given concentrations are dN/dlog(d$_p$) values. This kind of plot indicates the variation of the particle size distribution along the flight track. The most obvious variation on flight LH319 is caused by different air masses (UT air vs. LMS air; cf. Fig. 6.5a) and inside cloud measurements (marked with red arrows). The difference between the UT and LMS particle size distribution will be discussed in section 6.3.1.

The two overview plots introduced above, allow quick identification of interesting measurement sequences (e.g. pollution plumes, change of air mass), and some of these are discussed in Sec. 6.2.
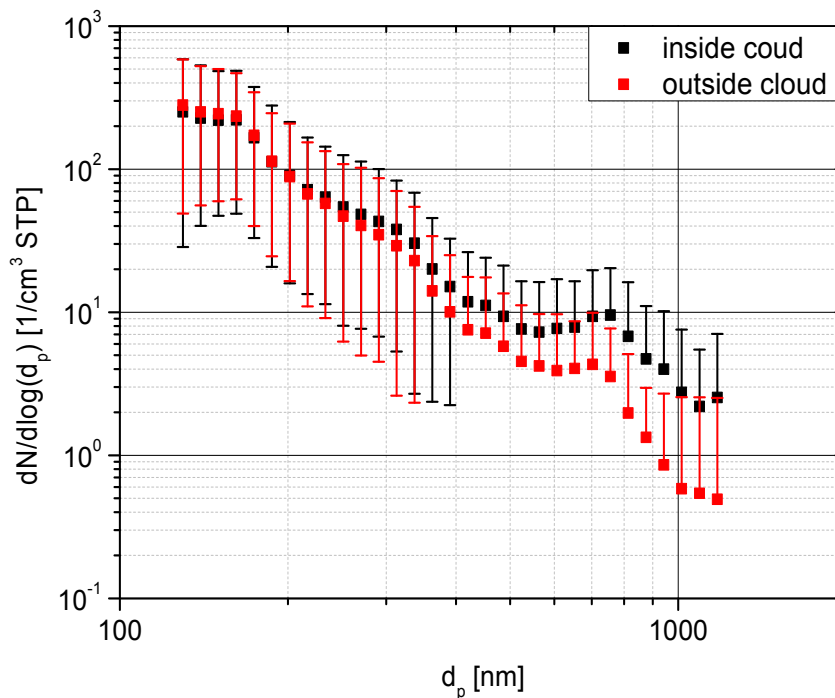
Figure 6.4: Comparison of the particle size distributions inside and outside clouds. Tropospheric data (PV < 1 PVU) were averaged for all CARIBIC flights from June 2010 to May 2011. Squares give the mean concentration and the error bars indicate the 10% and 90% percentiles. Particle concentrations are normalized to standard conditions (p = 1013.25 hPa, T = 273.15 K).

6.1.2 Artifact measurements inside clouds

As already indicated in the discussion to Fig. 6.2, high short-time peaks of the OPC particle number and mass concentration do correlate well with the occurrence of clouds. Following the Köhler theory, the accumulation and the coarse mode particle concentration and thus the total particle mass inside a cloud should decrease due to the activation of those particles to cloud droplets [Seinfeld and Pandis, 1998, p. 809-812; Ditas et al., 2012]. Fig. 6.3 shows on the contrary that particle concentrations increase for all measurements inside clouds on flight LH319 (marked with red arrows). This applies in particular for large particles. To illustrate the difference of the size distributions inside and outside a cloud more clearly, Fig. 6.4 compares the average of all cloud samples (black) to the average of all samples in cloud-free air (red) for all flights. The measurements inside clouds were identified using the CWC measurements and the modeled cloud data (cf. Sec. 6.1.1). Only tropospheric data (PV < 1 PVU; cf. Sec. 2.1 and Tab. 6.2) were used. While the squares give the mean concentration, the error bars indicate the 10% and 90% percentiles. Please note, if no percentile is given, it was zero. The larger the particle size, the higher the inside cloud concentrations increased above the outside cloud concentration. Only for particles smaller than ~ 200 nm the cloud seems to lower the particle number concentration slightly. This
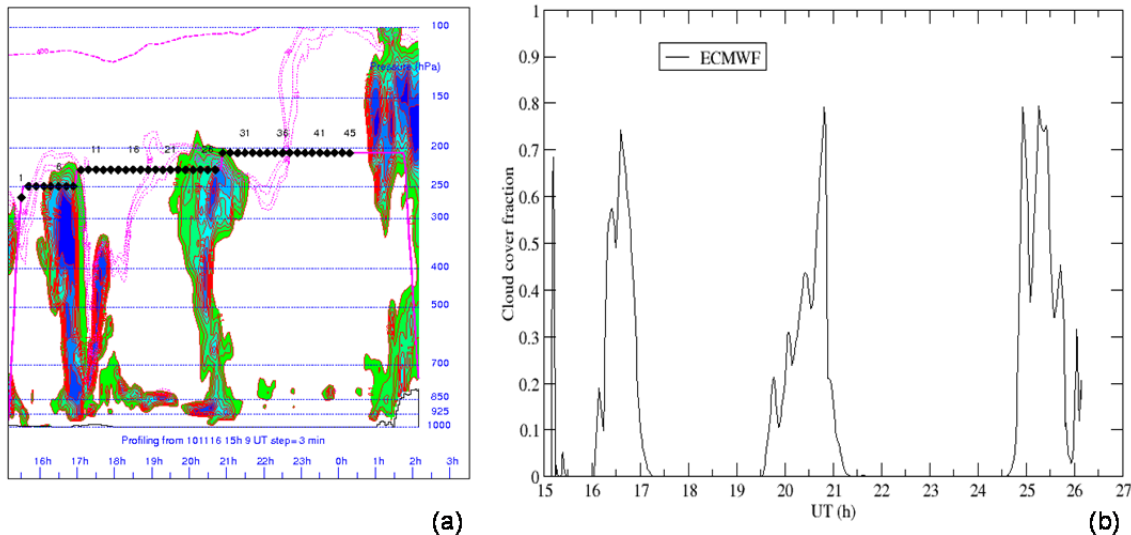
Figure 6.5: ECMWF cloud cover fraction along the CARIBIC flight LH319 from Frankfurt to Bogota as vertical profile (a) and number at the aircraft position (b). The color code in graph (a) indicates the cloud cover fraction with border values from >0.1 in light green to > 0.9 in dark blue by 0.1 steps. Thin purple dotted lines showing the potential vorticity between 1.5 and 3.5, indicate the tropopause. The aircraft flight level is marked as thick purple line. Both figures are taken from the KNMI CARIBIC support web page (http://www.knmi.nl/samenw/campaign_support/CARIBIC/ last access 20.07.2014).

finding is confirmed by a cloud contact analysis for the CPC data, which shows nearly always a lower Aitken mode[22] particle concentration when measuring inside clouds.

As no physical explanation can be given for the increased particle concentration inside the cloud, it is presumed that the OPC measures not only interstitial aerosol particles (the not-activated aerosol particles), but also artificial cloud particles. These artificial cloud or break-up particles may be generated when cloud droplets or ice crystals hit the inlet tip, but also when cloud droplets or ice crystals enter the aerosol inlet and break-up during the slowdown inside the inlet tube [Korolev et al., 2011]. Compared to the interstitial aerosol particles, these artificial particles might be large (a few micrometer). As they dry by evaporation or sublimation during transport from the inlet to the OPC unit (temperature increase ~90 K, Sec. 3.2), their residuals could be measured by the OPC as increased particle concentrations.

The occurrence of cloud artifacts was observed for all in-cloud measurements in the CARIBIC flights. As the number and size of newly formed particles by the above described processes cannot be quantified, in-cloud measurements were excluded from further analysis. As CWC data are available only for 27 of the 39 flights, the ECMWF were used for the flights without CWC data. The ECMWF vertical cloud structure along flight LH319 is shown in Fig. 6.5a. The fraction of the area of the model grid cells covered by clouds (0 to 1) is indicated by the color code. This plot shows also PV iso-lines, typical for the tropopause (1.5 - 3.5 PVU, purple dotted). The cruising altitude of the aircraft (pressure level) is given as thick purple line (other data visualized in the graph will not be discussed). During that flight the aircraft passed the first cloud near the cloud top and flew through the tropopause into LMS air. After flying back through the tropopause, the aircraft passed the second cloud near its top. When the aircraft left

---

[22] In the free and upper troposphere the number concentration of particles larger than 12 nm is dominated by Aitken mode particles (see Fig. 2.3).

the cloud due to a flight level change, the LMS was entered once again. At about 23:00 UTC the aircraft flew back into UT air and entered the third cloud (extended up to a pressure altitude of about 125 hPa) before descent. The occurrence of all three clouds was confirmed by the CWC measurements (cf. Fig. 6.2). To decide whether a measurement was obtained inside a cloud, KNMI provide a cloud cover fraction model output with a temporal resolution of one minute along the flight route (Fig. 6.5b). These data were averaged for the same three minute bins the particle size distributions were integrated for. If the cloud cover fraction was found to be above 0.1 and the model relative humidity was above 90 % for an individual bin, the measurement was marked as "obtained inside cloud" and was excluded for further analyses.

6.1.3 Comparison to literature data

As already mentioned in Chapter 1, only few measurements of the particle size distribution were carried out in the UT/LMS region up to 2011. The data published in the last 20 years are summarized in Tab. 6.1. Most of the data were obtained in geographical regions where the OPC unit did not measure up to May 2011. Thus all CARIBIC OPC data (obtained until flight LH344) were divided into three different major air mass data subsets: the mid-latitude UT, the mid-latitude LMS, and the tropical and subtropical mid- and upper troposphere (MUT). Due to the relatively long life time of accumulation mode particles in the UT/LMS (several weeks; cf. Sec. 2.3),

Table 6.1: Summary of previous measurements of the particle size distribution in the UT/LMS region (until 2010).

location and altitude	time	campaign	published in
west of Tenerife (9-11 km)	July 1997	Second Aerosol Characterization Experiment (ACE 2)	de Reus et al. [2000]
south of Male (8-12.5 km)	February-March 1999	Indian Ocean Experiment (INDOEX)	de Reus et al. [2001]
Berlin (10-12 km)	July-August 1998	Lindenberg Aerosol Characterization Experiment (LACE 98)	Schröder et al. [2002], Petzold et al. [2002]
Surinam (10-12.6 km)	March 1998	Large-Scale Biosphere-Atmosphere Experiment (LBA)	Krejci et al. [2003]
northwestern Pacific Ocean (south of Japan) (11 km)	February 2000	Pacific Atmospheric Chemistry Experiment (PACE-7)	Zaizen et al., [2004]
central USA (7-10 km)	December 2005	Stratosphere Troposphere Analyses of Regional Transport (START)	Young et al. [2007]

Table 6.2: Classification of the CARIBIC measurement regions for data comparison. To differ between UT and LMS the ECMWF PV along the flight track was used. (1 PVU = 10^{-6} K $\cdot$ m² $\cdot$ kg^{-1} $\cdot$ s^{-1})

region	latitude	longitude	UT/LMS separation
mid-latitude UT	> 40° N	averaged over all longitudes	PV < 1 PVU
mid-latitude LMS	> 40° N	averaged over all longitudes	PV > 3.5 PVU
tropical and subtropical MUT	35°S < lat < 35°N	averaged over all longitudes	PV < 1 PVU

measurements in the same air mass at different locations can be compared. As in the UT the longitudinal mixing is faster than the meridional one, the compared regions have to be within the same latitudes.

The air mass classification is given in Tab. 6.2. Before averaging the OPC data for each class, cloud measurements, as well as data obtained during ascend and descend were excluded. Because O_3 data were not available for all measurement flights, the PV was used to distinguish between tropospheric and stratospheric air masses. The measurement was attributed to the troposphere if the PV was lower than 1 PVU (1 PVU = 10^{-6} K $\cdot$ m² $\cdot$ kg^{-1} $\cdot$ s^{-1}) and to LMS if PV was larger than 3.5 PVU. Data with PV 1 PVU to 3.5 PVU were not used to have a clear separation.

Because the measurements (CARIBIC and literature) were obtained at different flight levels, a quantitative comparison is reasonable only by normalizing all data to standard pressure and temperature (STP: p=1013.25 hPa; T=273.15 K). Unfortunately only de Reus et al., [2001] and Krejci et al., [2003] presented their data at STP conditions. All other data were assumed to be given at ambient conditions and were converted to STP by using the US standard atmosphere [Seinfeld and Pandis 1998, p. 7, 1293] and the given altitude. The mean height was used if an altitude range was given. Uncertainties caused by the difference of the true measurement conditions compared to the US standard atmosphere values were estimated to be smaller than 20% (based on a pressure and temperature variation of ±30 hPa and ±15 K at a pressure altitude of 250 hPa).

Another uncertainty in the data comparison arises from the different measurement instruments and platforms. The published data were measured onboard research aircraft with usually relatively short sampling lines whereas the CARIBIC sampling line is quite long with 4 m length. Between inlet and the OPC unit the sample air is warmed by about 90 K from -55°C to +35°C and an initial relative humidity (rH) of 70% decrease to nearly 0% at +35°C. Consequently, nearly all water evaporates from the aerosol particles. Simulations performed by Jens Voigtländer (IfT/TROPOS) with the Computational Fluent Dynamics (CFD) program "FLUENT" showed that $H_2SO_4 - H_2O$ particles with a wet diameter of $d_{p,wet} = 1000$ nm and a corresponding dry

Table 6.3: Modeled drying of $H_2SO_4 - H_2O$ particles at the CARIBIC aerosol inlet system (inlet + sampling line). At the aerosol inlet the temperature and relative humidity was set to -55°C and 70%, respectively. At the sample line exit the temperature was set to +35°C. The residence time of the measurement air from the inlet towards the OPC unit was calculated to be 0.65 seconds. The dry diameter ($d_{p,dry}$) corresponding to a certain wet diameter ($d_{p,wet}$) gives the particle size if only the H_2O would evaporate and the H_2SO_4 would remain. The simulations were performed by Jens Voigtländer (IfT/TROPOS) with the Computational Fluent Dynamics (CFD) program "FLUENT".

$d_{p,wet}$ – at inlet [nm]	$d_{p,dry}$ – at inlet [nm]	$d_{p,wet}$ – at OPC [nm]	$d_{p,dry}$ – at OPC [nm]
150	102.3	118.1	99.8
300	204.6	240.5	203.2
500	341.1	402.5	340.2
700	477.5	564.3	476.8
1000	682.1	806.8	681.7

diameter of $d_{p,dry} = 682.1$ nm shrink during the sampling to a wet diameter of $d_{p,wet} = 806.8$ nm ($d_{p,dry} = 681.7$ nm)[23]. For other particle diameters the results of the CFD simulations are listed in Tab. 6.3.

The size distributions given in the literature were mostly measured using (much) shorter aerosol sampling lines with (much) shorter measurement air transport times. Unfortunately, the relative humidity at which the measurements took place was not given in the literature. However, the CFD simulations for the CARIBIC inlet system showed that the water evaporates instantaneously from the particles after entering the inlet, because of the strong temperature increase. Therefore it is assumed the particle size distributions given in the literature were measured at comparable humidity.

Figure 6.6 shows the averaged CARIBIC OPC size distributions as well as the literature data for the mid-latitude UT (a), the mid-latitude LMS (b), and the tropical and subtropical MUT (c). Within each graph red squares represent the CARIBIC mean value and the gray area indicates the 10 % and 90 % percentile. The OPC integration time was set to 900 s (cf. Sec. 5.3.1) for this comparison. Sometimes no particles were counted within 15 min in certain size channels (especially those counting particles larger than 800 nm), leading to a jump of the 10 % percentile to zero. For the routinely used 180 s resolution the 10% percentile drops to zero at much smaller particle diameters (cf. Fig. 6.4). However, the 180 s resolution was chosen for the routine analysis to detect also small scale changes of the particle size distribution. The size distributions taken from the literature are displayed as lines. While dashed lines in the same color indicate the range of the measured concentration from a study, solid lines represent data, already averaged by the authors. The general shape of the CARIBIC size distribution and its variation within the regions will be discussed in detail within the statistical analysis in Sec. 6.3. Within this section the focus lays on the comparison to other in situ measurements.

---

[23] The particle wet diameter ($d_{p,wet}$) describes the size of a certain aerosol particle at ambient humidity. The corresponding dry diameter ($d_{p,dry}$) gives the residual particle size if all H_2O evaporates from the particle.
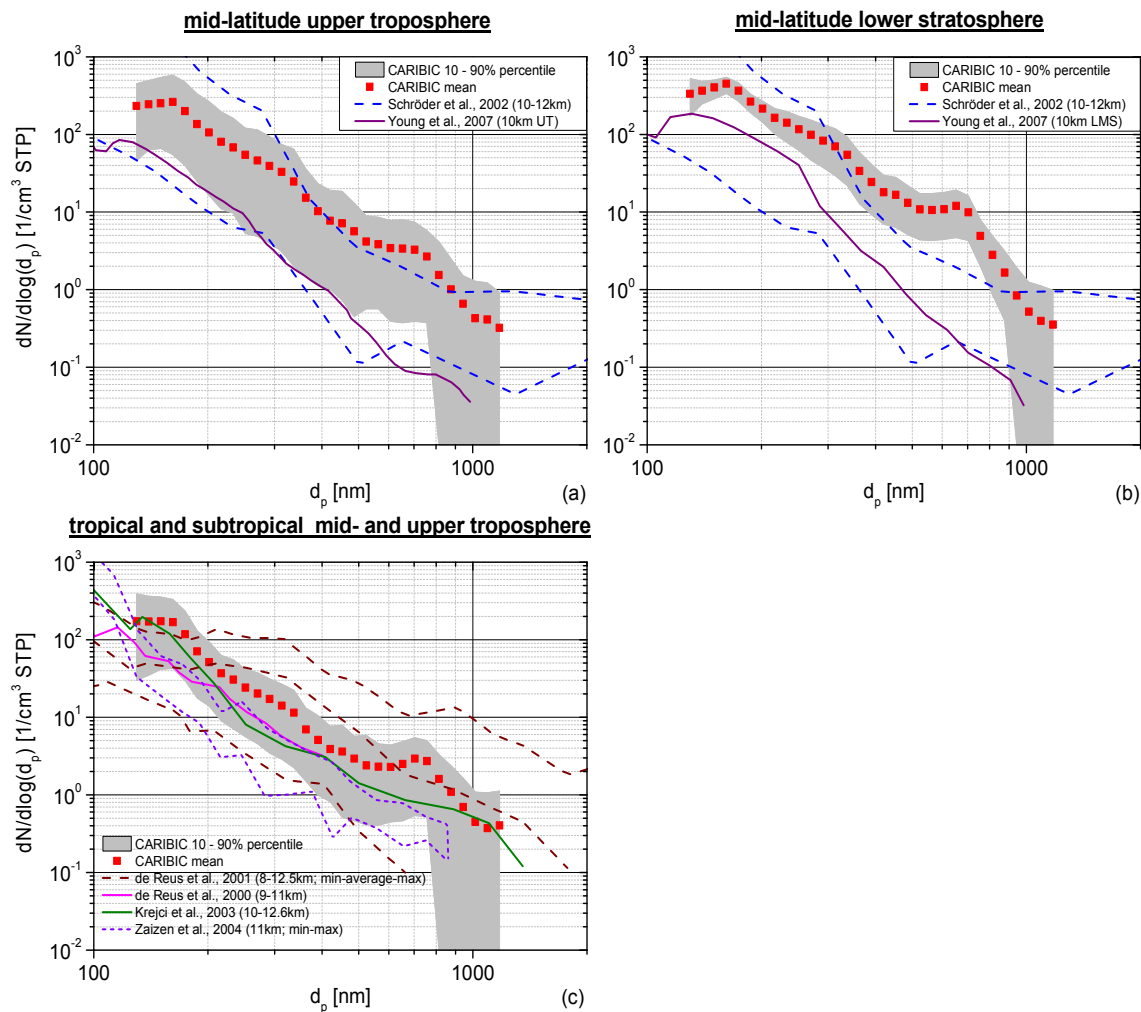
Figure 6.6: Comparison of particle size distributions measured in the mid-latitude UT (a), the mid-latitude LMS (b), and the tropical and subtropical MUT(c). The borders of the regions are given in Fig. 6.1 and Tab. 6.2. Gray areas indicate the CARIBIC 10- and 90% percentile (15 min average). The CARIBIC mean with the same averaging time is indicated with red squares. If not given, published data (solid and dashed lines) were normalized to standard conditions ($p = 1013.25$ hPa, $T = 273.15$ K) using the US standard atmosphere.

The CARIBIC mid-latitude tropospheric data in Fig. 6.6a are mostly within the concentration range published by Schröder et al., [2002]. The Schröder minimum concentration curve is similar to the CARIBIC 10% percentiles. Only for particles 450 nm < d_p < 900 nm the CARIBIC mean concentration is somewhat larger than the maximum concentration line of Schröder et al. [2002]. The slope of the two curves of Schöder et al. [2002] is similar to the CARIBIC data. The slope of the size distribution published by Young et al., [2007] is similar, too. However, the total particle concentration is much lower than the CARIBIC mean, reaching only the CARIBIC 10 % percentile and the lower limit curve of Schröder et al., respectively. As stated above, the atmospheric life time of UT accumulation mode particles is relatively long. Consequently, the different measurement locations (Young et al.: central USA, Schröder et al.: Germany, CARIBIC 120°W < θ < 140°E) can be not the only reason for this huge difference (up to one order of magnitude). Because all data were corrected for aerosol inlet efficiency, the data from different research aircraft with different aerosol inlets should be comparable. The normalization of concentrations to STP would explain

a difference of 20%, but not 500% to 1000%. Possible reasons for the much lower concentrations from Young et al. might be the measurement statistics and the season at which the measurements were carried out. The CARIBIC dataset is based on 39 measurement flights carried out over one year and Schröder et al. [2002] report averages over ten measurement flights in July and August. On the contrary, Young et al. reported a singular measurement on one measurement flight in December 2005 (region 1 in Young et al., [2007]). Thus the low concentration of accumulation mode particles measured by Young et al. might occur locally but might be not representative for the yearly average in the mid-latitude UT.

Schröder et al. [2002] attributed their measurement to the tropopause region and thus the data are shown in the mid-latitude LMS comparison, too. Young et al. [2007] differed between UT and LMS measurements by using the PV and the thermal tropopause definition. The UT measurement at 10 km altitude (PV < 2 PVU) was used for Fig. 6.6a, while the measurement above the thermal tropopause (07.12.2005 region 2, altitude also 10 km) is shown in Fig. 6.6b. In the LMS for particles smaller than ~300 nm, the CARIBIC concentrations are within the range given by Schöder et al. [2002]. Above 300 nm the slope of the maximum curve of Schröder et al. [2002] changes and the CARIBIC data are significantly higher. The stratospheric particle size distribution published by Young et al. [2007] is mostly within the range of data by Schröder et al. [2002] but lower than the CARIBIC data. The slope of all three data sets is similar. The higher CARIBIC concentration might be caused by the PV limit of 3.5 PVU for separating stratospheric air when compared to 2 PVU of Young et al. [2007] and tropopause of Schröder et al. [2002]. Therefore the latter two data sets might be more influenced by tropospheric air than the CARIBIC measurements. The occurrence of the peak (mode) in the CARIBIC size distribution at ~700 nm will be discussed in detail in Sec. 6.1.4

Most of the data were published for the tropics and subtropics (Fig. 6.6c). The particle size distributions measured west of Tenerife [de Reus et al., 2000] and the data from Surinam [Krejci et al., 2003] are comparable with the CARIBIC means. While the average concentration, given by de Reus et al. [2001] is higher for dp < 600 nm, the max-min range covers the CARIBIC 10- and 90% percentile. The data published by Zaizen et al., [2004] are generally somewhat lower than the CARIBIC data but higher than the CARIBIC the 10% percentile.

Considering that the measurements were obtained in different locations (longitude), on different times scales (number of flights, measurement season), and with different research aircrafts (aerosol inlets, measurement instruments), the CARIBIC data are generally in reasonable agreement with the published data. For all compared regions the published data are within the same range of the CARIBIC OPC and the size distribution slopes are similar. The best agreement is observed for the tropical and subtropical MUT. Consequently, it is concluded that the CARIBIC OPC data are comparable with other data sets and representative for the observation locations.

tropical and subtropical mid- and upper troposphere
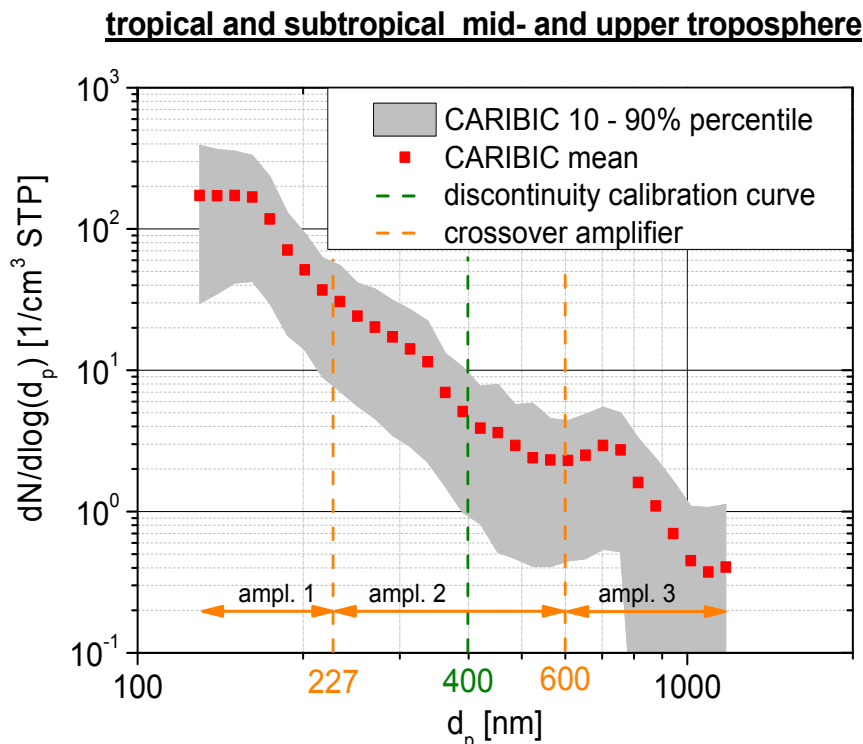
Figure 6.7: Particle size distribution for the tropical and subtropical MUT (same as Fig. 6.6c). The discontinuity of the calibration curve (green dashed line) is calculated to be at 400 nm (mid-latitude UTA calibration). The crossovers between the three amplifiers are calculated to be 227 nm and 600 nm, respectively (orange dashed lines).

6.1.4 Occurrence of secondary mode at ~700 nm

The comparison of the CARIBIC OPC data with published data in Sec. 6.1.3 shows the occurrence of a peak (mode) in the CARIBIC OPC particle size distribution at about 600 nm $<$ d_p $<$ 900 nm (Fig. 6.6). As this mode is observed within every region analyzed above, it raises the question whether it might be an artifact in the OPC data.

A discontinuity within the size calibration curve (Fig. 5.6 and the respective discussion) cannot be the reason for the 700 nm mode. The intersection of the two calibration curves is at ~400 nm (using the adapted fit function for UTA, Eq. 5.6). Figure 6.7 shows that the crossover between the two curves is located at a much smaller particle size (green dashed line) than the size of the mode. Moreover, the smooth crossover between the two power functions cannot cause any discontinuity.

As already described in Sec. 4.1 and 5.1, the scattering signal of KS-93 is amplified by three different linear amplifiers. The crossovers between the amplifiers (yellow dashed lines in Fig. 6.7) are calculated to be at 227 nm and 600 nm for the same calibration used to derive the ambient particles size distributions. The crossover between amplifier 1 and 2 seems not to affect the slope of the particle size distribution. However, the crossover of amplifier 2 to 3 is located at the lower end of the 700 nm mode. The third amplifier could cause the 700 nm mode due to a lower amplification of the scattering signal of large particles (d_p > 900 nm) compared to the amplification of smaller particles (600 nm $<$ d_p < 900 nm). The larger particles would then be seen smaller and thus added to the size channels 600 nm $<$ d_p < 900 nm. During
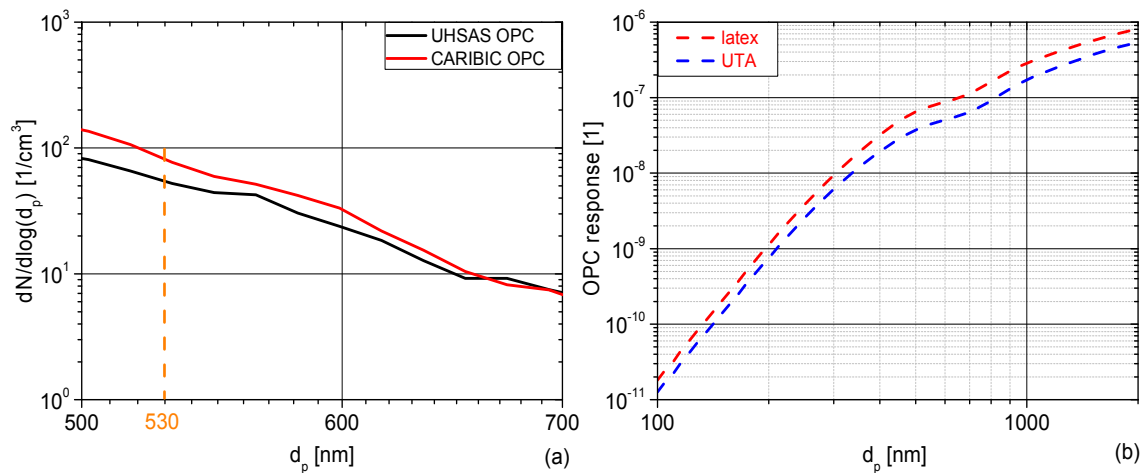
Figure 6.8: Comparison of an ambient (laboratory) air particle size distribution (a) measured with the CARIBIC OPC unit (red) and the Ultra High Sensitive Aerosol Spectrometer (UHSAS, black), both OPCs were calibrated for polystyrene latex (m = 1.59 – 0.0 · i). The CARIBIC OPC crossover between the second and the third amplifier was calculated to be 530 nm. The KS-93 theoretical response function for mid-latitude UTA (m = 1.48 – 0.0143 · i) and latex is indicated in (b).

characterization experiments in the laboratory the CARIBIC OPC unit was compared with an Ultra High Sensitive Aerosol Spectrometer (UHSAS, Droplet Measurement Technologies DMT) operated in parallel. For the comparison both OPC units measured ambient air and used a polystyrene latex calibration. Figure 6.8a shows the particle size distribution for the crossover size range between the second and the third amplifier of the CARIBIC OPC unit. From the latex calibration the crossover was calculated to be at 530 nm. Obviously, neither the CARIBIC OPC, nor the UHSAS OPC shows a peak (mode) within the displayed size range. Consequently, the observed mode in the UT/LMS particle size distributions is most likely no artifact caused by the crossover between the second and the third amplifier.

The KS-93 theoretical response function (Sec. 4.1) for UTA and polystyrene latex shows a small dip in the size range 600 nm < d_p < 900 nm for both materials (Fig. 6.8b). If this dip were responsible for the 700 nm mode in the UT/LMS size distributions (Fig. 6.6), this mode should also be present in the ambient air measurements (Fig. 6.8a). But the CARIBIC OPC data follow the UHSAS data without any additional mode. With the UTA calibration for the ambient air measurement the CARIBIC particle size distribution was slightly shifted to larger particle size but no additional mode was seen (not shown). Thus it is concluded that the dip in the theoretical response function also does not produce the additional mode in the UT/LMS size distributions. Nevertheless, future size calibrations should include more measurement points in the size range 500 nm < dp < 1000 nm (cf. Fig. 5.6).

The use of a uniform complex refractive index for all size channels might also cause an additional mode[24]. But then the mode should also be apparent in the published

---

[24] If the large particles (d_p > upper limit of discussed mode) would have a smaller real part or a larger imaginary part compared to smaller particles (d_p < upper limit of discussed mode), the intensity of the scattered light would be reduced. If so, those large particles would be seen somewhat smaller when using the UTA calibration for the whole size distribution. Therefore the underestimated particles would be counted additionally at smaller OPC size channels, causing the secondary mode at ~600 nm < d_p < 900 nm.

data, since these data were determined with optical methods and uniform refractive indices too. As the mode was not observed in the presented data, the use of a uniform refractive index for all size channels also cannot explain the occurrence of the mode.

So far several possible instrumental reasons were eliminated as the cause of the mode at ~ 600 nm $< d_p < 900$ nm, observed in all analyzed atmospheric regions. At the moment it is not clear whether this mode is real or an artifact caused by the OPC optics, data acquisition, or data analysis. As no reference is available for the in-flight measurements, it cannot be corrected. Consequently, this mode will be not discussed later in this work and is left over for future calibration work.

6.2   Case study results

6.2.1 CARIBIC volcanic ash flights (VAF)

In April 2010, Lufthansa approached the CARIBIC team with the request of conducting dedicated measurement flights to investigate the Eyjafjallajökull volcano plume, which was responsible for closing parts of the European airspace at that time. The results of these flights are presented in this section and are published [Rauthe-Schöch et al., 2012]. While the leading author of this publication is Dr. Armin Rauthe-Schöch from MPI-Chemistry, Mainz, the author of this thesis is first co-author, responsible for the OPC data and related sections. Hence, the following text is partly taken from that paper.

On April 14, 2010 the south Icelandic volcano Eyjafjallajökull erupted first since 1823 and the explosive phase lasted until May 22, 2010 [Sigmundsson et al., 2010]. Due to the contact of the melt water from the overlying glacier with the hot magma, the strength and explosivity of the eruption was strongly increased (phreatomagmatic explosions). The high explosive force caused the production of unusually fine particles: about 50% − 70% of them were smaller than 100 μm [Sanderson, 2010], 20% smaller than 10 μm, and 7% smaller than 2.6 μm [Gíslason and Alfredsson, 2010] in ash samples collected close to the volcano. Because of their slow gravitational settling, the smallest ash particles ($< \sim$20 μm) were transported over long distances. Larger particles fell out closer to the volcano [Ginoux, 2003; Schumann et al., 2011]. Due to the prevailing weather situation[25], the ash plume was transported rapidly to Central Europe, strongly affecting aviation. Over Europe the ash plume was trapped by re-circulation processes and hence caused numerous flight cancellations [Gertisser, 2010; Flentje et al., 2010].

There was hardly any information about the ash plume after the airspace above Germany was closed for the first time. Thus Lufthansa approached the CARIBIC team for a dedicated volcano cloud measurement flight. With only two days of preparation, the first CARIBIC volcano flight took place on April 20, 2010 over northern Germany, the Baltic Sea and southern Sweden. This was the first deployment of the new OPC unit and the unit worked well producing good data. Two further VAFs were requested and carried out: on May, 16 over Ireland and the Irish Sea and on May, 19 over the

---

[25] A vertical extended high pressure system was located south of Iceland (Petersen, 2010).

Norwegian Sea. The OPC unit did not work during the second flight because of an error in the communication with the master computer. The error was quickly corrected and the OPC unit worked well again during the third VAF.

As the size resolving OPC detection range (125 nm < d_p < 1.06 μm; volcanic ash calibration) did not cover the volcanic ash particle size distribution (d_p < 20 nm to 100 μm; Ginoux, 2003; Sanderson, 2010; Schumann et al., 2011), quantitative data for the total particle mass concentration were not expected. The objective was to document the location and spatial extent of the ash plume and to compare it with the results from the forecast models.

Several ash dispersion forecast models were used when planning the flight track: from a) the Volcanic Ash Advisory Centre (VAAC) London, b) the UK MetOffice (VAAC model with finer concentration steps), c) the University of Cologne (EURAD), d) the Finnish Meteorological Institute (SILAM), and e) the Norwegian Institute for Air Research (web interface for FLEXPART dispersion model). In addition, satellite data for SO_2 were taken from GOME2 (http://sacs.aeronomie.be/nrt/index.php; last access 20.07.2014). Aerosol vertical profiles were obtained from the space LIDAR CALIPSO (http://www-calipso.larc.nasa.gov/products/; last access 20.07.2014). A more detailed description of the flight planning can be found in Rauthe-Schöch et al., [2012].

During the first VAF on April 19 2010, volcanic ash particles were encountered at ~3 km altitude over northern Germany and the Baltic Sea. LIDAR measurements indicate a mixing of the volcanic ash into the continental boundary layer for this altitude [Ansmann et al., 2011] and thus the observed increase at the OPC derived particle mass was characterized by a mixture of volcanic ash and boundary layer aerosol. Increased particle mass concentrations along the third VAF were also attributed to volcanic ash particles. Within this thesis only data of this most interesting third VAF are presented.

Figure 6.9a shows the flight track of that flight lasting ~7 h. The altitude of the aircraft is color-coded along the flight track. The aircraft flew over the Norwegian Sea to the region around 75 °N, 10 °E for which the dispersion models had forecast a volcanic ash plume with concentrations exceeding 4 mg/m³ of ash. The aircraft flew at normal cruise altitude (~12 km) during the transfer flight to the region of interest in order to save fuel. At 75 °N, 10 °E, the aircraft turned east, descended rapidly to 5200 m, and flew to 75 °N, 15 °E. During the eastward flight, the altitude was stepwise reduced from 5200 m to 3700 m. From there the aircraft turned south and climbed back to cruise altitude after leaving the forecasted area of the ash plume at 72 °N, 14 °E.

The OPC overview plots for this VAF are shown in Fig. 6.9b and c. Within the destination area strongly increased accumulation mode particle number and mass concentration were observed between 11:00 and 11:39 UTC (marked in yellow). The maximum values are 220 1/cm³ STP and 60 μg/m³ STP, respectively. At the same time two very short time CO peaks of up to 179 ppbv were observed (background ~120 ppbv). The O_3 concentration indicates no significant change along the whole low altitude flight between 10:21 UTC and 11:45 UTC. The aerosol elemental composition analysis (cf. Sec. 3.3) indicated strong volcanic influence for the particle probe taken between 11:12 UTC and 12:01 UTC. The elemental mass fractions were analyzed to be 2.3% iron (Fe), 9.7% silicon (Si), 0.9% calcium (Ca), and 0.27% titanium (Ti), whereas the non-volcanic samples during the three VAF consist of on average 0.4% Fe, 0.5% Si,
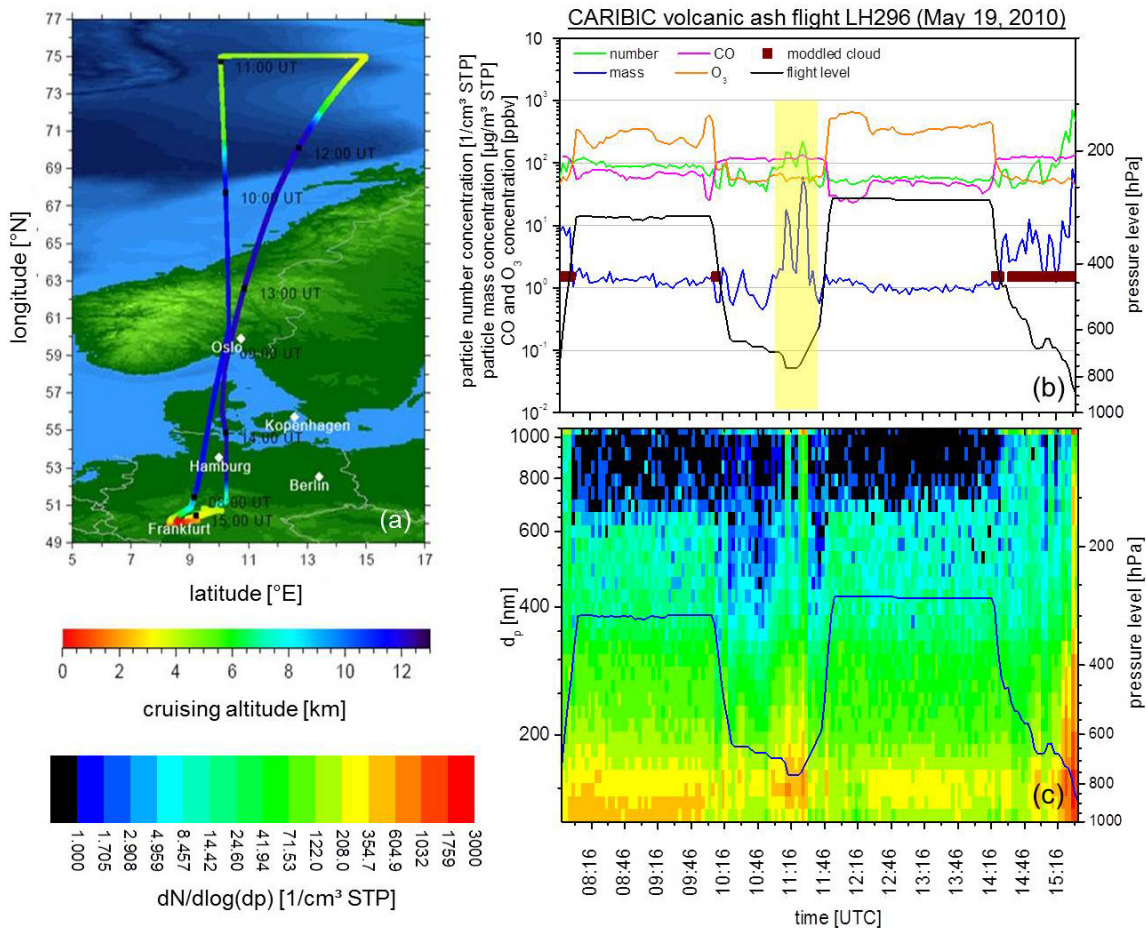
Figure 6.9: Overview of the third CARIBIC volcanic ash flight on May 19, 2010. The color code along the flight track (a) indicates the cruising altitude of the aircraft. Aerosol particle mass and accumulation mode particle number concentration, as well as CO and O_3 concentration along the flight track are shown in (b). The particle size distribution is shown in (c). The volcanic ash plume was encountered at 11:00 – 11:39 UTC and is highlighted in yellow.

0.15% Ca, and 0.03% Ti. Unfortunately the H_2O instrument did not work on the third VAF. However, the ECMWF data analysis suggests, the strong OPC signals were not caused by inside cloud measurements (cf. Sec. 6.1.2). The size resolving contour plot (Fig. 6.9c) indicates significant increased particle concentrations for all size channels between 11:00 and 11:39 UTC. As the dispersions models predicted the volcanic ash plume over the Norwegian Sea, the aerosol elemental analysis indicated volcanic ash, and other sources for accumulation mode particle plumes outside the boundary layer are rare in this region, it is very likely that the measured particle size distribution is dominated by volcanic ash particles. The high aerosol concentration during the holding pattern near Frankfurt (from 14:27 UTC until landing) was caused by the polluted air around the airport and inside cloud measurements.

To account for optical properties of the aerosol particles inside and outside the observed plume, for the VAF the OPC calibration was based on volcanic ash and ammonium sulfate (AS) optical properties, respectively (cf. Sec. 5.2.3). As the particle shape is unknown, the particles were assumed to be spherical. Data measured most likely inside the ash plume were processed using a complex refractive index of $m = 1.54 - 0.003 \cdot i$ and a particle density of $\rho = 2.65$ g/cm³, values within the range given by Schumann et al. [2011] for flights with the DLR Falcon. The AS calibration
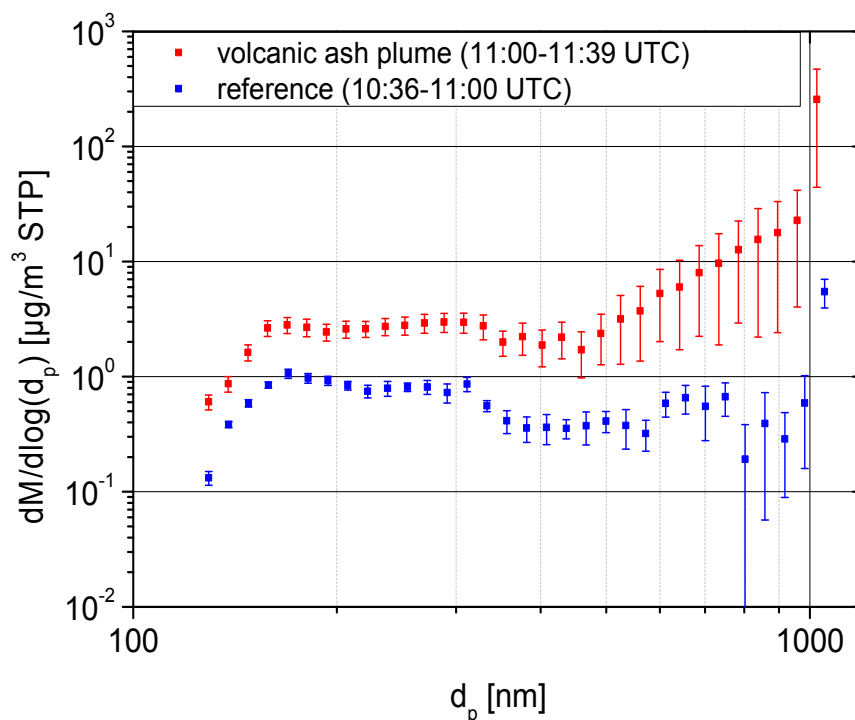
Figure 6.10: Particle mass size distribution inside (red) and outside (blue) the volcanic ash plume. The error bars indicate the one sigma standard deviation of the particle mass concentration within each size channel. This graph was also published in Rauthe-Schöch et al. [2012].

($m = 1.52 - 1.41 \cdot 10^{-7} \cdot i$, $\rho = 1.83$ g/cm³) was used for all other data, because the outside plume data (used as reference) were obtained at altitudes much lower than the normal CARIBIC cruise altitudes. Data from the transfer flights are not analyzed here. For the volcanic ash and the AS calibration, the upper detection limit of the OPC unit was calculated to be 1006 nm and 1009 nm, respectively.

Figure 6.10 shows the averaged particle mass size distribution obtained inside the ash plume (red). The averaged distribution obtained between 10:36 and 11:00 UTC is plotted as reference in blue. The error bars indicate the one sigma standard deviation from the averaged 13 three minute measurement intervals inside the plume and 8 outside the plume, respectively. Compared to the background air, the particle mass was substantially enhanced inside the ash plume for all particle size channels. The difference becomes more pronounced for particles larger than 450 nm. While in background air the mass distribution remains constant with increasing particle size, for the volcanic ash it increases strongly until the OPC upper detection limit. As already mentioned above, the Eyjafjallajökull plume was reported to contain even larger particles. Consequently, the true particle number and mass size distributions (Fig. 6.9c and 6.10) extend to much larger particle sizes. Particles larger than the upper OPC detection limit can pass the CARIBIC inlet system[26] and will be counted in the OPC uppermost size channel (cf. Fig. 6.10). Attributing these counts to larger "virtual" size channels, an "extended" total particle mass was estimated by A. Rauthe-Schöch (MPI-Chemistry, Mainz) as described in Rauthe-Schöch et al. [2012]. The "extended" particle mass calculation is used for a model intercomparison (see below).

---

[26] The justified estimate of the 50% inlet system sampling efficiency is ~5 µm in particle diameter.
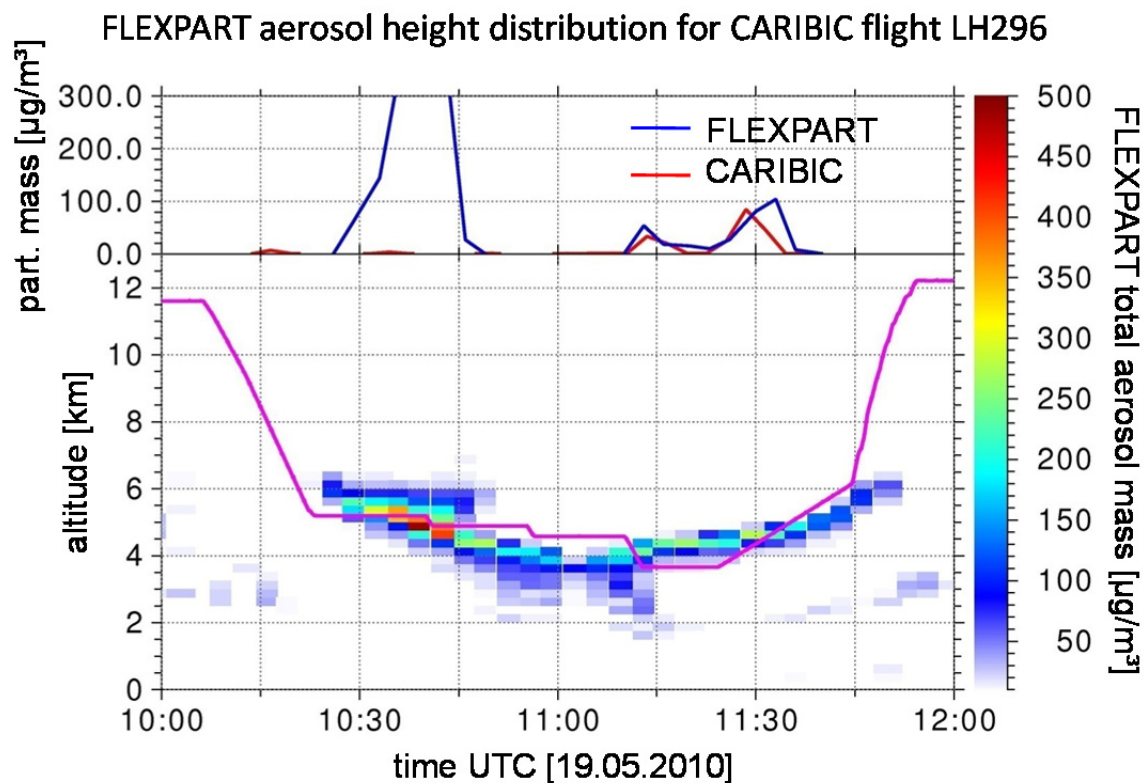
Figure 6.11: Comparison of the modeled and measured Eyjafjallajökull volcanic ash particle mass concentration along the third CARIBIC volcanic ash flight track. Modeled mass concentrations were calculated with the FLEXPART dispersion model, measured mass concentrations were obtained using the CARIBIC OPC data (upper graph). The lower graph shows vertical distribution of the FLEXPART total aerosol mass concentration along the flight track (solid magenta line). Concentrations are given at ambient conditions. This graph was taken from Rauthe-Schöch et al. [2012].

The integral particle mass was calculated along the flight track using the Lagrangian dispersion model FLEXPART (http://transport.nilu.no/flexpart; last access: 20.07.2014). The model itself, as well as the special model setup for the Eyjafjallajökull plume dispersion is described in detail in Stohl et al., [2005; 2011] and Rauthe-Schöch et al., [2012]. The particle density within the FLEXPART model was set to 3.0 g/cm³. To compare the particle mass directly to the OPC derived mass, the FLEXPART mass was decreased by 12 % to 2.65 g/cm³. The lower graph in Fig. 6.11 shows the FLEXPART volcanic ash concentration along the CARIBIC flight track between 10:00 UTC and 12:00 UTC (purple line). The color code indicates the total particle mass concentration originating from the Eyjafjallajökull eruption. The upper graph in Fig. 6.11 directly compares the "extended" OPC particle mass concentration (red) to the total FLEXPART particle mass concentration (blue) along the flight track. Please note that in Fig. 6.11 all concentrations are given at ambient conditions. While FLEXPART predicted huge amounts of volcanic ash between 10:35 and 10:45 UTC (up to 379 µg/m³), the OPC derived mass was only slightly increased to 3.2 µg/m³. Probably the plume was located somewhat differently from model predictions and the CARIBIC aircraft passed the plume only in the edge region. As such a plume causes a strong vertical gradient in the particle mass concentration, e.g. a slightly different emission height in the model initialization can lead to the observed huge difference. A strongly increased mass concentration was measured at 11:13 UTC and 11:28 UTC. For the peak
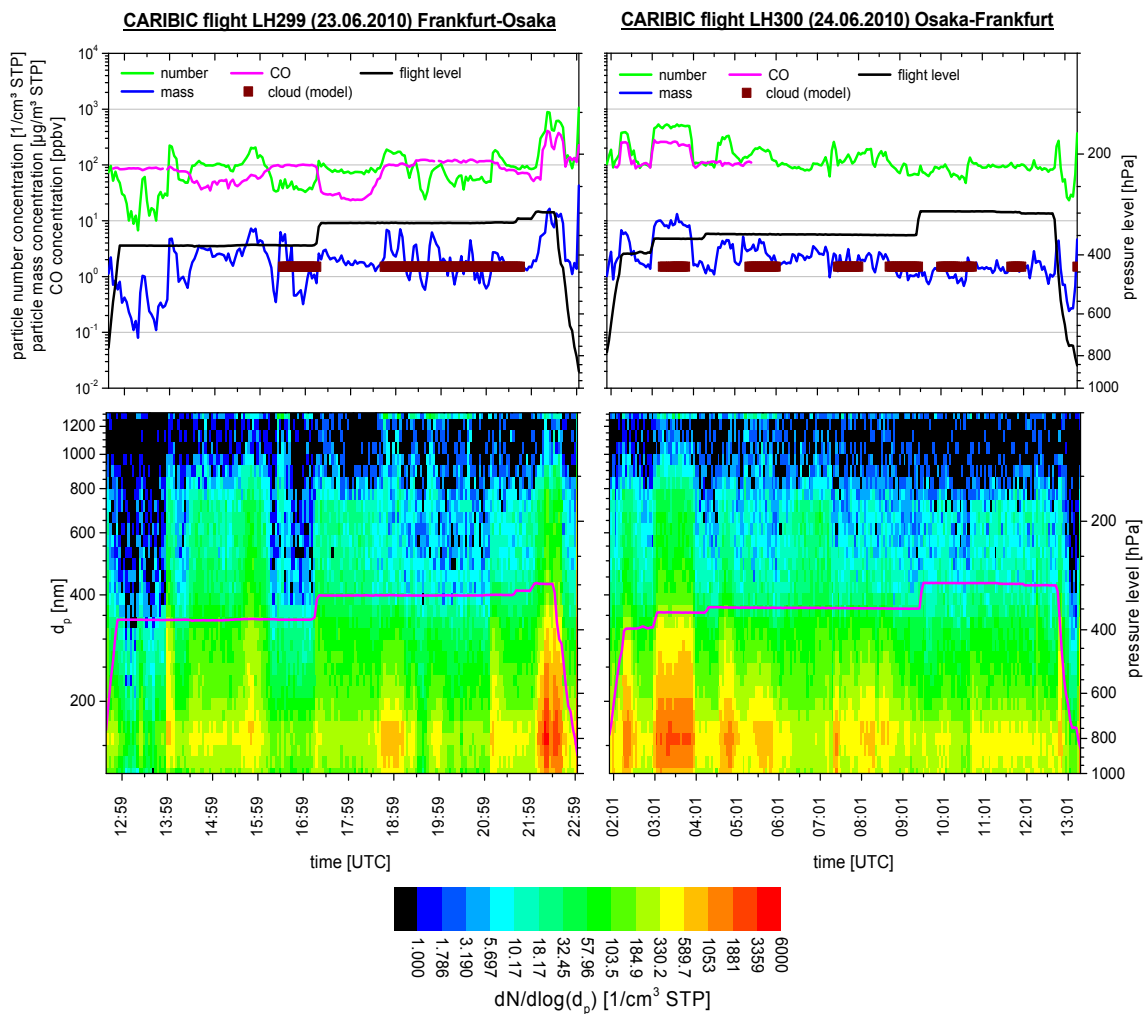
Figure 6.12: Overview plots for the CARIBIC flights LH299 from Frankfurt to Osaka on June, 23, 2010 (left) and LH300 back to Frankfurt on June, 24, 2010 (right).

at 11:13 UTC the FLEXPART mass was increased at the same time. For the later peak at 11:28 UTC the FLEXPART peak has a delay of 5 minutes or ~60 km (aircraft cruising speed ~190 m/s). Obviously, for these later plume crossings the modeled plume location was correct. The OPC "extended" mass concentration was calculated to be 35 µg/m³ for the first peak and 84 µg/m³ for the later one. The corresponding FLEXPART total mass concentrations are 54 µg/m³ and 104 µg/m³, providing a reasonable agreement to the measurements.

6.2.2 Pollution plume observed near Osaka

The trace gas data analysis presented in this section has been done by Dr. Tanja Schuck from MPI-Chemistry, Mainz. All analyses of aerosol data, trajectories, and satellite data have been done by the author of this thesis.

On June 23, 2010 the CARIBIC aircraft flew from Frankfurt to Osaka/Japan (flight LH299) and after three hours stay in Osaka back to Frankfurt (LH300). The highest OPC particle number and mass concentrations were observed before the landing (LH299) and after the takeoff (LH300) near Osaka (Fig. 6.12), accompanied by
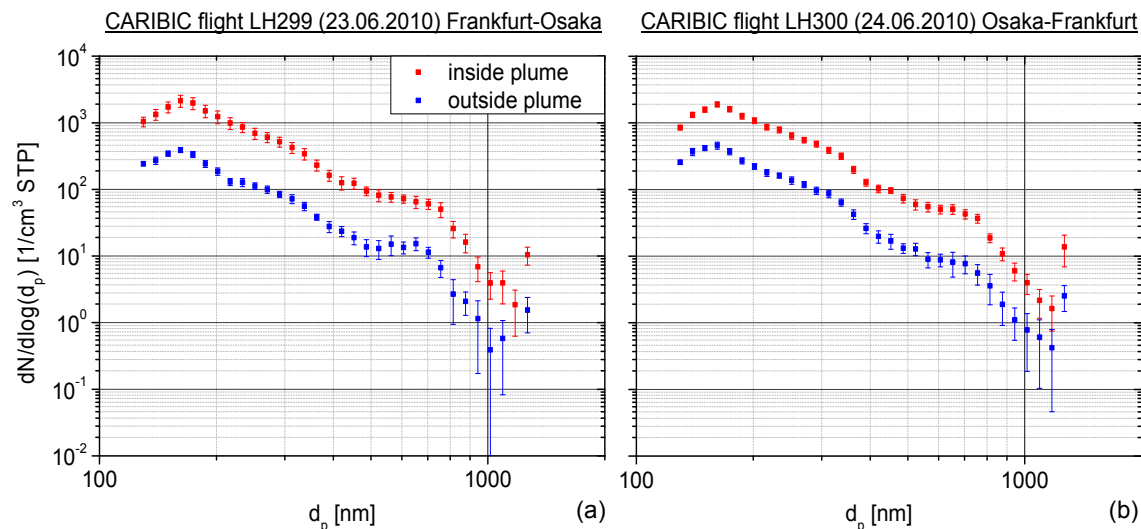
Figure 6.13: Averaged particle size distribution inside (red) and outside (blue) the pollution plume on flight LH299 (a) from Frankfurt to Osaka and LH300 (b) back to Frankfurt.

enhanced CO concentrations. The observed particle number and mass concentrations of up to 886 1/cm³ STP and 16.4 µg/m³ STP belong to the highest ones, recorded until LH344 with the CARIBIC OPC on all flight routes (except the CARIBIC VAF). Unfortunately for both flights no CWC and O_3 data are available. However, the ECMWF cloud data indicate that the strongly increased concentration between 22:07 and 22:43 UTC (LH299) was not caused by cloud artifacts. On flight LH300 the ECMWF data indicate cloud contacts between 13:15 and 13:51 UTC. Because the CO concentration was also significantly increased (up to 331 ppbv), it is assumed the strong OPC signals from 13:00 to 14:00 UTC were caused mainly by polluted air. Outside the Osaka region, the measured particle concentrations were at the atmospheric background concentration.

Figure 6.13 compares the particle size distribution inside the plume to reference periods just before or after the plume encountered. For flight LH299 (Fig. a), the inside plume measurements (red) were averaged between 22:10 and 22:43 UTC. Data obtained between 21:37 and 22:10 UTC were used as reference (blue). On flight LH300 the measurements obtained 30 minutes before and after the observed plume (02:30 to 03:00 UTC and 04:00 to 04:30 UTC) were averaged as reference (Fig. b). The error bars indicate the one sigma standard deviation. For both flights, the particle number concentration inside the plume was for nearly all size ranges about five to six times increased compared to the reference periods.

To illustrate the measurement locations Fig. 6.14 shows the integral OPC particle number concentration along the flight track of the aircraft. Red and blue arrows (plume/reference) indicate the measurement locations for the comparison in Fig. 6.13. On flight LH299 the plume was observed north-east of Osaka. On the flight back to Frankfurt (LH300) increased concentrations were observed west of Osaka at about 130°E. However, on LH300 a much wider plume with much higher particle concentrations was observed over the Yellow Sea, west of the Korean peninsula. To check whether the plume air, observed on flight LH299 has the same origin as the air analyzed four hours later over the Yellow Sea (LH300), KNMI backward trajectories are plotted in Fig. 6.14 too. The backward trajectories belonging to high concentration
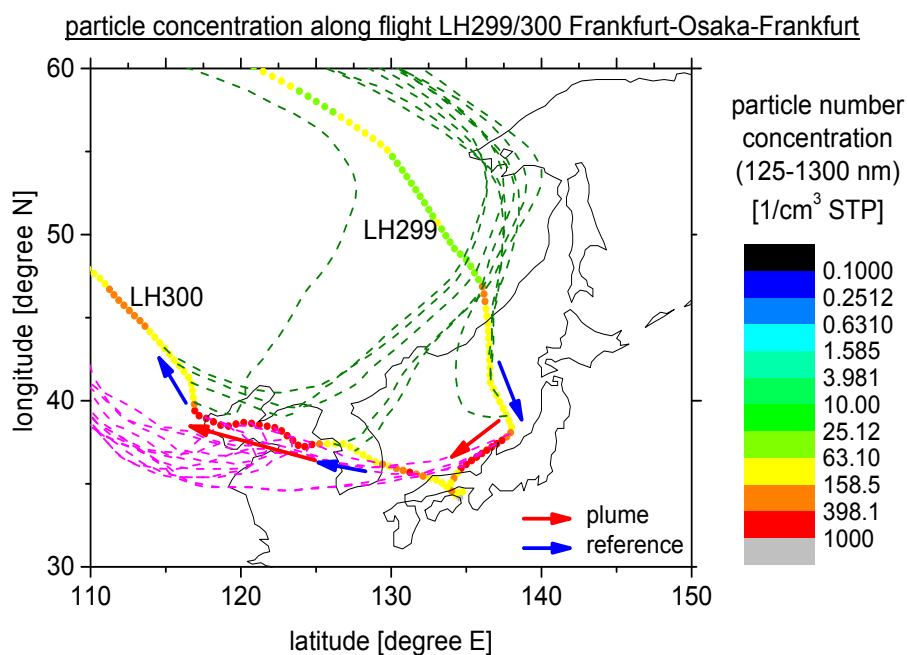
Figure 6.14: Particle concentration along flights LH299 and LH300 from Frankfurt to Osaka and back. The flight tracks around Osaka are indicated as dotted lines where the colour code gives the integral OPC particle number concentration. Red arrows indicate the location of the "inside plume" measurements, used for the comparison in Fig. 6.13. Blue arrows indicate the location of the "outside plume" measurements used as reference. Backward trajectories for the inside- and outside plume samples are indicated as magenta and olive dashed lines, respectively.

measurements (plume; red distributions in Fig. 6.13) are indicated as magenta dashed lines. The trajectories from the reference air (blue distributions) are plotted as olive dashed lines. Plume and reference air trajectories are shown only every 9 minutes along the aircraft flight track to maintain the readability of the figure. It is obvious that the polluted air passed eastern China during both flights whereas the reference air masses came from south-eastern Russia.

The concentration of CO, SF_6, and the CPC derived N_{12} particle number concentration (12 nm $<$ d_p) were also significantly increased inside the plume (Fig. 6.15). The CO concentrations inside the plume (upper panel) were 285 ppb on average and 500 ppb in maximum for flight LH299. For flight LH300 the numbers are 242 ppb and 331 ppb, respectively. The tropospheric background concentrations for the two regions were 114 ppb and 103 ppb during all previous CARIBIC measurements. Thus the CO concentration was increased by 150% and 135% in the plume. The NO_y concentration was on average increased by about 273% (LH299) and 166% (LH300) from 1.5 ppb to 5.6 and 4.0 ppb, respectively (not shown). One of the two air samples taken inside the plume on LH299, does indicate a strongly increased SF_6 (sulfur hexafluoride) concentration of 7.99 ppt, compared to the background of 7.11 ppt (Fig. 6.15). On flight LH300 all air samples inside the plume indicated significantly enhanced SF_6 concentrations of up to 7.62 ppt. Because SF_6 is produced mainly by industry, it is a very good tracer for industrial pollution. As the CO and the SF_6 concentrations are strongly increased, the plume probably originates from a mixture of combustion and non-combustion (industrial) sources.
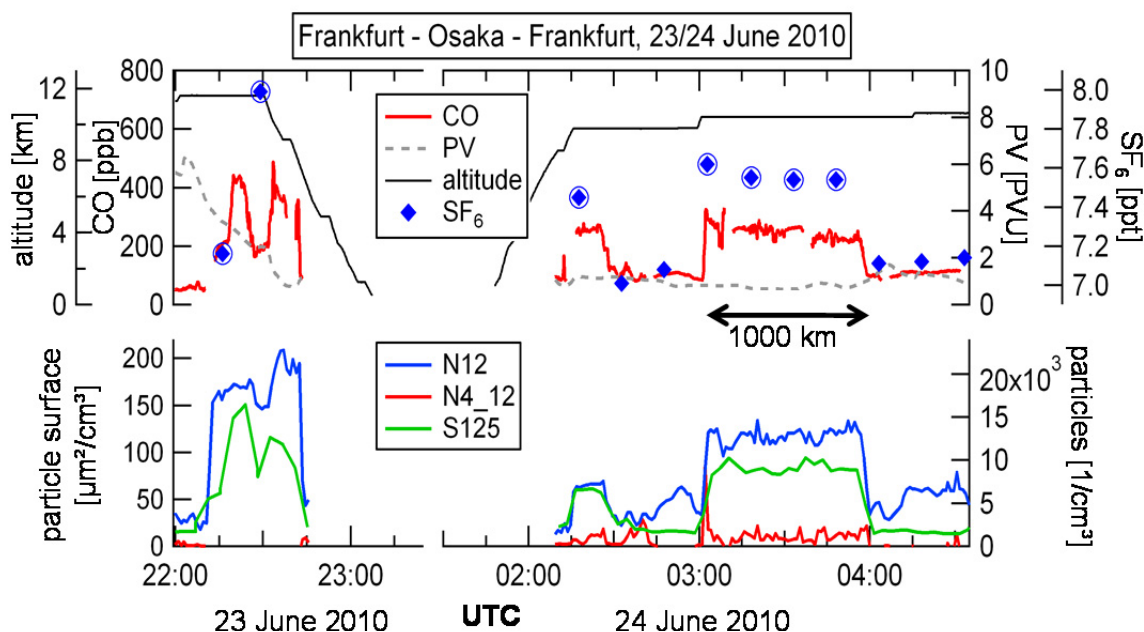
Figure 6.15: Overview of the CARIBIC measurements during the plume event on flight LH299 and LH300 from Frankfurt to Osaka/Japan and back. Figure by courtesy of T. Schuck, MPI-Chemistry, Mainz, Germany.

On June 23 2010, nearly no nucleation mode particles were observed (N4_12, lower panel of Fig. 6.15). This indicates no recent particle formation has taken place inside the plume. The strongly increased OPC derived total particle surface (S125) suggests that particle precursor gases preferentially condensed on existing particle surface instead of forming new particles. On the contrary to N4_12, the concentration of particles larger than 12 nm (N12) was strongly increased, indicating again strongly polluted air. However, on flight LH300 also N4_12 was somewhat increased, indicating weak particle formation inside the plume. This difference is remarkable, because on flight LH299 the averaged particle surface concentration inside the plume was only 11 % higher compared to LH300 (27.86 µm²/cm³ vs. 25.06 µm²/cm³). Higher precursor gas concentrations leading to an increased particle formation rate during LH300 might be a possible explanation for the occurrence of nucleation mode particles. Unfortunately, this assumption can be not proved because the CARIBIC system does not measure any particle precursor gas concentration.

The total gaseous mercury concentration (TGM, not shown) was also significantly increased inside the plumes. On both flights the averaged inside plume concentration was enhanced by about 70%[27] to 2.4 ng/m³ STP. Inside the plumes the concentrations are comparable to the mean concentration of 2.6 ng/m³ STP, found in the marine boundary layer over the Yellow Sea [Ci et al., 2011]. This might be an indication for convective uplifting of polluted air in coastal areas. The emission ratio $\Delta Hg/\Delta CO$ of 5.0 pg/m³/ppb (or $5.6 \cdot 10^{-7}$ ppb/ppb) is higher than reported by Ebinghaus et al. [2007 and references therein] for pure biomass burning plumes but is similar to emission ratios found in mixed Asian outflow [Slemr et al., 2009 and references therein].

---

[27] TGM free tropospheric background: 1.4 ng/m³ STP

MODIS fire counts (20 to 24 June, 2010)
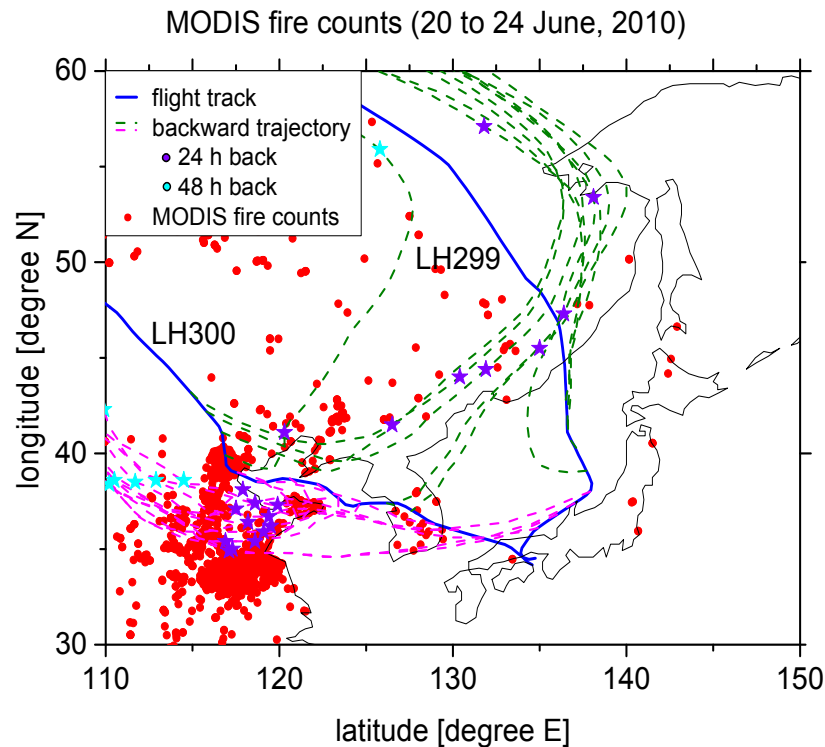
Figure 6.16: MODIS fire counts from June 20 to 24, 2010 in eastern Asia (red dots). The aircraft flight tracks for flight LH299 and LH300 from Frankfurt to Osaka and back are indicated as solid blue lines. Backward trajectories are indicated as dashed lines in magenta (plume) and olive (background). The position of the trajectories 24 and 48 hours back in time are illustrated as violet and light blue stars, respectively.

The CO concentration correlates in the plumes with methyl chloride (CH_3Cl, not shown), which is a good tracer for biomass burning. The simultaneous enhancement of SF_6 and non-methane hydrocarbons[28] (NMHCs, not shown), suggests that the polluted air masses originate from a region with a variety of pollution sources or that already polluted air from an industrial region passed a region with biomass burning activity.

Figure 6.16 shows the East Asian burning activity for June 20 to 24, 2011 as detected by the MODIS Rapid Response System [Davies et al., 2009; Justice et al., 2002] (FIRMS web fire archive http://firefly.geog.umd.edu/firms/ access 15.11.2012). Intensive burning activity was found south of Beijing and north of Shanghai. Streets et al. [2003] and Ohara et al., [2007] showed that eastern China - a highly industrialized and densely populated area - is a region with high anthropogenic emissions of CO, NO_x and NMHC. Hence the increased SF_6, and NMHC concentration originates most likely from local industry. The trajectory analysis indicates, the plume air passed the above described region about one to two days before measurement (Fig. 6.16). Because the air passed in about 350 hPa (~ 8.2 km), probably small scale convection (not captured by the trajectory model) lifted the pollutants to the trajectory level (see discussion to Fig. 6.17). The KNMI meteorological analyses indicate a small low pressure system in the region of interest (www.knmi.nl/samenw/campaign_support/CARIBIC/240610 /mapZ10062406L250.gif last access 20.07.2014).

---

[28] Tracer for biomass- and biofuel burning
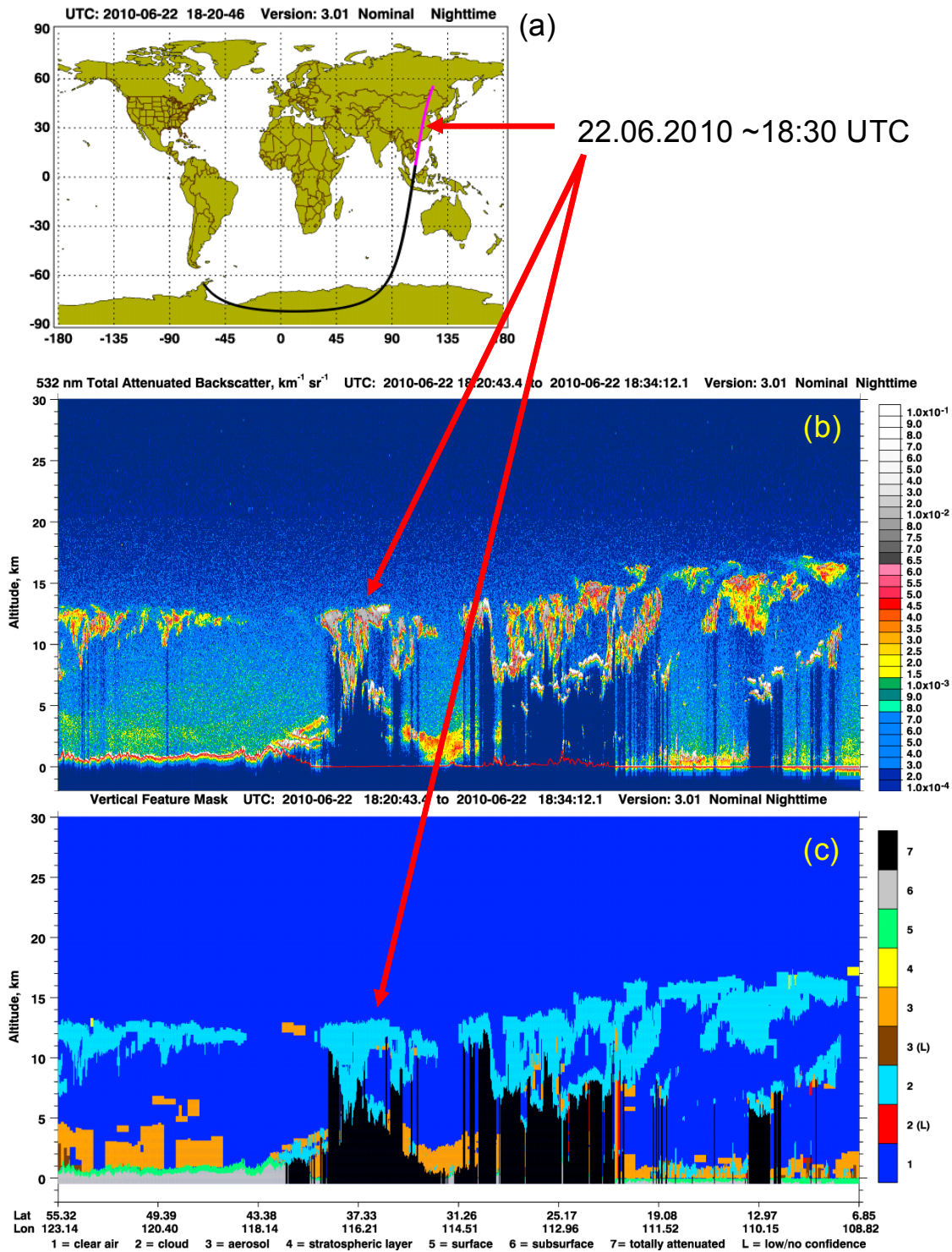
Figure 6.17: CALIPSO space LIDAR CALIOP level 1 data analysis product (http://www-calipso.larc.nasa.gov/products/ last access 20.07.2014) for June 22, 2010. Between 18:20:43 and 18:34:12 UTC the satellite passed east China from north-east to south-west (a; magenta marked track). The "532 nm Total Attenuated Backscatter" signal (b) indicates different vertical layers along the flight track. The "Vertical Feature Mask" analysis product (c) further provides an aerosol- cloud differentiation (explanation of colors given below the time line).

On June, 22 between 18:20 and 18:34 UTC the CALIPSO satellite (Cloud-Aerosol Lidar and Infrared Pathfinder Satellite Observation; http://www-calipso.larc.nasa.gov/ last access 20.07.2014) with the space LIDAR CALIOP (Cloud-Aerosol Lidar with Orthogonal Polarization) on board passed eastern China from north to south

(Fig. 6.17a), at nearly the same time as the air mass of interest (backward trajectories) were at this position. At 116°E, 37°N a strong deep convective cloud was observed by CALIOP (Fig. 6.17b). The CALIPSO "Vertical Feature Mask" product (Fig. 6.17c) indicates this cloud system to lift aerosol from the surface layer up to the cloud top (orange layer). All these observations strongly support the assumption that biomass burning and the industry in the region south of Beijing and north of Shanghai were the source for the observed plume.

In general, this finding emphasizes that deep convection of pollutants from the boundary layer into the UT region is an important transport process. However, the global contribution of such extreme events to the UT/LS aerosol budget is unknown and needs better statistics to be well addressed. Similar pollution events were observed over eastern Asia in May 2009 with the CARIBIC aircraft and in spring and early summer 2003 with MOZAIC measurements [Nedelec et al., 2005]. In future, CARIBIC will help to estimate the frequency and thus the global relevance of such extreme events.

6.2.3 Mass closure study

Besides in situ particle number concentration measurements, aerosol particles are collected on impactor foils during the CARIBIC flights for post-flight elemental analysis by Bengt Martinssons group at Lund University, Sweden [Nguyen et al., 2006; Breninkmeijer et al., 2007]. As the used methods (PIXE and PESA, cf. Sec. 3.3) can detect the majority of relevant elements, the sum of all elemental masses should yield the total particle mass concentration. This mass can be compared to the particle mass concentration derived from the OPC measured particle size distribution. It should be noted already at the beginning that because of the different measurement techniques and the associated uncertainties an agreement within a factor of two or three must already be considered reasonable. This work thus reports only a first attempt for a mass closure along one measurement flight with less variable conditions. Recently (August 2014), a more detailed mass closure study was published by Martinsson, et al., [2014]. The results of this later study are not part of this thesis.

For the comparison in this work the data from measurement flight LH312 are used. During this flight from Osaka to Frankfurt on September 24, 2010, the aircraft flew in stratospheric air for the whole flight (Fig. 6.18). The O_3 concentration was above 200 ppbv for nearly all the time (average 286 ppbv), clearly indicating stratospheric air [Zahn and Brenninkmeijer, 2003]. The CO concentration was mostly below 50 ppbv (average 39 ppbv). Only after takeoff and before landing the aircraft passed cloudy air. Inside the stratospheric air the OPC integral particle number concentration, the particle mass, as well as the shape of the particle size distribution were nearly constant. Even flight level changes (at 08:22 and 09:49 UTC) lead only to minor changes (cf. Fig. 6.18).

Six particle samples were taken consecutively between 01:22 UTC and 11:25 UTC along this flight (numbered red line sections in Fig. 6.18, 100 min each). As the samples were collected inside stratospheric air, for the presented analysis the LSA
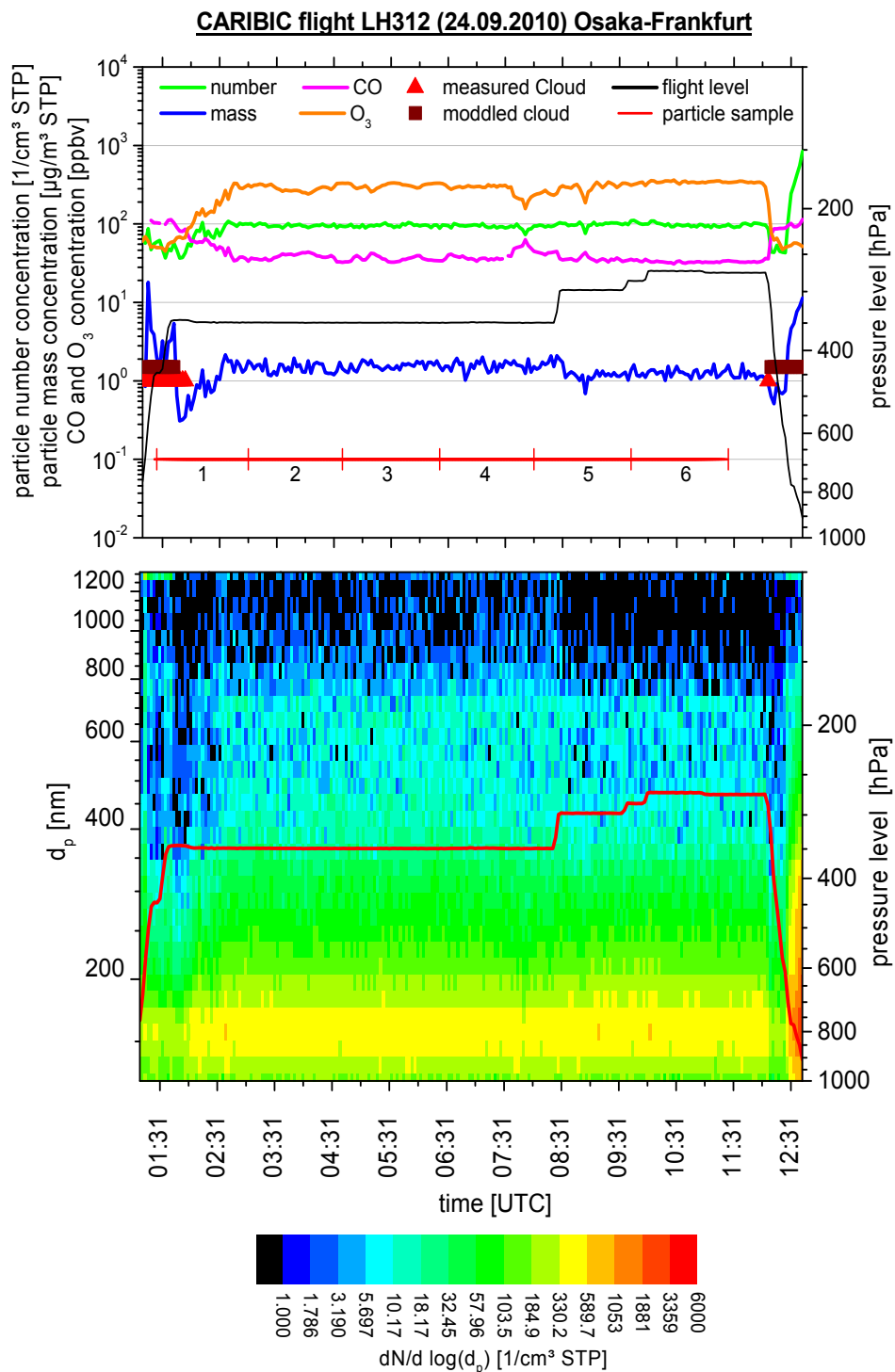
Figure 6.18: Overview plots for CARIBIC flight LH312 from Osaka to Frankfurt on September 24, 2010. The sampling times of the six particle samples (100 min each) are marked as red line and numbered from one to six.

calibration was used (cf. 5.2.3; $m_{c,total} = 1.43 - 0.0001 \cdot i$, $\rho = 1.72$ g/cm³). The impactor collects particles smaller than 2 μm diameter [Nguyen and Martinsson, 2007] but no information about size of the collected particles can be given. The resulting total impactor particle mass thus cannot be corrected for particle losses inside the inlet system. Consequently, the OPC data were also not corrected for inlet system particle losses. The upper cut-off diameter of the impactor samples is about 2 μm, i.e ~0.65 μm above the OPC upper detection limit (1.35 μm for LSA calibration). The OPC can count
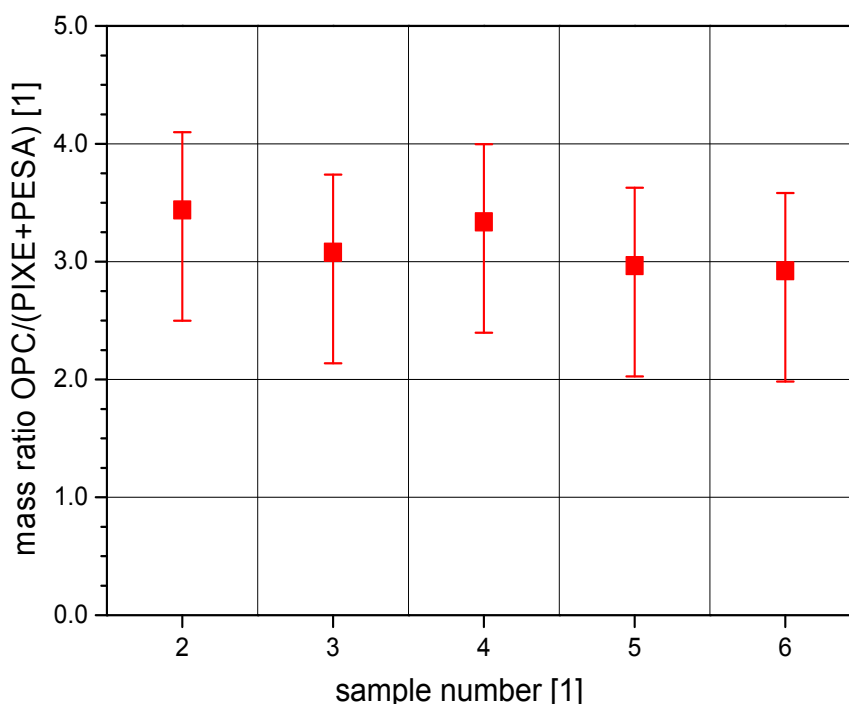
Figure 6.19: Ratio of the particle mass concentrations from the OPC analysis to the impactor masses along flight LH312 from Osaka to Frankfurt on September 24, 2010. The impactor sample particle mass concentration was derived by summing up the individual masses of all analyzed elemental materials from the PIXE and PESA analysis.

even larger particles than the particle sample cut-off[29] in uppermost size channel. During LH312 the contribution of the uppermost size channel to the total particle mass was about 12%[30]. The OPC dataset was averaged for the impactor sampling intervals. As the first particle sample was collected partly inside clouds (red triangles in Fig. 6.18), those data were not analyzed.

Figure 6.19 shows the ratio of the OPC-derived particle mass to the PESA+PIXE-derived particle mass. The mass ratio is between 2.9 and 3.4. On average (mean) the OPC derived particle mass is about 220% larger than the impactor mass[31]. However, one would expect a mass ratio below one because the OPC upper particle size detection limit is below the impactor limit. Even if the PIXE+PESA analysis is assumed to detect all important elements contributing to the total particle mass, this result does not automatically suggest that the OPC overestimates atmospheric particle mass. While the OPC based method is an online analysis[32], the impactor samples are analyzed in vacuum several weeks after the measurement flight. Thus volatile compounds (e.g. organics) may evaporate from the samples during the storage and analysis. The OPC might thus see larger particles with higher particle mass. As the stratospheric aerosol

---

[29] Justified estimate of the 50% inlet system sampling efficiency is ~5 μm particle diameter. RION gives 2 μm as the OPC upper detection limit for polystyrene latex

[30] For all counts in the uppermost size channel the particle mass was calculated, using the channel middle d_p (1301 nm).

[31] A ratio of 1 means the derived mass concentrations are equal. Therefore a ratio of 3.2 indicates the OPC derived particle mass is 220% larger than the impactor derived particle mass.

[32] The particle scattering signal is measured directly after sampling, having only the sampling line delay of ~0.65 s.

particles usually do not contain much organics (cf. Tab. 5.3 and related discussion), it is assumed that the evaporation of volatile compounds from the impactor samples would cause not more than 10% difference.

Table 6.3 and the associated discussion showed that at the end of the sampling line not all water has evaporated from the particles and the OPC measurements do represent $d_{p,wet}$ – at OPC. Due to the long storage and the vacuum analysis it is assumed the impactor samples do represent dry aerosol ($d_{p,dry}$ – at OPC). The 18% difference in d_p would cause another ~66% difference in the particle mass.

Spherical particles with a uniform complex refractive index and a uniform particle density are assumed in the estimation of the particle mass from OPC data. The uncertainty from this assumption, including uncertainties for particle sizing, the gas flow, and the OPC counting efficiency (Sec. 5.3.3) would explain a maximum OPC mass overestimation of about 33%. In addition, the detection limits of the two measurement methods are based on different physical principles. Whereas the impactor samples particles by their aerodynamic size[33], the particle sizing by the OPC is based on light scattering. Aerodynamic and optical particle diameters are difficult to convert to each other and thus the related uncertainties cannot be estimated here. The influence of the assumed calibration material (calibration curve and density of LSA vs. UTA and MTA) causes an uncertainty of about 20 % for LSA vs. UTA and 35 % for LSA vs. MTA. The values are calculated, using the same OPC response signal for the different calibration curves and particle densities. Both numbers indicate that the given OPC particle mass would be 20 % and 35 % higher if the true aerosol were not LSA, but UTA or MTA.

The biggest source of uncertainty for the OPC is the assumption of spherical particles. If a non-spherical particle passes the laser beam, the OPC measured particle diameter could be smaller or larger than the true (effective) particle diameter. The OPC detected size for a certain, non-spherical particle depends on the particle orientation inside the laser beam. For example, if a particle two times longer than wide passes the laser beam with the long side perpendicular to the beam, the effective particle diameter would be 50 % larger than the measured one. Because the particle volume and thus the particle mass depend on the diameter to the power of 3, the resulting mass would be 237 % higher than the analyzed one. However, by averaging for long periods, the shape error should be cancelled. Only if not spherical particles becomes systematically orientated inside the OPC optics (e.g. due to the aerodynamic focusing), the error would be still present. On the other hand, due to their long lifetime, stratospheric aerosol particles are assumed to be more or less spherical. Hence, also the shape error cannot explain the discrepancy between the OPC and the impactor derived particle mass concentration.

Finally, it is not clear which detection method give the correct mass concentration. As more assumptions are necessary for the OPC method, its uncertainty is higher. A combination of all above discussed uncertainties might explain a

---

[33] The aerodynamic particle size is based on the principle of the particle inertia in an air stream.

discrepancy of 94%[34] (except the not quantified disagreement between optical and aerodynamic particle diameter and the assumption of spherical particles). Consequently, further analyses are necessary to understand the 220% difference.

6.3 Size distribution statistics

CARIBIC measurements are carried out regularly, usually once per month along four intercontinental flights, making statistical analyses of temporal and spatial distributions possible. As within this work only OPC data from the first year of regular operation until LH344 (May 2011) are used, here only a limited analysis of the accumulation mode particle size distribution can be made. These analyses include vertical profiles relative to the tropopause, a comparison between the mid-latitude UT and LMS, a stratospheric seasonality analysis, as well as the meridional distribution over Africa. The results presented below do not claim to be statistically perfectly constrained. Rather the given examples shall provide an impression, what unique kind of analysis will become possible after a few years of measurement. Only CARIBIC measures the particle size distribution plus additional tracers in the UT/LMS region regularly and therefore provides the opportunity for detailed statistical analyses.

The CARIBIC aircraft is flying at a rather constant altitude between 9 and 12 km. Therefore vertical profiles relative to the TP are derived by the up and down moving air masses, i.e. the different TP altitudes relative to the flight altitude. For this analysis all mid-latitude outside-cloud measurements[35] were sorted into 1.0 wide PVU bins and the bin data were averaged. Measurements above 8 PVU are not considered because they are too rare for statistical purposes.

Figure 6.20a shows how the mid-latitude particle size distribution changes from the UT through the TP into the LMS. Different to the "flight overview" contour plot (e.g. Fig. 6.3) the particle size is displayed at the x-axis. The color code indicates again the number concentration in each particle size bin. The y-axis indicates the PV. The TP is located at PVU values between 1.6 and 3.5 (Sec. 2.2). Due to the increasing fraction of stratospheric air with increasing PV, the CO concentration (blue squares) decrease while the ozone concentration (brown squares) increase. At the PV bin 7-8 PVU the average potential temperature Θ is 345 K, which is still inside the mid-latitude LMS (cf. Fig. 2.2).

The contour plot shows that for nearly all size channels the particle concentration increased with increasing PV. Only for particles larger than 900 nm no vertical gradient seems to be apparent for the whole altitude range. The bin averaged integral particle number and mass concentrations emphasize this behavior (Fig. 6.20b).

---

[34] PIXE/PESA: 10%, evaporation of volatile compounds: 10%, difference $d_{p,wet}$ to $d_{p,dry}$ at the end of the sampling line: 60%, OPC maximum mass uncertainty: 33%, refractive index and density LSA vs. MTA: 35%; total uncertainty $= \sqrt{10^2 + 10^2 + 66^2 + 33^2 + 35^2} = 94\%$

[35] 3189 of the 5681 outside cloud measurements were obtained north of 40°N.
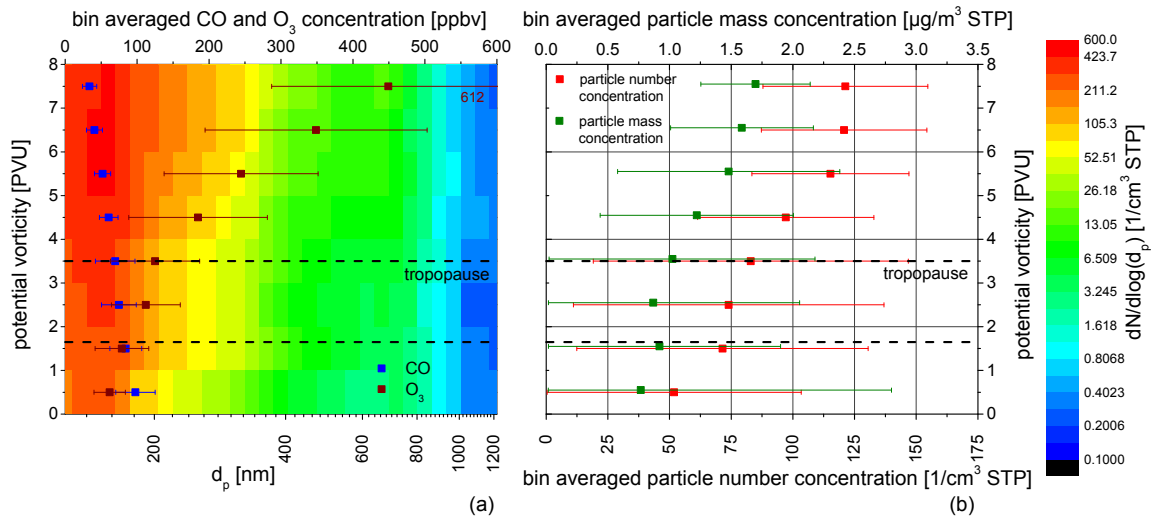
Figure 6.20: Vertical variation of the particle size distribution from the UT through the tropopause into the LMS (a). While the color code indicates the particle number concentration, CO and ozone concentrations are given as blue and brown squares. The OPC derived integral particle number and particle mass concentration is plotted against the PV in (b). All measurements were averaged for 1.0 PVU bins. In both figures the error bars indicate the one sigma standard deviation. The tropopause (1.6 < PV < 3.5) is indicated between the dashed lines.

The number concentration increased with increasing PV from 52 1/cm³ STP at 0.5 PVU to 121 1/cm³ STP at 7.5 PVU. The mass concentration increased from 0.8 to 1.7 µg/m³ STP.

The observed particle (and trace gas) gradients can be explained with the increasing fraction of stratospheric air with increasing PV and the longer life time of stratospheric particles compared to UT particles [Menzies and Tratt, 1995; Rasch et al., 2008]. Inside the UT accumulation mode particles are effectively removed by activation to cloud droplets and following wet deposition. In absence of clouds, which are less frequent in the LMS, the most important particle sink process is sedimentation and downwelling STE (Sec. 2.2 and 2.3; SPARC report N°4, [2006]). The sedimentation velocity depends on the particle weight and therefore on the particle size. Due to the low sedimentation velocity inside the LMS, accumulation mode particles have the longest lifetime (half a year or even longer; Sec. 2.3). In addition, new accumulation mode particles are formed by injection of Aitken mode particles into the tropical stratosphere [Brock et al., 1995], followed by condensational growth of these particles during transport from the tropics to mid-latitudes via the Brewer-Dobson circulation.

To better visualize the difference in the particle size distribution of mid-latitude UT air compared to mid-latitude LMS air, in Fig. 6.21 the averaged mid-latitude tropospheric measurements (latitude > 40°N, PV < 1 PVU, n = 461) and the mid-latitude stratospheric measurements (latitude > 40°N, PV > 3.5 PVU, n = 2155) are compared. As indicated in Fig. 6.20, for all size channels smaller than 900 nm the LMS particle concentration was up to 250% higher (average 120%) than in the UT. This finding was already suggested by the contour overview plot (Fig. 6.3) in the introduction to this chapter. The homogeneous structure inside the LMS (Fig. 6.3) is
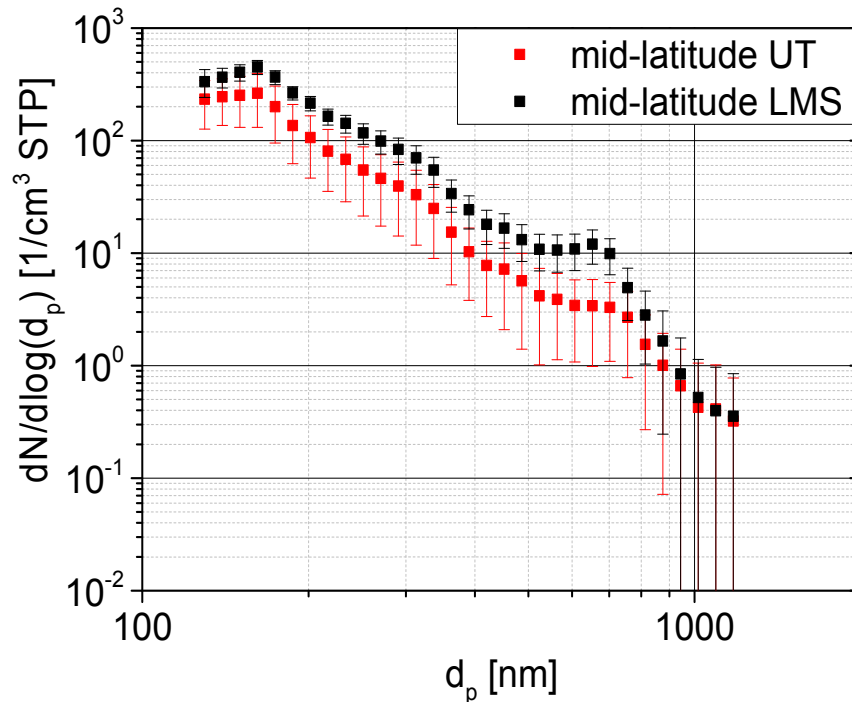
Figure 6.21: Comparison of the averaged particle size distribution of mid-latitude UT and mid-latitude LMS air. The air masses were classified by latitude and potential vorticity (both given in Tab. 6.2). Error bars indicate the one sigma standard deviation.

representative for all CARIBIC LMS measurements. Nearly all OPC derived LMS integral particle number concentrations and particle size distributions are similar to those shown in Fig. 6.2 and 6.3.

The error bars in Fig. 6.21 again represent one sigma standard deviation and are a measure for the variability of the concentration. For the UT particle size distribution the variability is about twice the variability in the LMS. This higher variability was probably caused by the stronger seasonality and the cloud sink in the UT. From June 2010 to May 2011 CARIBIC measurement flights were carried out along four intercontinental flight routes (cf. Fig. 6.1). The flight routes cross different regions with seasonal depending upwelling and downwelling STE (Škerlak et al., 2014). Unfortunately the CARIBIC aircraft did not fly year around on all four routes, making a seasonality analysis for the reduced data set difficult. In fact, with the one year dataset only for the mid-latitude LMS a first approach for a seasonal analysis is reasonable. As already described in Sec. 2.2, the upwelling air motion from the troposphere into the stratosphere in the northern hemisphere is most effective in late summer, fall, and early winter and smallest in late winter, spring, and early summer [Seo and Bowman, 2001; Škerlak et al., 2014]. Therefore the northern hemispheric mid-latitude stratospheric dataset was further split into measurements periods from March to July ("spring", n = 1051) and from September to January ("fall", n = 537).

Nearly no seasonal difference was observed for particles smaller than 230 nm (Fig. 6.22). On the contrary, for larger particles ($d_p > 230$ nm), the spring time concentrations were up to 190% higher than the fall time concentrations (average 120%). This seasonality reflects the troposphere to stratosphere air transport. In fall the transport of UT air into the LMS is most effective and therefore the fraction of UT air in the LMS is (much) higher than in spring [Seo and Bowman, 2001; Škerlak et al., 2014].
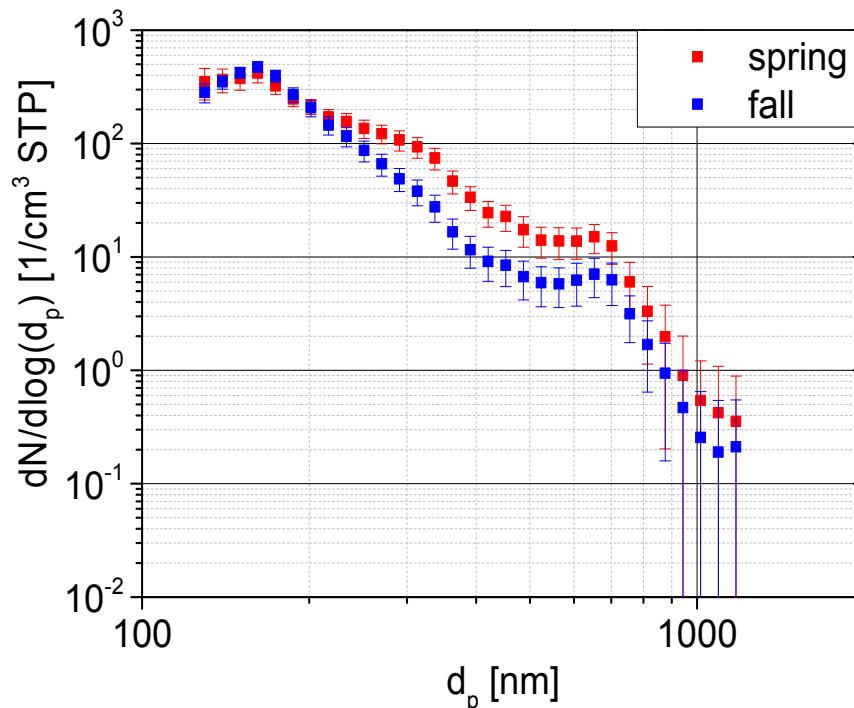
Figure 6.22: Seasonal variability of the particle size distribution in the mid-latitude LMS (latitude > 40°N, PV > 3.5 PVU). The spring/summer measurements were conducted from April to August and the fall/winter measurements from October to February. Error bars indicate one sigma standard deviation.

Accordingly in fall the CARIBIC measured mid-latitude LMS O_3 concentration was only half the spring concentration (214 ppbv vs. 466 ppbv). The mid-latitude LMS CO concentration was increased by 19% to 46 ppbv in fall. In Fig. 6.21 and also in the data from Young et al. [2007] (displayed in Fig. 6.6a, b) it was shown, inside the mid-latitude UT the concentration of accumulation mode particles is lower than in the LMS. Therefore, it is reasonable that in fall the LMS accumulation mode particle concentration was found to be only half the spring concentration. The variability (error bars in Fig. 6.22) was only slightly increased by 18% (average) in fall.

In order to derive information about the meridional distribution of the accumulation mode data, in Fig. 6.23 the median integral particle number and mass concentrations from the nine South Africa flights between November 2010 and March 2011 are plotted as a function of latitude. The measurements were sorted into 10° latitude bins and classified as tropospheric (PV < 1 PVU) and stratospheric (PV > 3.5 PVU) measurements. Data obtained in the tropopause region (1 < PV < 3.5 PVU) were not considered. The median was chosen here instead of the mean as it is less influenced by few extremely high or low concentrations. Hatched areas of the same color show the data range between the 25% and 75% percentiles. Note that the interpretation of the meridional gradients is ambiguous because the tropopause altitude increases from pole to equator (Fig.2.2) while the CARIBIC aircraft flies at nearly constant altitude (pressure level).

For the Africa route, neither for the particle number nor for the particle mass a significant meridional gradient was apparent in the free- and upper troposphere (Fig. 6.23, blue). The observed minimum in the particle number concentration at -15°N is probably caused by the scavenging of accumulation mode particles in convective clouds in the Intertropical Convergence Zone (ITCZ). During boreal winter the ITCZ is located
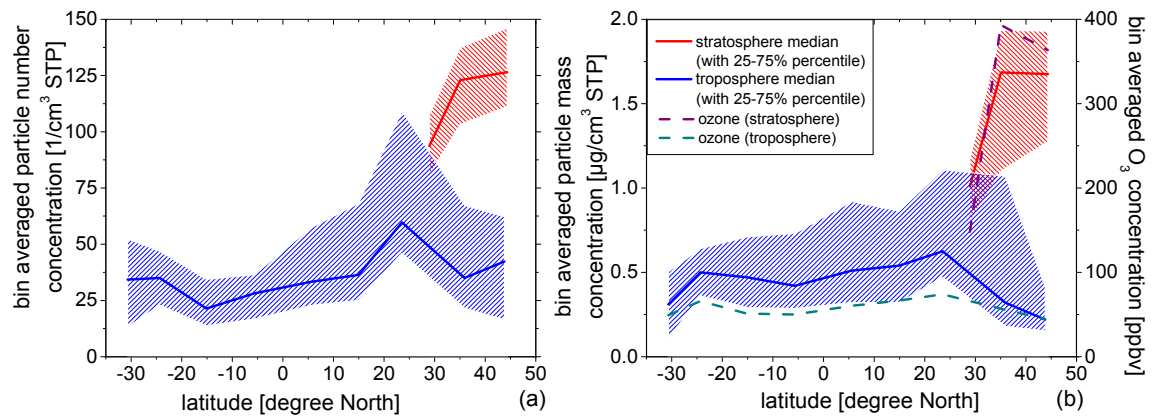
Figure 6.23: Meridional distribution of the integral particle number concentration ($125\,\text{nm} < d_p < 1.3\,\mu\text{m}$) (a) and the derived particle mass concentrations (b), measured along the CARIBIC South Africa flights between November 2010 and March 2011. Tropospheric (blue) and stratospheric (red) data were divided by the potential vorticity at the measurement location. The data were sorted into 10° latitude bins and averaged. While the solid lines indicate the median, the hatched areas give the data range between the 25% and 75% percentiles. Dashed lines give the corresponding bin averaged median ozone concentration.

over Africa at about 5°N to 15°S [Liljequist and Cehak 1984, p. 292-293], acting as a sink for accumulation mode particles. The maximum at 25°N is probably caused by a strong pollution plume, observed during flight LH333 on March 21, 2011. On that flight the highest accumulation mode particle number- and mass concentrations of up to 310 $1/\text{cm}^3$ STP and 3.1 $\mu\text{g/m}^3$ STP were measured in the latitude bin 20°N to 30°N. Beside accumulation mode particles, also the concentration of Aitken mode particles (N_{12}), as well as CO and NO_y were strongly enhanced. Excluding the data of LH333 would reduce the particle number concentration median and percentiles from 60 to 52 $1/\text{cm}^3$ STP (median), from 46 to 39 $1/\text{cm}^3$ STP (25% percentile), and from 109 to 66 $1/\text{cm}^3$ STP (75% percentile). For the particle mass concentration the median and percentiles would reduce from 0.63 to 0.52 $\mu\text{g/m}^3$ STP (median), from 0.47 to 0.42 $\mu\text{g/m}^3$ STP (25% percentile), and from 1.11 to 0.67 $\mu\text{g/m}^3$ STP (75% percentile), respectively. The nearly constant O_3 concentrations (Fig. 6.23b, dashed cyan line) suggest that the higher particle concentrations cannot be caused by mixing of stratospheric air into the UT.

Because of the high tropopause altitude in the tropics and subtropics no stratospheric measurements were available south of 28°N. The observed increasing meridional particle number- and mass gradient for the LMS is caused mainly by the vertical gradient above the tropopause (Fig. 6.20) as documented by the similar ozone meridional gradient (Fig. 6.23b, dashed purple line). Although ozone and accumulation mode particles are formed by different processes, both have their origin deep in the stratosphere, hence the good correlation.

In general at mid-latitudes the accumulation mode particle concentration was found to be higher in the LMS compared to the UT. The temporal variation inside the LMS does reflect the STE transport patterns. Over Africa the UT meridional variation of the accumulation mode particle number- and mass concentration is low. In the LMS the meridional gradient is induced by the relative height of the measurements toward the TP.

6.4   Increased particle surface as a sink for mercury inside the lowermost stratosphere

Mercury and its compounds are very toxic and therefore hazardous for human health and the environment. Therefore it is on the priority list of all international agreements and conventions dealing with environmental protection and human health, including the UNEP[36] Minamata convention on mercury (signed by 112 nations, www.mercuryconvention.org; last access: 20.07.2014). Gaseous elemental mercury (GEM) is relatively inert and has consequently a relatively long atmospheric lifetime of about one year [e.g. Selin et al., 2008]. Because of this long lifetime, GEM is well mixed inside the free troposphere, showing no vertical gradient [Swatzendruber et al., 2009]. The tropospheric GEM background concentration was found to vary between 1 and 2 ng/m³ STP [Swatzendruber et al., 2009]. Above the tropopause, the mercury concentration decreases strongly [Ebinghaus et al., 2007; Radke et al., 2007; Talbot et al., 2007; Slemr et al., 2009, Lyman and Jaffe, 2011, this study: Fig. 6.24a]. It is assumed, inside the LS GEM becomes effectively oxidized to gaseous oxidized mercury (GOM), which deposits onto existing aerosol particles [Lyman and Jaffe, 2011]. This assumption is supported by observations of high mercury concentrations on aerosol particles in the LMS but not in the UT [Murphy et al., 1998, 2006]. So far three GEM oxidation mechanisms have been proposed: reaction with O_3, OH, and Br [Lin et al., 2006; Lindberg et al., 2007, Hynes et al., 2009, p. 427-457]. However, their relative contribution is still not well known and the link between the gaseous and particulate mercury has not been unequivocally documented. The CARIBIC aerosol and mercury measurements provide the first insight into the correlation between gaseous mercury and the available particle surface area.

The CARIBIC mercury instrument was shown to measure the sum of GEM and GOM [Slemr et al., 2009], called total gaseous mercury (TGM). Figure 6.24a shows TGM concentrations and the OPC derived particle surface area concentration as a function of the potential vorticity. As in Fig. 6.20, the data up to 8 PVU were binned to 1.0 PVU bins. The squares represent the median concentrations and the error bars indicate again the 25% and the 75 % percentiles. Each bin represents at least 25 different flights and more than 170 data points. The area between 1.6 PVU and 3.5 PVU is marked as tropopause region. From the lower tropopause upward the particle surface area increased with increasing PV from 5.4 µm²/cm³ STP (0.5 PVU) to 17.0 µm²/cm³ STP (7.5 PVU). On the contrary the TGM concentration decreased with increasing PV from 1.30 ng/m³ STP (0.5 PVU) to 0.53 ng/m³ STP (7.5 PVU). This negative correlation suggests a direct link between the particle surface and the TGM concentration. Figure 6.24b shows for all measurements the TGM concentration as a function of the particle surface area concentration. To increase the readability for this graph, the scale for the particle surface area concentration was limited to 40 µm²/cm³ STP or 97.2 % of the individual measurement points (black squares). With only a few exceptions (e. g. caused by pollution plumes), the measurements indicate a clear

---

[36] United Nations Environment Program
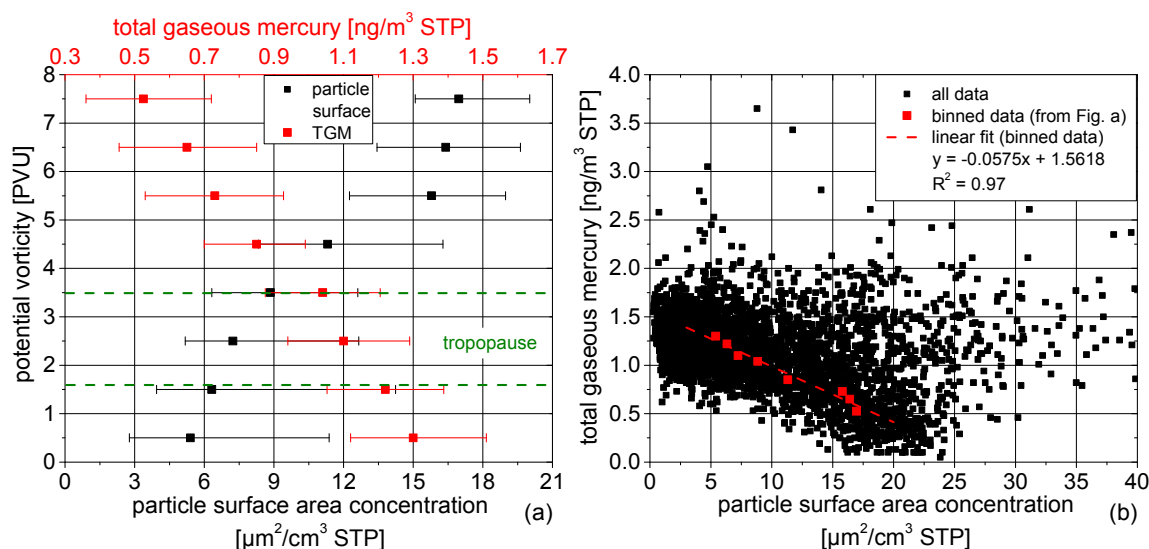
Figure 6.24: OPC derived particle surface area concentration and total gaseous mercury (TGM) concentration as a function of potential vorticity (a). The data were sorted into 1.0 PVU bins. While the squares give the median concentration, the error bars indicate the 25 % and 75 % percentiles for each bin. Figure (b) shows a scatter plot of all TGM measurements as a function of the particle surface area concentration. Because the x-axis is limited to 40 μm²/cm³, only 97.2 % of the measurement points are displayed here. The linear fit (red line) was adapted to the bin averaged data from (a) (red squares).

negative correlation with lower TGM concentrations at higher particle surface area. The data bins from Fig. 6.24a are shown in Fig. 6.24b as red squares. The adapted linear equation quantifies the relationship between the available stratospheric particle surface area and TGM. However, this finding is not a proof for the assumption of stratospheric aerosol particles do act as a sink for mercury. Therefore, the particle samples taken onboard CARIBIC should contain a distinct amount of Hg. Unfortunately, the PIXE measurements did not detect any Hg so far, despite the sufficient sensitivity of the PIXE technique. It is assumed that the particle bound mercury evaporates during the PIXE analysis in vacuum. Because of the missing evidence of particle bound mercury, the relation between TGM and particle surface area shown in Fig. 6.24 is still to interpret. Nevertheless, it presents the first statistical indication for the role of aerosols as sink for stratospheric gaseous mercury.

6.5 Comparison with the GLObal Model of Aerosol Processes (GLOMAP)

The, compared to research aircraft, high measurement frequency of CARIBIC leads to a unique dataset which is suitable for comparison with global aerosol models. The dataset used within this work (June 2010 to May 2011) is too small for a statistically well constrained comparison. But the variability in the concentration of accumulation mode particles in the UT/LMS is much smaller than the variability of e.g nucleation mode particles. Thus, even a "small" number of 37 flights provide enough data for a meaningful comparison which is presented in this section.

The GLObal Model of Aerosol Processes (GLOMAP) was developed by Ken Carslaw´s working group at Leeds University. It is a global atmospheric model, including aerosol microphysics and chemical processes. In GLOMAP, the Toulouse Off-line Model of Chemistry And Transport (TOMCAT; http://homepages.see.leeds.ac.uk/~lecmc/ tomcat.html; last access 20.07.2014) and the United Kingdom Chemistry and Aerosol climate model (UKCA; http://www.ukca.ac.uk/wiki/index.php/Main_Page; last access 20.07.2014) are combined [Mann et al., 2010]. The particle size distribution is simulated with a sectional two-momentum scheme with seven aerosol modes. The Aitken, accumulation, and coarse modes are further divided into soluble and insoluble modes. Only the nucleation mode is considered soluble and is thus not further divided. The model aerosol physics includes nucleation, condensational growth, coagulation, wet and dry deposition, as well as cloud processing. The GLOMAP horizontal resolution for this comparison was 2.8 ° in longitude and latitude. The vertical geometric resolution of the 31 layers varied between 60 m at the boundary layer and 1 km at the tropopause. The model is described in detail by Spracklen et al., [2005a, b] and Mann et al., [2010].

Unfortunately the GLOMAP data, provided by the Leeds group, were not available for the period of the OPC measurements. Nevertheless, the particle size distribution modeled for January 2001 to December 2005 could be compared to the CARIBIC measurements from June 2010 to May 2011. Of course this comparison cannot be exact but provides a first insight whether the modeled UT particle size distribution is similar to the measured one. To distinguish climatic regions, the GLOMAP data were zonally averaged for the mid-latitudes (40 °N < φ < 55 °N) and the tropics (1 °N < φ < 21 °N). Only data from altitude range 8 to 12 km were used. As the model data were restricted to the troposphere, only tropospheric OPC data (PV < 1.0 PVU) were averaged for the same regions. In Fig. 6.25 the OPC mean and median concentrations are shown both regions as dashed and solid blue line. The grey areas indicate the 25 % and 75 % percentiles. The OPC integration time was set to 900 s (cf. Sec. 5.3.1) to avoid the 25% percentile being zero (cf. introduction to Fig. 6.4 and 6.6), but for particle diameters larger than 850 nm this was still not enough.

The seven GLOMAP aerosol modes were summed up for each OPC size channel range, giving the final comparable model particle size distributions (magenta solid line). Since the model data were reported at ambient conditions, the CARIBIC data are given at ambient pressure and temperature, too.

At mid-latitudes the modelled and measured number concentrations for particles smaller 300 nm (Fig. 6.25a) are in good agreement. For particles with 300 nm < d_p < 500 nm the modeled particle size distribution has a slightly steeper slope than the measured one and therefore fits only the OPC 25% percentile at 400 nm. From 500 nm to 900 nm the measured particle concentration is significantly higher than the modeled, because of the unknown peak (mode) in the OPC particle size distribution (cf. Sec. 6.1.4). Above 900 nm the measured and the modeled concentration still have a significant offset (about a factor of three for the mean), but the slope is similar.

In the tropics the results are similar. For d_p < 250 nm the modeled concentration is at the OPC 75% percentile. From 250 nm to 400 nm the modeled slope is steeper and the number concentration decrease to the OPC 25% percentile. For particles larger than
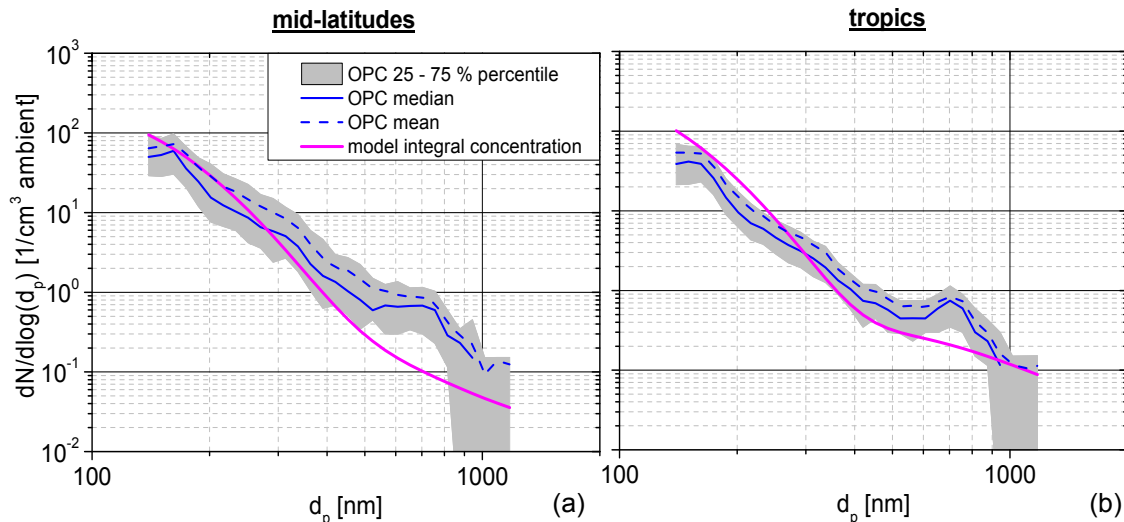
Figure 6.25: Comparison of the modeled (GLOMAP) and the measured (CARIBIC-OPC) particle size distributions for mid-latitudes (a) and tropics (b). The modeled and measured tropospheric data (PV < 1 PVU) from the altitude range 8-12 km were averaged for the latitude regions 40 °N < φ < 55 °N (mid-latitudes) and 1 °N < φ < 21 °N (tropics). While the modeled data represent 2001 to 2005 (monthly average), the CARIBIC data were obtained between June 2010 and May 2011 (averaged of 900 s). Both the modeled and CARIBIC data are given at ambient conditions.

350 nm the modeled particle size distribution follows the OPC 25% percentile with exception of the OPC peak (mode) between 600 nm and 900 nm.

Evaluating the differences between modeled and measured particle size distribution one has to take into account the difference in time and measurement location. While the GLOMAP data (2001-2005) were zonally averaged, representing data from all longitudes, the CARIBIC data (2010-2011) were measured on specific flight routes with varying longitudinal coverage (e.g. eastern vs. western longitude; continental vs. oceanic measurement region). The limitation to tropospheric measurements (PV < 1 PVU) further reduces the dataset. For the mid-latitudes the average in Fig. 6.25a is based on six flights on the Asian route, three flights on the Africa route, eight flights on the South America route, and two flights on the North America route (cf. Fig. 6.1). Thus, in this climatic region the measurements were distributed relatively uniformly over longitude[37] and over continent and ocean[38]. In the tropics the measurements are based on nine flights on the Africa route, as well as 13 flights on the South America route. Consequently, the measured tropical average is based on a relatively uniform number of over the ocean (13) and over the continent (9) measurements, but might be more representative for central- and western longitude air[39].

An additional reason for the modeled steeper slope and lower concentration of particles with d_p > 250 nm in both regions might be the exclusion of all in cloud measurements (cf. Sec. 6.1.2). While the model included inside cloud values and

---

[37] 6 flights to the east (Asian route); 3 fights in the center (Africa route); 10 flights to the west (North- and South America route)
[38] 10 flights over ocean; 9 flights over continent
[39] 9 flights in the center (Africa route); 13 flights to the west (South America route)

particle sink by cloud scavenging, the inside cloud CARIBIC measurements were not considered here.

Nevertheless, the measured and the modeled particle size distributions were found generally in reasonably good agreement for the mid-latitudes and the tropics. For most parts of the analyzed size range the modeled concentrations are within or close-by the OPC 25%- and 75%-percentiles. Only for the unknown OPC peak (mode) at $500\ \mathrm{nm} < d_p < 900\ \mathrm{nm}$ a significant difference is present. The presented analysis demonstrates the potential of the growing OPC dataset. Therefore, further studies with a much longer CARIBIC OPC dataset, covering larger areas and temporally matched with the GLOMAP dataset should be carried out in future to address the uncertainties and to compare seasonal variation.

6.6   Comparison of aerosol optical parameters from in situ CARIBIC measurements and satellite remote sensing

Satellite-borne measurements provide datasets with a global coverage. However, those data have to be evaluated with in situ measured data. This section compares data from satellites with the OPC data to illustrate a further possible application. As here data from two very different measurement techniques (remote sensing wide area scan vs. in situ single point measurement) are compared, the focus lies on qualitative rather than on quantitative comparison.

Several aerosol optical parameters were measured with a seven channel sun photometer onboard the Earth Radiation Budget Satellite (ERBS) within the Stratospheric Aerosol and Gas Experiment (SAGE II; www-sage2.larc.nasa.gov; last access 20.07.2014). The pole orbiting ERBS provided data from October 1984 to August 2005. Bauman et al., [2003a, b] published climatologies for the particle extinction coefficient at different wavelength, the particle surface area concentration, and the effective particle radius. The data are presented as function of latitude, geometric altitude and time between October 1984 and August 1999. On request the raw data for all figures in Bauman et al [2003b] were courtesy provided by Jill J. Bauman (NASA). Within this section the above mentioned aerosol parameters are compared to the corresponding parameters derived from the CARIBIC measurements. The extinction coefficient for $\lambda = 525\ \mathrm{nm}$ was calculated from the particle number size distribution using a custom Mie-scattering program [Schladitz et al., 2011], which is based on a Mie-code by Bohren and Huffman [1983]. The particle surface area concentration was directly obtained from the OPC analysis algorithm (Sec. 5.3). The effective particle radius was calculated from the integrals of particle volume and the particle surface according to Eq. 6.1:

$$r_{eff} = 3 \cdot \frac{\sum_{i=1}^{n_{OPC}} \frac{1}{6} \cdot \pi \cdot d_{p,i}^{3} \cdot \left[d_{p,i} \right]}{\sum_{i=1}^{n} \pi \cdot d_{p,i}^{2} \cdot \left[d_{p,i} \right]} \qquad (6.1)$$

r_{eff} effective particle radius [μm]

n_{OPC} number of size channels in the OPC particle size distribution [1]

$d_{p,i}$ mean particle diameter of a certain size channel (i) [μm]

$\left[d_{p,i} \right]$ measured particle concentration at a certain size channel with $d_{p,i}$ [1/cm^3]

As the SAGE II data were provided only for altitudes 2 km above the tropopause or higher, only stratospheric CARIBIC measurements with potential vorticity > 5 PVU were used for this comparison. 2036 measurement points in the northern hemisphere (north of 30°N) and none in the southern hemisphere fulfill this requirement.

Since the datasets originate from different periods, only a comparison of long-term averages of background values is expedient. To obtain representative background values, the SAGE II data were averaged over time from January 1989 to May 1991 and January 1996 to August 1999. Between June 1991 and December 1995 the Pinatubo eruption[40] strongly increased the particle extinction, surface, and effective radius. Before January 1989 the background concentrations were influenced by the Nevado del Ruiz eruption in November 1985 (cf. Fig. 2 to 5, 9, and 16 in Bauman et al., [2003b]). Comparing data from different periods is difficult, because Solomon et al [2011] showed that from 1996 to 2010 the global stratospheric aerosol optical depth increased by about 34%. On the contrary SAGE II data were measured at ambient conditions i.e. ambient humidity, whereas the CARIBIC data are representative for dried aerosol. With Tab. 6.3 and the associated discussion it was shown that the particles shrink inside the CARIBIC aerosol inlet system by about 25%. These effects of increasing stratospheric optical depth (i.e. increasing aerosol loading) on the one hand and the comparison of aerosol optical parameters from ambient and dry measurements on the other hand are opposed and therefore should compensate. Hence, the SATGE II and the CARIBIC data should be on the same order of magnitude.

Figure 6.26 shows the meridionally, zonally, and temporally averaged vertical profiles of the particle extinction coefficient at a wavelength of $\lambda = 525$ nm, the ambient particle surface area concentration, and the effective particle radius. The stratospheric CARIBIC data were measured up to 12.5 km and were sorted into 0.5 km altitude bins. SAGE II data start at 11 km[41] and have a vertical resolution of 1 km. For both datasets the solid line give the median value and the dashed lines in the same color

---

[40] The explosive phase of the Pinatubo eruption started in June 1991.

[41] As the given altitude is the middle of the individual altitude layer, the lines in Fig. 6.26 start in the middle (e.g. at 11.5 km). However, the given value is representative for the whole layer (i.e. from 11 km to 12 km).
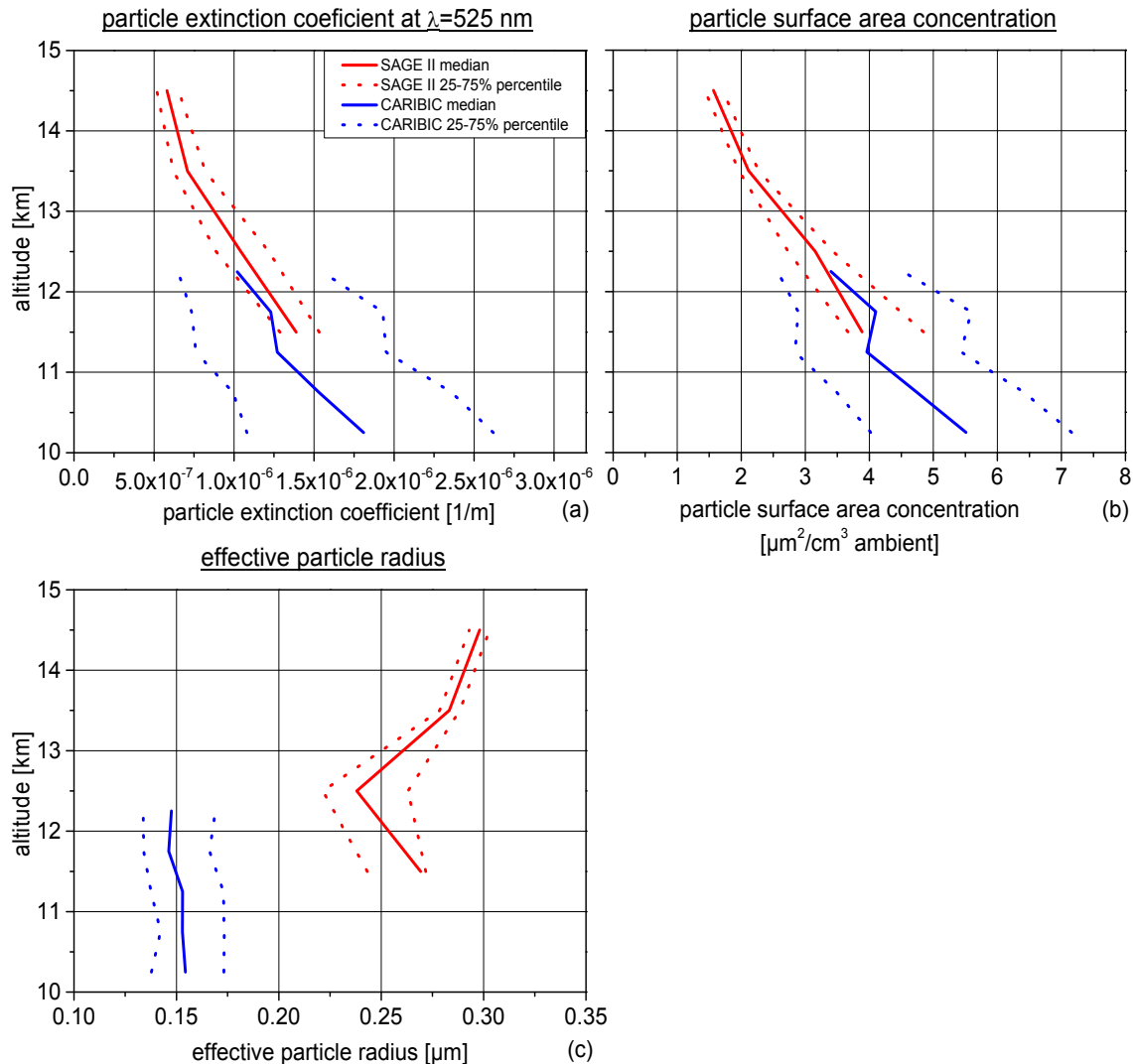
Figure 6.26: Vertical gradients of the particle extinction coefficient at $\lambda = 525$ nm (a), particle surface area concentration (b), and effective particle radius (c). The stratospheric CARIBIC measurements (PV > 5 PVU) were sorted into 0.5 km altitude bins. SAGE II data have a vertical resolution of 1 km. Both data sets were meridionally and zonally averaged. CARIBIC data were measured between June 2010 and February 2011, SAGE II data were averaged from 1989 to May 1991 and January 1996 to August 1999. While solid lines represent the median concentrations, dashed lines indicate the 25% and 75% percentiles. The CARIBIC particle surface area concentrations are given at ambient conditions to be comparable to SAGE II data.

indicate the 25% and 75% percentiles, respectively. Considering the above mentioned uncertainties, the good agreement of the two datasets within the crossover area (11 km to 12.5 km) for particle extinction coefficient (Fig. 6.26a) and particle surface area concentration (Fig. 6.26b) is remarkable. With $1.273 \cdot 10^{-6}$ 1/m the median SAGE II particle extinction coefficient is only 8.6% higher than the CARIBIC median[42]. The averaged SAGE II median for the particle surface area concentration of 3.64 µm²/cm³ is only 4.6% lower than the CARIBIC median (3.82 µm²/cm³). In addition, both techniques show the same slope with decreasing values for increasing altitude.

---

[42] For both datasets the median was averaged between 11.0 km and 12.5 km, giving a value of $1.273 \cdot 10^{-6}$ 1/m for SAGE II and $1.173 \cdot 10^{-6}$ 1/m for CARIBIC.

On the contrary, hardly any vertical gradient but a significant offset between the datasets was found for the effective particle radius (Fig. 6.26c). With 0.259 μm the averaged SAGE II median is 74% higher than the averaged CARIBIC median (0.149 μm). This is surprising after good agreements for particle extinction coefficient and surface area were found. The different measurement conditions (ambient humidity vs. dried aerosol) would explain the difference only partly. According to Eq. 6.1, the effective particle radius is calculated from the particle surface area and the particle volume concentration. Increasing the OPC measured particle size by 25% to match the ambient humidity particle size (cf. Tab. 6.3) would increase the particle surface by 56% and the particle volume by 95%. The resulting effective radius would be 25% larger. A methodical error explaining the remaining discrepancy of 50% is not apparent. As the particle surface area concentration was found to be in good agreement, the difference might be caused by an even higher SAGE II particle volume concentration.

Figure 6.26 shows that the CARIBIC observations have generally a much higher variability than the SAGE II measurements[43]. This is probably caused by the much shorter CARIBIC measurement period of one year compared to nearly six years for SAGE II. Please note, the different slopes in the vertical representation of the CARIBIC OPC data in figures 6.20b, 6.24a and 6.26b arise by the use of the different vertical coordinates (geometric altitude vs. PV) and different conditions (ambient vs. STP).

In summary, considering that large scale remote sensing data are compared with averages of in situ single particle measurements recorded several years later, the agreement is better than expected. As the increase of the stratospheric aerosol loading from 1996 to 2010 [Solomon et al., 2011] is compensated by the comparison of measurements at ambient humidity (SAGE II) with dry conditions (CARIBIC), the good agreement for the particle extinction coefficient and the particle surface area concentration is reasonable. However, the reason for the discrepancy of the effective particle radius was not found yet, but should be a focus of further studies. Nevertheless, this comparison clearly demonstrates that the increasing CARIBIC OPC dataset can be used to validate data from satellite and ground based remote sensing (e.g. LIDARs).

---

[43] The CARIBIC 25% and 75% percentiles were found to be about $\pm 40\%$ (particle extinction), $\pm 30\%$ (surface area), and $\pm 11\%$ (effective radius) around the medians. The corresponding SAGE II variability was calculated to be $\pm 13\%$ (particle extinction), $\pm 10\%$ (surface area), and $\pm 5\%$ (effective radius), respectively.

7 Conclusions and outlook

To improve the knowledge of the particle size distribution in the upper troposphere and lowermost stratosphere (UT/LMS) and to create a reference dataset for modelling and remote sensing validation, in this thesis an optical particle counter (OPC) was modified for regular measurements onboard an Airbus A340-600 passenger aircraft (Civil Aircraft for the Regular Investigation of the atmosphere Based on an Instrument Container (CARIBIC) project). The basic instrument is a RION KS-93 OPC with originally five size channels. This OPC is placed together with a new data acquisition and a flow control system in a 19" rack unit. From the original instrument only the optics and the electronic scattering signal amplification are still used for the new CARIBIC OPC unit. This new OPC unit had to be certified for aviation application, including documentation and Electro Magnetic Compatibly (EMC) tests. The new data acquisition and unit controller program is operated on a National Instruments PXI real time system. For every detected particle, the shape of the scattering signal intensity is recorded with three channels with a temporal resolution of 3 μs. The recording of the scattering raw signal allows a detailed post flight data analysis. So the temporal resolution and the number of the size channels can be set flexibly. Furthermore it is possible to recalculate all data in case the calibration changes. For the analysis of the data presented in this work, the resolution was set to 180 s and 32 size channels (exceptions are marked). The gas flow system was added to

    a) focus the measurement air to the center of the KS-93 optics
       (sheath air technique).
    b) reduce the transport time between aerosol inlet and OPC unit to 0.65 s.
    c) flush the OPC and the sampling lines with filtered air during take-off and
       landing to prevent contamination with polluted air around the airport.

The necessary implementation of the sheath air technique reduces the sample air flow to 0.015 l/min. However, with the sheath air technique the maximum counting efficiency is increased from 50% to 89%. The reason, why the counting efficiency does not reach 100% is not clear yet.

The new OPC unit was calibrated in laboratory with ammonium sulfate (AS, $m(\lambda) = 1.52 - 1.14 \cdot 10^{-7} \cdot i$, $\lambda = 830$ nm) and polystyrene latex particles ($m(\lambda) = 1.59 - 0.0 \cdot i$, $\lambda = 830$ nm). With a Mie scattering program the calibration points were related to characteristic internal mixtures of mid-latitude upper tropospheric aerosol (UTA)[44], mid-latitude lowermost stratosphere aerosol (LSA)[45], and tropical mid tropospheric aerosol (MTA)[46]. A sensitivity study along a measurement flight from Frankfurt to Cape Town/South Africa indicates an uncertainty of only -10.5% to +8.3% in the particle mass concentration when using the UTA calibration for all measurement regions. As most of the CARIBIC flights are located in the northern hemispheric upper tropospheric mid-latitudes and the UTA calibration is the one in the middle, the data analyzed within this work are based on the UTA calibration (except the volcanic ash flights and the stratospheric mass closure study). The overall relative uncertainty with respect to the integral particle number-, surface-, and mass concentration is calculated to be 40%, 31%, and 33%, respectively (including uncertainties due to sample air flow, counting efficiency, erroneous counts, particle sizing, and particle density). The overall relative uncertainty for the number concentration is largest, because of the large uncertainty of the counting efficiency due to the use of the UTA calibration for all measurement regions. At the OPC lower detection limit this uncertainty is largest and the particle concentration is highest, resulting in a high overall uncertainty. While the UT/LMS integral number concentration is dominated by Aitken mode particles [de Reus et al., 2001, this study], the integral particle surface and mass concentration is dominated by accumulation and small coarse mode particles [de Reus et al., 2001, this study]. With increasing particle size the OPC reaches the maximum asymptotic counting efficiency and the uncertainty of the counting efficiency converge to zero. All data are corrected for sampling line losses, OPC counting properties, and are normalized to standard conditions (STP, p=1013.25 hPa, T=0 °C).

Within the CARIBIC project (www.caribic-atmospheric.com; last accessed: 20.07.2014), this OPC unit is mounted into a modified standard air fright container. Besides the OPC 20 trace gases and aerosol instruments as well as a 112 camber air sampler and a 16 channel aerosol sampler are installed in the container. Usually ones a month the container is installed into the forward cargo bay of an Airbus A340-600 passenger aircraft from Lufthansa. When installed, the container pipes are connected to a permanent mounted gas- and aerosol inlet system at the aircraft fuselage. After a flight sequence of usually four to six intercontinental flights the container is removed from the aircraft and the data are downloaded and analyzed.

The OPC dataset is evaluated by comparison to published previous measurement data in the UT/LMS and by a CARIBIC internal mass closure study. Generally the CARIBIC particle size distributions are in reasonable agreement with previous measurements in different climatic regions. The compared data are within the same range and the size distribution slopes are similar. Consequently, it is concluded that the CARIBIC OPC data are representative for the investigated regions. A stratospheric

---

[44] 44% H_2SO_4, 44% $(NH_4)_2SO_4$, 10% organics, 2% soot; m = 1.48-0.0143 · i, ρ = 1.72 g/cm³

[45] 90% H_2SO_4, 10% organics; m = 1.43-0.0001 · i, ρ = 1.64 g/cm³

[46] 40% organics, 40% $(NH_4)_2SO_4$, 19% H_2SO_4, 1% soot; m = 1.48-0.0075 · i, ρ = 1.63 g/cm³

mass closure study of the impactor samples to the OPC derived particle mass yield an offset of 220%. This difference is outside the calculated individual method uncertainties, which would explain a discrepancy of 94%. For this value the not quantifiable uncertainties of optical particle diameter (OPC) vs. aerodynamic particle diameter (impactor) and the difference of the particle shape from an assumed sphere (OPC) are not considered. Currently the reason for the offset is not known. Therefore, further studies have to be carried out to identify and minimize the reason for the offset. Recently (August 2014), a more detailed mass closure study (not part of this thesis) was published by Martinsson, et al., [2014]. In this study the OPC and impactor data from 48 flights were processed with a slightly different analysis method, resulting in a much better agreement.

Most of the CARIBIC measured particle size distributions show a secondary peak (mode) in the size range $600\,nm < d_p < 900\,nm$. Currently, the question whether this mode is real or a measurement artifact cannot be conclusively answered. Several possible instrumental reasons were eliminated and therefore this mode is not corrected in the dataset. Furthermore, artificial particle measurements were observed on all CARIBIC flights when flying inside clouds. The integral particle number and mass concentration was enhanced by a factor of 3 on average. It is assumed the OPC measures residuals of cloud droplets, which evaporate in the aerosol inlet system. Consequently, all inside cloud measurements were excluded from the dataset.

The CARIBIC volcanic ash flights (VAF) in spring 2010 were the first mission for the new OPC unit. Between April 14 and May 22, 2010 the south Icelandic volcano Eyjafjallajökull erupted first since 1823. The volcano ash cloud strongly affected the aviation over central Europe. Lufthansa asked the CARIBIC team for dedicated volcano cloud measurement flights to document the location and spatial extent of the ash plume and to compare the data with the results from the forecast models. The size resolving OPC detection range ($125\,nm < d_p < 1.06\,\mu m$; volcanic ash calibration[47]) did not cover the volcanic ash particle size distribution ($20\,nm < d_p < 100\,\mu m$; Ginoux, 2003; Sanderson, 2010; Schumann et al., 2011) and therefore quantitative data for the total particle mass concentration were not expected. The most interesting results were obtained on the third VAF on May 19, 2010 and were published in Rauthe-Schöch et al., [2012]. The volcano plume was found at 75°N, 15°E in altitude ~4000 m with maximum particle number and mass concentrations of 220 1/cm³ STP and 60 µg/m³ STP, respectively. The supplementary information from the trace gas measurements, the aerosol elemental composition, and the trajectory analysis identified the measurement air as volcanic plume. The comparison of an "extended" OPC particle mass concentration (84 µg/m³ ambient) to results from a FLEXPART model run (104 µg/m³ ambient) gave good agreements for the plume location and mass concentration.

During the CARIBIC flights on June 23 and 24, 2010 a very strong plume was observed over eastern Asia near Osaka with accumulation mode particle number and mass concentrations of up to 886 1/cm³ STP and 16.4 µg/m³ STP. Inside the plume the concentration of CO, SF_6, NO, NO_y, CH_3Cl, NMHCs, total gaseous mercury, and the CPC derived N_{12} particle number concentration ($d_p < 12\,nm$) were also significantly

---

[47] m=1.54-0.003 · i, ρ = 2.65 g/cm³ (values within the range given by Schumann et al. [2011])

increased. A detailed analysis of all CARIBIC measurements, backward trajectories, MODIS[48] fire maps, and CALIPSO[49] space LIDAR[50] data indicated that probably biomass burning and the industry in the region south of Beijing and north of Shanghai were the source for the observed plume. About one day before measured, the plume air was lifted with a deep convective cloud from the boundary layer to the UT and moved to the measurement location. In general, this finding emphasizes that deep convection of pollutants from the boundary layer into the UT region is an important transport process. However, the global contribution of such extreme events to the UT/LS aerosol budget is unknown. Future CARIBIC measurements will help to estimate the frequency and thus to constrain the global relevance of such events.

Within this work the OPC data from the first year of regular operation until May 2011 were used for statistical analysis. These are 37 intercontinental flights along four different flight routes with a total measurement time of 381 hours or ~ 343 000 km. Plotting the average CARIBIC particle size distribution and therefrom derived aerosol parameter as function of potential vorticity (PV) indicates a stratospheric vertical increasing gradient for the mid-latitude particle number- and mass concentration. On average in the mid-latitude LMS the concentration of accumulation mode particles (d_p < 900 mn) was about 120% higher than in the mid-latitude UT. Only for particles larger 900 nm nearly no vertical gradient was observed. The increased particle number and mass concentration in the LMS is in agreement with CARIBIC measurements of the particulate sulfate mass [Papaspiropoulos et al., 2002]. The vertical increasing gradient can be explained with the longer life time for stratospheric particles compared to UT particles [Menzies and Tratt, 1995; Rasch et al., 2008].

The mid-latitude LMS particle size distribution show a seasonal variation for larger particles (d_p > 230 nm) with on average 120% higher concentrations during spring compared to fall. The observed seasonality was caused by the differences in the atmospheric dynamics. The upwelling air motion from the troposphere into the stratosphere in the northern hemisphere is most effective in late summer, fall, and early winter and smallest in late winter, spring, and early summer [Seo and Bowman, 2001; Škerlak et al., 2014]. On the contrary the downwelling stratosphere-troposphere air exchange (STE) is maximum in winter and spring and minimum in summer and fall [Seo and Bowman, 2001; Jordan et al., 2003; Škerlak et al., 2014]. As at mid-latitudes the accumulation mode aerosol loading in the stratosphere is higher than in the upper free troposphere [Hofmann 1990, Minikin et al., 2003; Young et al., 2007; this work Fig. 6.20, 6.21], the observed UT/LMS particle size distribution seasonality reflects the seasonality of the STE. This is confirmed by the CARIBIC measured O_3 concentration, which was during the analyzed period and region in fall only half the spring concentration.

Along the South Africa flights (boreal winter) neither for the accumulation mode particle number, nor for the particle mass concentration a significant meridional gradient was apparent in the free- and upper troposphere. Only in the Intertropical Convergence Zone (ITCZ) the concentrations were slightly decreased, probably due to

---

[48] MODerate-resolution Imaging Spectroradiometer
[49] Cloud-Aerosol Lidar and Infrared Pathfinder Satellite Observations
[50] LIght Detection and Ranging

cloud scavenging. An observed meridional gradient for the stratospheric accumulation mode particle number- and mass concentration was caused mainly by the vertical gradient above the tropopause.

Comparing the stratospheric concentration of Total Gaseous Mercury (TGM) with the OPC derived particle surface area concentration, a significant negative correlation ($R^2 = 0.97$) becomes apparent. It is assumed that inside the lower stratosphere gaseous elemental mercury becomes effectively oxidized and deposits onto existing aerosol particles [Lyman and Jaffe, 2011]. The CARIBIC OPC and mercury measurements provide the first insights into the correlation between gaseous mercury and the available particle surface area. However, the found negative correlation is not a proof for the assumption of stratospheric aerosol particles acting as a sink for gaseous mercury, because no Hg was found on the PIXE[51] analyzed particle samples. Currently it is assume that the particle bound mercury evaporates during the PIXE analysis in vacuum.

To demonstrate the benefit of the growing CARIBIC OPC dataset as a reference for modelling, the averaged particle size distribution was compared to results from the GLObal Model of Aerosol Processes (GLOMAP; Mann et al., [2010]). In general, a reasonably good agreement between measurements and model results is apparent for the compared regions (mid-latitude- and tropical troposphere). For most parts of the analyzed size range the modeled concentrations are within or close-by the OPC 25%- and 75%-percentiles. Only between 250 nm and 500 nm the modeled particle size distribution in both regions has a slightly steeper slope than the measured one and therefore the modeled particle concentration decrease to the OPC 25% percentile for $d_p > 400$ nm. As only for the OPC dataset all inside cloud measurements were excluded, particle scavenging inside clouds might cause the modelled lower concentration.

As another example for the value of CARIBIC data for validating efforts, the OPC derived aerosol optical parameters extinction coefficient, surface area, and effective particle radius were compared to data from satellite remote sensing (Stratospheric Aerosol and Gas Experiment; SAGE II). For this comparison SAGE II derived climatologies from October 1984 to August 1999 were used (published by Bauman et al., [2003b]). Before January 1989 and between June 1991 and December 1995 the LS aerosol optical parameters were strongly influenced by volcanic aerosols. Hence, only data from January 1989 to May 1991 and January 1996 to August 1999 were averaged over time and compared to the stratospheric CARIBIC dataset. The vertical gradients of the particle extinction coefficient and the particle surface area concentration match very well with only 8.6% and 4.6% difference and similar slopes in the crossover region. This agreement is better than expected, because Solomon et al [2011] showed that from 1996 to 2010 the global stratospheric aerosol optical depth increased by about 34%. On the contrary SAGE II data were measured at ambient relative humidity, whereas the OPC measured dried aerosol particles (particle shrinking by about 25%). Obviously these two effects compensate each other. Comparing the effective particle radius, in the crossover region the SAGE II median was found to be 74% higher than the CARIBIC median. This is surprising after good agreements for the

---

[51] Particle-Induced X-ray Emission

other parameter were found. The measurement at different humidity can explain only a difference of 25%. A methodical error, responsible for the remaining discrepancy of 50% is not apparent. The effective particle radius is obtained from the particle volume concentration divided by the particle surface area concentration. As the later one was found to be in good agreement, the difference might be caused by an even higher SAGE II particle volume concentration. However, considering that large scale remote sensing data are compared with averages of in situ single particle measurements recorded several years later, the agreement is still quite satisfying.

The results from the two case studies do address to the third scientific question[52], raised in the introduction of this work. The statistical analyses of the particle size distribution vertical and meridional variability and the seasonal variation in the LMS is related to the first, second, and fourth question. The negative correlation of TGM with the particle surface area concentration is linked to the fifth question. Finally, the comparisons of the CARIBIC OPC dataset to data from the GLOMAP model and the SAGE II satellite are examples for the sixth question. Please consider that all above summarized statistical analyses and comparisons are based on the first year of regular measurements. Therefore, the results do not claim to be statistically well constrained. The given examples do provide an impression, what unique kind of analysis will become possible after a few years of measurement. Only CARIBIC provides such a regular, in situ, and detailed picture of the UT/LMS region and therefore provides the opportunity for detailed statistical analyses.

Future technical work on the OPC unit should be conducted to figure out why the OPC maximum counting efficiency is 89%, but not 100%. As already shown with Fig. 5.3 and 5.8, the observed additional erroneous particle counts can be not the reason. Although it is possible to correct for the time-stable maximum counting efficiency of 89%, a higher counting efficiency would provide better statistics and thus allow to increase the temporal resolution. Moreover, a continuative work should examine whether the observed additional mode in the particle size distribution (about 600 to 900 nm) is real or an instrumental artifact.

For the particle sizing, currently (2014), the scattering signal pulse maximum is used. In future the data analysis could make use of the pulse shape and pulse area, too. The use of those additional information could allow a better size channel resolution and would probably reduce the uncertainty of the Gaussian signal distribution (Fig. 5.12). As the scattering signal pulse shape is routinely recorded for all measurements, all flight data since 2010 can be recalculated with this potential new data analysis method.

The OPC upper detection limit for size resolved measurements is 1312 nm (UTA calibration). As shown with Fig. 6.10 and 6.13, even larger particles can occur in

---

[52] Scientific questions raised in Sec. 1:
- What is the average UT/LMS particle size distribution in different climatic regions?
- Is there a trend in the UT/LMS particle size distribution?
- What are the source and sink processes for accumulation mode particles in the UT/LMS and how effective are they?
- How does the air mass exchange between UT and LS influence the particle size distribution in the tropopause region?
- How does the particle surface area concentration influence the concentration of trace gases?
- How well do remote sensing measurements and global models represent the UT/LMS aerosol?

polluted air in the UT/LMS. Therefore an expanded particle size range up to the CARIBIC aerosol inlet cut off (about 5 μm) is desirable. For the next modification of the CARIBIC container (planned for end 2016) one should aspire to install an additional particle sizing instrument with an upper detection limit of at least 5 μm (e.g. Met One OPC "GT-526"; www.metone.com; last access: 20.07.2014). Furthermore the installation of an in situ SO_2 instrument would be very helpful for a better identification of combustion- and volcanic plumes on the one hand and for a better understanding of free tropospheric/stratospheric particle nucleation on the other hand [SPARC report N°4, 2006]. Currently SO_2 is measured with the Differential Optical Absorption Spectrometer (DOAS), providing only an integral SO_2 concentration in a column between aircraft and the ground, and this only for high SO_2 concentration situations.

Bibliography

Agrawal, Y. C.: The optical volume scattering function: Temporal and vertical variability in the water column off the New Jersey coast, Limnol. Oceanogr., 50(6), 1787–1794, doi:10.4319/lo.2005.50.6.1787, 2005.

Albrecht, B. A.: Aerosols, cloud microphysics, and fractional cloudiness., Science, 245(4923), 1227–30, doi:10.1126/science.245.4923.1227, 1989.

Ansmann, A., Petzold, A., Kandler, K., Tegen, I., Wendisch, M., Müller, D., Weinzierl, B., Müller, T. and Heintzenberg, J.: Saharan Mineral Dust Experiments SAMUM-1 and SAMUM-2: what have we learned?, Tellus B, 63(4), 403–429, doi:10.1111/j.1600-0889.2011.00555.x, 2011.

Ansmann, a., Tesche, M., Seifert, P., Groß, S., Freudenthaler, V., Apituley, A., Wilson, K. M., Serikov, I., Linné, H., Heinold, B., Hiebsch, A., Schnell, F., Schmidt, J., Mattis, I., Wandinger, U. and Wiegner, M.: Ash and fine-mode particle mass profiles from EARLINET-AERONET observations over central Europe after the eruptions of the Eyjafjallajökull volcano in 2010, J. Geophys. Res., 116(D20), D00U02, doi:10.1029/2010JD015567, 2011.

Appenzeller, C., Davies, H. C. and Norton, W. A.: Fragmentation of stratospheric intrusions, J. Geophys. Res., 101(D1), 1435, doi:10.1029/95JD02674, 1996.

Bacmeister, J. T., Eckermann, S. D., Tsias, A., Carslaw, K. S. and Peter, T.: Mesoscale Temperature Fluctuations Induced by a Spectrum of Gravity Waves: A Comparison of Parameterizations and Their Impact on Stratospheric Microphysics, J. Atmos. Sci., 56(12), 1913–1924, doi:10.1175/1520-0469(1999)056, 1999.

Baltensperger, U., and Nyeki, S.: Atmospheric aerosols, in: Physical and Chemical Properties of Aerosols, p. 280-330, edited by Colbeck, I., Blackie Academic & Professional, London, Ed. 1, pp. 465, ISBN: 978-0-7514-0402-9, 1998.

Baron, P. A. and Willeke, K.: Gas and particle motion, in: Aerosol Measurement - Principles, Techniques, and Applications, edited by Baron, P. A. and Willeke, K., p. 61–82, John Wiley & Sons, New York, pp. 1160, ISBN: 0-471-35636-0, 2001.

Bauman, J. J., Russell, P. B., Geller, M. A. and Hamill, P.: A stratospheric aerosol climatology from SAGE II and CLAES measurements: 1. Methodology, J. Geophys. Res., 108(D13), 4382, doi:10.1029/2002JD002992, 2003a.

Bauman, J. J., Russell, P. B., Geller, M. A. and Hamill, P.: A stratospheric aerosol climatology from SAGE II and CLAES measurements: 2. Results and comparisons, 1984–1999, J. Geophys. Res., 108(D13), 4383, doi:10.1029/2002JD002993, 2003b.

Bigg, E. K.: A mechanism for the formation of new particles in the atmosphere, Atmos. Res., 43(2), 129–137, doi:10.1016/S0169-8095(96)00020-8, 1997.

Birmili, W., Stratmann, F., Wiedensohler, A., Covert, D., Russell, L. M. and Berg, O.: Determination of Differential Mobility Analyzer Transfer Functions Using Identical Instruments in Series, Aerosol Sci. Technol., 27(2), 215–223, doi:10.1080/02786829708965468, 1997.

Bischof, W.: Carbon Dioxide Measurements from Aircraft, Tellus, 22(5), 545–549, doi:10.1111/j.2153-3490.1970.tb00521.x, 1970.

Bohren, C. F. and Huffman, D. R.: Absorption and Scattering of Light by Small Particles, 1st ed., John Wiley & Sons, New York, pp. 530, ISBN: 0-471-05772-x, 1983.

Bolin, B. and Bischof, W.: Variations of the carbon dioxide content of the atmosphere in the northern hemisphere, Tellus, 22(4), 431–442, doi:10.1111/j.2153-3490.1970.tb00508.x, 1970.

Bond, T. C. and Bergstrom, R. W.: Light Absorption by Carbonaceous Particles: An Investigative Review, Aerosol Sci. Technol., 40, 27–67, doi:10.1080/02786820500421521, 2006.

Brenguier, J. L., Chuang, P. Y., Fouquart, Y., Johnson, D. W., Parol, F., Pawlowska, H., Pelon, J., Schuller, L., Schroder, F. and Snider, J.: An overview of the ACE-2 CLOUDYCOLUMN closure experiment, Tellus B, 52(2), 815–827, doi:10.1034/j.1600-0889.2000.00047.x, 2000.

Brenninkmeijer, C. A. M., Crutzen, P. J., Fischer, H., Güsten, H., Hans, W., Heinrich, G., Heintzenberg, J., Hermann, M., Immelmann, T., Kersting, D., Maiss, M., Nolle, M., Pitscheider, A., Pohlkamp, H., Scharffe, D., Specht, K. and Wiedensohler, A.: CARIBIC—Civil Aircraft for Global Measurement of Trace Gases and Aerosols in the Tropopause Region, J. Atmos. Ocean. Technol., 16(10), 1373–1383, doi:10.1175/1520-0426(1999)016<1373:CCAFGM>2.0.CO;2, 1999.

Brenninkmeijer, C. A. M., Crutzen, P., Boumard, F., Dauer, T., Dix, B., Ebinghaus, R., Filippi, D., Fischer, H., Franke, H., Frieβ, U., Heintzenberg, J., Helleis, F., Hermann, M., Kock, H. H., Koeppel, C., Lelieveld, J., Leuenberger, M., Martinsson, B. G., Miemczyk, S., Moret, H. P., Nguyen, H. N., Nyfeler, P., Oram, D., O'Sullivan, D., Penkett, S., Platt, U., Pupek, M., Ramonet, M., Randa, B., Reichelt, M., Rhee, T. S., Rohwer, J., Rosenfeld, K., Scharffe, D., Schlager, H., Schumann, U., Slemr, F., Sprung, D., Stock, P., Thaler, R., Valentino, F., van Velthoven, P., Waibel, A., Wandel, A., Waschitschek, K., Wiedensohler, A., Xueref-Remy, I., Zahn, A., Zech, U. and Ziereis, H.: Civil Aircraft for the regular investigation of the atmosphere based on an instrumented container: The new CARIBIC system, Atmos. Chem. Phys., 7(18), 4953–4976, doi:10.5194/acp-7-4953-2007, 2007.

Brewer, A. W.: Evidence for a world circulation provided by the measurements of helium and water vapour distribution in the stratosphere, Q. J. R. Meteorol. Soc., 75(326), 351–363, doi:10.1002/qj.49707532603, 1949.

Brock, C. A., Hamill, P., Wilson, J. C., Jonsson, H. H. and Chan, K. R.: Particle Formation in the Upper Tropical Troposphere: A Source of Nuclei for the Stratospheric Aerosol, Science (80-.)., 270(5242), 1650–1653, doi:10.1126/science.270.5242.1650, 1995.

Brockmann, J. E.: Sampling and transport of aerosols, in Aerosol Measurement - Principles, Techniques, and Applications, edited by Baron, P. A. and Willeke, K., pp. 537–568, John Wiley & Sons, New York., pp. 1160, ISBN: 0-471-35636-0, 2001.

BRONKHORST: data sheet "LOW-ΔP-FLOW MASSEDURCHFLUSSMESSER/-REGLER," Nijverheidsstraat 1a, 7261 AK Ruurlo, Netherlands. [online] Available from: www.bronkhorst.com, past access: 20.07.2014, 2009.

Brühl, C., Lelieveld, J., Crutzen, P. J. and Tost, H.: The role of carbonyl sulphide as a source of stratospheric sulphate aerosol and its impact on climate, Atmos. Chem. Phys., 12(3), 1239–1253, doi:10.5194/acp-12-1239-2012, 2012.

Brunner, D., Staehelin, J., Jeker, D., Wernli, H. and Schumann, U.: Nitrogen oxides and ozone in the tropopause region of the northern hemisphere: Measurements from commercial aircraft in 1995/1996 and 1997, J. Geophys. Res., 106(D21), 27673, doi:10.1029/2001JD900239, 2001.

Carslaw, K. S., Peter, T., Bacmeister, J. T. and Eckermann, S. D.: Widespread solid particle formation by mountain waves in the Arctic stratosphere, J. Geophys. Res., 104(D1), 1827, doi:10.1029/1998JD100033, 1999.

Chen, P.: Isentropic cross-tropopause mass exchange in the extratropics, J. Geophys. Res., 100(D8), 16661, doi:10.1029/95JD01264, 1995.

Ci, Z. J., Zhang, X. S., Wang, Z. W., Niu, Z. C., Diao, X. Y. and Wang, S. W.: Distribution and air-sea exchange of mercury (Hg) in the Yellow Sea, Atmos. Chem. Phys., 11(6), 2881–2892, doi:10.5194/acp-11-2881-2011, 2011.

Clarke, A. D. and Kapustin, V. N.: A Pacific Aerosol Survey. Part I: A Decade of Data on Particle Production, Transport, Evolution, and Mixing in the Troposphere*, J. Atmos. Sci., 59(3), 363–382, doi:10.1175/1520-0469(2002)059<0363:APASPI>2.0.CO;2, 2002.

Clement, C. F., Ford, I. F., Twohy, C. H., Weinheimer, A. and Campos, T.: Particle production in the outflow of a midlatitude storm, J. Geophys. Res., 107(D21), 4559, doi:10.1029/2001JD001352, 2002.

Cooper, O. R., Moody, J. L., Parrish, D. D., Trainer, M., Holloway, J. S., Hübler, G., Fehsenfeld, F. C. and Stohl, A.: Trace gas composition of midlatitude cyclones over the western North Atlantic Ocean: A seasonal comparison of O_3 and CO, J. Geophys. Res., 107, ACH 2–1 to 2–14, doi:10.1029/2001JD000902, 2002a.

Cooper, O. R., Moody, J. L., Parrish, D. D., Trainer, M., Ryerson, T. B., Holloway, J. S., Hübler, G., Fehsenfeld, F. C. and Evans, M. J.: Trace gas composition of midlatitude cyclones over the western North Atlantic Ocean: A conceptual model, J. Geophys. Res., 107(D7), 4056, doi:10.1029/2001JD000901, 2002b.

Cui, Z. and Carslaw, K. S.: Enhanced vertical transport efficiency of aerosol in convective clouds due to increases in tropospheric aerosol abundance, J. Geophys. Res., 111(D15), D15212, doi:10.1029/2005JD006781, 2006.

Davies, D. K., Ilavajhala, S. and Justice, C. O.: Fire Information for Resource Management System: Archiving and Distributing MODIS Active Fire Data, IEEE Trans. Geosci. Remote Sens., 47(1), 72–79, doi:10.1109/TGRS.2008.2002076, 2009.

de Reus, M., Ström, J., Kulmala, M., Pirjola, L., Lelieveld, J., Schiller, C. and Zöger, M.: Airborne aerosol measurements in the tropopause region and the dependence of new particle formation on preexisting particle number concentration, J. Geophys. Res., 103(D23), 31255, doi:10.1029/1998JD100011, 1998.

de Reus, M., Ström, J., Curtius, J., Pirjola, L., Vignati, E., Arnold, F., Hansson, H. C., Kulmala, M., Lelieveld, J. and Raes, F.: Aerosol production and growth in the upper free troposphere, J. Geophys. Res., 105(D20), 24751, doi:10.1029/2000JD900382, 2000.

de Reus, M., Krejci, R., Williams, J., Fischer, H., Scheele, R. and Ström, J.: Vertical and horizontal distributions of the aerosol number concentration and size distribution over the northern Indian Ocean, J. Geophys. Res., 106(D22), 28629 – 28641, doi:0148-0227/01/2001JD900017, 2001.

Deshler, T., Hervig, M. E., Hofmann, D. J., Rosen, J. M. and Liley, J. B.: Thirty years of in situ stratospheric aerosol size distribution measurements from Laramie, Wyoming (41°N), using balloon-borne instruments, J. Geophys. Res., 108(D5), 4167, doi:10.1029/2002JD002514, 2003.

Deshler, T.: A review of global stratospheric aerosol: Measurements, importance, life cycle, and local stratospheric aerosol, Atmos. Res., 90(2-4), 223–232, doi:10.1016/j.atmosres.2008.03.016, 2008.

Dessler, A. E.: The effect of deep, tropical convection on the tropical tropopause layer, J. Geophys. Res., 107(D3), 4033, doi:10.1029/2001JD000511, 2002.

Dessler, A. E. and Sherwood, S. C.: Effect of convection on the summertime extratropical lower stratosphere, J. Geophys. Res., 109(D23), D23301, doi:10.1029/2004JD005209, 2004.

Detwiler, A. G., Johnson, L. R. and Schauer, A. G.: Exploratory analysis of the distribution of condensation nuclei in the northern hemisphere upper troposphere and lower stratosphere during the late 1970s, J. Geophys. Res., 105(D7), 9265, doi:10.1029/2000JD900022, 2000.

Dias-Lalcaca, P., Brunner, D., Imfeld, W., Moser, W. and Staehelin, J.: An Automated System for the Measurement of Nitrogen Oxides and Ozone Concentrations from a Passenger Aircraft: Instrumentation and First Results of the NOXAR Project, Environ. Sci. Technol., 32(20), 3228–3236, doi:10.1021/es980119w, 1998.

Dibb, J. E., Talbot, R. W., Scheuer, E. M., Blake, D. R., Blake, N. J., Gregory, G. L., Sachse, G. W. and Thornton, D. C.: Aerosol chemical composition and distribution during the Pacific Exploratory Mission (PEM) Tropics, J. Geophys. Res., 104, 5785–5800, doi:10.1029/1998JD100001, 1999.

Dibb, J. E., Talbot, R. W. and Scheuer, E. M.: Composition and distribution of aerosols over the North Atlantic during the Subsonic Assessment Ozone and Nitrogen Oxide Experiment (SONEX), J. Geophys. Res., 105(D3), 3709, doi:10.1029/1999JD900424, 2000.

Dibb, J. E., Talbot, R. W., Scheuer, E., Seid, G., DeBell, L., Lefer, B. and Ridley, B.: Stratospheric influence on the northern North American free troposphere during TOPSE: 7 Be as a stratospheric tracer, J. Geophys. Res., 108(D4), 8363, doi:10.1029/2001JD001347, 2003.

Dick, W. D., Ziemann, P. J. and McMurry, P. H.: Multiangle Light-Scattering Measurements of Refractive Index of Submicron Atmospheric Particles, Aerosol Sci. Technol., 41(5), 549–569, doi:10.1080/02786820701272012, 2007.

Ditas, F., Shaw, R. a., Siebert, H., Simmel, M., Wehner, B. and Wiedensohler, A.: Aerosols-cloud microphysics-thermodynamics-turbulence: evaluating supersaturation in a marine stratocumulus cloud, Atmos. Chem. Phys., 12(5), 2459–2468, doi:10.5194/acp-12-2459-2012, 2012.

Dobson, G. M. B., Brewer, A. W. and Cwilong, B. M.: Bakerian Lecture. Meteorology of the Lower Stratosphere, Proc. R. Soc. A Math. Phys. Eng. Sci., 185(1001), 144–175, doi:10.1098/rspa.1946.0010, 1946.

Dye, J. E., Ridley, B. A., Skamarock, W., Barth, M., Venticinque, M., Defer, E., Blanchct, P., Thery, C., Laroche, P., Baumann, K., Hubler, G., Parrish, D. D., Ryerson, T., Trainer, M., Frost, G., Holloway, J. S., Matejka, T., Bartels, D., Fehsenfeld, F. C., Tuck, A., Rutledge, S. A., Lang, T., Stith, J. and Zerr, R.: An overview of the Stratospheric-Tropospheric Experiment: Radiation, Aerosols, and Ozone (STERAO)-Deep Convection experiment with results for the July 10, 1996 storm, J. Geophys. Res., 105, 10023–10046, doi:0148-0227100119991D0111, 2000.

Ebinghaus, R., Slemr, F., Brenninkmeijer, C. a. M., van Velthoven, P., Zahn, a., Hermann, M., O'Sullivan, D. a. and Oram, D. E.: Emissions of gaseous mercury from biomass burning in South America in 2005 observed during CARIBIC flights, Geophys. Res. Lett., 34(8), 1–5, doi:10.1029/2006GL028866, 2007.

Eichkorn, S., Wilhelm, S., Aufmhoff, H., Wohlfrom, K. H. and Arnold, F.: Cosmic ray-induced aerosol-formation: First observational evidence from aircraft-based ion mass spectrometer measurements in the upper troposphere, Geophys. Res. Lett., 29(14), 1698, doi:10.1029/2002GL015044, 2002.

Ekman, A. M. L., Wang, C., Ström, J. and Krejci, R.: Explicit Simulation of Aerosol Physics in a Cloud-Resolving Model: Aerosol Transport and Processing in the Free Troposphere, J. Atmos. Sci., 63(2), 682–696, doi:10.1175/JAS3645.1, 2006.

English, J. M., Toon, O. B., Mills, M. J. and Yu, F.: Microphysical simulations of new particle formation in the upper troposphere and lower stratosphere, Atmos. Chem. Phys., 11(17), 9303–9322, doi:10.5194/acp-11-9303-2011, 2011.

Esler, J. G., Tan, D. G. H., Haynes, P. H., Evans, M. J., Law, K. S., Plantevin, P.-H. and Pyle, J. A.: Stratosphere-troposphere exchange: Chemical sensitivity to mixing, J. Geophys. Res., 106(D5), 4717, doi:10.1029/2000JD900405, 2001.

Fabian, P. and Pruchniewicz, P. G.: Meridional distribution of ozone in the troposphere and its seasonal variations, J. Geophys. Res., 82(15), 2063–2073, doi:10.1029/JC082i015p02063, 1977.

Fischer, H., Wienhold, F. G., Hoor, P., Bujok, O., Schiller, C., Siegmund, P., Ambaum, M., Scheeren, H. A. and Lelieveld, J.: Tracer correlations in the northern high latitude lowermost stratosphere: Influence of cross-tropopause mass exchange, Geophys. Res. Lett., 27(1), 97–100, doi:10.1029/1999GL010879, 2000.

Fischer, H., de Reus, M., Traub, M., Williams, J., Lelieveld, J., de Gouw, J., Warneke, C., Schlager, H., Minikin, A., Scheele, R. and Siegmund, P.: Deep convective injection of boundary layer air into the lowermost stratosphere at midlatitudes, Atmos. Chem. Phys., 3(3), 739–745, doi:10.5194/acp-3-739-2003, 2003.

Flagan, R. C.: Electrical techniques, in Aerosol Measurement - Principles, Techniques, and Applications, edited by Baron, P. A. and Willeke, K., pp. 537–568, John Wiley & Sons, New York., pp. 1160, ISBN: 0-471-35636-0, 2001.

Flentje, H., Claude, H., Elste, T., Gilge, S., Köhler, U., Plass-Dülmer, C., Steinbrecht, W., Thomas, W., Werner, a. and Fricke, W.: The Eyjafjallajökull eruption in April 2010 – detection of volcanic plume using in-situ measurements, ozone sondes and lidar-ceilometer profiles, Atmos. Chem. Phys., 10(20), 10085–10092, doi:10.5194/acp-10-10085-2010, 2010.

Fromm, M., Alfred, J., Hoppel, K., Hornstein, J., Bevilacqua, R., Shettle, E., Servranckx, R., Li, Z. and Stocks, B.: Observations of boreal forest fire smoke in the stratosphere by POAM III, SAGE II, and lidar in 1998, Geophys. Res. Lett., 27(9), 1407–1410, doi:10.1029/1999GL011200, 2000.

Fromm, M. D. and Servranckx, R.: Transport of forest fire smoke above the tropopause by supercell convection, Geophys. Res. Lett., 30(10), n/a–n/a, doi:10.1029/2002GL016820, 2003.

Fromm, M., Bevilacqua, R., Servranckx, R., Rosen, J., Thayer, J. P., Herman, J. and Larko, D.: Pyro-cumulonimbus injection of smoke to the stratosphere: Observations and impact of a super blowup in northwestern Canada on 3–4 August 1998, J. Geophys. Res., 110(D8), D08205, doi:10.1029/2004JD005350, 2005.

Froyd, K. D., Murphy, D. M., Sanford, T. J., Thomson, D. S., Wilson, J. C., Pfister, L. and Lait, L.: Aerosol composition of the tropical upper troposphere, Atmos. Chem. Phys., 9(13), 4363–4385, doi:10.5194/acp-9-4363-2009, 2009.

Fujiwara, M. and Takahashi, M.: Role of the equatorial Kelvin wave in stratosphere-troposphere exchange in a general circulation model, J. Geophys. Res., 106(D19), 22763, doi:10.1029/2000JD000161, 2001.

Gertisser, R.: Eyjafjallajökull volcano causes widespread disruption to European air traffic, Geol. Today, 26(3), 94–95, doi:10.1111/j.1365-2451.2010.00757.x, 2010.

Gettelman, A. and Sobel, A. H.: Direct Diagnoses of Stratosphere–Troposphere Exchange, J. Atmos. Sci., 57(1), 3–16, doi:10.1175/1520-0469(2000)057<0003:DDOSTE>2.0.CO;2, 2000.

Gettelman, A., Salby, M. L. and Sassi, F.: Distribution and influence of convection in the tropical tropopause region, J. Geophys. Res., 107(D10), 4080, doi:10.1029/2001JD001048, 2002.

Gettelman, A., Kinnison, D. E., Dunkerton, T. J. and Brasseur, G. P.: Impact of monsoon circulations on the upper troposphere and lower stratosphere, J. Geophys. Res., 109(D22), D22101, doi:10.1029/2004JD004878, 2004.

Gettelman, A., Hoor, P., Pan, L. L., Randel, W. J., Hegglin, M. I. and Birner, T.: THE EXTRATROPICAL UPPER TROPOSPHERE AND LOWER STRATOSPHERE, Rev. Geophys., 49(3), RG3003, doi:10.1029/2011RG000355, 2011.

Ginoux, P.: Effects of nonsphericity on mineral dust modeling, J. Geophys. Res., 108(D2), 4052, doi:10.1029/2002JD002516, 2003.

Gíslason, S. R. and Alfredsson, H. A.: Travelogue: Sampling the volcanic ash from the Eyjafjallajökull volcano, Iceland, Elements, 6(4), 269–270, ISSN: 1811-5217 (online), 2010.

Hamill, P., Jensen, E. J., Russell, P. B. and Bauman, J. J.: The Life Cycle of Stratospheric Aerosol Particles, Bull. Am. Meteorol. Soc., 78, 1395–1410, doi:10.1175/1520-0477(1997)078, 1997.

Hanisco, T. F., Moyer, E. J., Weinstock, E. M., St. Clair, J. M., Sayres, D. S., Smith, J. B., Lockwood, R., Anderson, J. G., Dessler, A. E., Keutsch, F. N., Spackman, J. R., Read, W. G. and Bui, T. P.: Observations of deep convective influence on stratospheric water vapor and its isotopic composition, Geophys. Res. Lett., 34(4), L04814, doi:10.1029/2006GL027899, 2007.

Hanson, D. R., Ravishankara, A. R. and Solomon, S.: Heterogeneous reactions in sulfuric acid aerosols: A framework for model calculations, J. Geophys. Res., 99(D2), 3615, doi:10.1029/93JD02932, 1994.

Haverkamp, H., Wilhelm, S., Sorokin, A. and Arnold, F.: Positive and negative ion measurements in jet aircraft engine exhaust: concentrations, sizes and implications for aerosol formation, Atmos. Environ., 38(18), 2879–2884, doi:10.1016/j.atmosenv.2004.02.028, 2004.

Hegglin, M. I., Brunner, D., Wernli, H., Schwierz, C., Martius, O., Hoor, P., Fischer, H., Spelten, N., Schiller, C., Krebsbach, M., Parchatka, U., Weers, U., Staehelin, J. and Peter, T.: Tracing troposphere-to-stratosphere transport above a mid-latitude deep convective system, Atmos. Chem. Phys. Discuss., 4(1), 169–206, doi:10.5194/acpd-4-169-2004, 2004.

Heintzenberg, J., Hermann, M., Martinsson, B. G. and Papaspiropoulos, G.: Number and sulfur derived 3-parameter aerosol size distributions in the tropopause region from CARIBIC flights between Germany and the Indic, J. Aerosol Sci., 33(4), 595–608, doi:10.1016/S0021-8502(01)00196-3, 2002.

Heintzenberg, J., Hermann, M., Weigelt, A., Clarke, A., Kapustin, V., Anderson, B., Thornhill, K., Velthoven, P. Van, Zahn, A. and Brenninkmeijer, C.: Near-global aerosol mapping in the upper troposphere and lowermost stratosphere with data from the CARIBIC project, Tellus B, 63(5), 875–890, doi:10.1111/j.1600-0889.2011.00578.x, 2011.

Hermann, M. and Wiedensohler, A.: Counting efficiency of condensation particle counters at low-pressures with illustrative data from the upper troposphere, J. Aerosol Sci., 32(8), 975–991, doi:10.1016/S0021-8502(01)00037-4, 2001.

Hinds, W. C.: Aerosol Technology - Properties, Behavior, and Measurement of Airborne Particles, 2nd ed., John Wiley & Sons, New York., pp. 504, ISBN: 978-0-471-19410-1, 1999.

Hintsa, E. J., Boering, K. A., Weinstock, E. M., Anderson, J. G., Gary, B. L., Pfister, L., Daube, B. C., Wofsy, S. C., Loewenstein, M., Podolske, J. R., Margitan, J. J. and Bui, T. P.: Troposphere-to-stratosphere transport in the lowermost stratosphere from measurements of H_2O, CO_2 , N_2O and O_3, Geophys. Res. Lett., 25(14), 2655–2658, doi:10.1029/98GL01797, 1998.

Hobbs, P. V.: Aerosol-cloud interactions, in Aerosol-Cloud-Climate Interactions, International Geophysics Series, edited by P. V. Hobbs, Vol. 54, Academic Press, San Diego, pp. 233, ISBN: 0-12-350725-1, 1993.

Hoerling, M. P., Schaack, T. K. and Lenzen, A. J.: Global Objective Tropopause Analysis, Mon. Weather Rev., 119(8), 1816–1831, doi:10.1175/1520-0493(1991)119, 1991.

Hofmann, D. J.: Increase in the stratospheric background sulfuric Acid aerosol mass in the past 10 years., Science, 248(4958), 996–1000, doi:10.1126/science.248.4958.996, 1990.

Holton, J. R., Haynes, P. H., McIntyre, M. E., Douglass, A. R., Rood, R. B. and Pfister, L.: Stratosphere-troposphere exchange, Rev. Geophys., 33(4), 403–440, doi:10.1029/95RG02097, 1995.

Hoor, P., Fischer, H. and Lelieveld, J.: Tropical and extratropical tropospheric air in the lowermost stratosphere over Europe: A CO-based budget, Geophys. Res. Lett., 32(7), L07802, doi:10.1029/2004GL022018, 2005.

Horvath, H.: Influence of atmospheric aerosols upon the global radiation balance, p. 543-596, in: Atmospheric Particles - IUPAC Series on Analytical and Physical Chemistry of Environmental Systems, edited by R. M. Harrison and R. van Grieken, Vol. 5, *John Wiley & Sons*, Chichester, Edition 1, pp. 622, ISBN: 0-471-95935-9, 1998.

Hummel, J. R., Shettle, E. P. and Longtin, D. R.: A New Background Stratospheric Aerosol Model for Use in Atmospheric Radiation Models, AFGL–TR–88–0166, Air Force Geophysics Laboratory, 1988.

Hynes, A. J., Donohue, D. L., Goodsite, M. E. and Hedgecock, I. M.: Our current understanding of major chemical and physical processes affecting mercury dynamics in the atmosphere and at the air-water/terrestrial interfaces., pp. 427–457, in Mercury Fate and Transport in the Global Atmosphere, edited by N. Pirrone and R. Mason, Springer, Dordrecht., pp. 637, ISBN: 978-0-387-93958-2, 2009.

IPCC (Intergovernmental Panel on Climate Change): Climate Change 2013 The Physical Science Basis, edited by T. F. Stocker, D. Qin, G.-K. Plattner, M. M. B. Tignor, S. K. Allen, J. Boschung, A. Nauels, Y. Xia, V. Bex, and P. M. Midgley, Cambridge University Press, New York., 2013.

Jacobson, M. Z., Wilkerson, J. T., Naiman, a. D. and Lele, S. K.: The effects of aircraft on climate and pollution. Part I: Numerical methods for treating the subgrid evolution of discrete size- and composition-resolved contrails from all commercial flights worldwide, J. Comput. Phys., 230(12), 5115–5132, doi:10.1016/j.jcp.2011.03.031, 2011.

Jaenicke, R.: Tropospheric aerosols, in: Aerosol-Cloud-Climate Interactions, edited by P. V. Hobbs, p. 1–31, Academic Press, San Diego, Ed. 1, Vol. 54, pp. 234, ISBN: 0-12-350725-1, 1993.

Jaenicke, R.: Atmospheric aerosol size distribution, in: Atmospheric Particles - IUPAC Series on Analytical and Physical Chemistry of Environmental Systems, edited by Harrison, R. M. and R. van Grieken, p. 1-28, John Wiley & Sons, Chichester, Ed. 1, Vol.   5,   pp.   610, ISBN: 0-471-95935-9, 1998.

James, R. and Legras, B.: Mixing processes and exchanges in the tropical and the subtropical UT/LS, Atmos. Chem. Phys., 9(1), 25–38, doi:10.5194/acp-9-25-2009, 2009.

Jing, P., Cunnold, D. M., Wang, H. J. and Yang, E.-S.: Isentropic Cross-Tropopause Ozone Transport in the Northern Hemisphere, J. Atmos. Sci., 61(9), 1068–1078, doi:10.1175/1520-0469(2004)061<1068:ICOTIT>2.0.CO;2, 2004.

Jing, P.: Influence of isentropic transport on seasonal ozone variations in the lower stratosphere and subtropical upper troposphere, J. Geophys. Res., 110(D10), D10110, doi:10.1029/2004JD005416, 2005.

Jordan, C. E., Dibb, J. E. and Finkel, R. C.: ^{10}Be/ ^{7}Be tracer of atmospheric transport and stratosphere-troposphere exchange, J. Geophys. Res., 108(D8), 4234, doi:10.1029/2002JD002395, 2003.

Jost, H.-J., Drdla, K., Stohl, A., Pfister, L., Loewenstein, M., Lopez, J. P., Hudson, P. K., Murphy, D. M., Cziczo, D. J., Fromm, M., Bui, T. P., Dean-Day, J., Gerbig, C., Mahoney, M. J., Richard, E. C., Spichtinger, N., Pittman, J. V., Weinstock, E. M., Wilson, J. C. and Xueref, I.: In-situ observations of mid-latitude forest fire plumes deep in the stratosphere, Geophys. Res. Lett., 31(11), L11101, doi:10.1029/2003GL019253, 2004.

Junge, C. E., Chagnon, C. W. and Manson, J. E.: Stratospheric aerosols, J. Meteorol., 18(1), 81–108, doi:10.1175/1520-0469(1961)018, 1961.

Justice, C. ., Giglio, L., Korontzi, S., Owens, J., Morisette, J. ., Roy, D., Descloitres, J., Alleaume, S., Petitcolin, F. and Kaufman, Y.: The MODIS fire products, Remote Sens. Environ., 83(1-2), 244–262, doi:10.1016/S0034-4257(02)00076-7, 2002.

Kanawade, V. and Tripathi, S. N.: Evidence for the role of ion-induced particle formation during an atmospheric nucleation event observed in Tropospheric Ozone Production about the Spring Equinox (TOPSE), J. Geophys. Res., 111(D2), D02209, doi:10.1029/2005JD006366, 2006.

Kavouras, I. G., Mihalopoulos, N. and Stephanou, E. G.: Formation of atmospheric particles from organic acids produced by forests, Nature, 395(6703), 683–686, doi:10.1038/27179, 1998.

Khosrawi, F. and Konopka, P.: Enhanced particle formation and growth due to mixing processes in the tropopause region, Atmos. Environ., 37, 903–910, doi:10.1016/S1352-2310(02)00976-7, 2003.

Kim, Y. K., Lee, H. W., Park, J. K. and Moon, Y. S.: The stratosphere–troposphere exchange of ozone and aerosols over Korea, Atmos. Environ., 36(3), 449–463, doi:10.1016/S1352-2310(01)00370-3, 2002.

Klekociuk, A. R., Brown, P. G., Pack, D. W., ReVelle, D. O., Edwards, W. N., Spalding, R. E., Tagliaferri, E., Yoo, B. B. and Zagari, J.: Meteoritic dust from the atmospheric disintegration of a large meteoroid., Nature, 436(7054), 1132–5, doi:10.1038/nature03881, 2005.

Kojima, T., Buseck, P. R., Wilson, J. C., Reeves, J. M. and Mahoney, M. J.: Aerosol particles from tropical convective systems: Cloud tops and cirrus anvils, J. Geophys. Res., 109(D12), D12201, doi:10.1029/2003JD004504, 2004.

Korhonen, P., Kulmala, M., Laaksonen, A., Viisanen, Y., McGraw, R. and Seinfeld, J. H.: Ternary nucleation of H_2SO_4, NH_3 and H_2O in the atmosphere, J. Geophys. Res., 104(D21), 26326–349353, 1999.

Korolev, a. V., Emery, E. F., Strapp, J. W., Cober, S. G., Isaac, G. a., Wasey, M. and Marcotte, D.: Small Ice Particles in Tropospheric Clouds: Fact or Artifact? Airborne Icing Instrumentation Evaluation Experiment, Bull. Am. Meteorol. Soc., 92(8), 967–973, doi:10.1175/2010BAMS3141.1, 2011.

Kulmala, M., Pirjola, L. and Mäkelä, M.: Stable sulphate clusters as a source of new atmospheric particles, Nature, 404, 66–69 [online] Available from: http://www.nature.com/nature/journal/v404/n6773/abs/404066a0.html, 2000.

Krejci, R., Ström, J., de Reus, M., Hoor, P., Williams, J., Fischer, H. and Hansson, H.-C.: Evolution of aerosol properties over the rain forest in Surinam, South America, observed from aircraft during the LBA-CLAIRE 98 experiment, J. Geophys. Res., 108(D18), 4561, doi:10.1029/2001JD001375, 2003.

Kulmala, M.: Atmospheric science. How particles nucleate and grow., Science, 302(5647), 1000–1, doi:10.1126/science.1090848, 2003.

Kulmala, M., Vehkamäki, H., Petäjä, T., Dal Maso, M., Lauri, A., Kerminen, V.-M., Birmili, W. and McMurry, P. H.: Formation and growth rates of ultrafine atmospheric particles: a review of observations, J. Aerosol Sci., 35(2), 143–176, doi:10.1016/j.jaerosci.2003.10.003, 2004.

Kulmala, M., Reissell, A., Sipilä, M., Bonn, B., Ruuskanen, T. M., Lehtinen, K. E. J., Kerminen, V.-M. and Ström, J.: Deep convective clouds as aerosol production engines: Role of insoluble organics, J. Geophys. Res., 111(D17), D17202, doi:10.1029/2005JD006963, 2006.

Laakso, L., Mäkelä, J. M., Pirjola, L. and Kulmala, M.: Model studies on ion-induced nucleation in the atmosphere, J. Geophys. Res., 107(D20), 4427, doi:10.1029/2002JD002140, 2002.

Laaksonen, A., Pirjola, L., Kulmala, M., Arnold, F. and Raes, F.: Upper tropospheric SO$_2$ conversion into sulfuric acid aerosols and cloud condensation nuclei, J. Geophys. Res., 105(D1), 1459–1469, doi:10.1029/1999JD900933, 2000.

Lacis, A., Hansen, J. and Sato, M.: Climate forcing by stratospheric aerosols, Geophys. Res. Lett., 19(15), 1607–1610, doi:10.1029/92GL01620, 1992.

Lauer, A. and Hendricks, J.: Simulating aerosol microphysics with the ECHAM4/MADE GCM – Part II: Results from a first multiannual simulation of the submicrometer aerosol, Atmos. Chem. Phys., 6(12), 5495–5513, doi:10.5194/acp-6-5495-2006, 2006.

Lee, S.-H., Reeves, J. M., Wilson, J. C., Hunton, D. E., Viggiano, A. A., Miller, T. M., Ballenthin, J. O. and Lait, L. R.: Particle formation by ion nucleation in the upper troposphere and lower stratosphere., Science, 301(5641), 1886–9, doi:10.1126/science.1087236, 2003.

Lee, S.-H., Wilson, J. C., Baumgardner, D., Hermann, R. L., Weinstock, E. M., LaFleur, B. G., Kok, G., Anderson, B., Lawson, P., Baker, B., Strawa, A., Pittman, J. V, Reeves, J. M. and Bui, T. B.: New particle formation observed in the tropical/subtropical cirrus clouds, J. Geophys. Res., 109(D20), D20209, doi:10.1029/2004JD005033, 2004.

Li, J., Posfai, M., Hobbs, P. V. and Buseck, P. R.: Individual aerosol particles from biomass burning in southern Africa: 2, Compositions and aging of inorganic particles, J. Geophys. Res., 108(D13), 8484, doi:10.1029/2002JD002310, 2003.

Liljequist, G. H. and Cehak, K., Eds.: Allgemeine Meteorologie, 3rd ed., vieweg, Braunschweig/Wiesbaden., pp. 412, ISBN: 3-528-23555-1, 1984.

Lin, C.-J., Pongprueksa, P., Lindberg, S. E., Pehkonen, S. O., Byun, D. and Jang, C.: Scientific uncertainties in atmospheric mercury models I: Model science evaluation, Atmos. Environ., 40(16), 2911–2928, doi:10.1016/j.atmosenv.2006.01.009, 2006.

Lindberg, S., Bullock, R., Ebinghaus, R., Engstrom, D., Feng, X., Fitzgerald, W., Pirrone, N., Prestbo, E. and Seigneur, C.: A Synthesis of Progress and Uncertainties in Attributing the Sources of Mercury in Deposition, AMBIO A J. Hum. Environ., 36(1), 19–33 [online] Available from: http://www.bioone.org/doi/full/10.1579/0044-7447(2007)36[19:ASOPAU last access: 20.07.2014, 2007.

LKM electronic GmbH: data sheet - LKM electronic TYP 104, [online] Available from: www.LKMelectronic.de, last access: 20.07.2014, 2004.

Lohmann, U. and Feichter, J.: Global indirect aerosol effects: a review, Atmos. Chem. Phys., 5(3), 715–737, doi:10.5194/acp-5-715-2005, 2005.

Lovejoy, E. R., Curtius, J. and Froyd, K. D.: Atmospheric ion-induced nucleation of sulfuric acid and water, J. Geophys. Res., 109(D8), D08204, doi:10.1029/2003JD004460, 2004.

Lyman, S. N. and Jaffe, D. a.: Formation and fate of oxidized mercury in the upper troposphere and lower stratosphere, Nat. Geosci., 5(2), 114–117, doi:10.1038/ngeo1353, 2011.

Machida, T., Matsueda, H., Sawa, Y., Nakagawa, Y., Hirotani, K., Kondo, N., Goto, K., Nakazawa, T., Ishikawa, K. and Ogawa, T.: Worldwide Measurements of Atmospheric CO 2 and Other Trace Gas Species Using Commercial Airlines, J. Atmos. Ocean. Technol., 25(10), 1744–1754, doi:10.1175/2008JTECHA1082.1, 2008.

Mäkelä, J. M., Aalto, P., Jokinen, V., Pohja, T., Nissinen, A., Palmroth, S., Markkanen, T., Seitsonen, K., Lihavainen, H. and Kulmala, M.: Observations of ultrafine aerosol particle formation and growth in boreal forest, Geophys. Res. Lett., 24(10), 1219–1222, doi:10.1029/97GL00920, 1997.

Mann, G. W., Carslaw, K. S., Spracklen, D. V, Ridley, D. A., Manktelow, P. T., Chipperfield, M. P., Pickering, S. J. and Johnson, C. E.: Description and evaluation of GLOMAP-mode: a modal global aerosol microphysics model for the UKCA composition-climate model, Geosci. Model Dev., 3(2), 519–551, doi:10.5194/gmd-3-519-2010, 2010.

Marenco, A., Thouret, V., Nédélec, P., Smit, H., Helten, M., Kley, D., Karcher, F., Simon, P., Law, K., Pyle, J., Poschmann, G., Von Wrede, R., Hume, C. and Cook, T.: Measurement of ozone and water vapor by Airbus in-service aircraft: The MOZAIC airborne program, an overview, J. Geophys. Res., 103(D19), 25631, doi:10.1029/98JD00977, 1998.

Martinsson, B. G., Brenninkmeijer, C. a. M., Carn, S. a., Hermann, M., Heue, K.-P., van Velthoven, P. F. J. and Zahn, A.: Influence of the 2008 Kasatochi volcanic eruption on sulfurous and carbonaceous aerosol constituents in the lower stratosphere, Geophys. Res. Lett., 36(12), L12813, doi:10.1029/2009GL038735, 2009.

Martinsson, B. G., Friberg, J., Andersson, S. M., Weigelt, A., Hermann, M., Assmann, D., Voigtländer, J., Brenninkmeijer, C. A. M., van Velthoven, P. J. F. and Zahn, A.: Comparison between CARIBIC Aerosol Samples Analysed by Accelerator-Based Methods and Optical Particle Counter Measurements, Atmos. Meas. Tech., 7(8), 2581–2596, doi:10.5194/amt-7-2581-2014, 2014.

Matsueda, H. and Inoue, H. Y.: Measurements of atmospheric CO_2 and CH_4 using a commercial airliner from 1993 to 1994, Atmos. Environ., 30(10-11), 1647–1655, doi:10.1016/1352-2310(95)00374-6, 1996.

McCaffery, S. J., McKeen, S. A., Hsie, E.-Y., Parrish, D. D., Cooper, O. R., Holloway, J. S., Hübler, G., Fehsenfeld, F. C. and Trainer, M.: A case study of stratosphere-troposphere exchange during the 1996 North Atlantic Regional Experiment, J. Geophys. Res., 109(D14), D14103, doi:10.1029/2003JD004007, 2004.

McCormick, M. P., Thomason, L. W. and Trepte, C. R.: Atmospheric effects of the Mt Pinatubo eruption, Nature, 373(6513), 399–404, doi:10.1038/373399a0, 1995.

Meilinger, S. K., Koop, T., Luo, B. P., Huthwelker, T., Carslaw, K. S., Krieger, U., Crutzen, P. J. and Peter, T.: Size-dependent stratospheric droplet composition in Lee wave temperature fluctuations and their potential role in PSC freezing, Geophys. Res. Lett., 22(22), 3031–3034, doi:10.1029/95GL03056, 1995.

Menzies, R. T. and Tratt, D. M.: Evidence of seasonally dependent stratosphere-troposphere exchange and purging of lower stratospheric aerosol from a multiyear lidar data set, J. Geophys. Res., 100(D2), 3139, doi:10.1029/94JD02848, 1995.

Mészáros, E.: The atmospheric aerosol, in: Atmospheric Particles and Nuclei, p. 17-84, edited by Götz, G., Mészáros, E., and Vali, G., Akadémiai Kiadó, Budapest, Ed. 1, pp. 274, ISBN: 963-05-5682-0, 1991.

Mie, G.: Beiträge zur Optik trüber Medien, speziell kolloidaler Metallösungen, Ann. Phys., Vierte Folge, 25 (3), p. 377-445, 1908.

Minikin, A., Petzold, A., Ström, J., Krejci, R., Seifert, M., van Velthoven, P., Schlager, H. and Schumann, U.: Aircraft observations of the upper tropospheric fine particle aerosol in the Northern and Southern Hemispheres at midlatitudes, Geophys. Res. Lett., 30(10), doi:10.1029/2002GL016458, 2003.

Morgan, W. T., Allan, J. D., Bower, K. N., Capes, G., Crosier, J., Williams, P. I. and Coe, H.: Vertical distribution of sub-micron aerosol chemical composition from North-Western Europe and the North-East Atlantic, Atmos. Chem. Phys., 9(15), 5389–5401, doi:10.5194/acp-9-5389-2009, 2009.

Morgenstern, O. and Carver, G. D.: Comparison of cross-tropopause transport and ozone in the upper troposphere and lower stratosphere region, J. Geophys. Res., 106(D10), 10205, doi:10.1029/2000JD900802, 2001.

Mühle, J., Brenninkmeijer, C. A. M., Rhee, T. S., Slemr, F., Oram, D. E., Penkett, S. A. and Zahn, A.: Biomass burning and fossil fuel signatures in the upper troposphere observed during a CARIBIC flight from Namibia to Germany, Geophys. Res. Lett., 29(19), 1910, doi:10.1029/2002GL015764, 2002.

Mullendore, G. L., Durran, D. R. and Holton, J. R.: Cross-tropopause tracer transport in midlatitude convection, J. Geophys. Res., 110(D6), D06113, doi:10.1029/2004JD005059, 2005.

Murphy, D. M., Thomson, D. S. and Mahoney, M. J.: In Situ Measurements of Organics, Meteoritic Material, Mercury, and Other Elements in Aerosols at 5 to 19 Kilometers, Science (80)., 282(5394), 1664–1669, doi:10.1126/science.282.5394.1664, 1998.

Murphy, D. M., Hudson, P. K., Thomson, D. S., Sheridan, P. J. and Wilson, J. C.: Observations of Mercury-Containing Aerosols, Environ. Sci. Technol., 40(10), 3163–3167, doi:10.1021/es052385x, 2006.

Murphy, D. M., Cziczo, D. J., Hudson, P. K. and Thomson, D. S.: Carbonaceous material in aerosol particles in the lower stratosphere and tropopause region, J. Geophys. Res., 112(D4), D04203, doi:10.1029/2006JD007297, 2007.

Nedelec, P., Thouret, V., Brioude, J., Sauvage, B., Cammas, J.-P. and Stohl, A.: Extreme CO concentrations in the upper troposphere over northeast Asia in June 2003 from the in situ MOZAIC aircraft data, Geophys. Res. Lett., 32(14), doi:10.1029/2005GL023141, 2005.

Nguyen, H. N., Gudmundsson, A. and Martinsson, B. G.: Design and Calibration of a Multi-Channel Aerosol Sampler for Tropopause Region Studies from the CARIBIC Platform, Aerosol Sci. Technol., 40(8), 649–655, doi:10.1080/02786820600767807, 2006.

Nguyen, H. N. and Martinsson, B. G.: Analysis of C, N and O in aerosol collected on an organic backing using internal blank measurements and variable beam size, Nucl. Instruments Methods Phys. Res. Sect. B Beam Interact. with Mater. Atoms, 264(1), 96–102, doi:10.1016/j.nimb.2007.08.001, 2007.

Nguyen, H. N., Martinsson, B. G., Wagner, J. B., Carlemalm, E., Ebert, M., Weinbruch, S., Brenninkmeijer, C. A. M., Heintzenberg, J., Hermann, M., Schuck, T., van Velthoven, P. F. J. and Zahn, A.: Chemical composition and morphology of individual aerosol particles from a CARIBIC flight at 10 km altitude between 50°N and 30°S, J. Geophys. Res., 113(D23), D23209, doi:10.1029/2008JD009956, 2008.

Nilsson, E. D. and Kulmala, M.: The potential for atmospheric mixing processes to enhance the binary nucleation rate, J. Geophys. Res., 103(D1), 1381, doi:10.1029/97JD02629, 1998.

Nilsson, E. D., Pirjola, L. and Kulmala, M.: The effect of atmospheric waves on aerosol nucleation and size distribution, J. Geophys. Res., 105(D15), 19917, doi:10.1029/1999JD901102, 2000.

Notholt, J., Luo, B. P., Fueglistaler, S., Weisenstein, D., Rex, M., Lawrence, M. G., Bingemer, H., Wohltmann, I., Cort, T., Warneke, T., Kuhlmann, R. von and Peter, T.: Influence of tropospheric SO 2 emissions on particle formation and the stratospheric humidity, Geophys. Res. Lett., 32(7), L07810, doi:10.1029/2004GL022159, 2005.

O'Dowd, C. D., Aalto, P., Hmeri, K., Kulmala, M. and Hoffmann, T.: Aerosol formation: atmospheric particles from organic vapours., Nature, 416(6880), 497–8, doi:10.1038/416497a, 2002.

Ohara, T., Akimoto, H., Kurokawa, J., Horii, N., Yamaji, K., Yan, X. and Hayasaka, T.: An Asian emission inventory of anthropogenic emission sources for the period 1980–2020, Atmos. Chem. Phys., 7(16), 4419–4444, doi:10.5194/acp-7-4419-2007, 2007.

Olsen, M. a.: Stratosphere-troposphere exchange of mass and ozone, J. Geophys. Res., 109(D24), D24114, doi:10.1029/2004JD005186, 2004.

Paladino, J. D., Hagen, D. E., Whitefield, P. D., Hopkins, A. R., Schmid, O., Wilson, M. R., Schlager, H. and Schulte, P.: Observations of particulates within the North Atlantic Flight Corridor: POLINAT 2, September-October 1997, J. Geophys. Res., 105(D3), 3719, doi:10.1029/1999JD901071, 2000.

Pan, L. L., Randel, W. J., Gary, B. L., Mahoney, M. J. and Hintsa, E. J.: Definitions and sharpness of the extratropical tropopause: A trace gas perspective, J. Geophys. Res., 109(D23), D23103, doi:10.1029/2004JD004982, 2004.

Pandis, S. N., Wexler, A. S. and Seinfeld, J. H.: Dynamics of Tropospheric Aerosols, J. Phys. Chem., 99(24), 9646–9659, doi:10.1021/j100024a003, 1995.

Papaspiropoulos, G., Mentes, B., Kristiansson, P. and Martinsson, B. .: A high sensitivity elemental analysis methodology for upper tropospheric aerosol, Nucl. Instruments Methods Phys. Res. Sect. B Beam Interact. with Mater. Atoms, 150(1-4), 356–362, doi:10.1016/S0168-583X(98)01082-9, 1999.

Papaspiropoulos, G., Martinsson, B. G., Zahn, A., Brenninkmeijer, C. A. M., Hermann, M., Heintzenberg, J., Fischer, H. and van Velthoven, P. F. J.: Aerosol elemental concentrations in the tropopause region from intercontinental flights with the Civil Aircraft for Regular Investigation of the Atmosphere Based on an Instrument Container (CARIBIC) platform, J. Geophys. Res., 107(D23), 4671, doi:10.1029/2002JD002344, 2002.

Perkins, P. J. and L. C. Papathakos, Global sensing of gaseous and aerosol trace species using automated instrumentation on 747 airliners, p. 307-312, Proceedings of the 4th Joint Conference on Sensing Environmental Pollutants, New Orleans, Louisiana, 6.-11. November, 1977, Washington, D.C., American Chemical Society, 1977.

Petersen, G. N.: A short meteorological overview of the Eyjafjallajökull eruption 14 April-23 May 2010, Weather, 65(8), 203–207, doi:10.1002/wea.634, 2010.

Petzold, A., Fiebig, M., Flentje, H., Keil, A., Leiterer, U., Schröder, F., Stifter, A., Wendisch, M. and Wendling, P.: Vertical variability of aerosol properties observed at a continental site during the Lindenberg Aerosol Characterization Experiment (LACE 98), J. Geophys. Res., 107(D21), 8128, doi:10.1029/2001JD001043, 2002.

Pinnick, R. G. and Auvermann, H. J.: Response characteristics of knollenberg light-scattering aerosol counters, J. Aerosol Sci., 10(1), 55–74, doi:10.1016/0021-8502(79)90136-8, 1979.

Pratt, K. A. and Prather, K. A.: Aircraft measurements of vertical profiles of aerosol mixing states, J. Geophys. Res., 115(D11), D11305, doi:10.1029/2009JD013150, 2010.

Presto, A. a., Nguyen, N. T., Ranjan, M., Reeder, A. J., Lipsky, E. M., Hennigan, C. J., Miracolo, M. a., Riemer, D. D. and Robinson, A. L.: Fine particle and organic vapor emissions from staged tests of an in-use aircraft engine, Atmos. Environ., 45(21), 3603–3612, doi:10.1016/j.atmosenv.2011.03.061, 2011.

Radke, L. F., Friedli, H. R. and Heikes, B. G.: Atmospheric mercury over the NE Pacific during spring 2002: Gradients, residence time, upper troposphere lower stratosphere loss, and long-range transport, J. Geophys. Res., 112(D19), 1–17, doi:10.1029/2005JD005828, 2007.

Rasch, P. J., Tilmes, S., Turco, R. P., Robock, A., Oman, L., Chen, C.-C., Stenchikov, G. L. and Garcia, R. R.: An overview of geoengineering of climate using stratospheric sulphate aerosols., Philos. Trans. A. Math. Phys. Eng. Sci., 366(1882), 4007–37, doi:10.1098/rsta.2008.0131, 2008.

Rauthe-Schöch, A., Weigelt, A., Hermann, M., Martinsson, B. G., Baker, a. K., Heue, K.-P., Brenninkmeijer, C. a. M., Zahn, A., Scharffe, D., Eckhardt, S., Stohl, A. and van Velthoven, P. F. J.: CARIBIC aircraft measurements of Eyjafjallajökull volcanic clouds in April/May 2010, Atmos. Chem. Phys., 12(2), 879–902, doi:10.5194/acp-12-879-2012, 2012.

Reichelt, M.: Entwicklung und atmosphärische Anwendung eines optischen Partikelspektrometers für Tropopausenbedingungen, dissertation, 288 pp., Universität Leipzig., 2007.

Riese, M., Ploeger, F., Rap, A., Vogel, B., Konopka, P., Dameris, M. and Forster, P.: Impact of uncertainties in atmospheric mixing on simulated UTLS composition and related radiative effects, J. Geophys. Res., 117(D16), D16305, doi:10.1029/2012JD017751, 2012.

RION CO., LTD.: Instruction manual process counter KS-93. pp. 47, http:///www.rion.co.jp/english/, 2008.

RTCA/DO-160E , RTCA, Inc., RTCA/DO-160E Environmental Conditions and Test Procedures for Airborne Equipment, Section 21: Emission of Radio Frequency Energy, 1828 L Street, NW Suite 805, Washington DC 20036, 2004.

Sanderson, K.: Volcanology: Out of the ashes., Nature, 465(7298), 544–5, doi:10.1038/465544a, 2010.

Scheele, M. P., Siegmund, P. C. and Van Velthoven, P. F. J.: Sensitivity of trajectories to data resolution and its dependence on the starting point: In or outside a tropopause fold, Meteorol. Appl., 3(3), 267–273, doi:10.1002/met.5060030308, 2007.

Schladitz, A., Müller, T., Nordmann, S., Tesche, M., Groß, S., Freudenthaler, V., Gasteigner, J. and Wiedensohler, A.: In situ aerosol characterization at Cape Verde, Tellus B, 63(4), 549–572, doi:10.1111/j.1600-0889.2011.00568.x, 2011.

Schoeberl, M. R., Lait, L. R., Newman, P. A. and Rosenfield, J. E.: The structure of the polar vortex, J. Geophys. Res., 97(D8), 7859, doi:10.1029/91JD02168, 1992.

Schröder, F., Kärcher, B., Fiebig, M. and Petzold, A.: Aerosol states in the free troposphere at northern midlatitudes, J. Geophys. Res., 107(D21), 8126, doi:10.1029/2000JD000194, 2002.

Schumann, U., Weinzierl, B., Reitebuch, O., Schlager, H., Minikin, A., Forster, C., Baumann, R., Sailer, T., Graf, K., Mannstein, H., Voigt, C., Rahm, S., Simmet, R., Scheibe, M., Lichtenstern, M., Stock, P., Rüba, H., Schäuble, D., Tafferner, A., Rautenhaus, M., Gerz, T., Ziereis, H., Krautstrunk, M., Mallaun, C., Gayet, J.-F., Lieke, K., Kandler, K., Ebert, M., Weinbruch, S., Stohl, A., Gasteiger, J., Groß, S., Freudenthaler, V., Wiegner, M., Ansmann, A., Tesche, M., Olafsson, H. and Sturm, K.: Airborne observations of the Eyjafjalla volcano ash cloud over Europe during air space closure in April and May 2010, Atmos. Chem. Phys., 11(5), 2245–2279, doi:10.5194/acp-11-2245-2011, 2011.

Schwarz, J. P., Gao, R. S., Fahey, D. W., Thomson, D. S., Watts, L. A., Wilson, J. C., Reeves, J. M., Darbeheshti, M., Baumgardner, D. G., Kok, G. L., Chung, S. H., Schulz, M., Hendricks, J., Lauer, A., Kärcher, B., Slowik, J. G., Rosenlof, K. H., Thompson, T. L., Langford, A. O., Loewenstein, M. and Aikin, K. C.: Single-particle measurements of midlatitude black carbon and light-scattering aerosols from the boundary layer to the lower stratosphere, J. Geophys. Res., 111(D16), D16207, doi:10.1029/2006JD007076, 2006.

Schwarz, J. P., Spackman, J. R., Gao, R. S., Watts, L. A., Stier, P., Schulz, M., Davis, S. M., Wofsy, S. C. and Fahey, D. W.: Global-scale black carbon profiles observed in the remote atmosphere and compared to models, Geophys. Res. Lett., 37(18), n/a–n/a, doi:10.1029/2010GL044372, 2010.

Seinfeld, J. H. and Pandis, S. N.: Atmospheric Chemistry and Physics, 1st ed., John Wiley & Sons, New York, pp. 1326, ISBN: 0-471-17816-0, 1998.

Selin, N. E., Jacob, D. J., Yantosca, R. M., Strode, S., Jaeglé, L. and Sunderland, E. M.: Global 3-D land-ocean-atmosphere model for mercury: Present-day versus preindustrial cycles and anthropogenic enrichment factors for deposition, Global Biogeochem. Cycles, 22(2), doi:10.1029/2007GB003040, 2008.

SENSORTECHNICS: data sheet - BTE5000 / PTE5000 / PTU5000 Series Precision differential pressure transmitters, [online] Available from: www.sensortechnics.com, last access: 20.07.2014, 2008.

Seo, K.-H. and Bowman, K. P.: A climatology of isentropic cross-tropopause exchange, J. Geophys. Res. Atmos., 106(D22), 28159–28172, doi:10.1029/2000JD000295, 2001.

Seo, K.-H. and Bowman, K. P.: Lagrangian estimate of global stratosphere-troposphere mass exchange, J. Geophys. Res., 107(D21), 4555, doi:10.1029/2002JD002441, 2002.

Sigmundsson, F., Hreinsdóttir, S., Hooper, A., Arnadóttir, T., Pedersen, R., Roberts, M. J., Oskarsson, N., Auriac, A., Decriem, J., Einarsson, P., Geirsson, H., Hensch, M., Ofeigsson, B. G., Sturkell, E., Sveinbjörnsson, H. and Feigl, K. L.: Intrusion triggering of the 2010 Eyjafjallajökull explosive eruption., Nature, 468(7322), 426–30, doi:10.1038/nature09558, 2010.

Singh, H. B., Anderson, B. E., Avery, M. A., Viezee, W., Chen, Y., Tabazadeh, A., Hamill, P., Pueschel, R., Fuelberg, H. E. and Hannan, J. R.: Global distribution and sources of volatile and nonvolatile aerosol in the remote troposphere, J. Geophys. Res., 107(D11), 4121, doi:10.1029/2001JD000486, 2002.

Škerlak, B., Sprenger, M. and Wernli, H.: A global climatology of stratosphere–troposphere exchange using the ERA-Interim data set from 1979 to 2011, Atmos. Chem. Phys., 14(2), 913–937, doi:10.5194/acp-14-913-2014, 2014.

Slade, W. H. and Boss, E. S.: Calibrated near-forward volume scattering function obtained from the LISST particle sizer, Opt. Express, 14(8), 3602, doi:10.1364/OE.14.003602, 2006.

Slemr, F., Ebinghaus, R., Brenninkmeijer, C. a. M., Hermann, M., Kock, H. H., Martinsson, B. G., Schuck, T., Sprung, D., van Velthoven, P., Zahn, A. and Ziereis, H.: Gaseous mercury distribution in the upper troposphere and lower stratosphere observed onboard the CARIBIC passenger aircraft, Atmos. Chem. Phys., 9(6), 1957–1969, doi:10.5194/acp-9-1957-2009, 2009.

Solomon, S., Daniel, J. S., Neely, R. R., Vernier, J.-P., Dutton, E. G. and Thomason, L. W.: The persistently variable "background" stratospheric aerosol layer and global climate change., Science, 333(6044), 866–70, doi:10.1126/science.1206027, 2011.

Solomons, T. W. G.: Organic Chemistry, John Wiley & Sons, New York, pp. 568, ISBN: 978-0471120919, 1996.

Spackman, J. R., Weinstock, E. M., Anderson, J. G., Hurst, D. F., Jost, H.-J. and Schauffler, S. M.: Aircraft observations of rapid meridional transport from the tropical tropopause layer into the lowermost stratosphere: Implications for midlatitude ozone, J. Geophys. Res., 112(D12), D12308, doi:10.1029/2006JD007618, 2007.

Spracklen, D. V, Pringle, K. J., Carslaw, K. S., Chipperfield, M. P. and Mann, G. W.: A global off-line model of size-resolved aerosol microphysics: I. Model development and prediction of aerosol properties, Atmos. Chem. Phys., 5(8), 2227–2252, doi:10.5194/acp-5-2227-2005, 2005a.

Spracklen, D. V., Pringle, K. J., Carslaw, K. S., Chipperfield, M. P. and Mann, G. W.: A global off-line model of size-resolved aerosol microphysics: II. Identification of key uncertainties, Atmos. Chem. Phys., 5(12), 3233–3250, doi:10.5194/acp-5-3233-2005, 2005b.

SPARC Report No. 4 from the WMO (World Meteorological Organization): WMO/SPARC Scientific Assessment of Stratospheric Aerosol Properties (ASAP), edited by: Thomason, L. and Peter, T. [online] Available from: http://www.sparc-climate.org/publications/sparc-reports/sparc-report-no4/, last access: 20.07.2014, pp. 348, 2006.

Sprenger, M.: Tropopause folds and cross-tropopause exchange: A global investigation based upon ECMWF analyses for the time period March 2000 to February 2001, J. Geophys. Res., 108(D12), 8518, doi:10.1029/2002JD002587, 2003.

Sprenger, M. and Wernli, H.: A northern hemispheric climatology of cross-tropopause exchange for the ERA15 time period (1979–1993), J. Geophys. Res., 108(D12), 8521, doi:10.1029/2002JD002636, 2003.

Stohl, A.: A 1-year Lagrangian "climatology" of airstreams in the northern hemisphere troposphere and lowermost stratosphere, J. Geophys. Res., 106(D7), 7263, doi:10.1029/2000JD900570, 2001.

Stohl, A., Forster, C., Frank, A., Seibert, P. and Wotawa, G.: Technical note: The Lagrangian particle dispersion model FLEXPART version 6.2, Atmos. Chem. Phys., 5(9), 2461–2474, doi:10.5194/acp-5-2461-2005, 2005.

Stohl, A., Prata, A. J., Eckhardt, S., Clarisse, L., Durant, A., Henne, S., Kristiansen, N. I., Minikin, A., Schumann, U., Seibert, P., Stebel, K., Thomas, H. E., Thorsteinsson, T., Tørseth, K. and Weinzierl, B.: Determination of time- and height-resolved volcanic ash emissions and their use for quantitative ash dispersion modeling: the 2010 Eyjafjallajökull eruption, Atmos. Chem. Phys., 11(9), 4333–4351, doi:10.5194/acp-11-4333-2011, 2011.

Streets, D. G., Bond, T. C., Carmichael, G. R., Fernandes, S. D., Fu, Q., He, D., Klimont, Z., Nelson, S. M., Tsai, N. Y., Wang, M. Q., Woo, J.-H. and Yarber, K. F.: An inventory of gaseous and primary aerosol emissions in Asia in the year 2000, J. Geophys. Res., 108(D21), 8809, doi:10.1029/2002JD003093, 2003.

Swartzendruber, P. C., Jaffe, D. A. and Finley, B.: Development and First Results of an Aircraft-Based, High Time Resolution Technique for Gaseous Elemental and Reactive (Oxidized) Gaseous Mercury, Environ. Sci. Technol., 43(19), 7484–7489, doi:10.1021/es901390t, 2009.

Talbot, R., Mao, H., Scheuer, E., Dibb, J. and Avery, M.: Total depletion of Hg° in the upper troposphere–lower stratosphere, Geophys. Res. Lett., 34(23), 1–5, doi:10.1029/2007GL031366, 2007.

Thornton, D. C., Bandy, A. R., Blomquist, B. W., Bradshaw, J. D. and Blake, D. R.: Vertical transport of sulfur dioxide and dimethyl sulfide in deep convection and its role in new particle formation, J. Geophys. Res., 102 (D23), 20,501–520,509, 1997.

Toon, O. B., Pollack, J. B. and Khare, B. N.: The optical constants of several atmospheric aerosol species: Ammonium sulfate, aluminum oxide, and sodium chloride, J. Geophys. Res., 81(33), 5733–5748, doi:10.1029/JC081i033p05733, 1976.

TSI: Model 3010 Condensation Particle Counter - Instruction Manual, [online] Available from: http://www.iac.ethz.ch/education/master/curriculum/lab_field_work/atmospheric_phys ics_lab_work/TSI-3010.pdf, last access: 30.03.2011, 2002.

TSI: Model 3076 Constant Output Atomizer - Operation and Service Manual, [online] Available from: http://tsi.hosting.onvoy.com/documents/1933076K-3076.pdf, last access: 30.03.2011, 2008.

Tsias, A., Prenni, A. J., Carslaw, K. S., Onasch, T. P., Luo, B. P., Tolbert, M. A. and Peter, T.: Freezing of polar stratospheric clouds in orographically induced strong warming events, Geophys. Res. Lett., 24(18), 2303–2306, doi:10.1029/97GL02181, 1997.

Tuck, a. F.: Exchange between the upper tropical troposphere and the lower stratosphere studied with aircraft observations, J. Geophys. Res., 108(D23), 4734, doi:10.1029/2003JD003399, 2003.

Twohy, C. H., Clement, C. F., Gandrud, B. W., Weinheimer, A. J., Campos, T. L., Baumgardner, D., Brune, W. H., Faloona, I., Sachse, G. W., Vay, S. A. and Tan, D.: Deep convection as a source of new particles in the midlatitude upper troposphere, J. Geophys. Res., 107(D21), 4560, doi:10.1029/2001JD000323, 2002.

Twomey, S.: The influence of Pollution on the Shortwave Albedo of Clouds, J. Atmos. Sci., 34, 1149–1152, 1977.

van de Hulst, H. C.: Light Scattering by Small Particles, 2nd ed., Dover Publications, New York, pp. 470, ISBN: 0-486-64228-3, 1981.

van Velthoven, P. F. J.: Meteorological analysis of CARIBIC, [online] Available from: http://www.knmi.nl/samenw/campaign_support/CARIBIC/, last access: 20.07.2014.

Wang, P. K.: Moisture plumes above thunderstorm anvils and their contributions to cross-tropopause transport of water vapor in midlatitudes, J. Geophys. Res., 108(D6), 4194, doi:10.1029/2002JD002581, 2003.

Weigelt, A., Hermann, M., van Velthoven, P. F. J., Brenninkmeijer, C. A. M., Schlaf, G., Zahn, A. and Wiedensohler, A.: Influence of clouds on aerosol particle number concentrations in the upper troposphere, J. Geophys. Res., 114(D1), D01204, doi:10.1029/2008JD009805, 2009.

Wiedensohler, A.: Die bipolare Diffusionsaufladung von Partikeln in chemisch trägen Reinstgasen, Ph.D. thesis Universität (GHS) Duisburg., pp. 110, 1989.

Wiedensohler, A., Orsini, D., Covert, D. S., Coffmann, D., Cantrell, W., Havlicek, M., Brechtel, F. J., Russell, L. M., Weber, R. J., Gras, J., Hudson, J. G. and Litchy, M.: Intercomparison Study of the Size-Dependent Counting Efficiency of 26 Condensation Particle Counters, Aerosol Sci. Technol., 27(2), 224–242, doi:10.1080/02786829708965469, 1997.

Williams, J., Fischer, H., Wong, S., Crutzen, P. J., Scheele, M. P. and Lelieveld, J.: Near equatorial CO and O_3 profiles over the Indian Ocean during the winter monsoon: High O_3 levels in the middle troposphere and interhemispheric exchange, J. Geophys. Res., 107(D19), 8007, doi:10.1029/2001JD001126, 2002a.

Williams, J., de Reus, M., Krejci, R., Fischer, H. and Ström, J.: Application of the variability-size relationship to atmospheric aerosol studies: estimating aerosol lifetimes and ages, Atmos. Chem. Phys., 2(2), 133–145, doi:10.5194/acp-2-133-2002, 2002b.

Wilson, J. C., Lee, S.-H., Reeves, J. M., Brock, C. A., Jonsson, H. H., Lafleur, B. G., Loewenstein, M., Podolske, J., Atlas, E., Boering, K., Toon, G., Fahey, D., Bui, T. P., Diskin, G. and Moore, F.: Steady-state aerosol distributions in the extra-tropical, lower stratosphere and the processes that maintain them, Atmos. Chem. Phys., 8, 6617–6626, doi:10.5194/acp-8-6617-2008, 2008.

Winkler, P.: Verteilung und Chemie des atmosphärischen Aerosols - Atmosphärisches Aerosol, in: Handbuch der Umweltveränderungen und Ökotoxikologie – Band 1B: Atmosphäre: Aerosol/Multiphasenchemie - Ausbreitung und Deposition von Spurenstoffen - Auswirkungen auf Strahlung und Klima, edited by R. Guderian, Springer, Berlin, Ed. 2, pp. 516, ISBN: 3-540-66185-9, 2000.

Winklmayr, W., Reischl, G. P., Lindner, A. O. and Berner, A.: A new electromobility spectrometer for the measurement of aerosol size distributions in the size range from 1 to 1000 nm, J. Aerosol Sci., 22(3), 289–296, doi:10.1016/S0021-8502(05)80007-2, 1991.

WMO (World Meteorological Organization): Atmospheric Ozone 1985 - Assessment of our Understanding of the Processes Controlling its Present Distribution and Change, in Global Ozone Research and Monitoring Project Report No. 16, Vol. 1-3, p. 1096, Geneva, Switzerland., 1986.

Yin, Y., Carslaw, K. S. and Feingold, G.: Vertical transport and processing of aerosols in a mixed-phase convective cloud and the feedback on cloud development, Q. J. R. Meteorol. Soc., 131(605), 221–245, doi:10.1256/qj.03.186, 2005.

Young, L.-H., Benson, D. R., Montanaro, W. M., Lee, S.-H., Pan, L. L., Rogers, D. C., Jensen, J., Stith, J. L., Davis, C. A., Campos, T. L., Bowman, K. P., Cooper, W. A. and Lait, L. R.: Enhanced new particle formation observed in the northern midlatitude tropopause region, J. Geophys. Res., 112(D10), D10218, doi:10.1029/2006JD008109, 2007.

Yu, F. and Turco, R. P.: The role of ions in the formation and evolution of particles in aircraft plumes, Geophys. Res. Lett., 24(15), 1927–1930, doi:10.1029/97GL01822, 1997.

Zachariasse, M., Smit, H. G. J., van Velthoven, P. F. J. and Kelder, H.: Cross-tropopause and interhemispheric transports into the tropical free troposphere over the Indian   Ocean,   J.   Geophys.   Res.,   106(D22),   28441–28452, doi:10.1029/2001JD900061, 2001.

Zahn, A., Brenninkmeijer, C. A. M., Maiss, M., Scharffe, D. H., Crutzen, P. J., Hermann, M., Heintzenberg, J., Wiedensohler, A., Güsten, H., Heinrich, G., Fischer, H., Cuijpers, J. W. M. and van Velthoven, P. F. J.: Identification of extratropical two-way troposphere-stratosphere mixing based on CARIBIC measurements of O_3, CO, and ultrafine particles, J. Geophys. Res., 105(D1), 1527, doi:10.1029/1999JD900759, 2000.

Zahn, A. and Brenninkmeijer, C. A. .: New Directions: A Chemical Tropopause Defined, Atmos. Environ., 37(3), 439–440, doi:10.1016/S1352-2310(02)00901-9, 2003.

Zaizen, Y., Okada, K., Ikegami, M., Sawa, Y. and Makino, Y.: Number-size Distributions of Aerosol Particles in the Free Troposphere over the Northwestern Pacific Ocean-Influence of Asian Outflow and Tropical Air Transport, J. Meteorol. Soc. Japan, 82(4), 1147–1160, doi:10.2151/jmsj.2004.1147, 2004.

Zeng, G. and Pyle, J. A.: Influence of El Niño Southern Oscillation on stratosphere/troposphere exchange and the global tropospheric ozone budget, Geophys. Res. Lett., 32(1), L01814, doi:10.1029/2004GL021353, 2005.

Acknowledgements

Curriculum Vitae (28.05.2015)

Dipl.-Met. Andreas Weigelt

Dorfstr. 191b
21365 Adendorf, Germany

Mobile	+49 (0) 162 6325278
Email	Andreas-Weigelt@gmx.de
Birthday	10/07/1982
Nationality	German
Family status	married, 1 child

Professional Experience

05/2011 – 05/2015   **Helmholtz Zentrum Geesthacht**, Geesthacht (Germany)
Institute of Costal Research
Department: Environmental Research
Position: Scientist
- Organization, preparation, and accomplishment of several measurement campaigns on board different research and civil aircraft (as flight operator)
- Responsible for maintenance and scientific data analysis of ground based speciated atmospheric mercury measurements at measurement sites in Germany, Ireland, and South Africa

07/2007 – 04/2011   **Leibniz-Institut for Tropospheric Research,** Leipzig (Germany)
Department: Atmospheric Aerosols
Position: PhD student
- Preparation of dissertation "An optical particle counter for the regular application onboard a passenger aircraft: instrument modification, characterization and results from the first year of operation"

05/2006 – 06/2007   **Leibniz-Institut for Tropospheric Research,** Leipzig (Germany)
Department: Atmospheric Aerosols
Position: Diploma student (equivalent to master student)
- Preparation of diploma thesis "Modification of aerosol particles by clouds in the upper troposphere"

10/2004 – 02/2006   **Universität Leipzig,** Leipzig (Germany)
Faculty: Physic and Earth Sciences
Institute: Meteorology
Position: student assistant
- Seminar assistance

Academic Career
10/2001 – 06/2007   **Universität Leipzig,** Leipzig (Germany)
Study: Meteorology (diploma)

Publications (May 2015)

<u>Per reviewed publications:</u>

Song, S., Selin, N. E., Soerensen, A. L., Angot, H., Artz, R., Brooks, S., Brunke, E.-G., Conley, G., Dommergue, A., Ebinghaus, R., Holsen, T. M., Jaffe, D. A., Kang, S., Kelley, P., Luke, W. T., Magand, O., Marumoto, K., Pfaffhuber, K. A., Ren, X., Sheu, G.-R., Slemr, F., Warneke, T., **Weigelt, A.**, Weiss-Penzias, P., Wip, D. C. and Zhang, Q.: Top-down constraints on atmospheric mercury emissions and implications for global biogeochemical cycling, Atmos. Chem. Phys. Discuss., 15, 5269–5325, doi:10.5194/acpd-15-5269-2015, 2015.

Slemr, F., Angot, H., Dommergue, A., Magand, O., Barret, M., **Weigelt, A.**, Ebinghaus, R., Brunke, E.-G., Pfaffhuber, K. A., Edwards, G., Howard, D., Powell, J., Keywood, M. and Wang, F.: Comparison of mercury concentrations measured at several sites in the Southern Hemisphere, Atmos. Chem. Phys., 15, 3125–3133, doi:10.5194/acp-15-3125-2015, 2015.

Weigelt, A., Ebinghaus, R., Manning, A. J., Derwent, R. G., Simmonds, P. G., Spain, G. T., Jennings, S. G. and Slemr, F.: Analysis and interpretation of 18 years of mercury observations since 1996 at Mace Head, Ireland, Atmos. Environ., 100, 85–93, doi:10.1016/j.atmosenv.2014.10.050, 2014

Martinsson, B. G., Friberg, J., Andersson, S. M., **Weigelt, A.**, Hermann, M., Assmann, D., Voigtländer, J., Brenninkmeijer, C. A. M., van Velthoven, P. J. F. and Zahn, A.: Comparison between CARIBIC Aerosol Samples Analysed by Accelerator-Based Methods and Optical Particle Counter Measurements, Atmos. Meas. Tech., 7(8), 2581–2596, doi:10.5194/amt-7-2581-2014, 2014.

Slemr, F., **Weigelt, A.**, Ebinghaus, R., Brenninkmeijer, C., Baker, A., Schuck, T., Rauthe-Schöch, A., Riede, H., Leedham, E., Hermann, M., van Velthoven, P., Oram, D., O'Sullivan, D., Dyroff, C., Zahn, A. and Ziereis, H.: Mercury Plumes in the Global Upper Troposphere Observed during Flights with the CARIBIC Observatory from May 2005 until June 2013, Atmosphere (Basel)., 5(2), 342–369, doi:10.3390/atmos5020342, 2014.

Bieser, J., De Simone, F., Gencarelli, C., Geyer, B., Hedgecock, I., Matthias, V., Travnikov, O. and **Weigelt, A**.: A diagnostic evaluation of modeled mercury wet depositions in Europe using atmospheric speciated high-resolution observations., Environ. Sci. Pollut. Res. Int., doi:10.1007/s11356-014-2863-2, 2014.

Weigelt, A., Temme, C., Bieber, E., Schwerin, A., Schuetze, M., Ebinghaus, R. and Kock, H. H.: Measurements of atmospheric mercury species at a German rural background site from 2009 to 2011 – methods and results, Environ. Chem., 10(2), 102–110, doi:10.1071/EN12107, 2013.
--- Chosen as one of 20 "highlight papers 2013 in Environmental Chemistry" ---

Rauthe-Schöch, A., **Weigelt, A.**, Hermann, M., Martinsson, B. G., Baker, a. K., Heue, K.-P., Brenninkmeijer, C. a. M., Zahn, A., Scharffe, D., Eckhardt, S., Stohl, A. and van Velthoven, P. F. J.: CARIBIC aircraft measurements of Eyjafjallajökull volcanic clouds in April/May 2010, Atmos. Chem. Phys., 12(2), 879–902, doi:10.5194/acp-12-879-2012, 2012.

Heintzenberg, J., Hermann, M., **Weigelt, A.**, Clarke, A., Kapustin, V., Anderson, B., Thornhill, K., Velthoven, P. Van, Zahn, A. and Brenninkmeijer, C.: Near-global aerosol mapping in the upper troposphere and lowermost stratosphere with data from the CARIBIC project, Tellus B, 63(5), 875–890, doi:10.1111/j.1600-0889.2011.00578.x, 2011.

Lai, S. C., Baker, A. K., Schuck, T. J., van Velthoven, P., Oram, D. E., Zahn, A., Hermann, M., **Weigelt, A.**, Slemr, F., Brenninkmeijer, C. A. M. and Ziereis, H.: Pollution events observed during CARIBIC flights in the upper troposphere between South China and the Philippines, Atmos. Chem. Phys., 10(4), 1649–1660, doi:10.5194/acp-10-1649-2010, 2010.

Weigelt, A., Hermann, M., van Velthoven, P. F. J., Brenninkmeijer, C. A. M., Schlaf, G., Zahn, A. and Wiedensohler, A.: Influence of clouds on aerosol particle number concentrations in the upper troposphere, J. Geophys. Res., 114(D1), D01204, doi:10.1029/2008JD009805, 2009.

C. Brenninkmeijer, F. Slemr, T. Schuck, D. Scharffe, C. Koeppel, M. Pupek, P. Jöckel, J. Lelieveld, P. Crutzen, T. S. Rhee, M. Hermann, **A. Weigelt**, M. Reichelt, J. Heintzenberg, A. Zahn, D. Sprung, H. Fischer, H. Ziereis, H. Schlager, U. Schumann, B. Dix, U. Friess, U. Platt, R. Ebinghaus, B. Martinsson, H. N. Nguyen, D. Oram, D. O'Sullivan, S. Penkett, P. van Velthoven, T. Röckmann, G. Pieterse, S. Assonov, M. Ramonet, I. Xueref-Remy, P. Ciais, S. Reimann, M. Vollmer, M. Leuenberger, and F. L. Valentino: The CARIBIC aircraft system for detailed, long-term, global-scale measurement of trace gases and aerosol in a changing atmosphere, IGACtivities, *37*, 2-9, 2007

International reports:

Pirrone, N., …, **Weigelt, A**., …: UNEP Mercury Air Transport and Fate Research Partnership Area; Section C: Atmospheric Pathways, Transport and Fate; Subsection 5: Atmospheric Mercury Measurements and Trends Worldwide, Editor: Pirrone, N., UNEP, http://www.unep.org/hazardoussubstances/Mercury/MercuryPublications/GlobalAtmosphericMercuryAss essmentSourcesEm/tabid/3618/language/en-US/Default.aspx, 2012

Invited talks:

Weigelt, A., Ebinghaus, R., Bieser, J., Schwerin, A., Schütze, M., Bieber, E., Hawkins, L.: Long term speciated atmospheric mercury measurements at a Central European rural background site, University of Yantai, China, Institute of Atmosphere, September 27, 2014

Contribution to conferences (only first or presenting authorships):

Weigelt, A., Ebinghaus, R., Pirrone, N., Bödewadt, J., Ammoscato, A., Esposito, Bieser, J., and Slemr, F., Mercury vertical profiles, measured in August 2013 over different locations in central Europe. Oral presentation at the 17th International Conference on Heavy Metals in the Environment (ICHMET 2014), Guiyang, China, September 22.- 26., 2014.

Weigelt, A., Ebinghaus, R., Pirrone, N., Bödewadt, J., Ammoscato, A., Esposito, Bieser, J., and Slemr, F., Airborne measurements of mercury emissions from a modern coal fired power plant in central Europe. Oral presentation at the 17th International Conference on Heavy Metals in the Environment (ICHMET 2014), Guiyang, China, September 22.- 26., 2014.

Weigelt, A., Ebinghaus, R., Pirrone, N., Bödewadt, J., Ammoscato, A., Esposito, Sprovieri, F. Mannario, V., Montagnoii, M., and Slemr, F., Airborne mercury measurements in the plume of the Mt. Etna volcano (Italy) in July/August 2012. Poster presentation at the 17th International Conference on Heavy Metals in the Environment (ICHMET 2014), Guiyang, China, September 22.- 26., 2014.

Slemr, F., **Weigelt, A.**, Ebinghaus, R., Manning, A.J., Derwent, R.G., Simmonds, P.G., Spain, T.G., and Jennings, S.G., Analysis and interpretation of 18 years of mercury observations since 1996 at Mace Head, Ireland. Poster presentation by Weigelt, A. at the 17th International Conference on Heavy Metals in the Environment (ICHMET 2014), Guiyang, China, September 22.- 26., 2014.

Weigelt, A., Ebinghaus, R., Pirrone, N., Ammoscato, A., Esposito, G., Mather, T., Aiuppa, A., Glasow, R. and, Slemr, F., GMOS - European Tropospheric Mercury Experiment (ETMEP) Part-1: Trans-Italy flights and the Mt. Etna region. Oral presentation at the 11th International Conference on Mercury as a Global Pollutant (ICMGP2013), Edinburgh, Scotland, July 28.- August 02., 2013.

Weigelt, A., Bieber, E., Temme, C., Kock, H.H., Schwerin, A., Schuetze, M., and Ebinghaus, R., Speciated mercury measurements in ambient air from 2009 to 2011 at a Central European rural background monitoring site, Oral presentation at the 16th International Conference on Heavy Metals in the Environment (ICHMET2012), Rome,Italy, September 23.- 27., 2012.

Ebinghaus, R., Jennings, S.G., Kock, H.H., Derwent, R.G., Manning, A.J., Spain, T.G., and **Weigelt, A.**, Decreasing trends in total gaseous mercury observations in baseline air at Mace Head, Ireland from 1996 to 2011, Poster presentation by Weigelt, A. at the 16th International Conference on Heavy Metals in the Environment (ICHMET2012), Rome,Italy, September 23.- 27., 2012.

Weigelt A., M. Hermann, F. Höpner, P. F. J. van Velthoven, C. A. M. Brenninkmeijer, J. Heintzenberg, and A. Wiedensohler, Influence of clouds on aerosol particle number concentrations in the middle and upper troposphere in different climatic regions, Poster presentation at the International Aerosol Conference (IAC), Helsinki, Finland, August 29. - September 3. 2010.

Weigelt A., M. Hermann, P. F. J. van Velthoven, C. A. M. Brenninkmeijer, J. Heintzenberg, and A. Wiedensohler, Influence of clouds on aerosol particle number concentrations in the upper troposphere – Results from the CARIBIC project, Poster presentation at the European Aerosol Conference (EAC), Salzburg, Austria, September 9.-14. 2007.

Contribution to international workshops (only first or presenting authorships):

Weigelt, A., Slemr, F., Weber, S., Scharffe, D., and Zahn, A.: Hg instrument – status and prospects, CARIBIC workshop 2014, Mainz/Germany, October 21 – 23, 2014.

Weigelt, A., Ebinghaus, R., Boedewadt, J., Bieser, J., Matthias, V., Pirrone, N., Ammoscato, I., Esposito, G., Sprovieri, F., Mannarino, V., Montagnoli, M., Slemr, F., Brenninkmeijer, C., and many others: Highlights from the European Tropospheric Mercury Experiment (ETMEP) in 2012 and 2013, Global Mercury Observation System (GMOS) meeting 2014, Rome/Italy, July 09 – 10, 2014.

Weigelt, A., Ebinghaus, R., Schwerin, A., Schuetze, M.: Low GOM concentration at GMOS master site Waldhof/Germany, Global Mercury Observation System (GMOS) meeting 2014, Rome/Italy, July 09 – 10, 2014.

Weigelt, A., Ebinghaus, R., Bieser, J., Bödewadt, J., Matthias, V., Pirrone, N., Sprovieri, F., Ammoscato, I., Esposito, G., Mannarino, V., Montagnoli, M., von Glasow, R., Mather, T., Witt, M., Aiuppa, A., Slemr, F., and many others: Airborne mercury measurements within the GMOS project, Global Mercury Observation System (GMOS) WP-7,8 workshop 2014, Hamburg/Germany, February 12, 2014

Weigelt, A.: CARIBIC in the GMOS project, CARIBIC workshop 2013, Mainz/Germany, November 27 – 29, 2013.

Weigelt, A., Ebinghaus, R., Schwerin, A., Schuetze, M., Spain, G., Brunke, E.-G., Labuschagne, C., Slemr, F., Brenninkmeijer, C., Pirrone, N., Ammoscato, I., Esposito, G., Sprovieri, F., and many others: Measurement sites Waldhof (Germany), Mace Head (Ireland), Cape Point (South Africa), as well as CARIBIC and ETMEP (both airborne), Global Mercury Observation System (GMOS) meeting 2013, Rome/Italy, June 10 – 12, 2013.

Weigelt, A., Ebinghaus, R., Bödewadt, J., Pirrone, N., Sprovieri, F., Ammoscato, I., Esposito, G., Mannarino, V., Montagnoli, M., Brenninkmeijer, C., Rauthe-Schöch, A., Slemr. F., and van Velthoven, P.: Aircraft-based measurements during the 2012 Mt. Etna campaign, Etna campaign 2012 – data workshop, Hamburg/Germany, March 18-20, 2013.

Weigelt, A., Kock, H.-H., Ebinghaus, R., Bieber, E., Schwerin, A., Schütze, and M., Temme, C.: Atmosphärische Quecksilbermessungen im GMOS Projekt, Waldhof workshop 2012, Langenbrügge/Germany, May 02 – 04, 2012

Weigelt, A., Hermann, M., Brenninkmeijer, van Velthoven, P., Wiedensohler, A., Heintzenberg, J., and others: different talks to the development and data analysis of the new CARIBIC OPC during the annual CARIBIC meetings/workshops between 2007 and 2012, Karlsruhe/Germany, Mainz/Germany, Ringberg/Germany, Seeheim/Germany, 2007 – 2012.